DAMAGE OF AERO ENGINE DISKS IN FUNCTION OF CYCLIC MATERIAL PROPERTIES AND TYPE OF ENGINE START-STOP CYCLES

S. Posavljak[1)], M. Jankovic[2)], K. Maksimovic[3)]

[1] University of Banja Luka, Faculty of Mechanical Engineering
Vojvode Stepe Stepanovica 75, 78000 Banja Luka, Republic of Srpska
Bosnia and Herzegovina
e-mail: s.posavljak@urc.rs.ba
[2] University of Belgrade, Faculty of Mechanical Engineering
Kraljice Marije 16, 11120 Belgrade, Serbia
e-mail: mjankovic@mas.bg.ac.rs
[3] City of Belgrade, City Government, Secretariat for Communal and Housing Affairs,
Office of Water Management, Belgrade, Serbia
e-mail: tince@net.rs

Abstract. Damage of one aero engine disk, dominantly exposed to centrifugal forces of blades and own centrifugal forces, was discussed in this paper. It was assumed that steel 23H11N2V2MF in delivered and heat treatment state will be used for disk workmanship. One blade and critical disk area were observed as separated ideal elastic bodies. Their stress response for maximum rotation frequency was determined using the finite element method. Equivalent stress at critical point of disk was brought in relation with equivalent stress at corresponding point of disk when the same observed as blisk reduced on axisymmetrical problem. So-called equivalent stress concentration factor, was obtained in that way. This factor was used for defining of Sonsino-Birger's curve, which in combination with cyclic stress-strain and Masing's curves, used for determining of specters of real (elasto-plastic) strain amplitudes at disk critical point for three different start-stop cycles. These start-stop cycles, defined as blocks of rotation frequency, were decomposed at simple cycles. Elemental damages provoked by all simple cycles and damages per blocks were determined applying Palmgren-Miner's rule. Specters of real strain amplitudes, used for that purpose, were brought in relation with Morrow's curves of low cycle fatigue life. Both states, of above mentioned steel, known cyclic properties, were taken into account.

Keywords: aero engine disk, engine start-stop cycle, equivalent stress concentration factor, cyclic material properties, damages

1. Introduction

The damage of aero engine disks presents material degradation during their exploitation. Degree and rate of degradation depend on the material properties and realized engine start-stop cycles. Engine start-stop cycles can be described on different ways. For disks, dominantly exposed to centrifugal forces of blades and own centrifugal forces (fan and compressor disks), engine start-stop cycles are described by blocks of rotation frequency /n/ in time /t/. These disks work in conditions of low cycle fatigue (LCF) and their cyclic material properties are key properties.

Damage estimation of certain disk, dominantly exposed to centrifugal forces of blades and own centrifugal forces, understands knowing: engine start-stop cycles defined by blocks of rotation frequency, cyclic events in those blocks, cyclic properties of material used or nominated for workmanship and stress-strain response at critical point or point of expected crack initiation. Here observed certain disk is the first stage low pressure compressor rotor disk, of R25-300 aero engine.

2. The first stage low pressure compressor rotor disk of R25-300 aero engine

2.1. Engine start-stop cycles defined by blocks of rotation frequency

Three blocks of rotation frequency (blocks A, B and C) of the first stage low pressure compressor rotor, of R25-300 aero engine, in Fig. 1, here taken into account [1]. Block A presents one engine ground control and blocks B and C present two training flights.

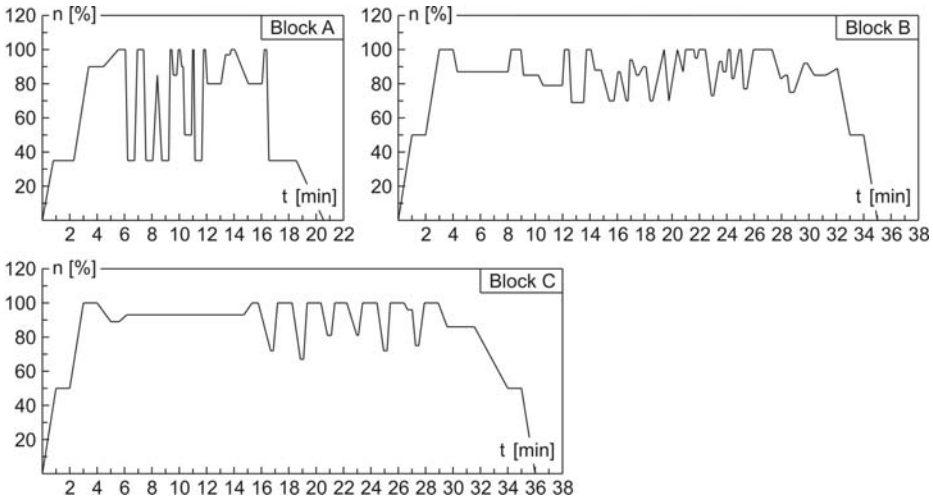

Figure 1. Blocks of rotation frequency of the first stage low pressure compressor rotor, of R25-300 aero engine

2.2. Cyclic events in blocks of rotation frequency

The blocks that shown in Fig. 1, were satisfying modified and decomposed on simple X-Y-X cycles of rotation frequency. Decomposition of mentioned blocks was carried out using method of "reservoir" [1,2]. All simple cycles present cyclic events within blocks A, B and C. Modified blocks with identified X-Y-X cycles of rotation frequency are shown in Fig. 2.

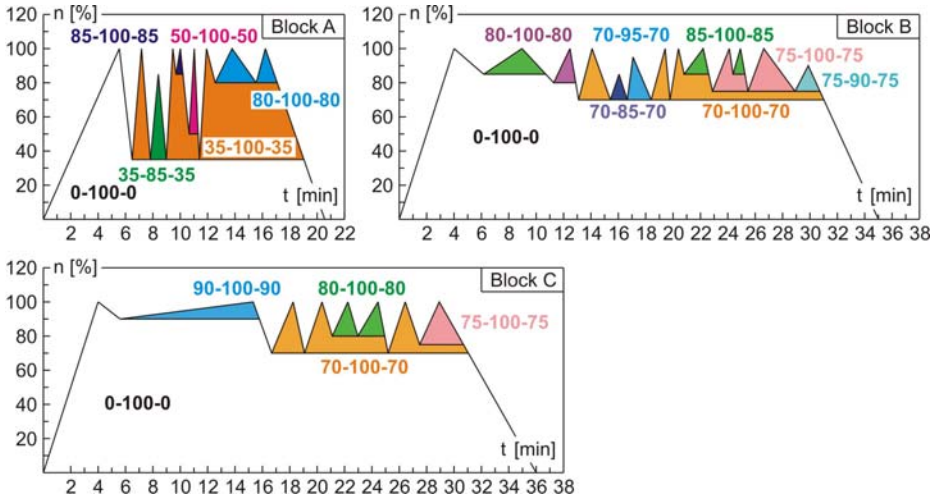

Figure 2. Modified blocks of rotation frequency with identified X-Y-X cycles of rotation frequency

Cyclic events (as simple X-Y-X cycles of rotation frequency) in the engine start-stop cycles (blocks of rotation frequency), sorted according to level /i/ and number /N_i/ of appearance within corresponding blocks, are included in Table 1.

Table 1. X-Y-X cycles of rotation frequency within blocks A, B and C, sorted according to level /i/ and number of apearance /N_i/ within blocks

Block A			Block B			Block C		
i	X_i - Y_i - X_i	N_i	i	X_i - Y_i - X_i	N_i	i	X_i - Y_i - X_i	N_i
1	0-100-0	1	1	0-100-0	1	1	0-100-0	1
2	35-100-35	3	2	70-100-70	3	2	70-100-70	3
3	50-100-50	1	3	75-100-75	2	3	75-100-75	1
4	80-100-80	2	4	80-100-80	1	4	80-100-80	2
5	85-100-85	1	5	85-100-85	3	5	90-100-90	1
6	35-85-35	1	6	70-95-70	1			
			7	75-90-75	1			
			8	70-85-70	1			

2.3. Cyclic material properties

Material that used for workmanship of the first stage low pressure compressor rotor disk, of R25-300 aero engine, is steel 13H11N2V2MF. Cyclic properties of this steel in delivered and heat treatment state, obtained experimentally [1], are contained in Table 2.

Table 2. Cyclic properties of steel 13H11N2V2MF in delivered state (DS) and heat treatment state (HTS)

No	PROPERTY	VALUE	
		DS	HTS
1.	Modulus of elasticity, E [MPa]	206682.0	229184.6
2.	Cyclic strength coefficient, K' [MPa]	1103.0	1140.0
3.	Cyclic strain hardening coefficient, n'	0.118	0.0579
4.	Fatigue strength coefficient, σ'_f [MPa]	1818.8	1557.3
5.	Fatigue strength exponent, b	-0.144	-0.0851
6.	Fatigue ductility coefficient, ε'_f	0.5351	0.3175
7.	Fatigue ductility exponent, c	-0.6619	-0.7214

2.3. Stress-strain response at critical disk point

For determining of stress-strain response at critical disk point, it was enough observe one blade and critical disk area (at the first as ideal elastic bodies). Linear stress response of blade and nodal reactions at the blade root contact surfaces, in conditions of maximal rotation frequency n = 100 % (186 s^{-1}), were obtained using the finite element method [1,3] (FEM). Using FEM and the same rotation frequency, mentioned reactions in transformed form used as nodal forces for obtaining of linear stress response of critical disk area. Axisymmetrical linear stress response of disk, when it observed as blisk (**bl**aded d**isk**), was obtained also (see Fig. 3). Modulus of elasticity E=229184.6 MPa, Poison's coefficient ν=0.29, shear modulus G=88831.24 and mass density ρ=7820 kg/m^2, of steel 13H11N2V2MF in heat treatment state, assigned to all FEM models.

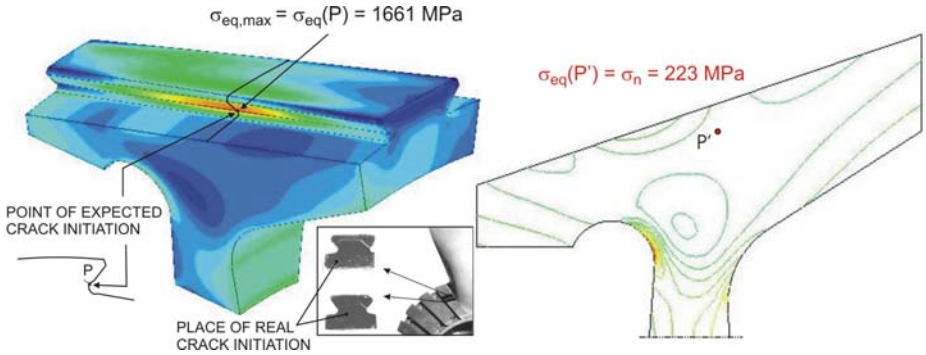

Figure 3. Linear stress response of critical disk area (left) and linear axisymmetrical stress response of the same disk when it observed as blisk (right)

According to Fig. 3, maximal equivalent stress $\sigma_{eq,max}$ at point of expected crack initiation (critical point P) and belonging strain are unreal (mentioned stress is much higher than tensile strength R_m=1000 MPa, of steel 13H11N2V2MF in heat treatment state). It can see

that critical point P corresponds to real crack initiation. Equivalent stress at point P' of blisk, which corresponds to critical disk point P, taken as nominal stress σ_n, was used for calculation of so-called equivalent stress concentration factor K_{eq} = 7.45. This factor, defined as ratio of $\sigma_{eq,max}$ and σ_n was served for transformation of linear stress-strain response at critical disk point, into nonlinear. Respecting memory of metals, nonlinear stress-strain response at critical disk point, using Sonsino-Birger's approach, here described by stabilized hysteresis loops assigned to all cycles of rotation frequency contained in Table 1. Sonsino-Birger's approach [4,5,6] presents one of Neuber's rule modifications. This approach is based on application of the next systems of equations.

$$\begin{aligned}
&\varepsilon = \frac{1}{2}\frac{K_{eq}\cdot\sigma_{ni}}{E}\left(\frac{K_{eq}\cdot\sigma_{ni}}{\sigma}+1\right)\\
&\varepsilon = \frac{\sigma}{E}+\left(\frac{\sigma}{K'}\right)^{\frac{1}{n'}} \qquad .\\
&\left(i_A = i_B = i_C = 1\right)
\end{aligned} \tag{1}$$

$$\begin{aligned}
&\Delta\varepsilon = \frac{1}{2}\frac{K_{eq}\cdot\Delta\sigma_{ni}}{E}\left(\frac{K_{eq}\cdot\Delta\sigma_{ni}}{\Delta\sigma}+1\right)\\
&\Delta\varepsilon = \frac{\Delta\sigma}{E}+2\left(\frac{\Delta\sigma}{2K'}\right)^{\frac{1}{n'}} \qquad .\\
&\left(i_A / i_B / i_C = 1,2,...,6 / 1,2,...,8 / 1,2,...,5\right)
\end{aligned} \tag{2}$$

The first equations in systems (1) and (2) are two forms of Sinsinio-Birger's curve. The second equation in (1) is equation of cyclic stress-strain curve and the second equation in (2) is equation of Masing's curve [7]. The values of nominal stresses σ_{ni} and their ranges $\Delta\sigma_{ni}$, that used in (1) and (2), were calculated using the next expressions

$$\begin{aligned}
&\sigma_{ni} = 223\cdot\left(\frac{Y_i}{100}\right)^2\\
&\Delta\sigma_{ni} = 223\cdot\left[\left(\frac{Y_i}{100}\right)^2-\left(\frac{X_i}{100}\right)^2\right] \qquad .\\
&\left(i_A / i_B / i_C = 1,2,...,6 / 1,2,...,8 / 1,2,...5\right)
\end{aligned} \tag{3}$$

The values of cyclic properties, used in (1) and (2), with known equivalent stress concentration factor K_{eq}, were taken from Table 2. The example of nonlinear stress-strain response at critical disk point, provoked by block of rotation frequency A, is shown in Fig. 4.

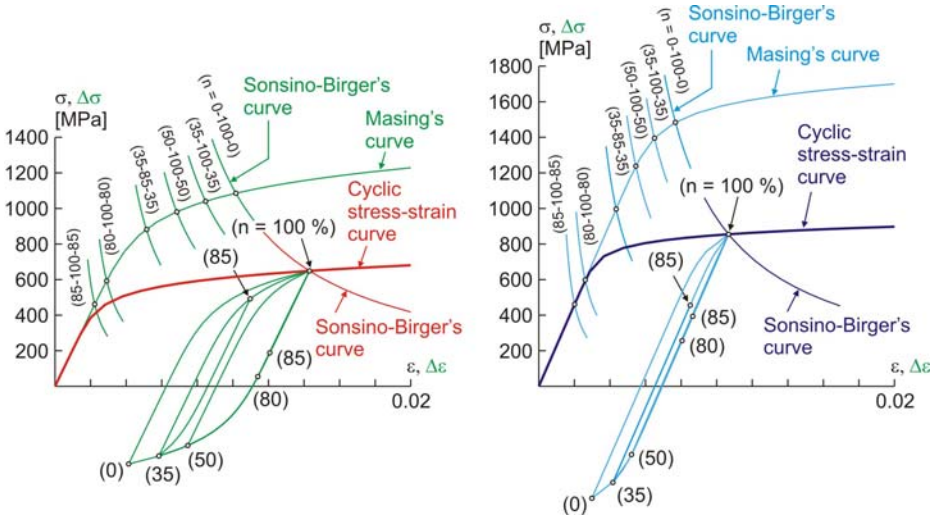

Figure 4. Nonlinear stress-strain response at critical disk point, provoked by block of rotation frequency A, in the case of steel 13H11N2V2MF in delivered state (left) and heat treatment state (right)

The first point of nonlinear stress-strain response at critical disk point (n=100 %) obtained using system of equation (1). Dimensions ($\Delta\varepsilon\times\Delta\sigma$) of stabilized hysteresis loops were obtained using system of equation (2). Modeling of these hysteresis loops was carried out using corresponding Masing's curves. Numerical results of nonlinear stress-strain response at critical disk point are included in Table 3, Table 4 and Table 5. Mean stresses in those tables marked with σ_{mi}.

Table 3. Block of rotation frequency A: Numerical results of nonlinear stress-strain response at critical disk point provoked by X-Y-X cycles in the case of steel 13H11N2V2MF in delivered state (DS) and heat treatment state (HTS)

i	$X_i - Y_i - X_i$ [%]	DS			HTS		
		σ_{mi} [MPa]	$\Delta\sigma_i$ [MPa]	$\Delta\varepsilon_i$	σ_{mi} [MPa]	$\Delta\sigma_i$ [MPa]	$\Delta\varepsilon_i$
1	0-100-0	106.149	1085.673	0.01016932	112.778	1484.231	0.00768147
2	35-100-35	128.664	1040.643	0.00846854	157.173	1395.440	0.00650403
3	50-100-50	158.157	981.656	0.00684357	235.722	1238.343	0.00545603
4	80-100-80	351.909	594.152	0.00290441	555.780	598.227	0.00261026
5	85-100-85	418.642	460.687	0.00223237	624.315	461.157	0.00201214
6	35-85-35	50.092	883.498	0.00513218	-42.239	996.615	0.00434976

Table 4. Block of rotation frequency B: Numerical results of nonlinear stress-strain response at critical disk point provoked by X-Y-X cycles in the case of steel 13H11N2V2MF in delivered state (DS) and heat treatment state (HTS)

i	$X_i - Y_i - X_i$ [%]	DS			HTS		
		σ_{mi} [MPa]	$\Delta\sigma_i$ [MPa]	$\Delta\varepsilon_i$	σ_{mi} [MPa]	$\Delta\sigma_i$ [MPa]	$\Delta\varepsilon_i$
1	0-100-0	106.149	1085.673	0.01016932	112.778	1484.231	0.00768147
2	70-100-70	249.921	798.129	0.00422408	431.368	847.050	0.00369601
3	75-100-75	294.500	708.971	0.00356308	491.333	727.121	0.00317266
4	80-100-80	351.909	594.152	0.00290441	555.780	598.227	0.00261026
5	85-100-85	418.642	460.687	0.00223237	624.315	461.157	0.00201214
6	70-95-70	187.661	673.610	0.00334528	350.542	685.396	0.00299058
7	75-90-75	145.545	411.061	0.00199016	410.124	564.704	0.00246396
8	70-85-70	43.759	385.805	0.00186740	200.794	385.902	0.00168384

Table 5. Block of rotation frequency C: Numerical results of nonlinear stress-strain response at critical disk point provoked by X-Y-X cycles in the case of steel 13H11N2V2MF in delivered state (DS) and heat treatment state (HTS)

i	$X_i - Y_i - X_i$ [%]	DS			HTS		
		σ_{mi} [MPa]	$\Delta\sigma_i$ [MPa]	$\Delta\varepsilon_i$	σ_{mi} [MPa]	$\Delta\sigma_i$ [MPa]	$\Delta\varepsilon_i$
1	0-100-0	106.149	1085.673	0.01016932	112.778	1484.231	0.00768147
2	70-100-70	249.921	798.129	0.00422408	431.368	847.050	0.00369601
3	75-100-75	294.500	708.971	0.00356308	491.333	727.121	0.00317266
4	80-100-80	351.909	594.152	0.00290441	555.780	598.227	0.00261026
5	90-100-90	491.416	291.168	0.00140885	699.721	291.171	0.00127051

2.4. Damages at critical disk point

Damages D_A, D_B and D_C provoked by blocks of rotation frequency A, B and C, of observed disk, here is determined using Palmgren-Miner's rule of linear damage accumulation [8,9,10,11].

$$D_A = \sum_{i=1}^{6} (D_i)_A = \sum_{i=1}^{6} \left(\frac{N_i}{N_{fi}} \right)_A$$
$$D_B = \sum_{i=1}^{8} (D_i)_B = \sum_{i=1}^{8} \left(\frac{N_i}{N_{fi}} \right)_B \quad (4)$$
$$D_C = \sum_{i=1}^{5} (D_i)_C = \sum_{i=1}^{5} \left(\frac{N_i}{N_{fi}} \right)_C$$

In the above expressions, the damages provoked by X_i–Y_i–X_i cycles of rotation frequency, are marked with D_i. These damages present relation between number of appearance N_i of certain cycle, and number N_{fi} of the same cycle which material of disk can endure up to appearance of initial crack. Number N_i are contained in Table 1 and numbers N_{fi} were determined by solving of systems of equations

$$\frac{\Delta\varepsilon}{2} = \frac{\sigma_f^{'} - \sigma_{mi}}{E} N_f^b + \varepsilon_f^{'} N_f^c$$
$$\frac{\Delta\varepsilon}{2} = \frac{\Delta\varepsilon_i}{2} \quad (5)$$
$$\left(i_A / i_B / i_C = 1,2,...,6 / 1,2,...,8 / 1,2,...,5 \right)$$

The first equation in (5) is equation of Morrow's curve of LCF that mean stresses σ_{mi} takes into account [7,12,13]. The values $\Delta\varepsilon_i$ in the second equation, were taken from Tables 3, 4 and 5. Needed cyclic properties used in system (5) were taken from Table 2. N_i, N_{fi}, D_i, D_A, D_B and D_C data set, for blocks A, B and C, are included in Tables 6, 7 and 8.

Table 6. Block of rotation frequency A: N_i, N_{fi}, D_i and D_A data set, in the case of steel 13H11N2V2MF in delivered state (DS) and heat treatment state (HTS)

i	X_i - Y_i - X_i	N_i	DS		HTS	
			N_{fi}	D_i	N_{fi}	D_i
1	0-100-0	1	3308	0.00030230	4361	0.00022931
2	35-100-35	3	5226	0.00057405	9141	0.00032819
3	50-100-50	1	9278	0.00010778	20263	0.00004935
4	80-100-80	2	162040	0.00001234	1616158	0.00000124
5	85-100-85	1	495345	0.00000202	8436377	0.00000012
6	35-85-35	1	28078	0.00003562	968810	0.00000103
			D_A=	0.00103411	D_A=	0.00060924

Table 7. Block of rotation frequency B: N_i, N_{fi}, D_i and D_B data set, in the case of steel 13H11N2V2MF in delivered state (DS) and heat treatment state (HTS)

i	X_i - Y_i - X_i	N_i	DS		HTS	
			N_{fi}	D_i	N_{fi}	D_i
1	0-100-0	1	3308	0.00030230	4361	0.00022931
2	70-100-70	3	41444	0.00007239	144149	0.00002081
3	75-100-75	2	75107	0.00002663	385402	0.00000519
4	80-100-80	1	162040	0.00000617	1616158	0.00000062
5	85-100-85	3	495345	0.00000606	8436377	0.00000036
6	70-95-70	1	128512	0.00000778	2808943	0.00000036
7	75-90-75	1	2603688	0.00000038	1269290413	0.00000000
8	70-85-70	1	5644896	0.00000018	8942212789	0.00000000
			D_B =	0.00042188	D_B =	0.00025664

Table 8. Block of rotation frequency C: N_i, N_{fi}, D_i and D_C data set, in the case of steel 13H11N2V2MF in delivered state (DS) and heat treatment state (HTS)

i	X_i - Y_i - X_i	N_i	DS		HTS	
			N_{fi}	D_i	N_{fi}	D_i
1	0-100-0	1	3308	0.00030230	4361	0.00022931
2	70-100-70	3	41444	0.00007239	144149	0.00002081
3	75-100-75	1	75107	0.00002663	385402	0.00000259
4	80-100-80	2	162040	0.00000617	1616158	0.00000124
5	90-100-90	1	3342689	0.00000090	448824959	0.00000000
			D_C =	0.00040838	D_C =	0.00025395

Systematized data about damages of the first stage low pressure compressor rotor disk of R25-300 aero engine, in the case of application of steel 13H11N2V2MF in delivered and heat treatment state, for three start-stop cycles (blocks of rotation frequency), are given in Table 9.

Table 9. Systematized data about damages of the first stage low pressure compressor rotor disk, of R25-300 aero engine, in the case of application of steel 13H11N2V2MF in delivered and heat treatment state

No	Material	Damages				
		Block A	Block B	Block C	Average B and C	
		1	2	3	4	1/4
1	Steel 13H11N2V2MF in delivered state	0.00103411	0.00042188	0.00040838	0.00041513	2.49
2	Steel 13H11N2V2MF in heat treatment state	0.00060924	0.00025664	0.00025395	0.000255295	2.39
1/2		1.70	1.64	1.61	1.63	

According to Table 9 it can see that damages of our disk, in the case of steel 13H11N2V2MF in delivered state are significantly higher than damages in the case of the same steel in heat treatment state. On the other hand, greater differences we have between damages caused by engine ground controls (block A) and damages caused by engine flights (blocks B and C). Differences in damages are presented and by hystogram in Fig. 5.

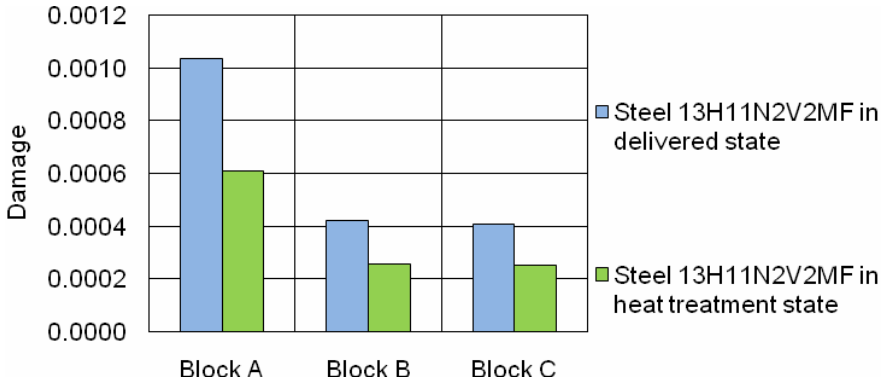

Figure 5. Hystogram of damages

3. Conclusion

Methodology of damage estimation, applied for the first stage low pressure compressor rotor disk, of R25-300 aero engine, can be applied for all disks dominantly exposed to centrifugal forces of blades and own centrifugal forces.
This methodology can be applied and for temperature loaded disks. In that case, estimated damage caused by centrifugal forces, is one of two or more components of caused damage.
Monitoring of exploitation of aero engine disks, for the purpose of aero engine maintenance according to the state, should be based on automatic recording accumulated damages during aero engine ground controls and during flights.
In accordance with a rule of linear damage accumulation, aero engine disks would be pulld from exploitation with damage equal to one.
Complete results of this paper can serve for further investigations in relation with damages and fatigue life of aero engine disks in function of cyclic material properties and in function of engine start-stop cycles.
The final goal of designers should be directed to reducing possible damages in critical disk areas using alloys with satisfying cyclic properties.

References

[1] Posavljak, S. (2008) Fatigue Life Investigation of Aero Engine Rotating Disks, Doctoral dissertation (in Serbian), University of Belgrade, Faculty of Mechanical Engineering.
[2] Kostaes, D. (1994) Fatigue Behaviour and Analysis, Talat Lecture 2401, Technishe Universität München, EAA – European Aluminium Association.
[3] Lawry M. H. (1998) I-DEAS Master Series, Mechanical CAE/CAD/CAM Software, Student Guide, Structural Dynamics Research Corporation, SDRC Part Number P-60002
[4] Sonsino, C.M. (1993), Zur Bewertung des Schwingfestigkeitsverhaltens von Bauteilen mit Hilife örtlicher Beanspruchungen, Konstruktion 45, 25-33.
[5] Sonsino, C.M. (1982) Einfluss von Kaltverformungen bis 5% auf das Kurzzeitschwingfestigkeits-verhalten metallischer Werkstoffe, Dissertation, Vom Fachbereich Machinenbau an der Technischen Hochschule Darmstadt.
[6] Birger, I. A. (1985) Prognozirovanie resursa pri malociklovoj ustalosti, Problemy prochnosti, No 10, 39-44.
[7] Bannantine, J.A., Comer, J., Handrock, J. (1990) Fundamentals of Material Fatigue Analysis, Prentice-Hall, Englewood Clifs, New Jersy.
[8] Jankovic, M. (2001) Low Cycle Fatigue (in Serbian), University of Belgrade, Faculty of Mechanical Engineering.
[9] Palmgren, A. (1924) Die Lebensdauer von Kugellagern, Verfahenstechnik, Berlin, 68, 339-341.
[10] Miner, M. A. (1945), Cumulative Damage in Fatigue, Journal of Applied Mechanics, 76, A159-164.
[11] Fatemy, A., Yang, L. (1998) Cumulative Fatigue Damage and Life Prediction Theories: A Survey of the State af the Art for Homogeneous Materials, International Journal of Fatigue, Vol. 20, No. 1, pp. 9-34
Morrow, J. (1968) Fatigue Design Handbook, Advances in Fatigue, Vol. 4. Society of Automotive Engineers, Warrendale, Pa., Sec 3.2, pp. 21-29.
[12] Maksimovic, S., Posavljak, S., Maksimovic, K., Nikolic, V., Djurkovic, V. (2010) Total Fatigue Life Estimation of Notched Structural Components Using Low Cycle Fatigue Properties, Journal STRAIN, The paper accepted for publication, http://onlinelibrary.wiley.com.proxy.kobson.nb.rss:2048/journal/10.1111/(ISSN)1475-1305/earlyview
[13] Posavljak S., Jankovic, M., Djurdjevic, M. (2011), Crack Initiation Life of Turbojet Engine Disks Expressed in Equivalent Cycles, The 7th International Conference, Research and Development of Mechanical Components and Systems, Proceedings, Universiti og Nis, Mechanical Engineering Faculty, April 27th to 28th, Zlatibor, Serbia.

STRESS INTEGRATION OF THE MOHR-COULOMB MATERIAL MODEL USING INCREMENTAL PLASTICITY THEORY

D. Rakić[1], M. Živković[2]

[1] Faculty of Mechanical Engineering
The University of Kragujevac, Sestre Janjić 6, 34000 Kragujevac
e-mail: drakic@kg.ac.rs
[2] Faculty of Mechanical Engineering,
The University of Kragujevac, Sestre Janjić 6, 34000 Kragujevac
e-mail: zile@kg.ac.rs

Abstract. This paper presents the formulation of the stress integration procedure for the Mohr-Coulomb material model with non-associative yielding condition by using the incremental plasticity theory. The idea of this method is to reach the solution by calculating the constitutive plastic matrix according to the method of incremental plasticity (used for elastic constitutive matrix corrections), and with use of the total strain increment. The computational procedure is implemented within the PAK program package. Results of this procedure were compared with the solutions obtained by the other program packages that contain this material model.

1. Introduction

Stress integration represents calculation of stress change during an incremental step, corresponding to strain increments in the step [1]. It is in essence the incremental integration of inelastic constitutive relations to trace the history of material deformation. The stress integration is an important ingredient in the overall finite element inelastic analysis of structures. It is important that the integration algorithm accurately reproduces the material behavior since the mechanical response of the entire structure is directly dependent on this accuracy. The algorithm should be also computationally efficient because the stress integration is performed at all integration points. For general applications, this computational procedure should be robust, providing reliable results under all possible loading conditions. In this paper we present a formulation of the computational algorithm for the Mohr-Coulomb material model using an incremental plasticity approach. The results using this approach were compared with the results obtained using the similar material models, like Drucker-Prager [2], as well as with results obtained by using other software packages.
In the next section we present formulation the Mohr-Coulomb material model, followed by the derivation of the elastic-plastic constitutive matrix in general associated plasticity. Then, the general relations are implemented in Mohr-Coulomb material model.

2. Formulation of the Mohr-Coulomb model

This material model is defined by the yield surface called the Mohr-Coulomb yield surface. In the space of principal stresses, this surface represents by hexagonal pyramid, whose axis

matches the space diagonal of the coordinate system of principal stresses $\sigma_1, \sigma_2, \sigma_3$ (Figure 1).

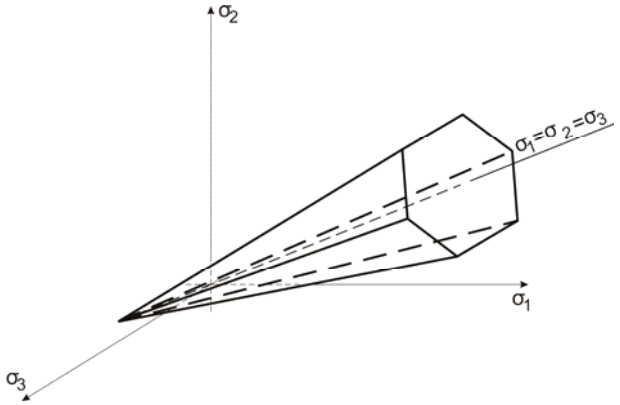

Figure 1. Mohr-Coulomb yield surface

In deviatoric plane model can be represented together with Drucker-Prager material model (Figure 2). The figure shows that two yield surfaces can be defined in few ways relative to each other, depending on what type of analysis is performed.

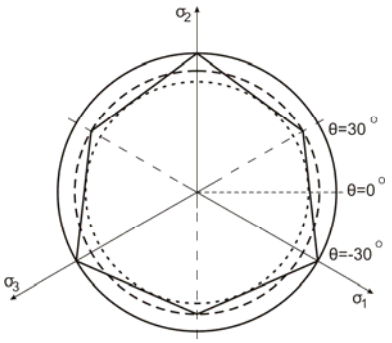

Figure 2. Mohr-Coulomb and Drucker-Prager material model in deviatoric plane

The material constants of Mohr-Coulomb material model, in relation to Drucker-Prager model can be recalculated using the following expressions [3]:

$$\alpha = \frac{2\sin\phi}{\sqrt{3}\left(3-\sin\phi\right)}, \quad k = \frac{6c\cos\phi}{\sqrt{3}\left(3-\sin\phi\right)} \tag{1}$$

where c and ϕ are material constants (cohesion and internal friction angle) for Mohr-Coulomb material model and k and α are material constants for Drucker-Prager material model.

The elastic domain is bounded by the Mohr-Coulomb yield surface and by the maximum tension line – with the tension cutoff limit stress T. If the stress point of a trial solution is out of the Mohr-Coulomb hexagonal pyramid, the stress at the end of step has to be reduced to satisfy the following yield condition (Mohr-Coulomb yield surface):

$$F = \frac{I_1}{3}\sin\phi + \sqrt{{}^{t}J_{2D}}\left(\cos\theta - \frac{1}{\sqrt{3}}\sin\theta\sin\phi\right) - c\cos\phi \tag{2}$$

where:

$$I_1 = 3\sigma_m = \sigma_{ij}\delta_{ij} = \sigma_{ii} \tag{3}$$

is the first stress invariant, and

$$J_{2D} = \frac{1}{2}S_{ij}S_{ij} \tag{4}$$

is the second invariant of the deviatoric stress. Deviatoric stress S_{ij} is defined as:

$$S_{ij} = \sigma_{ij} - \sigma_m\delta_{ij} \tag{5}$$

If the stress exceeds the allowed tension stress value, the stress reduction is performed by using next equation [4]:

$$\sigma_{11} = \sigma_{22} = \sigma_{33} = \frac{T}{3} \tag{6}$$

while the shear stress components are set to zero:

$$\sigma_{ij} = 0 \qquad i \neq j \tag{7}$$

3. Elastic-plastic constitutive matrix

For an elastic-plastic material, the stress increment $\{d\sigma\}$ can be expressed by the total strain increment $\{de\}$ as

$$\{d\sigma\} = \left[C^{EP}\right]\{de\} \tag{8}$$

where $\left[C^{EP}\right]$ is the elastic-plastic constitutive matrix defined below. In the case of small strain, the total strain increment can be divided into elastic and plastic part:

$$\{de\} = \{de^E\} + \{de^P\} \tag{9}$$

The stress and elastic strain increments are related by the elastic constitutive law:

$$\{d\sigma\} = \left[C^E\right]\{de^E\} \tag{10}$$

where $\left[C^E\right]$ is elastic constitutive matrix. Substituting (9) into (10), we obtain:

$$\{d\sigma\} = \left[C^E\right]\left(\{de\} - \{de^P\}\right) \tag{11}$$

We next include into this derivation a yield function *F*, which in general has a form:

$$F = F(\boldsymbol{\sigma}) \equiv F(\sigma_{ij}) \tag{12}$$

A differential of the yield function can be expressed as:

$$dF = \frac{\partial F}{\partial \sigma_{xx}} d\sigma_{xx} + \frac{\partial F}{\partial \sigma_{yy}} d\sigma_{yy} + \frac{\partial F}{\partial \sigma_{zz}} d\sigma_{zz} + \frac{\partial F}{\partial \sigma_{xy}} d\sigma_{xy} + \frac{\partial F}{\partial \sigma_{yz}} d\sigma_{yz} + \frac{\partial F}{\partial \sigma_{zx}} d\sigma_{zx} \tag{13}$$

or in matrix form:

$$dF = \left\{\frac{\partial F}{\partial \sigma}\right\}^T \{d\sigma\} \tag{14}$$

In the incremental theory of plasticity we have that the yield function during plastic deformation must be equal to zero (when $F \le 0$ we have elastic unloading), hence $F = 0$ and consequently $dF = 0$ is satisfied over the load step. Using this condition, the last equation can be written in the following form:

$$dF = \left\{\frac{\partial F}{\partial \sigma}\right\}^T \{d\sigma\} = 0 \tag{15}$$

where $\left\{\frac{\partial F}{\partial \sigma}\right\}^T$ is

$$\left\{\frac{\partial F}{\partial \sigma}\right\}^T = \left[\frac{\partial F}{\partial \sigma_{xx}} \quad \frac{\partial F}{\partial \sigma_{yy}} \quad \frac{\partial F}{\partial \sigma_{zz}} \quad \frac{\partial F}{\partial \sigma_{xy}} \quad \frac{\partial F}{\partial \sigma_{yz}} \quad \frac{\partial F}{\partial \sigma_{zx}}\right] \tag{16}$$

whereas $\{d\sigma\}$ is

$$\{d\sigma\} = \left[d\sigma_{xx} \quad d\sigma_{yy} \quad d\sigma_{zz} \quad d\sigma_{xy} \quad d\sigma_{yz} \quad d\sigma_{zx}\right] \tag{17}$$

Further, we assume a non-associative plasticity, therefore the increment of plastic strain is

$$\{de^P\} = d\lambda \left\{\frac{\partial G}{\partial \sigma}\right\} \tag{18}$$

where: $G(\boldsymbol{\sigma})$ is the plastic potential function, and $d\lambda$ is a plastic scaling factor.
Substituting the plastic strain increment (18) into (11), we obtain the stress increment:

$$\{d\sigma\} = \left[C^E\right]\{de\} - d\lambda\left[C^E\right]\left\{\frac{\partial G}{\partial \sigma}\right\} \tag{19}$$

Now, we substitute this stress increment into (15):

$$dF = \left\{\frac{\partial F}{\partial \sigma}\right\}^T \left(\left[C^E\right]\{de\} - d\lambda\left[C^E\right]\left\{\frac{\partial G}{\partial \sigma}\right\}\right) = 0 \tag{20}$$

Using (20) plastic scaling factor $d\lambda$ is:

$$d\lambda = \frac{\left\{\frac{\partial F}{\partial \sigma}\right\}^T \left[C^E\right]\{de\}}{\left\{\frac{\partial F}{\partial \sigma}\right\}^T \left[C^E\right]\left\{\frac{\partial G}{\partial \sigma}\right\}} \tag{21}$$

Finally, substituting $d\lambda$ from (21) into (19), obtain the relationship between $\{d\sigma\}$ and the total strain increment $\{de\}$:

$$\{d\sigma\} = \left[C^E\right]\{de\} - \frac{\left[C^E\right]\left\{\frac{\partial G}{\partial \sigma}\right\}\left\{\frac{\partial F}{\partial \sigma}\right\}^T \left[C^E\right]\{de\}}{\left\{\frac{\partial F}{\partial \sigma}\right\}^T \left[C^E\right]\left\{\frac{\partial G}{\partial \sigma}\right\}} \tag{22}$$

Comparing (22) and equation (8) it follows:

$$\left[C^{EP}\right] = \left[C^E\right] - \frac{\left[C^E\right]\left\{\frac{\partial G}{\partial \sigma}\right\}\left\{\frac{\partial F}{\partial \sigma}\right\}^T \left[C^E\right]}{\left\{\frac{\partial F}{\partial \sigma}\right\}^T \left[C^E\right]\left\{\frac{\partial G}{\partial \sigma}\right\}} \tag{23}$$

This is a general expression for the elastic-plastic constitutive matrix. Also, by substituting (21) into (18) we can calculate the plastic strain increment $\left\{de^P\right\}$.

In the case of associative plasticity the yield function F is at the same time the plastic potential function G. In our implementation of the above general expressions to the Mohr-Coulomb model we will adopt the non-associative plasticity assumption. This representation of the model is suitable for development of the computational procedure for each material model, whose yield function can be expressed in terms of stress invariants.

4. Implementation of the general associative plasticity relations to the Mohr-Coulomb material model

Mohr-Coulomb yield function is defined by the equation (2), while the plastic potential function is defined by:

$$G = \frac{I_1}{3}\sin\psi + \sqrt{{}^t J_{2D}}\left(\cos\theta - \frac{1}{\sqrt{3}}\sin\theta\sin\psi\right) - c\cos\psi \tag{24}$$

where I_1 represents the first stress invariant, while J_{2D} is the second deviatoric stress invariant, as given by (3) and (4), while ψ is dilatation angle.

In the equation of the yield surface (2) and the plastic potential function (24) entity θ represents Lode's angle which is given by:

$$\theta = \frac{1}{3}\arcsin\left(-\frac{3\sqrt{3}}{2}\frac{J_{3D}}{J_{2D}^{3/2}}\right) \tag{25}$$

where J_{3D} is third deviatoric stress invariant.

In the case when in equations (2) and (24) $\phi = \psi$ we have the case of so-called associative flow rule, when the yield function is identical as the plastic potential.

Derivative of Mohr-Coulomb yield function with respect stress can be calculated using the chain rule:

$$\left\{\frac{\partial F}{\partial \sigma}\right\}^T = \frac{\partial F}{\partial I_1}\left\{\frac{\partial I_1}{\partial \sigma}\right\}^T + \frac{\partial F}{\partial J_{2D}}\left\{\frac{\partial J_{2D}}{\partial \sigma}\right\}^T + \frac{\partial F}{\partial \theta}\left\{\frac{\partial \theta}{\partial \sigma}\right\}^T \tag{26}$$

Derivative of Mohr-Coulomb yield function (2) with respect first stress invariant is:

$$\frac{\partial F}{\partial I_1} = -\frac{\sin\phi}{3} \tag{27}$$

and derivative yield function with respect second stress invariant:

$$\frac{\partial F}{\partial J_{2D}} = \frac{1}{2\sqrt{J_{2D}}}\left\{\cos\theta - \frac{1}{\sqrt{3}}\sin\theta\sin\phi\right\} \tag{28}$$

while the derivative of yield function with respect Lode's angle is:

$$\frac{\partial F}{\partial \theta} = -\sqrt{J_{2D}}\left(\sin\theta + \frac{\cos\theta\sin\phi}{\sqrt{3}}\right) \tag{29}$$

Derivative of the first stress invariant is:

$$\left\{\frac{\partial I_1}{\partial \sigma}\right\}^T = \begin{bmatrix}1 & 1 & 1 & 0 & 0 & 0\end{bmatrix} \tag{30}$$

and derivative of the second stress invariant:

$$\left\{\frac{\partial J_{2D}}{\partial \sigma}\right\}^T = \begin{bmatrix}\frac{1}{3}(2\sigma_1 - \sigma_2 - \sigma_3) & \frac{1}{3}(-\sigma_1 + 2\sigma_2 - \sigma_3) & \frac{1}{3}(-\sigma_1 - \sigma_2 + 2\sigma_3) & 2\sigma_4 & 2\sigma_5 & 2\sigma_6\end{bmatrix} \tag{31}$$

while derivative of the Lode's angle is:

$$\left\{\frac{\partial \theta}{\partial \sigma}\right\}^T = \frac{\partial \theta}{\partial J_{3D}}\left\{\frac{\partial J_{3D}}{\partial \sigma}\right\}^T + \frac{\partial \theta}{\partial J_{2D}}\left\{\frac{\partial J_{2D}}{\partial \sigma}\right\}^T \tag{32}$$

Derivative of the Lode's angle with respect the second and third deviatoric stress invariant:

$$\frac{\partial \theta}{\partial J_{2D}} = \frac{3J_{3D}}{2J_{2D}^{5/2}\sqrt{\frac{4}{3} - \frac{9J_{3D}^2}{J_{2D}^3}}} \tag{33}$$

$$\frac{\partial \theta}{\partial J_{3D}} = -\frac{1}{J_{2D}^{3/2}\sqrt{\frac{4}{3} - \frac{9J_{3D}^2}{J_{2D}^3}}} \tag{34}$$

Derivative of the third deviatoric stress invariant can be calculated as:

$$\left\{\frac{\partial J_{3D}}{\partial \sigma}\right\}^T = \frac{\partial J_{3D}}{\partial I_1}\left\{\frac{\partial I_1}{\partial \sigma}\right\}^T + \frac{\partial J_{3D}}{\partial I_2}\left\{\frac{\partial I_2}{\partial \sigma}\right\}^T + \frac{\partial J_{3D}}{\partial I_3}\left\{\frac{\partial I_3}{\partial \sigma}\right\}^T \tag{35}$$

where the derivative of the third deviatoric stress invariant with respect the first stress invariant is:

$$\frac{\partial J_{3D}}{\partial I_1} = \frac{2}{9}I_1^2 + \frac{1}{3}I_2 \tag{36}$$

Derivative of the third deviatoric stress invariant with respect the second stress invariant:

$$\frac{\partial J_{3D}}{\partial I_2} = \frac{1}{3}I_1 \tag{37}$$

while the derivative with respect third stress invariant:

$$\frac{\partial J_{3D}}{\partial I_3} = 1 \tag{38}$$

Derivative of the first stress invariant is given by (30), while the derivative of the second stress invariant with respect stress tensor is:

$$\left\{\frac{\partial I_2}{\partial \sigma}\right\}^T = \begin{bmatrix}\sigma_2+\sigma_3 & \sigma_1+\sigma_3 & \sigma_1+\sigma_2 & -2\sigma_4 & -2\sigma_5 & -2\sigma_6\end{bmatrix} \tag{39}$$

Derivative of the third stress invariant with respect stress tensor is:

$$\left\{\frac{\partial I_3}{\partial \sigma}\right\}^T = \begin{bmatrix}\sigma_2\sigma_3-\sigma_4^2 & \sigma_1\sigma_3-\sigma_5^2 & \sigma_1\sigma_2-\sigma_6^2 & 2\sigma_5\sigma_6-2\sigma_1\sigma_4 & 2\sigma_4\sigma_6-2\sigma_2\sigma_5 & 2\sigma_4\sigma_5-2\sigma_6\sigma_6\end{bmatrix} \tag{40}$$

In a similar way we can calculate the plastic potential function derivative, where in equations (27) to (29) we replace yield function F by the plastic potential function G. In the case of the associative flow rule, these functions are identical.

Table 1. Algorithm for incremental stress integration

Known quantities: $\left\{{}^{t+\Delta t}e\right\}$, $\left\{{}^{t}e\right\}$, $\left\{{}^{t}\sigma\right\}$, $\left\{{}^{t}e^{p}\right\}$
A. **Trial (elastic) solutions**:
$\{d\sigma\} = [C_e]\{de^E\} = [C_e]\left(\left\{{}^{t+\Delta t}e\right\} - \left\{{}^{t}e\right\}\right)$
$\left\{{}^{t+\Delta t}\sigma\right\} = \left\{{}^{t}\sigma\right\} + \{d\sigma\}$
$I_1 = \sigma_1 + \sigma_2 + \sigma_3$
$I_2 = \sigma_1\sigma_2 + \sigma_2\sigma_3 + \sigma_3\sigma_1 - \sigma_4^2 - \sigma_5^2 - \sigma_6^2$

$$I_3 = \sigma_1\sigma_2\sigma_3 - \sigma_1\sigma_5^2 - \sigma_2\sigma_6^2 - \sigma_3\sigma_4^2 + 2\sigma_4\sigma_5\sigma_6$$

$$J_{2D} = \frac{1}{6}\left[(\sigma_1-\sigma_2)^2 + (\sigma_2-\sigma_3)^2 + (\sigma_3-\sigma_1)^2\right] + \sigma_4^{\,2} + \sigma_5^{\,2} + \sigma_6^{\,2}$$

$$J_{3D} = I_3 - \frac{1}{3}I_1I_2 + \frac{2}{27}I_1^3$$

$$\theta = \frac{1}{3}arcsin\left(-\frac{3\sqrt{3}}{2}\frac{J_{3D}}{J_{2D}^{3/2}}\right) \qquad \left(-\frac{\pi}{6} \le \theta \le \frac{\pi}{6}\right)$$

Yield function:

$$F = \frac{I_1}{3}\sin\phi + \sqrt{{}^{t}J_{2D}}\left(\cos\theta - \frac{1}{\sqrt{3}}\sin\theta\sin\phi\right) - c\cos\phi$$

B. **Yielding condition check**:

IF ($F < 0$) trial solutions correct are elastic (go to **E**)

IF ($F \ge 0$) elastic-plastic solution (CONTINUE)

$$\left\{\frac{\partial F_{MC}}{\partial\sigma}\right\}^T = \frac{\partial F_{MC}}{\partial I_1}\left\{\frac{\partial I_1}{\partial\sigma}\right\}^T + \frac{\partial F_{MC}}{\partial J_{2D}}\left\{\frac{\partial J_{2D}}{\partial\sigma}\right\}^T + \frac{\partial F_{MC}}{\partial\theta}\left\{\frac{\partial\theta}{\partial\sigma}\right\}^T$$

$$\left\{\frac{\partial G_{MC}}{\partial\sigma}\right\}^T = \frac{\partial G_{MC}}{\partial I_1}\left\{\frac{\partial I_1}{\partial\sigma}\right\}^T + \frac{\partial G_{MC}}{\partial J_{2D}}\left\{\frac{\partial J_{2D}}{\partial\sigma}\right\}^T + \frac{\partial G_{MC}}{\partial\theta}\left\{\frac{\partial\theta}{\partial\sigma}\right\}^T$$

IF $\left(\left|\frac{\pi}{6} - \theta\right| \le \varepsilon\right) \quad \rightarrow \quad \theta = \pm\frac{\pi}{6} = const.$

$$\frac{\partial F_{MC}}{\partial I_1} = \frac{\sin\phi}{3}, \qquad \frac{\partial G_{MC}}{\partial I_1} = \frac{\sin\psi}{3}$$

$$\frac{\partial F_{MC}}{\partial J_{2D}} = \frac{1}{2\sqrt{J_{2D}}}\left\{\cos\theta - \frac{1}{\sqrt{3}}\sin\theta\sin\phi\right\}, \qquad \frac{\partial G_{MC}}{\partial J_{2D}} = \frac{1}{2\sqrt{J_{2D}}}\left\{\cos\theta - \frac{1}{\sqrt{3}}\sin\theta\sin\psi\right\}$$

$$\frac{\partial F_{MC}}{\partial\theta} = -\sqrt{J_{2D}}\left(\sin\theta + \frac{\cos\theta\sin\phi}{\sqrt{3}}\right), \qquad \frac{\partial G_{MC}}{\partial\theta} = -\sqrt{J_{2D}}\left(\sin\theta + \frac{\cos\theta\sin\psi}{\sqrt{3}}\right)$$

$$\left\{\frac{\partial I_1}{\partial\sigma}\right\}^T = \begin{bmatrix}1 & 1 & 1 & 0 & 0 & 0\end{bmatrix}$$

$$\left\{\frac{\partial J_{2D}}{\partial\sigma}\right\}^T = \begin{bmatrix}\frac{1}{3}(2\sigma_1-\sigma_2-\sigma_3) & \frac{1}{3}(-\sigma_1+2\sigma_2-\sigma_3) & \frac{1}{3}(-\sigma_1-\sigma_2+2\sigma_3) & 2\sigma_4 & 2\sigma_5 & 2\sigma_6\end{bmatrix}$$

$$\left\{\frac{\partial\theta}{\partial\sigma}\right\}^T = \frac{\partial\theta}{\partial J_{3D}}\left\{\frac{\partial J_{3D}}{\partial\sigma}\right\}^T + \frac{\partial\theta}{\partial J_{2D}}\left\{\frac{\partial J_{2D}}{\partial\sigma}\right\}^T$$

$$\frac{\partial\theta}{\partial J_{3D}} = -\frac{1}{J_{2D}^{3/2}\sqrt{\frac{4}{3} - \frac{9J_{3D}^2}{J_{2D}^3}}}$$

$$\left\{\frac{\partial J_{3D}}{\partial\sigma}\right\} = \begin{bmatrix}A - \sigma_5^{\,2} + \sigma_2\sigma_3 - \sigma_m(\sigma_2+\sigma_3) + (\sigma_2\sigma_3 - \sigma_5^{\,2})B \\ A - \sigma_6^{\,2} + \sigma_1\sigma_3 - \sigma_m(\sigma_1+\sigma_3) + (\sigma_3\sigma_1 - \sigma_6^{\,2})B \\ A - \sigma_4^{\,2} + \sigma_1\sigma_2 - \sigma_m(\sigma_1+\sigma_2) + (\sigma_1\sigma_2 - \sigma_4^{\,2})B \\ -2\sigma_3\sigma_4 + 2\sigma_5\sigma_6 + 2\sigma_4\sigma_m + 2(\sigma_5\sigma_6 - \sigma_3\sigma_4)B \\ -2\sigma_1\sigma_5 + 2\sigma_6\sigma_4 + 2\sigma_5\sigma_m + 2(\sigma_6\sigma_4 - \sigma_1\sigma_5)B \\ -2\sigma_2\sigma_6 + 2\sigma_4\sigma_5 + 2\sigma_6\sigma_m + 2(\sigma_4\sigma_5 - \sigma_2\sigma_6)B\end{bmatrix}$$

$$A = \frac{1}{3}\left(\sigma_4^{\,2} + \sigma_5^{\,2} + \sigma_6^{\,2} - \sigma_1\sigma_2 - \sigma_2\sigma_3 - \sigma_3\sigma_1\right), \quad B = \frac{2}{9}\left(2\sigma_4\sigma_5\sigma_6 + \sigma_1\sigma_2\sigma_3 - \sigma_1\sigma_5^{\,2} - \sigma_2\sigma_6^{\,2} - \sigma_3\sigma_4^{\,2}\right)^2$$

$$\frac{\partial\theta}{\partial J_{2D}} = \frac{3J_{3D}}{2J_{2D}^{5/2}\sqrt{\frac{4}{3} - \frac{9J_{3D}^2}{J_{2D}^3}}} \qquad d\lambda = \frac{\left\{\frac{\partial F_{MC}}{\partial\sigma}\right\}^{\mathrm{T}}[C_e]\{de\}}{\left\{\frac{\partial F_{MC}}{\partial\sigma}\right\}^{\mathrm{T}}[C_e]\left\{\frac{\partial G_{MC}}{\partial\sigma}\right\}}$$

C. **Stress correction (bisection loop)**:

$$\{de^P\} = d\lambda\left\{\frac{\partial G_{MC}}{\partial\sigma}\right\}$$

$$\{de^E\} = \{de\} - \{de^P\}$$

$$\{d\sigma\} = [C_e]\{de^E\}$$

$$\{^{t+\Delta t}\sigma\} = \{^{t}\sigma\} + \{d\sigma\}$$

New invariants calculation:

I_1 , I_2 , I_3 , J_{2D} , J_{3D}

$$\theta = \frac{1}{3}arcsin\left(-\frac{3\sqrt{3}}{2}\frac{J_{3D}}{J_{2D}^{3/2}}\right)$$

Yield check:

$$F = \frac{I_1}{3}\sin\phi + \sqrt{^{t}J_{2D}}\left(\cos\theta - \frac{1}{\sqrt{3}}\sin\theta\sin\phi\right) - c\cos\phi$$

D. **IF** ($ABS(F) \geq TOL$) go to **C** with new $d\lambda$

$$\{^{t+\Delta t}e^P\} = \{^{t}e^P\} + \{de^P\}$$

E. **End**: $\{^{t+\Delta t}\sigma\}$, $\{^{t+\Delta t}e^P\}$

5. Verification of the computational procedure

Verification of the proposed computational procedure was done by solving elastic-plastic deformation of a sand box specimen, as specified in the literature [4]. The loading is modeled by prescribed displacement on the top of the model, while vertical sliding is allowed on the lateral sides. The bottom of the model is completely restricted. A half of the specimen is modeled with the use of the appropriate symmetry boundary conditions (Figure 3). Eight-node 3D finite elements were used. Displacement is applied at the nodes on the model top side.

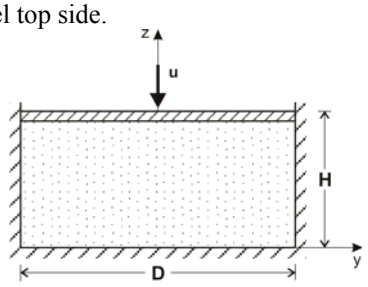

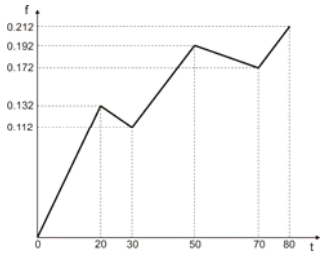

Material data:

Young's modulus,	$E = 100$ kPa	Tension Cutoff limit,	$T = 0.01$
Poisson's ratio,	$\nu = 0.3$	Dimension,	$D = 1.0$ m
Angle of internal friction,	$\phi = 7.153°$	Dimension,	$H = 0.5$ m
Cohesion,	$c = 0.125$ kPa		

Figure 3. Sand specimen – geometry, material data and load function

The problem is solved using the program package PAK [5], by employing the described incremental plasticity method-IPM and the governing parameter method-GPM [4], both are built into the program PAK. Also, these results were compared with those obtained by the program ADINA [6]. Results of the analysis are given in Figure 4.

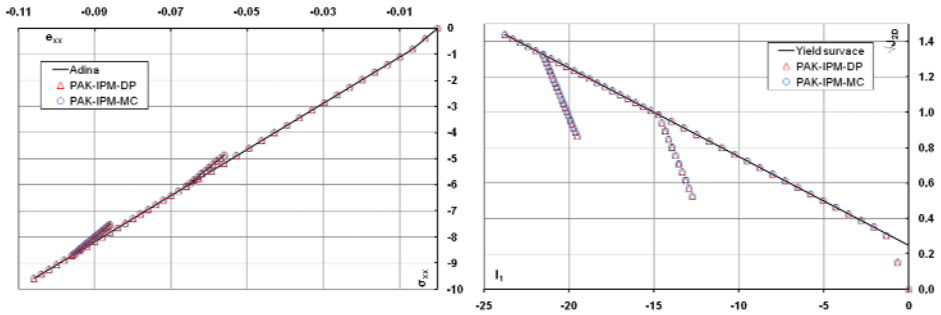

Figure 4. Stress-strain relation (a) and the second invariant deviatoric stress as function of first stress invariant (b)

6. Conclusions

The results of the presented material model are compared with results obtained by Drucker-Prager material model and as can be seen, these two models give similar results in the analyzed case. Results are also compared with the results of the other software solution and found very matching results. The advantage of the presented computational procedure is that it is formulated in general form so that it can be applied to various yield functions, whose yield function can be expressed in terms of stress invariants. Also, this procedure can be implemented in an explicit computationally efficient incremental scheme, where yield condition check D (Table 1) is not performed, but then very small load steps are necessary.

Acknowledgement. The part of this research is supported by Ministry of Education and Science, Republic of Serbia, Grant TR32036 and TR37013.

References

[1] Bathe K. J. (1996)., Finite Element Procedures in Engineering Analysis, Prentice-Hall, Inc., Englewood Cliffs, New Jersey 07632
[2] DiMaggio, F.L., and Sandler, I. S. (1971), Material model for granular soils, *J. Engng. Mech. Div.*, ASCE 97 (EM3), 935-950, Proc. Paper 8212.
[3] Geo-Slope Office: Sigma/W for Finite Element Stress and Deformation Analysis, User's Guide, Calgary, Alberta, Canada (2002).
[4] Kojic M., K.J. Bathe (2005), Inelastic Analysis of Solids and Structures, Springer Berlin Heidelberg New York.
[5] Kojic M., Slavkovic R., Zivkovic M., Grujovic N. (1998), PAK-finite element program for linear and nonlinear structural analysis and heat transfer, Faculty for Mechanical Engineering, Kragujevac, University of Kragujevac.
[6] ADINA User Manual - USA : ADINA Engineering, Inc., (1981).

NUMERICAL DETERMINATION OF CRITICAL STRESSES AND CRACK GROWTH IN A SPUR GEAR TOOTH ROOT

D. Ristić[1], J. Kramberger[2]

[1] TEHNIKUM TAURUNUM Advance School of Engineering
Nade Dimić 4, 11080 Belgrade-Zemun, Serbia
e-mail: daniela.ristic@gmail.com
[2] Faculty of Mechanical Engineering,
University of Maribor, Smetanova 17, 2000 Maribor, Slovenia
e-mail: jkramberger@uni-mb.si

Abstract. Gear service life and stress state at the gear tooth root and its analysis are a contemporary topic of scientific investigations. Great influence on gear tooth root strength that is one of the primary subjects of this paper, are tooth root form and fillet radius. Special attention is given to analysis on impact of gear tooth fillet radius at the critical cross section on stress value and distribution. Stress intensity factor and gear working life depends directly on tooth root stress. Optimal gear form discovery relative to stress concentration is one of the main problems of gears design. In the first part this paper research is focused on finding the optimal fillet tooth root radius to minimize the root stress intensity. The problem of spur gear tooth root crack growth is analyzed in a second part of this paper. It is well known that a first initial crack appears at the gear tooth affected the most by tooth root stress concentration. Cyclic loading growth leads to the initiations of fatigue crack in the gear tooth fillet radius. After crack initiation the simple Paris equation is used for the further simulation of the fatigue crack growth. The stress intensity factor and its relationship with crack length $K = f(a)$ are used for determination of a number of loading cycles N_p that causes crack propagation from the initial to the critical length a_c when the failure is occurred. This paper provides results achieved by application of numerical methods: finite element method (FEM) and real working conditions simulation.

Keywords: finite element method - FEM, tooth root stress concentration, tooth root fillet radius, fatigue crack growth, service life.

1. Introduction

Gear load capacity and stress state depends to a large extent on main gear profile configuration parameters, which makes it one of the key areas of interest for scientific analysis. To support this analysis, gear kinematics, carrying capacity, strength, production and some other characteristics are being actively investigated. Great deal of gear tooth root load capacity have tooth root form, tooth root fillet radius, respectively. It has direct influence on the stress intensity factor as on gear service life.
Real gear transmitters are multiple statically undetermined systems and stress concentration in a gear tooth root depends on many parameters. Optimal gear form and meshing parameters discovery relative to stress concentration is one of the main problems of gears design.

Tooth root critical cross section, according to ISO recommendation, is determined by tooth fillet radius tangent that is positioned 30° against gear symmetry line, and its dimensions are critical cross section width s_{Fn} and face width b.

Tooth root critical cross section is exposed to a pressure load under radial component, and under tangential component it is exposed to bending and shearing. It all shows complex load state in the tooth root critical cross section. However, unwanted phenomenon as plastic deformations, crack initiation, even a gear failure appears on a tensile side of gear tooth. Because of that all, stress values on the tensile side of gear tooth are important for determination of applied stresses.

It is well known that a first initial crack appears at the gear tooth affected the most by root stress concentration. The complete process of fatigue failure of mechanical elements may be divided into the following stages [1]:

1) microscopic nucleation;
2) short crack growth;
3) long crack growth;
4) final failure appearance.

The crack initiation period accounts microscope nucleation and short crack growth, hence crack propagation period means long crack growth. The most of the service life depends to the crack propagation period. The complete gear service life may be determined from the sum of the number of stress cycles N_i required for the fatigue crack initiation and the number of stress cycles N_p required for the fatigue crack propagation to the critical crack length when the final crack is possible to occur:

$$N = N_i + N_p \tag{1}$$

The initiation phase of fatigue life of mechanical elements presents the growth of short cracks up to the size a_{th}. The threshold crack length a_{th} presents the transition point between short and long cracks. The Kitagawa-Takahashi plot [2] represents the fatigue crack growth, applied stress range ($\Delta\sigma$) against crack lenght (a) using logarithmic scale (Fig. 1).

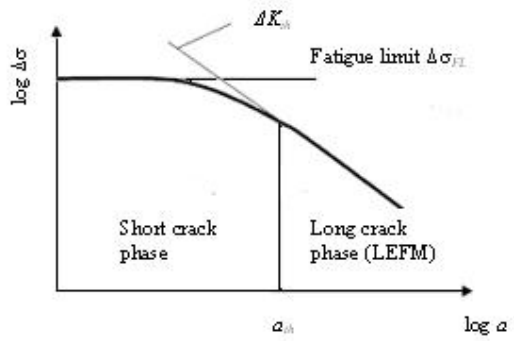

Figure 1. Applied stress values in a function of crack length

2. Determination of the gear load capacity according to tooth root strength

Tooth root applied load caused by normal force F_{bn} acts in contact points on the meshed teeth profiles. For analyzing the stress conditions at the gear tooth root, the tooth is approximated with the console shaped mechanical model, embedded in the gear body, at the end of which the load acts in the direction of the teeth profile pressure line.
Normal force can be divided in two components:

- radial $F_r = F_{bn} \sin \alpha_{F_{an}}$ and
- tangential $F_t = F_{bn} \cos \alpha_{F_{an}}$,

where the gear is exposed to a pressure load under radial component, and under tangential component, with the force arm h_{Fa}, it is exposed to bending and shearing. According to that, complex stress condition in a tooth root characterizes pressures and bending normal stresses and shear tangential stresses.
Bending normal stress in a critical cross section is [3]:

$$\sigma_S = \frac{M}{W} = \frac{F_{bn} \cos \alpha_{F_{an}} \, h_{F_a}}{b s_{F_n}^2 / 6} \tag{2}$$

and after some transformations we come to normal stress equation:

$$\sigma_{Fn} = \frac{F_t}{b m_n} \frac{6(h_{Fa}/m_n)\cos \alpha_{Fan}}{(s_{Fn}/m_n)^2 \cos \alpha} = \frac{F_t}{b m_n} Y_{Fa} \tag{3}$$

where:
Y_{Fa} – shape factor
α_{Fan} – angle between normal force F_{bn} and horizontal line
Maximal normal stress of cylindrical spur gears in a tooth root cross section, according to stress concentration factor, is:

$$\sigma_{\max} = \sigma_{F_n} Y_s K_F \tag{4}$$

where

$$K_F = K_A K_V K_{F_\alpha} K_{F_\beta} \tag{5}$$

is total load factor which consider disagreement between real and theoretical working conditions (K_A-application factor, K_v-dynamic factor, $K_{F\alpha}$-unequal load distribution factor, $K_{F\beta}$-load distribution factor).
Tooth root fillet radius ρ_F is given in the form of:

$$\rho_F = \frac{c_p}{(1 - \sin \alpha_0)} \tag{6}$$

where c_p presents gear tip clearance (c_p=(0.1÷0.3)m, m-module).

3. Characteristics of analyzed gear

All analytical and numerical researches are carried out on a real construction with real condition simulation. Considered gear is a part of structural elements of great power planetary transmitter (big excavator of power 2x550kW) with following characteristics:

- module m=24mm,
- profile movement coefficient x_1=0 and x_2=0.326,
- face width b=350mm,
- rotation moment T=2528.8kNm,
- number of rotation n=4.1596min^{-1},
- number of teeth z_1=20 and z_2=96,
- gear material is carburized steel 17CrNiMo6 (according to DIN) with Young's modulus E=2.1x10^{5}MPa and Poissons's ratio v=0.3.

As a consequence of working conditions and irregular formed tooth root shapes appearance of failures is often remarked during the exploitation [4]. Because of that, the topic of this work is determination of exact tooth root stress and optimal tooth root shape.

According to the theory, at the contact points B and D, double mesh follow transforms to single and reverse. In that points F_{bn} force acts in total value, while in points A and E, F_{bn} force acts with half of its total value. Hence, the most important loads for stress concentration appearance are the loads in contact points E and D for the driving gear, respectively contact points A and B at driven gear. Loads in other mesh contact points have no big influence on critical cross section stress concentration and they don't cause failures and crack initiation in a tooth root. In this work shall be represented only results for the driving gear and its D contact point because load in this point causes tooth root failures.

Researches in this paper are deduced to stress determination for a driving gear tooth of observed planetary transmitter according to various tooth root fillet radius ρ_F. The tooth root fillet radius ρ_F has the most important influence on tooth root stress concentration, so that is one of the topics of this work. It is analyzed for eight different values of tooth root fillet radius ρ_F. The lowest value is ρ_F=4.56mm and it is incrementally increased to the value of ρ_F=10.94mm. Fig.2. shows dimensions of critical section for a driving gear tooth.

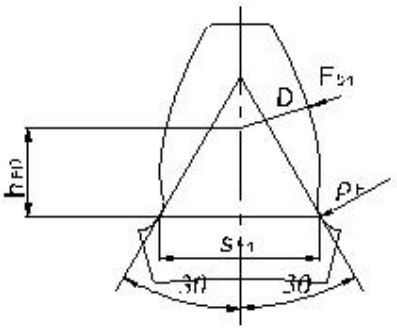

Figure 2. Dimensions of the critical section for driving gear tooth

4. Analysis of results by FEM

Numerical analysis in the first part of this paper is deduced to determination of Von Mises stresses and normal stresses for a driving gear of planetary transmitter according to the tooth root fillet radius ρ_F. Finite element method (FEM) is used for numerical analysis here. For that purpose finite element package FEMAP v.9.3 [5] is used. On the basis of the gear data, the 3D finite element model is made. One driving gear tooth has 12489 elements and 14301 nodes. The mesh is refined in the tooth fillet region in order to show the best possible way the stress condition in that section. Only 50mm width layer of tooth is analyzed according to a supposition that load is equally arranged along the instantaneous tooth side contact line. The gear tooth is loaded with the normal force F_{bn} which is acting at the inner point of single tooth contact (D). Fig.3. shows 3D finite element model for the analyzed gear tooth.

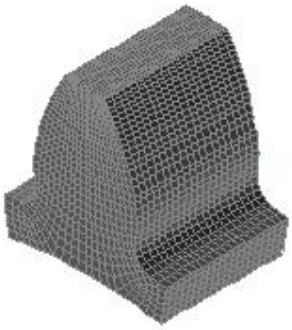

Figure 3. 3D finite element model for driving gear tooth

Outer load, respectively, normal force F_{bn} that is equally arranged along the instantaneous tooth side contact line is changed with concentrated force at nodes along that line (21 nodes along the width b_1). It is possible to get equal force distribution along the tooth width if it is possible to have more layers of finite elements and that sooths influence of concentrate force in the instant contact point.
For the numerical simulation of failure crack propagation FRANC2D program is used [6]. A unique feature of FRANC2D finite element package is automatic crack propagation capability.
Developed FEM (finite element method) of stress determination in gear tooth root allows not only good picture of stress distribution but even defines exact position of maximum stress value point. In the same time, it is possible to consider crack initiation and its growth up to the fatigue failure which is very important in engineering.

5. Tooth root critical stress determination

As it is said before, the normal force F_{bn} which is acting at the inner point of single tooth contact D causes tooth root stress concentration and fatigue failure. So, in this paper, only

results of Von Mises and normal stresses at tooth root critical cross section caused by load at D contact point shall be presented (Table1).

Table 1. Von Mises σ_e and normal σ_y stresses at critical section of the gear tooth for the various values of fillet radius ρ_F

Fillet radius ρ_F [mm]	Tensile side		Pressured side	
	σ_e [MPa]	σ_y [MPa]	σ_e [MPa]	σ_y [MPa]
4.56	277.6251	246.4310	323.4744	286.6890
5.47	261.8667	244.8961	303.9231	282.9113
6.38	247.4392	224.7813	288.7467	262.7499
7.29	233.5653	205.0326	271.2920	237.3590
8.22	222.7844	192.2681	259.0119	222.4591
9.12	213.8899	181.0111	248.1438	209.1441
10.03	204.7536	170.2814	237.4938	196.9606
10.94	198.0450	162.6787	229.6540	188.7827

For researching in this paper the most important are stress values in the critical section nodes of tensile side of the gear because these stresses cause damages and failures of the gear at the end [3]. But because of whole stress state presentation in this paper critical stress values on the both sides of the gear tooth root are shown [7].
It may be seen from Table1 that Von Mises σ_e and normal σ_y stresses become less as fillet radius ρ_F grows up and it is in agreement with analytical results (Eq.3). So, there is a recommendation for higher values of fillet radius, but only in allowed boundaries (Eq.6).
Fig.4 shows the functional relationship between equivalent and normal stresses and various values of fillet radius ρ_F for the tensile and pressured sides of analyzed gear. This graph shows again a fact that tooth root stresses become less as fillet radius ρ_F grows up.

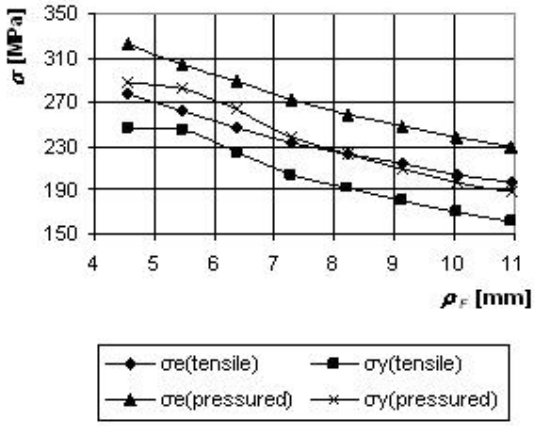

Figure 4. Equivalent stress σ_e and normal stress σ_y in function of fillet radius ρ_F for the tensile and pressured side of a driving gear tooth

The greatest values of normal and equivalent stresses in the tooth root appear in the moment when the contact between two meshed gears is in the outer point of single mesh. It is supposed that tooth root stresses change linearly in exact range along contact line (A-B, B-D, D-E), so the diagrams of stresses in this paper show good agreement with that supposition.
For driving gear there is some stress values disagreement of linear distribution for fillet radius less than ρ_F =5.47mm (Fig.4), but for driven gear disagreements of linear distribution are for fillet radius higher than ρ_F =10.03mm (not presented in this work) [7, 11, 12]. For that reason, these values of fillet radius should be boundary (5.47mm<ρ_F <10.03mm).
Graphs in this research show that appropriate selection of fillet radius should reduce critical stresses for 30% and that is important information for designers.

5.Fatigue crack propagation

In this paper the simple Paris equation is used to describe a crack growth rate [8]:

$$\frac{da}{dN} = C\Delta K^m \tag{7}$$

where a is a crack length, N is a number of loading cycles, and C and m are material parameters. The fatigue crack growth rate, $\frac{da}{dN}$, according to LEFM (linear elastic fracture mechanics) is a function of stress intensity range $\Delta K = K_{\max} - K_{\min}$. The number of loading cycles N_p, in respect to the crack propagation period is determined by integration of equation (7):

$$\int_0^{N_p} dN = \frac{1}{C}\int_{a_{th}}^{a_c} \frac{da}{\Delta K^m} \tag{8}$$

and that is number of cycles of period in which crack propagate from initial a_{th} to critical length a_c.
According to complicated geometry of gear tooth root for the numerical simulation of failure crack propagation FRANC2D program is used [6]. The determination of the stress intensity factor is based on the displacement correlation method using singular quarter-point six node triangular elements around the crack tip (Fig. 5) [9, 10].
The stress intensity factor can be determined from the nodal displacement as:

$$\begin{aligned} K_I &= \frac{2G}{(3-4\nu)+1}\sqrt{\frac{\pi}{2L}}\left[4\upsilon_d - \upsilon_e - 4\upsilon_b + \upsilon_c\right] \\ K_{II} &= \frac{2G}{(3-4\nu)+1}\sqrt{\frac{\pi}{2L}}\left[4u_d - u_e - 4u_b + u_c\right] \end{aligned} \tag{9}$$

where G is the share modules of the material, v is the Poisson ratio, L is the finite element length on the crack face, u and v are displacements of the finite elements nodes b, c, d and e (Fig.5).

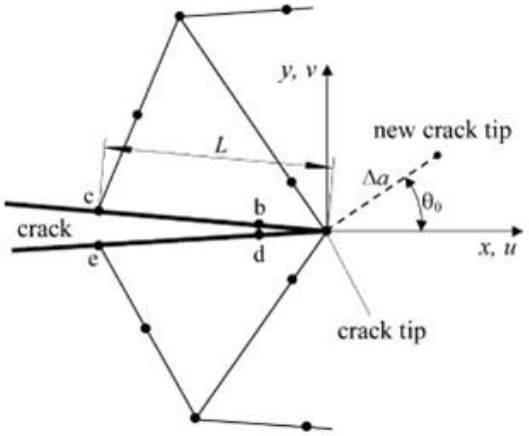

Figure 5. Crack tip with triangular quarter-point elements

The combined stress intensity factor is:

$$K = \sqrt{\left(K_I^2 + K_{II}^2\right) \cdot \left(1 - \nu^2\right)} \tag{10}$$

The computation method is based on incremental crack extensions where the size of increment is prescribed in advance [9, 10]. The equation for predicted crack propagation angle is:

$$\theta_0 = 2\tan^{-1}\left[\frac{1}{4}\cdot\frac{K_I}{K_{II}} \pm \sqrt{\left(\frac{K_I}{K_{II}}\right)^2 + 8}\right] \tag{11}$$

It is proposed that crack propagates from the crack tip in a radial direction in a plane perpendicular to the direction of the maximum tangential tensile stress. After the end of every crack increment around the new crack tip is made new local mesh. This procedure is repeated until the stress intensity factor reaches its critical value K_c, the value of its fracture toughness (K=K_{Ic}). That is the moment when the crack reaches its critical length and when the tooth fracture is inspected.

6. Practical example

The initial crack can occur at the both sides of tooth root critical section but more important and dangerous is a crack at the tensile side of tooth. The normal force F_{bn} which is acting at

the inner point of single tooth contact (D) causes the highest stresses at tooth root critical section and it is the most important for crack initiation.
In this paper only crack propagation of gear tooth with fillet radius ρ_F=7.29mm is analyzed. For the numerical simulation of failure crack propagation FRANC2D program is used [6]. A unique feature of FRANC2D finite element package is automatic crack propagation capability. The initial crack is placed perpendicularly to the surface at the point where the crack initiation has been determined previously (Fig.6).

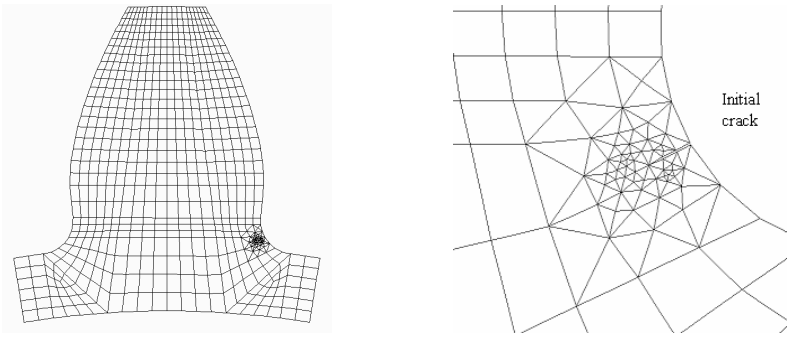

Figure 6. Finite element mesh around initial crack at tooth root

The material parameters considered in this paper are [9, 10]:

- σ_{Flim}=500MPa,
- K_{th}=269MPa√mm,
- K_{Ic}=2620MPa√mm,
- C=3.31x10^{-17}mm/cycle/ (MPa√mm)^m,
- m=4.16.

Table 2. Stress intensity factor K in function of crack length a and gear tooth crack propagation life

a [mm]	K_I [MPa mm^{0,5}]	K_{II} [MPa mm^{0,5}]	K [MPa mm^{0,5}]	N [cycles]
2	549,9	2,724	524,578	141175
4	627,8	17,5	599,116	363069
6	685,4	21,78	654,16	521808
8	718,1	19,08	685,265	634249
10	790,1	21,75	753,99	713532
12	829,2	9,18	791,05	769572
14	927,2	30,59	884,97	809538
16	981,7	15,69	936,6	838346
18	1119	20,64	1067,64	859138
20	1223	12,27	1166,73	873772
22	1397	39,26	1333,18	883306
24	1583	24,9	1510,27	888485
26	1793	2,445	1710,41	890226
28	2100	64,95	2005,32	890102

30	2418	70,64	2307,61	890832
31	2767	1,26	2639,55	892799

As it is said before, the initial crack corresponds to the threshold crack length a_{th} and it is adopted that length is a_{th}=1mm. During numerical simulation of crack propagation the crack increment size was Δa=2mm up to the crack length a=30mm and than Δa=1mm up to the a_c=31mm when the total failure occurs.
Table 2 presents numerical results for the stress intensity factor K_I and K_{II}, combined stress intensity factor K (Eq.10) and results for the crack propagation period number of cycles N_p (Eq.8).

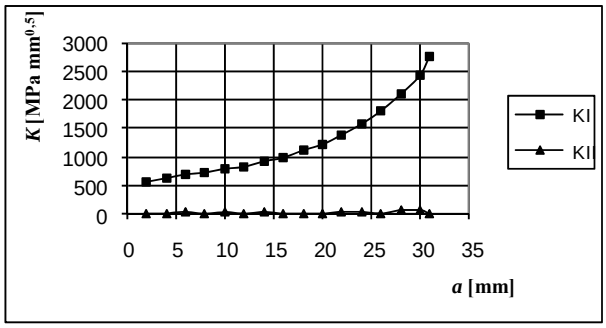

Figure 7. Stress intensity factor K_I and K_{II} in function of a crack length a

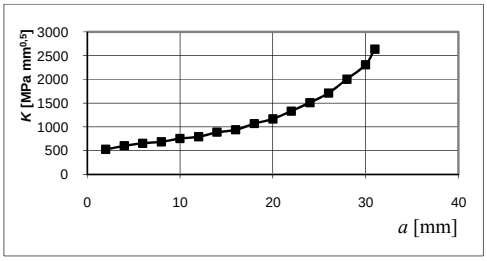

Figure 8. Combine stress intensity factor K in function of crack length a

Fig.7 presents functional relationship between stress intensity factors K_I and K_{II} and crack length a. Analytical analysis shows that value of stress intensity factor K_{II} is less than 5% of factor K_I value for all crack lengths. Combine stress intensity factor values K in function of crack length a are presented on Fig.8.

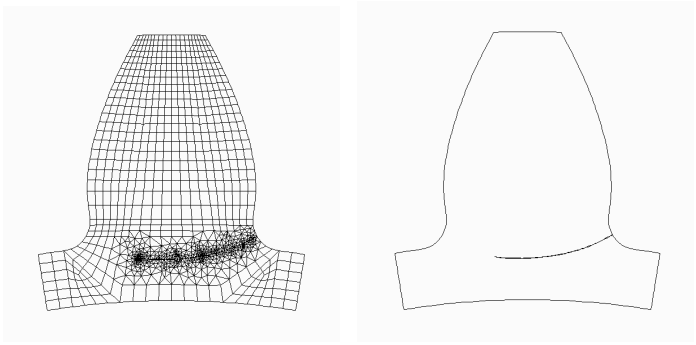

Figure 9. Numerically determined crack propagation path

Fig.9 shows the numerically determined crack propagation path in a gear tooth root.

Service life of cracked gear tooth root is presented on Fig.10.

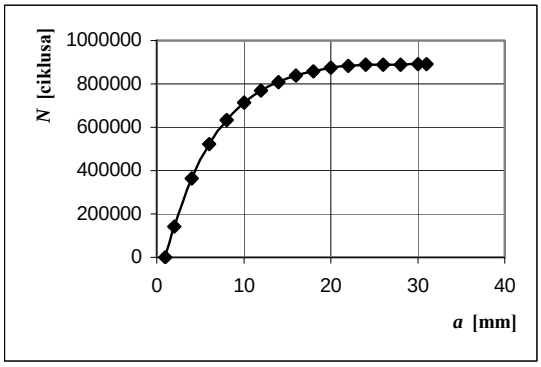

Figure 10. Service life of cracked gear tooth root

It is obvious from graph $N=f(a)$ (Fig.10) that the crack length a grows continually up to the value of a=20mm and then, for the short time period, it reaches its critical value a_c. Crack length reaches its critical value when stress intensity factor get its fracture toughness what is in the same time its critical value ($K=K_{Ic}$).
It is very important to determine precisely gear service life and because of that it is possible to change damaged parts on time and to prevent catastrophic failures.

7. Conclusions

Topic of this paper is forming efficient and reliable numerical model for the determination of tooth root phenomena caused by geometrical discontinuity under static and cyclic loads and gear service life determination. Results in this research show good agreement with data in literature and practice, so this methodology may be applied in practice.
Critical tooth root stress concentration is caused by inner contact point load of single mesh follow (D) and this load is a main cause of initial cracks appearance so it is only researched in this paper.

The most important are tooth root stresses caused by load in the inner contact point of mesh, because they are the greatest and the most dangerous for failure appearance.
It can be concluded, analyzing results of this research, that stresses reduce as tooth fillet radius grows up. Reduction of stress concentration acts directly on gear service life elongation because it deflects danger of initial cracks appearance and increases safety factor S_F on that place. Although the stresses on pressured side are higher than on the tensile, stress concentration on the tensile side is more important for initial crack appearance. But for the better tooth root stress consideration, stresses on both tooth root sides are presented in this paper.
In this research Von Mises and normal tooth root stresses are presented. All results show that Von Mises stresses have greater values then normal stresses.
This paper shows that appropriate fillet radius selection can increase tooth root stresses in its critical section even by 30%. It was an intention of this research, because in that case it could succeed better tooth root load capacity and service life elongation.
In the second part of this work it is presented computation model for determination of gear service life in regard to bending fatigue in gear tooth root.
The initial crack can occur at the both sides of tooth root critical section but more important and dangerous is a crack at the tensile side of tooth.
In this paper only crack propagation of gear tooth with fillet radius ρ_F=7.29mm is analyzed.
The initial crack is placed perpendicularly to the surface at the point where the crack initiation has been determined previously.
For the crack growth determination it is proposed that crack propagates from the crack tip in a radial direction in a plane perpendicular to the direction of the maximum tangential tensile stress. After the end of every crack increment around the new crack tip is made new local mesh. This procedure is repeated until the stress intensity factor reaches its critical value K_c, the value of its fracture toughness ($K=K_{Ic}$). That is the moment when the crack reaches its critical length a_c and when the tooth fracture is inspected.
Graph $N=f(a)$ (Fig.10) shows that the crack length a grows continually up to the value of a=20mm and then, for the short time period, it reaches its critical value a_c.
The estimated fatigue life of the gear deviates from real service life because some effects like non-homogenous material and possible causes of retardation of the crack propagation (crack closure) were not taken into account in the numerical analysis.
We still don't have acceptable data for the parameters that describe tooth root phenomena, so these analyses are actual further more. Accordingly, experimental results are required to provide the material parameters and further theoretical and numerical research is of great interest for science development.

References

[1] Glodež S. Šraml M. Kramberger J, A computational model for determination of service life of gears, Int J Fatigue 2002. 24, pp.1013-1020.
[2] Kitagawa, H., Takahashi, S., Applicability of fracture mechanics of very small cracks or cracks in the early stage, In: Proceedings of the Second International Conference on the Behaviour of Materials, Boston; 1976. pp.627-631.
[3] Linke H. Stirnrad-verzahnung, Berechnung, Werkstoffe, Fertigung, Carl Hanser Verlag München, Wien, 2002.

[4] Nikolić V., Mehanička analiza elemenata zupčastih prenosnika, monografija, Kragujevac, 1999.
[5] NASTRAN, Application manual, The MACNEEL SCHWENDLER CORPORATION, 1990.
[6] FRANC2D, User's Guide, Version 2.7, Cornell University, 1998.
[7] Ristić Daniela, Gear Tooth Root Stress Concentration and Initial Crack Appearance, PhD Thesis, University of Kragujevac, Faculty of Mechanical Engineering, Kragujevac, 2009.
[8] Paris, P.C., Erdogen, F., A Critical Analysis of Crack Propagation Laws, Journal of Basic Engeneering, Vol. 85, pp. 528-534, 1963.
[9] Kramberger, J., Šraml, M., Glodež, S., Flašker, J., Potrč, I, Computational model for the analysis of bending fatigue in gears, Int J Fatigue 2002, 24, pp.1013-1020.
[10] Kramberger, J., Šraml, M., Potrč, I., Flašker, J., Numerical calculation of bending fatigue life of thin-rim spur gears, *Engineering Fracture Mechanics 71*, pp. 647-656, 2004.
[11] Daniela S. Ristić, COMPUTATION MODEL FOR THE ANALYSIS OF GEAR TOOTH ROOT STRESSES, *Proceedings of 2nd International Congress of Serbian Society of Mechanics*, M2-01:1-15, Palić (Subotica), Serbia, 1-5 june 2009.
[12] Ristić, D., Numerical Model for the Critical Stress Determination in Spur Gears, *Scientific Technical Review*, Vol. LVIX, No. 1, pp. 78-86, 2009.

STRESS INTEGRATION FOR FCC CRYSTAL PLASTICITY BY FINITE ELEMENT METHOD

R.Slavković[1], V. Slavković[2], M.Živković[3], V. Dunić[4]

[1] Faculty of Mechanical Engineering,
University of Kragujevac, Sestre Janjić 6, 34000 Kragujevac, Serbia
e-mail: radovan@kg.ac.rs
[2] Faculty of Mechanical Engineering,
University of Kragujevac, Sestre Janjić 6, 34000 Kragujevac, Serbia
e-mail: vukasinsl@gmail.com
[3] Faculty of Mechanical Engineering,
The University of Kragujevac, Sestre Janjić 6, 34000 Kragujvac, Serbia
e-mail: zile@kg.ac.rs
[4] Faculty of Mechanical Engineering,
University of Kragujevac, Sestre Janjić 6, 34000 Kragujevac, Serbia
e-mail: dunic@kg.ac.rs

Abstract. In this paper are given crystallographic theory basics with emphasis on crystal lattice types, possible slip directions, planes and systems. The material model implemented in ABAQUS is analyzed, and plastic deformation process of crystals is explained. The constitutive relations are considered, and Schmidt factors are given and explained. It ‘s also given connection between deformation hardening of crystal materials and slip rate by two hardening low: Assaro-Peirce-Needelman and Wu-Bassani. Structure of input file and results that we get using UMAT subroutine in ABAQUS are given on copper mono-crystal example. Different behavior of reverse oriented crystals is given on copper bi-crystal example, while results validation obtained using different element type is given on another poly-crystal example. Implicit stress integration for material model is developed based on papers [2],[17] and implemented to PAK finite element program. Solution results for single crystal and bi-crystal are given and compared with results given in [2] obtained by ABAQUS UMAT subroutine.

1. Introduction

Metals are usually polycrystalline; that is, made up of many crystals in which atoms are stacked in regular array. The grain size is usually about 100μm .

If we assume that there is no preferred crystallographic orientation, but that the orientation changes randomly from one grain to the next, and if our sample of material contains a sufficiently large number of grains, we can get a reasonable physical feel that macro scale yielding of the material will be isotropic. Observations on single crystals show that slip tends to occur preferentially on certain crystal planes and in certain specific crystal directions. The combination of a slip plane and a slip direction is called a slip system. These tend to be the most densely packed planes and the directions in which the atoms are packed closest together. In face centered cubic (FCC) materials, the most densely packed planes are the diagonal planes of the unit cell.

2. Material model

Crystalline materials and their lattice undergo elastic deformation and rotation. Inelastic deformation of a single crystal is assumed here to arise solely from crystalline slip. Greek letters will be used in work to note slip systems and lattice letters sums 1-3. Bold characters denote vectors and tensors and first derivatives are denoted with point.

2.1. Deformation gradient and velocity gradient

Total deformation gradient is given by:

$$\mathbf{F} = \mathbf{F}^{*} \cdot \mathbf{F}^{\mathbf{P}} \tag{1}$$

Where elastic part $\mathbf{F}^{*}$ denotes rotation and elastic deformation (stretching) of lattice and $\mathbf{F}^{\mathbf{P}}$ denotes plastic shear of material to an intermediate reference configuration in which lattice orientation and spacing are the same as in the original reference configuration.

Velocity gradient can be defined as:

$$\mathbf{L} = \dot{\mathbf{F}} \cdot \mathbf{F}^{-1} \tag{2}$$

Using $\mathbf{F}^{\mathbf{P}} \cdot \mathbf{F}^{\mathbf{P}-1} = \mathbf{I}$ final formulation of velocity gradient is:

$$\mathbf{L} = \dot{\mathbf{F}}^{*} \cdot \mathbf{F}^{*-1} + \mathbf{F}^{*} \cdot \dot{\mathbf{F}}^{\mathrm{P}} \cdot \mathbf{F}^{\mathbf{P}-1} \cdot \mathbf{F}^{*-1} \tag{3}$$

Rate of change $\mathbf{F}^{\mathbf{P}}$ is connected with slip rate $\dot{\gamma}^{(\alpha)}$ on α slip system:

$$\dot{\mathbf{F}}^{\mathrm{P}} \cdot \mathbf{F}^{\mathbf{P}-1} = \sum_{\alpha} \dot{\gamma}^{(\alpha)} (\mathbf{m}^{(\alpha)} \otimes \mathbf{n}^{(\alpha)}) \tag{4}$$

$\mathbf{n}^{(\alpha)}$ is unit vector in perpendicular direction of slip plain, $\mathbf{m}^{(\alpha)}$ is unit vector in slip direction and $\dot{\gamma}^{(\alpha)}$ is slip rate on α slip system.

Velocity gradient in current configuration using sum of elastic and plastic velocity gradient:

$$\mathbf{L} \equiv \dot{\mathbf{F}} \cdot \mathbf{F}^{-1} = \mathbf{L}^{*} + \mathbf{L}^{\mathrm{P}} \tag{5}$$

And also:

$$\mathbf{L} \equiv \dot{\mathbf{F}} \cdot \mathbf{F}^{-1} = \mathbf{D} + \boldsymbol{\Omega} \tag{6}$$

Where symmetric part of velocity gradient tensor $\mathbf{D}$, and asymmetric part $\boldsymbol{\Omega}$ are given by:

$$\mathbf{D} = \frac{1}{2}\left(\mathbf{L} + \mathbf{L}^{\mathrm{T}}\right) \tag{7}$$

$$\boldsymbol{\Omega} = \frac{1}{2}\left(\mathbf{L} - \mathbf{L}^{\mathrm{T}}\right) \tag{8}$$

2.2 Schmid's factors

Shear stress τ^{α} in system is main mechanism for arrival of dislocations, for current configuration is given by:

$$\tau^{\alpha} = \boldsymbol{\sigma} : \mathrm{S}_{0}^{\alpha} \tag{9}$$

In equation (1) $\mathbf{S}_{0}^{\alpha}$ represents Schmid's tensor which is defined with dyadic product of vectors $\mathbf{m}^{(\alpha)}$ and $\mathbf{n}^{(\alpha)}$. This, generally, non-symmetric tensor, can be decomposed on symmetric and asymmetric part:

$$\mathbf{P}^{\alpha} = \frac{1}{2}(\mathbf{m}^{(\alpha)} \otimes \mathbf{n}^{(\alpha)} + \mathbf{n}^{(\alpha)} \otimes \mathbf{m}^{(\alpha)}) \tag{10}$$

$$\mathbf{Q}^{\alpha} = \frac{1}{2}(\mathbf{m}^{(\alpha)} \otimes \mathbf{n}^{(\alpha)} - \mathbf{n}^{(\alpha)} \otimes \mathbf{m}^{(\alpha)}) \tag{11}$$

2.3 Hardening of rate-dependent crystalline materials

For rate deformation models, slip rate is directly connected with shear stress:

$$\dot{\gamma}^{(\alpha)} = \dot{a}^{(\alpha)} f^{(\alpha)}\left(\frac{\tau^{(\alpha)}}{g^{(\alpha)}}\right) \tag{12}$$

where $\dot{a}^{(\alpha)}$ is referent deformation rate in current slip system α, $g^{(\alpha)}$ is variable that describes current strength of the system, while non-dimensional function $f^{(\alpha)}$ describes dependence of shear deformation rate on shear stress.

2.3.1 Constitutive model Pierce-Assaro-Needelman

Pierce, Assaro and Needelman have used simple form for the self hardening modulus [2]:

$$h_{\alpha\alpha} = h(\gamma) = h_0 \sec h^2\left|\frac{h_0\gamma}{\tau_s - \tau_0}\right| \tag{13}$$

γ is the Taylor cumulative shear strain on all slip systems:

$$\gamma = \sum_{\alpha}\int_0^t \left|\dot{\gamma}^{(\alpha)}\right| dt \tag{14}$$

Latent hardening modulus is given by:

$$h_{\alpha\beta} = qh(\gamma) \quad (\alpha \neq \beta) \tag{15}$$

q is constant. These expressions of hardening modulus neglect the Bauschinger effect in a crystalline solid.

2.3.2. Constitutive model Bassani-Wu

Bassani and Wu used [7]:

$$h_{\alpha\alpha} = \left\{(h_0 - h_s)\sec h^2\left[\frac{(h_0 - h_s)\gamma^{(\alpha)}}{\tau_s - \tau_0}\right] + h_s\right\} G(\gamma^{(\beta)}; \beta \neq \alpha) \tag{16}$$

to express hardening modulus at crystalline materials. This expression depends of shear deformation $\gamma^{(\alpha)}$ on all slip systems:

$$h_{\beta\alpha} = qh_{\alpha\alpha} \quad (\beta \neq \alpha) \tag{17}$$

where h_s is the hardening modulus during easy glide within the stage I hardening.

2.4 Incremental formulation (rate-independent)

Incremental formulation has been used for specific materials where variables are not functions of time (rate independent plasticity). This formulation is detailed described in papers of various authors [8], [10], [11] and others, using two basic formulations Total Lagrange (TL) and Updated Lagrange (UL).
Presented incremental formulation for plasticity of crystals is based on papers of [13] and [15]. Incremental formulation is convenient for numerical implementation.
For this model we are using:

- Cauchy stress, $\mathbf{T}$,
- deformation gradient $\mathbf{F}$,
- slip systems are denoted with α, every system is defined with unit normal vector $\mathbf{n}_0^\alpha$ and unit vector $\mathbf{m}_0^\alpha$ which denote slip direction, assumption is that slip systems are defined in referent configuration ($\mathbf{m}_0^\alpha, \mathbf{n}_0^\alpha$)
- plastic deformation gradient $\mathbf{F}^\mathbf{P}$ with
- yield stress on slip system $s^\alpha > 0$

If t is current moment and Δt is time increment, then we have $\tau = t + \Delta t$. We suppose that next quantities are known:

- deformation gradients in referent and current configuration $\left(\mathbf{F}(t), \mathbf{F}(\tau)\right)$
- unit vectors in referent configuration ($\mathbf{m}_0^\alpha, \mathbf{n}_0^\alpha$)
- Cauchy stress $\mathbf{T}(\tau)$, plastic deformation gradient $\mathbf{F}^p(\tau)$ and yield stress $s^\alpha(\tau)$ in referent configuration at beginning of time step

Values that should be determined at the end of time step are $\mathbf{T}(\tau), \mathbf{F}^p(\tau), s^\alpha(\tau)$, and orientation of slip systems in deformed configuration in moment τ is given by next relations:

$$\mathbf{m}_\tau^\alpha = \mathbf{F}^*(\tau)\mathbf{m}_0^\alpha \tag{18}$$

$$\mathbf{n}_\tau^\alpha = \mathbf{F}^*(\tau)^{-T}\mathbf{n}_0^\alpha \tag{19}$$

Elastic stretch for metals is usually infinitesimal, so that constitutive equation can be treated as linear function:

$$\mathbf{T}^*(\tau) = \mathbb{C}\left[\mathbf{E}^*(\tau)\right] \tag{20}$$

$\mathbb{C}$ is fourth-order elastic tensor, $\mathbf{T}^*(\tau)$ is resolved stress related to assumed elastic solution in step and $\mathbf{E}^*(\tau)$ is Green-Lagrange elastic deformation. Next equation:

$$\mathbf{T}^*(\tau) = \mathbf{F}^*(\tau)^{-1}\left\{\left(\det\mathbf{F}^*(\tau)\right)\mathbf{T}(\tau)\right\}\mathbf{F}^*(\tau)^{-T} \tag{21}$$

gives relation between Cauchy stress $\mathbf{T}(\tau)$ and second Piola Kirchhoff stress $\mathbf{T}^*(\tau)$ which is energetically conjugate with Green-Lagrange elastic deformation.
If we use previous equation we get next relation for shear stress:

$$\tau^*(\tau) = \left\{\mathbf{C}^*(\tau)\mathbf{T}^*(\tau)\right\}\cdot\mathbf{S}_0^\alpha \tag{22}$$

shear stress on slip system α for $\tau = t + \Delta t$.
Now, we define trial elastic deformation and stress in moment $\tau = t + \Delta t$, with trial shear stress:

$$\tau^\alpha(\tau)^{tr} = \mathbf{T}^*(\tau)^{tr}\cdot S_0^\alpha \tag{23}$$

Potentially active system can be determined using:

$$\Delta\gamma^{\alpha} = \begin{cases} 0 & \text{if} \quad \left|\tau^{\alpha}(\tau)^{tr}\right| < s^{\alpha}(t) \\ \geq 0 & \text{if} \quad \left|\tau^{\alpha}(\tau)^{tr}\right| > s^{\alpha}(t) \end{cases} \tag{24}$$

System that satisfies condition:

$$\left|\tau^{\alpha}(\tau)^{tr}\right| \leq s^{\alpha}(t) \tag{25}$$

is potentially inactive, and one with:

$$\left|\tau^{\alpha}(\tau)^{tr}\right| > s^{\alpha}(t) \tag{26}$$

is potentially active. Now, we can denote:

$$PA = \{\alpha \mid \alpha = 1,...,n\} \tag{27}$$

as a set of potentially active slip systems, where are $m \leq n$ slip systems which have slip rate different of zero and they represent active slip systems:

$$A = \{\alpha \mid \alpha = 1,...,m \leq n\} \tag{28}$$

Set of equations:

$$\sum_{\beta \in A} A^{\alpha\beta} x^{\beta} = b^{\alpha} \tag{29}$$

in matrix form:

$$\mathbf{Ax} = \mathbf{b} \tag{30}$$

Coefficients of set matrix **A** are given with relation:

$$A^{\alpha\beta} = h_{\alpha\beta}(t) + \left\{ \text{sign}\left(\tau^{\alpha}(\tau)^{tr}\right) \text{sign}\left(\tau^{\beta}(\tau)^{tr}\right) S_0^{\alpha} \cdot \mathbb{C}\left[\text{sym}\left(C^{*}(\tau)^{tr} S_0^{\beta}\right)\right] \right\} \tag{31}$$

Right hand side vector is:

$$b^{\alpha} = \left|\tau^{\alpha}(\tau)^{tr}\right| - s^{\alpha}(t) > 0 \tag{32}$$

Unknown represent increment of slip deformation:

$$x^{\beta} \equiv \Delta\gamma^{\beta} > 0 \tag{33}$$

Set of equations is solved iteratively to get vector of increments $\Delta\gamma^{\alpha}$, which is used to solve all variables dependent on γ^{α}.

2.5 Rate dependent formulation

In this section the two integration schemes [2] related to time will be represented. The first assumes a linear relationship between stress increments, strain and state variables such as shear deformation, shear stresses, and yield strength in the slip system and so on. Stresses and state variables are calculated at the beginning of time increment. Second scheme solves the non-linear incremental equations using Newton – Raphson iterative method. Implicit time integration is used to solve stresses and state variables at the end of time increment.

First slip deformation increment is defined $\Delta\gamma^{(\alpha)}$ on slip system α in time increment Δt:

$$\Delta\gamma^{(\alpha)} = \gamma^{(\alpha)}(t + \Delta t) - \gamma^{(\alpha)}(t) \tag{34}$$

Using linear interpolation for Δt:

$$\Delta\gamma^{(\alpha)} = \Delta t\left[(1-\theta)\dot{\gamma}_t^{(\alpha)} + \theta\dot{\gamma}_{t+\Delta t}^{(\alpha)}\right] \tag{35}$$

where the lower index represents time period of time for $\dot{\gamma}_t^{(\alpha)}$. Parameter θ can take values between 0 and 1, where for the $\theta = 0$ we have the Euler integration scheme. Recommended values of θ are in 0.5 to 1 range. Slip rate $\dot{\gamma}_t^{(\alpha)}$ is function of shear stress $\tau^{(\alpha)}$ and yield stress $g^{(\alpha)}$. With Taylor development of slip rate we get:

$$\dot{\gamma}_{t+\Delta t}^{(\alpha)} = \dot{\gamma}_t^{(\alpha)} + \frac{\partial\dot{\gamma}^{(\alpha)}}{\partial\tau^{(\alpha)}}\Delta\tau^{(\alpha)} + \frac{\partial\dot{\gamma}^{(\alpha)}}{\partial g^{(\alpha)}}\Delta g^{(\alpha)} \tag{36}$$

2.6 Non-linear incremental formulation

We will use incremental equation for shear deformation $\gamma^{(\alpha)}$ on α slip system, but we will not use Taylor development for slip rate. All incremental equations in this formulation are current but they become non-linear because stresses and state variables are solved at the end of the time step. We get non-linear equation for shear deformation increment using Schmid's law:

$$\Delta\gamma^{(\alpha)} - (1-\theta)\Delta t\dot{\gamma}_t^{(\alpha)} - \theta\Delta t\dot{a}^{(\alpha)} f^{(\alpha)}\left(\frac{\tau_t^{(\alpha)} + \Delta\tau^{(\alpha)}}{g_t^{(\alpha)} + \Delta g^{(\alpha)}}\right) = 0 \tag{37}$$

Where $\Delta\tau^{(\alpha)}$ and $\Delta g^{(\alpha)}$ are shear stress and critical yield stress increments, respectively. Equation above is solved using Newton-Raphson iterative method, and linear solution is used as referent value.

3. Examples and results

3.1 Cooper mono-crystal rod example

Uniaxial loading of copper mono crystal is analyzed as shown [2]. Rod is loaded by pressure of 200MPa, length is 100mm and square cross section is 10x10mm. Two edges of cross section are in [010] and [-101] crystal directions. Copper has FCC structure with elastic constants $c_{11} = 168400\text{MPa}$, $c_{12} = 121400\text{MPa}$, i $c_{44} = 75400\text{MPa}$. We have only one set of slip system {111}<110>. Assaro and Pierce hardening law is used with advised values for starting hardening modulus $h_0 = 541.5\text{MPa}$, stress on part I $\tau_s = 109.5\text{MPa}$ and $\tau_0 = 60.8\text{MPa}$ that are obtained experimentally for copper mono-crystal.

Results for stress components are given on Fig 1. to Fig 6. Displacements are given on Fig. 7 to Fig. 9.

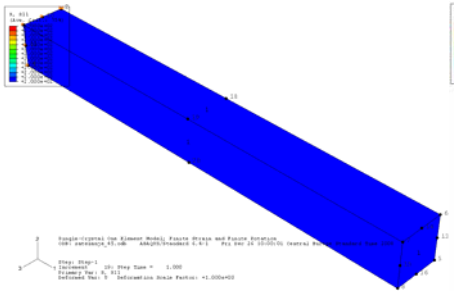

Figure 1. Stress component - σ_{11}

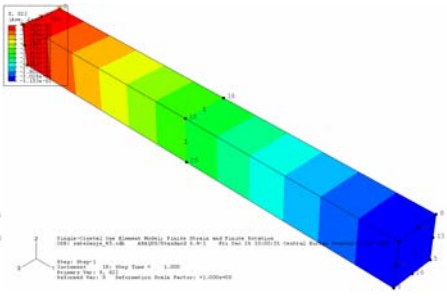

Figure 2. Stress component - σ_{22}

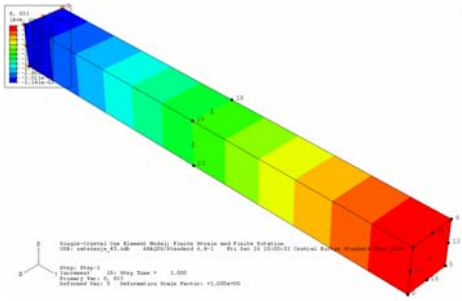

Figure 3. Stress component - σ_{33}

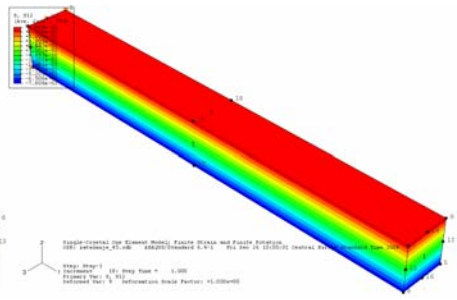

Figure 4. Stress component - σ_{12}

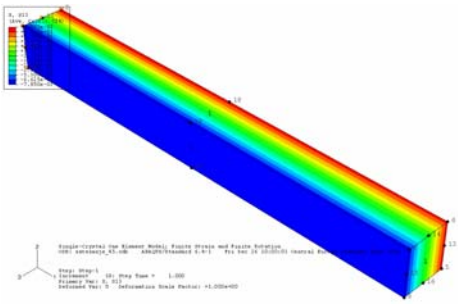

Figure 5. Stress component - σ_{23}

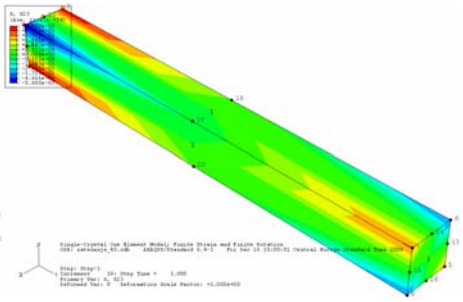

Figure 6. Stress component - σ_{13}

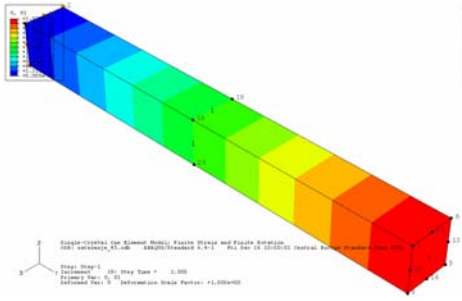

Figure 7. Displacement in 1 – direction

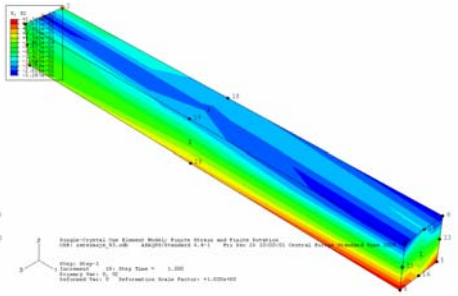

Figure 8. Displacement in 2 - direction

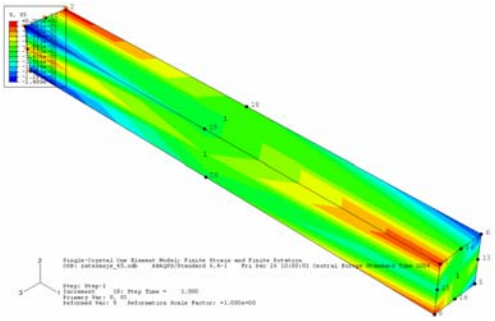

Figure 9. Displacement in 3 - direction

3.2 Copper bi-crystal cube example

Similar to previous mono crystal model, it is possible to generate mesh for poly crystals, bi –crystal in our case. As we explained, elements in input file are grouped in sets, and each set of elements are given one material. In this example we define material characteristics by changing material orientation of crystal grains and material constants are same as in previous example (copper). Copper bi-crystal made from two crystals of different orientation is analyzed. Some of stress components are shown in Fig. 10 to Fig. 12. Displacements are shown in Fig. 13 to Fig. 15.

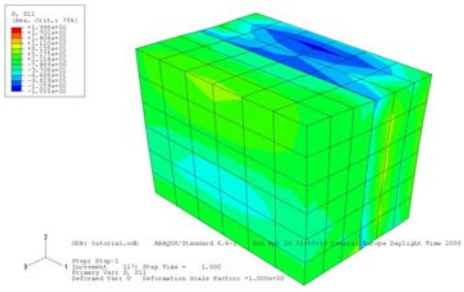

Figure 10. Stress component - σ_{11}

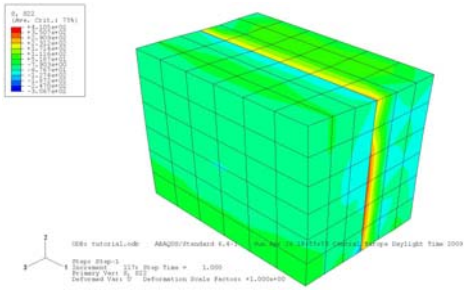

Figure 11. Stress component - σ_{22}

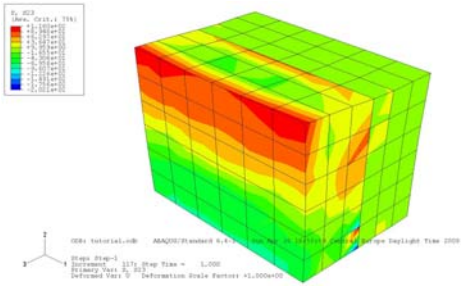

Figure 12. Stress component - σ_{23}

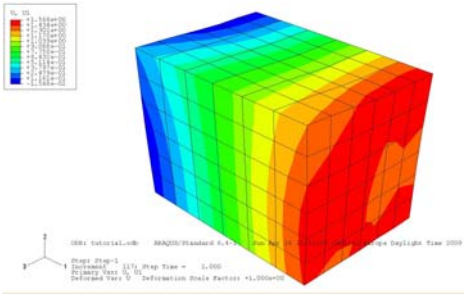

Figure 13. Displacement in 1 – direction

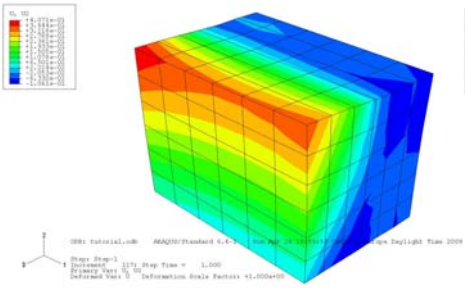

Figure 14. Displacement in 2 – direction

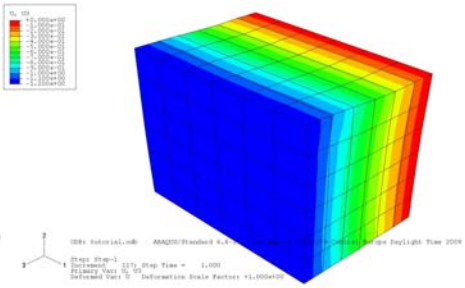

Figure 15. Displacement in 3 - direction

4. Implementation of material model in program PAK

Program PAK requires extra changes beside programming subroutine. UMAT material model is used as main subroutine as explained in previous chapter. All function and subroutine are connected in exact same procedure. Beside that, it was necessary to make certain changes in part connected with calling of subroutine. We are working on procedure for implementation some material models developed as UMAT routine for the ABAQUS program to PAK and vice versa.

Acknowledgement. The part of this research is supported by Ministry of Education and Science - TR32036.

References

[1] Harewood F. J., McHugh P. E. (2007) Comparasion of the implicit and explicit FEM using crystal plasticity, Computational materials science.
[2] Huang Y., Jeffrey W. (1991) Addendum to a user material subroutine incorporating single crystal plasticity in the ABAQUS finite element program, *Harvard University*.
[3] Nikolić Ružica (2008) Kristalografija – skripta, *Mašinski fakultet u Kragujevcu*.
[4] ABAQUS User's manual version 6.9-2
[5] Mićunović M. (1990) Mehanika kontinuuma*, Naučna knjiga, Beograd*.

[6] Fionn Dunne, Nik Petrinić (2005) Introduction to Computational Plasticity, *Oxford University Press*.
[7] Tien-Yue Wu, John L. Bassani, Campbell Laird (1991) Latent hardening in single crystals – I Theory and experiments, *Proc. R. Soc. Lond. A* vol. 435 no. 1893 1-19
[8] Živković M. (2006) Nelinearna analiza konstrukcija, *Mašinski Fakultet Kragujevac*.
[9] Kojić M., Slavković R., Živković M., Grujović N. (1998) PAK – Program za nelinearnu analizu konstrukcija, *Mašinski fakultet u Kragujevcu.*
[10] Bathe K., J. (1996) Finite Element Procedures, *Prentice Hall*.
[11] Kojić M., Bathe K.J. (2005) Inelastic Analysis of Solids and Structures, *Springer*.
[12] Slavković V. (2009) Seminarski rad iz mehanike kontinuuma, *Mašinski fakultet u Kragujevcu*.
[13] Kothari M. (1995) Rate Independent Crystal Plasticity", *MIT*.
[14] Raabe D. (2005) Geschichte der Metalle*, Class Notes, RWTH Aachen, Max-Planck Institut Düsseldorf.*
[15] Anand L., Kothari M. (1996) A computational procedure for rate-independent crystal plasticity, *J. Mech. Phys. Solids, Vol. 44, No. 4, pp. 525-558.*
[16] Hill R., Rice J. R. (1972) Constitutive analysis of elastic-plastic crystals at arbitrary strain, *J. Mech. Phys. Solids, 1972, Vol. 20, pp. 401-413.*
[17] Kysar J.W., Hall P. (1997) http://www.columbia.edu/~jk2079/fem/Addendum%20to%20umat.pdf

BUCKLING OF ELASTICALLY CONNECTED TIMOSHENKO THREE-BEAM SYSTEM UNDER COMPRESSIVE AXIAL LOADING

V. Stojanović[1], P. Kozić[2], D. Jovanović[3]

[1] Faculty of Mechanical Engineering
University of Niš, A. Medvedeva 14., 18000, Niš, Serbia
e-mail: stojanovic.s.vladimir@gmail.com
[2] Faculty of Mechanical Engineering
University of Niš, A. Medvedeva 14., 18000, Niš, Serbia
e-mail: kozicp@yahoo.com
[3] Faculty of Mechanical Engineering
University of Niš, A. Medvedeva 14., 18000, Niš, Serbia
e-mail: jdragan@masfak.ni.ac.rs

Abstract. Buckling instability of simply supported elastic Timoshenko three-beam system, continuously joined by Winkler elastic layers and subjected to the same compressive axial loads, is studied. The model of Timoshenko beam includes the effects of axial loading, shear deformation and rotary inertia. Explicit analytical expressions are derived for the critical buckling load of single, double and triple beam system. It can be observed from these expressions that the critical buckling load depends on the Winkler elastic layer stiffness per length K, while the instability of the system increases with the increase in the number of beams and elastic layers. These results are of considerable practical interest and have wide application in engineering practice.

1. Introduction

Vibration and buckling problems of beams or beam-columns on elastic foundations occupy an important place in many fields of structural and foundation engineering. This problem is very often encountered in aeronautical, mechanical, and civil engineering applications. Its solution demands the modeling of (a) the mechanical behavior of the beam, (b) the mechanical behavior of the soil and (c) the form of interaction between the beam and the soil. As far as the beam is concerned, most engineering analyses are based on the classical Bernoulli–Euler beam theory, in which straight lines or planes normal to the neutral beam axis remain straight and normal after deformation. This theory thus neglects the effect of transverse shear deformations, a condition that holds only in the case of slender beams. To confront this problem, the well-known Timoshenko beam model, in which the effect of transverse shear deflections is considered, can be used. Matsunaga [1] studies buckling instabilities of a simply supported thick elastic beam subjected to axial stresses. Taking into account the effects of shear deformations and thickness changes, buckling loads and buckling displacement modes of thick beams are obtained. Based on the power series expansion of displacement components, a set of fundamental equations of a one-dimensional higher-order beam theory is derived through the principle of virtual displacement. Several sets of truncated approximate theories are applied to solve the

eigenvalue problems of a thick beam. The convergence properties of the buckling loads of a simply supported thick beam are examined in detail and the comparison of the results with previously published ones is also made. On the basis of the Bernoulli–Euler beam theory, the properties of free transverse vibration and buckling of a double-beam system under compressive axial loading are investigated in paper Zhang et al. [2]. Explicit expressions are derived for the natural frequencies and the associated amplitude ratios of the two beams, and the analytical solutions of the critical buckling load is obtained. The influences of the compressive axial loading on the responses of the double-beam system are discussed. It is shown that the critical buckling load of the system is related to the axial compression ratio of the two beams and the Winkler elastic layer, and the properties of free transverse vibration of the system greatly depend on the axial compressions. Kelly and Srinivas [3] investigate the problem of the free vibrations of a set of n axially loaded, stretched Bernoulli–Euler beams connected by elastic layers and connected to a Winkler type foundation. A normal-mode solution is applied to the governing partial differential equations to derive a set of coupled ordinary differential equations which are used to determine the natural frequencies and mode shapes. It is shown that the set differential equations can be written in self-adjoint form with an appropriate inner product. An exact solution for the general case is obtained, but numerical procedures must be used to determine the natural frequencies and mode shapes. The numerical procedure is difficult to apply, especially in determining higher frequencies. For the special case of identical beams, an exact expression for the natural frequencies is obtained in terms of the natural frequencies of a corresponding set of unstretched beams and the eigenvalues of the coupling matrix. Stojanović et al. [4] study the influence of rotary inertia and shear on the free vibration and buckling of a double-beam system under axial loading. It is assumed that the system under consideration is composed of two parallel and homogeneous simply supported beams continuously joined by a Winkler elastic layer. Both beams have the same length. It is also supposed that buckling can only occur in the plane where the double-beam system lies. The explicit expressions are derived for natural frequencies and associated amplitude ratio of the two beams, and the analytical solution of the critical buckling is obtained. The influence of the characteristics of the Winkler elastic layer on natural frequencies, and the critical buckling force is determined. Li et al. [5] analyze an exact dynamic stiffness matrix established for an elastically connected three-beam system, which is composed of three parallel beams of uniform properties with uniformly distributed-connecting springs among them. The formulation includes the effects of shear deformation and rotary inertia of the beams. The dynamic stiffness matrix is derived by rigorous use of the analytical solutions of the governing differential equations of motion of the three-beam system in free vibration. The use of the dynamic stiffness matrix to study the three vibration characteristics of the three-beam system is demonstrated by applying the Muller root search algorithm. De Rosa [6] studies the free vibration frequencies on Timoshenko beams on two-parameter elastic foundation. Two variants of the equation of motion are deduced, in which the second foundation parameter is a function of the total rotation of the beam or a function of the rotation due to bending only. Ariaei [7] investigate the dynamic response of an elastically connected multiple-beam system. The identical prismatic Timoshenko beams are assumed to be parallel and connected by a finite number of springs. The motion of the system is described by a coupled set of $2n$ partial differential equations. The method involves a change of variables and modal analysis to decouple and to solve the governing differential equations, respectively.

In this paper, buckling instability of simply supported elastic Timoshenko beams, continuously joined by Winkler elastic layers and subjected to the same compressive axial load, is studied. The beams have the same length *l*, and it is also supposed that buckling can only occur in plane where the system beams lies. The model of Timoshenko beams includes the effects of axial loading, shear deformation and rotary inertia. Explicit analytical expressions are determined for the critical buckling load of single, double and triple beam models. It can be observed from these expressions that the critical buckling load depends on the Winkler elastic layer stiffness per length K, while the instability of the system increases with the increase in the number of beams and elastic layers.

2. Formulation of the differential equations of the dynamic equilibrium and structural model

It can be seen from the literature on the dynamic analysis of the elastically parallel-beam system that it is concentrated primarily on the case of a double-beam system of two parallel simply supported beams continuously joined by a Winkler elastic layer. Very few research papers can be found that deal with the problem related to the elastically connected three-beam system. Those studies of this region are limited to the particular cases of identical beams with some prescribed boundary conditions. It can also be seen that in most of the references, the simple Bernoulli–Euler beam theory has been used to derive the necessary equation. The basic differential equations of motion for the analysis will be deduced by considering the Timoshenko beam of length *l*, Fig. 1a, subjected to axial compressive force *F* and distributed lateral loads of intensity q_1 and q_2 which vary with the distance *z* along the beam. Also, this will be applied on the basis of the following assumptions: (a) the behavior of the beam material is linear elastic; (b) the cross-section is rigid and constant throughout the length of the beam and has one plane of symmetry; (c) shear deformations of the cross-section of the beam are taken into account while elastic axial deformations are ignored; (d) the equations are derived bearing in mind the geometric axial deformations; (e) the axial forces *F* acting on the ends of the beam are not changed with time.

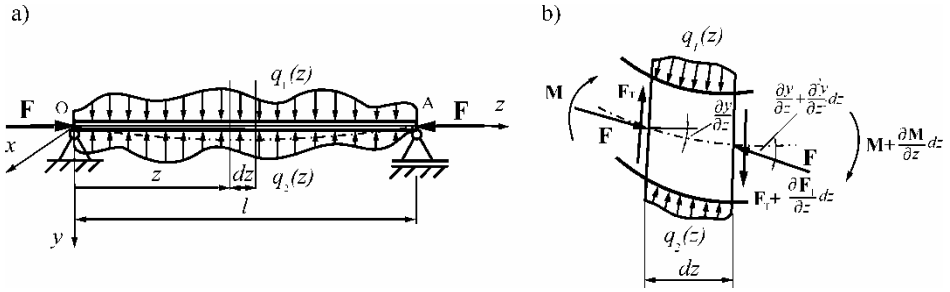

Figure 1. The physical model of the Timoshenko beam subjected to an axial compressive force F and distributed lateral loads of intensity q_1 and q_2.

An element of length dz between two cross sections is taken to be normal to the deflected axis of the beam, Fig. 1b. Since the slope of the beam is small, the normal forces acting on the sides of the element can be taken to be equal to the axial compressive force *F*. The shearing force F_T is related to the following relationship

$$F_T = kGA\left(\frac{\partial w}{\partial z} - \psi\right), \qquad (1)$$

where $w = w(z,t)$ is the displacement of a cross-section in y direction, $\frac{\partial w}{\partial z}$ is the global rotation of the cross-section, ψ is the bending rotation, G is the shear modulus, A is the area of the beam cross section, and k is the shear factor. Analogously, the relationship between bending moments M and bending angles $\psi = \psi(z,t)$ is given by

$$M = -EI_x\frac{\partial \psi}{\partial z}, \qquad (2)$$

where E is the Young modulus and I_x is the second moment of the area of the cross-section. Finally, forces and moments of inertia are given by

$$f_i = -\rho A\frac{\partial^2 w}{\partial t^2}, \quad J_i = -\rho I_x\frac{\partial^2 \psi}{\partial t^2}, \qquad (3)$$

respectively, where ρ is the mass density. The forces acting on a differential layered-beam element are shown in Fig. 1b. The dynamic-force equilibrium conditions of these forces are given by the following equations

$$\rho A\frac{\partial^2 w}{\partial t^2} - kGA\left(\frac{\partial^2 w}{\partial z^2} - \frac{\partial \psi}{\partial z}\right) + F\frac{\partial^2 w}{\partial z^2} - q_2(z) + q_2(z) = 0, \qquad (4a)$$

$$\rho I\frac{\partial^2 \psi}{\partial t^2} - EI_x\frac{\partial^2 \psi}{\partial x^2} - kGA\left(\frac{\partial w}{\partial z} - \psi\right) = 0. \qquad (4b)$$

Fig. 2 presents the development and solution of the differential equations of motion governing the free flexural vibrations of the elastically connected identical three-beam systems considering the effects of shear deformation and rotary inertia.

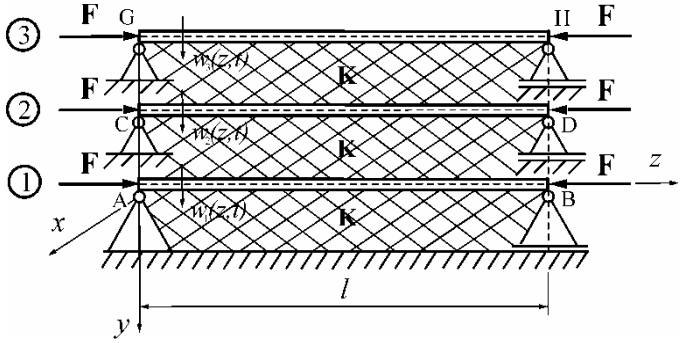

Figure 2. Identical three-beam systems.

Each beam is made of some material with the Young modulus E, and mass density ρ, and has a cross-section with a uniform cross-section of area A and moment of inertia $I = I_x$, while beams are subjected to the same compressive axial loading. The first beam is

connected to Winkler foundation of the stiffness per length *K*, and the second and third beams are also connected by a continuous linear elastic layer of Winkler type of the same stiffness per length K. The transverse displacements of the beams are $w_i = w_i(z,t), i = 1,2,3$ and $\psi_i = \psi_i(z,t), i = 1,2,3$ are bending rotations. If we apply the abovementioned procedure to a differential element of each beam, the following set of coupled differential equations will be obtained:

$$\rho A\frac{\partial^2 w_1}{\partial t^2} - kGA\left(\frac{\partial^2 w_1}{\partial z^2} - \frac{\partial \psi_1}{\partial z}\right) + F\frac{\partial^2 w_1}{\partial z^2} + 2Kw_1 - Kw_2 = 0, \qquad (5a)$$

$$\rho I\frac{\partial^2 \psi_1}{\partial t^2} - EI\frac{\partial^2 \psi_1}{\partial x^2} - kGA\left(\frac{\partial w_1}{\partial z} - \psi_1\right) = 0, \qquad (5b)$$

$$\rho A\frac{\partial^2 w_2}{\partial t^2} - kGA\left(\frac{\partial^2 w_2}{\partial z^2} - \frac{\partial \psi_2}{\partial z}\right) + F\frac{\partial^2 w_2}{\partial z^2} - Kw_1 + 2Kw_2 - Kw_3 = 0, \qquad (6a)$$

$$\rho I\frac{\partial^2 \psi_2}{\partial t^2} - EI\frac{\partial^2 \psi_2}{\partial x^2} - kGA\left(\frac{\partial w_2}{\partial z} - \psi_2\right) = 0, \qquad (6b)$$

$$\rho A\frac{\partial^2 w_3}{\partial t^2} - kGA\left(\frac{\partial^2 w_3}{\partial z^2} - \frac{\partial \psi_3}{\partial z}\right) + F\frac{\partial^2 w_3}{\partial z^2} - Kw_2 + Kw_3 = 0, \qquad (7a)$$

$$\rho I\frac{\partial^2 \psi_3}{\partial t^2} - EI\frac{\partial^2 \psi_3}{\partial x^2} - kGA\left(\frac{\partial w_3}{\partial z} - \psi_3\right) = 0. \qquad (7b)$$

3. The axial buckling load of the elastically connected identical three-beam system

The stability behavior of simply supported Timoshenko beam systems on a Winkler elastic foundation is of great interest to both practicing engineers and researchers. The usual approach to formulating this problem is by including the foundation reaction into corresponding differential equation of the beam. The buckling of an elastically connected simply supported Timoshenko beams under some static compressive axial load is investigated. The analytical solution for the critical buckling load of the system is derived. The second-order partial differential Eqs. (5a) and (5b), (6a) and (6b), and (7a) and (7b), which are couplet together, can be further reduced by eliminating ψ_1, ψ_2 and ψ_3, respectively, to the following system fourth-order partial differential equations

$$EI\left(1 - \frac{F}{kAG}\right)\frac{\partial^4 w_1}{\partial z^4} + \left(\rho A + 2\frac{K\rho I}{kAG}\right)\frac{\partial^2 w_1}{\partial t^2} - \frac{K\rho I}{kAG}\frac{\partial^2 w_2}{\partial t^2} + \left(F - 2\frac{KEI}{kAG}\right)\frac{\partial^2 w_1}{\partial z^2}$$
$$+ \frac{KEI}{kAG}\frac{\partial^2 w_2}{\partial z^2} - \left(\rho I + \frac{\rho EI}{kG} - \frac{F\rho I}{kAG}\right)\frac{\partial^4 w_1}{\partial z^2 \partial t^2} + \frac{\rho^2 I}{kG}\frac{\partial^4 w_1}{\partial t^4} + 2Kw_1 - Kw_2 = 0, \qquad (9a)$$

$$EI\left(1 - \frac{F}{kAG}\right)\frac{\partial^4 w_2}{\partial z^4} - \frac{K\rho I}{kAG}\frac{\partial^2 w_1}{\partial t^2} + \left(\rho A + 2\frac{K\rho I}{kAG}\right)\frac{\partial^2 w_2}{\partial t^2} - \frac{K\rho I}{kAG}\frac{\partial^2 w_3}{\partial t^2} + \frac{KEI}{kAG}\frac{\partial^2 w_1}{\partial z^2}$$
$$+ \left(F - \frac{KEI}{kAG}\right)\frac{\partial^2 w_2}{\partial z^2} + \frac{KEI}{kAG}\frac{\partial^2 w_3}{\partial z^2} - \left(\rho I + \frac{\rho EI}{kG} - \frac{F\rho I}{kAG}\right)\frac{\partial^4 w_2}{\partial z^2 \partial t^2} + \frac{\rho^2 I}{kG}\frac{\partial^4 w_2}{\partial t^4} - Kw_1$$

$$+2Kw_2 - Kw_3 = 0, \tag{9b}$$

$$EI\left(1-\frac{F}{kAG}\right)\frac{\partial^4 w_3}{\partial z^4} - \frac{K\rho I}{kAG}\frac{\partial^2 w_2}{\partial t^2} + \left(\rho A + \frac{K\rho I}{kAG}\right)\frac{\partial^2 w_3}{\partial t^2} + \frac{KEI}{kAG}\frac{\partial^2 w_2}{\partial z^2} + \left(F - \frac{KEI}{kAG}\right)\frac{\partial^2 w_3}{\partial z^2}$$
$$-\left(\rho I + \frac{\rho EI}{kG} - \frac{F\rho I}{kAG}\right)\frac{\partial^4 w_3}{\partial z^2 \partial t^2} + \frac{\rho^2 I}{kG}\frac{\partial^4 w_3}{\partial t^4} - Kw_2 + Kw_3 = 0, \tag{9c}$$

The initial conditions in general form and boundary conditions for simply supported beams of the same length l are assumed as follows

$$w_i(z,0) = w_{i0}(z), \quad \dot{w}_i(z,0) = v_{i0}(z), \quad \varphi_i(z,0) = \varphi_{i0}(z), \quad \dot{\varphi}_i(z,0) = \omega_{i0}(z),$$
$$w_i(z,0) = w''_i(0,t) = w_i(l,0) = w''_i(l,t) = 0, \quad i = 1,2,3. \tag{11}$$

Assuming time harmonic motion and using separation of variables, the solutions of Eqs. (9a), (9b) and (9c), and the governing boundary conditions (11) can be written in the form

$$w_i(z,t) = \sum_{n=1}^{\infty} X_n(z) T_{in}(t), \quad i = 1,2,3, \tag{12}$$

where $T_{in}(t)$ is the unknown time function, and $X_n(z)$ is the known mode shape function for simply supported single beam, which is defined as

$$X_n(x) = \sin(k_n z), \quad k_n = n\pi/l, \quad n = 1,2,3,\cdots. \tag{13}$$

Introducing the general solutions (12) into Eqs. (9) one gets the system ordinary differential equations

$$\sum_{n=1}^{\infty}\left\{\frac{1}{C_s^2}\frac{d^4 T_{1n}}{dt^4} + \left[1 + C_p^2 k_n^2\left(1 + \frac{C_\beta^2}{C_s^2 C_p^2}\right) + \frac{1}{C_s^2}(2H - F\eta)\right]\frac{d^2 T_{1n}}{dt^2} - \frac{H}{C_s^2}\frac{d^2 T_{2n}}{dt^2}\right.$$
$$\left. + \left[C_\beta^2 k_n^4 + (2H - F\eta)\left(1 + \frac{C_\beta^2}{C_s^2 C_p^2}k_n^2\right)\right]T_{1n} - H\left(1 + \frac{C_\beta^2}{C_s^2 C_p^2}k_n^2\right)T_{2n}\right\} = 0, \tag{14a}$$

$$\sum_{n=1}^{\infty}\left\{\frac{1}{C_s^2}\frac{d^4 T_{2n}}{dt^4} - \frac{H}{C_s^2}\frac{d^2 T_{1n}}{dt^2} + \left[1 + C_p^2 k_n^2\left(1 + \frac{C_\beta^2}{C_s^2 C_p^2}\right) + \frac{1}{C_s^2}(2H - F\eta)\right]\frac{d^2 T_{2n}}{dt^2} - \frac{H}{C_s^2}\frac{d^2 T_{3n}}{dt^2}\right.$$
$$-H\left(1 + \frac{C_\beta^2}{C_s^2 C_p^2}k_n^2\right)T_{1n} + \left[C_\beta^2 k_n^4 + (2H - F\eta)\left(1 + \frac{C_\beta^2}{C_s^2 C_p^2}k_n^2\right)\right]T_{2n}$$
$$\left. -H\left(1 + \frac{C_\beta^2}{C_s^2 C_p^2}k_n^2\right)T_{3n}\right\} = 0, \tag{14b}$$

$$\sum_{n=1}^{\infty}\left\{\frac{1}{C_s^2}\frac{d^4 T_{3n}}{dt^4} - \frac{H}{C_s^2}\frac{d^2 T_{2n}}{dt^2} + \left[1 + C_p^2 k_n^2\left(1 + \frac{C_\beta^2}{C_s^2 C_p^4}\right) + \frac{1}{C_s^2}(H - F\eta)\right]\frac{d^2 T_{3n}}{dt^2}\right.$$

$$-H\left(1+\frac{C_\beta^2}{C_s^2C_r^2}k_n^2\right)T_{2n}+\left[C_\beta^2k_n^4+(H-F\eta)\left(1+\frac{C_\beta^2}{C_s^2C_r^2}k_n^2\right)\right]T_{3n}\Big\}=0, \qquad (14c)$$

where

$$H=\frac{K}{\rho A}, \qquad \eta=\frac{k_n^2}{\rho A}.$$

The coefficients

$$C_b=\sqrt{\frac{EI}{\rho A}}, \qquad C_s=\sqrt{\frac{GAk}{\rho I}}, \qquad C_r=\sqrt{\frac{I}{A}},$$

related to bending stiffness, shear stiffness and rotational effects, respectively, are now introduced. The shear beam model, the Rayleigh beam model and the simple Euler beam model can be obtained from the Timoshenko beam model by setting C_r to zero (that is, ignoring the rotational effect), C_s to infinity (ignoring the shear effect) and setting both C_r to zero and C_s to infinity, respectively. The solutions of Eq. (14a), (14b) and (14c) can be assumed to have the following forms

$$T_{1n}=A_ne^{j\omega_nt}, \qquad T_{2n}=B_ne^{j\omega_nt}, \qquad T_{3n}=C_ne^{j\omega_nt} \qquad j=\sqrt{-1}, \qquad (15)$$

where ω_n denotes the natural frequency of the system. Substituting Eq. (15) into Eqs. (14a), (14b) and (14c) results in the following system of homogeneous algebraic equations for the unknown constants A_n, B_n, C_n

$$\left\{\frac{\omega_n^4}{C_s^2}-\left[1+C_r^2k_n^2\left(1+\frac{C_\beta^2}{C_s^2C_r^2}\right)+\frac{1}{C_s^2}(2H-F\eta)\right]\omega_n^2+\left[C_\beta^2k_n^4+(2H-F\eta)\left(1+\frac{C_\beta^2}{C_s^2C_r^2}k_n^2\right)\right]\right\}A_n+H\left[\frac{\omega_n^2}{C_s^2}-\left(1+\frac{C_\beta^2}{C_s^2C_r^2}k_n^2\right)\right]$$
$$+H\left[\frac{\omega_n^2}{C_s^2}-\left(1+\frac{C_\beta^2}{C_s^2C_r^2}k_n^2\right)\right]B_n=0, \qquad (16a)$$

$$H\left[\frac{\omega_n^2}{C_s^2}-\left(1+\frac{C_\beta^2}{C_s^2C_r^2}k_n^2\right)\right]A_n+\left\{\frac{\omega_n^4}{C_s^2}-\left[1+C_r^2k_n^2\left(1+\frac{C_\beta^2}{C_s^2C_r^2}\right)+\frac{1}{C_s^2}(2H-F\eta)\right]\omega_n^2+\left[C_\beta^2k_n^4+(2H-F\eta)\left(1+\frac{C_\beta^2}{C_s^2C_r^2}k_n^2\right)\right]\right\}B_n+H\left[\frac{\omega_n^2}{C_s^2}-\left(1+\frac{C_\beta^2}{C_s^2C_r^2}k_n^2\right)\right]C_n=0, \qquad (16b)$$

$$H\left[\frac{\omega_n^2}{C_s^2}-\left(1+\frac{C_\beta^2}{C_s^2C_r^2}k_n^2\right)\right]B_n+\left\{\frac{\omega_n^4}{C_s^2}-\left[1+C_r^2k_n^2\left(1+\frac{C_\beta^2}{C_s^2C_r^2}\right)+\frac{1}{C_s^2}(H-F\eta)\right]\omega_n^2+\left[C_\beta^2k_n^4+(H-F\eta)\left(1+\frac{C_\beta^2}{C_s^2C_r^2}k_n^2\right)\right]\right\}C_n=0. \qquad (16c)$$

Equations (16a), (16b) and (16c) have non-trivial solutions in the case when the determinant at the system matrix coefficients of the A_n, B_n and C_n is equal to zero. This yields the following frequency (characteristic) equation, which is a twelfth order polynomial in ω_n. When the natural frequency of the system vanishes under the axial loading, the system begins to buckle. By introducing $\omega_n = 0$ into Eqs. (16a), (16b) and (16c), expressed in matrix form, they become

$$\begin{bmatrix} x+2RH & -HR & 0 \\ -HR & x+2RH & -HR \\ 0 & -HR & x+RH \end{bmatrix} \begin{Bmatrix} A_n \\ B_n \\ C_n \end{Bmatrix} = 0. \qquad (17)$$

where

$$R = 1 + \frac{C_S^2}{C_L^2 C_T^2} k_n^2, \quad x = C_S^2 k_n^4 - RF\eta. \qquad (18)$$

Using Gauss elimination and expanding the determinant

$$[(x^3 + 5RHx^2 + 6(RH)^2 x + (RH)^3)]T = 0 \quad \text{with} \quad T = A_n, B_n \text{ or } C_n. \qquad (19)$$

where

$$a_0 = 1, \quad a_1 = 5RH, \quad a_2 = 6(RH)^2, \quad a_3 = (RH)^3.$$

Solution to Eq. (19) is taken from (http://mathword.wolfram.com/search/) as follows

$$x_1 = -\frac{5}{3}RH + 2\sqrt{-\frac{p}{3}}\cos\left(\frac{\varphi}{3}\right) = -0.198062RH,$$

$$x_2 = -\frac{5}{3}RH + 2\sqrt{-\frac{p}{3}}\cos\left(\frac{\varphi+2\pi}{3}\right) = -1.55496RH,$$

$$x_3 = -\frac{5}{3}RH + 2\sqrt{-\frac{p}{3}}\cos\left(\frac{\varphi+4\pi}{3}\right) = -3.24698RH, \qquad (20)$$

where

$$p = \frac{a_2}{a_0} - \frac{a_1^2}{3a_0^2}, \quad q = \frac{a_3}{a_0} - \frac{a_1 a_2}{3a_0^2} + \frac{2a_1^3}{27a_0^3}, \quad D = \frac{q^2}{4} + \frac{p^3}{27} < 0,$$

$$\varphi = \cos^{-1}\left[-\frac{q}{2}\left(-\frac{p}{3}\right)^{-\frac{1}{2}}\right].$$

If solutions x_1, x_2 and x_3 are substituted into the above Eq. (18), then the corresponding buckling loads for different vibration mode *n* will be obtained

$$(F)_b^I = \frac{0.198062H}{\eta} + \frac{C_E^2 k_n^4}{R\eta}, \quad (F)_b^{II} = \frac{1.554962H}{\eta} + \frac{C_E^2 k_n^4}{R\eta},$$

$$(F)_b^{III} = \frac{3.24698H}{\eta} + \frac{C_E^2 k_n^4}{R\eta}. \qquad (21)$$

As it can be seen, the values of the buckling loads $(F)_b^I$, $(F)_b^{II}$, and $(F)_b^{III}$ are positive and $(F)_b^I > (F)_b^{II} > (F)_b^{III}$. Consequently, $(F)_b^I$ is the critical buckling load corresponding to vibration mode $n = 1$, namely

$$(F)_b^{cr} = \frac{0.198062\,K l^2}{\pi^2} + \frac{EI\pi^2}{l^2\left(1 + \frac{EI}{GAk}\frac{\pi^2}{l^2}\right)}. \qquad (22)$$

For $K = 0$ we obtain the critical buckling load of the Timoshenko beam:

$$F = \frac{EI\pi^2}{l^2\left(1 + \frac{EI}{GAk}\frac{\pi^2}{l^2}\right)},$$

as shown in [8, pp. 134], representing the smallest load at which the beam ceases to be in stable equilibrium.

3. 1. Critical buckling load to system with two Timoshenko beams

Let us consider a system which consists of one Timoshenko beam on a Winkler elastic foundation connected to the other Timoshenko beam by a Winkler elastic layer. Each beam is subjected to the same compressive axial loading. Then matrix equation (17) is reduced, and it is as follows for the system shown in Fig. 3

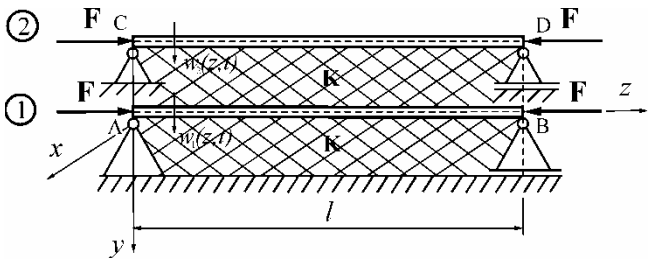

Figure 3. Identical two-beam systems.

$$\begin{bmatrix} x + 2RH & -HR \\ -HR & x + RH \end{bmatrix} \begin{Bmatrix} A_n \\ B_n \end{Bmatrix} = 0. \qquad (23)$$

Expanding the determinant we obtain

$$[(x^2 + 3RHx + (RH)^2)]T = 0 \quad \text{with} \quad T = A_n \text{ or } B_n . \qquad (24)$$

Solutions to Eq. (24) are

$$x_{1/2} = \frac{-3RH \pm RH\sqrt{5}}{2} \Rightarrow x_1 = \frac{-3RH + RH\sqrt{5}}{2} = -0{,}382RH,$$
$$x_2 = \frac{-3RH - RH\sqrt{5}}{2} = -2{,}618RH.$$

If solutions x_1 and x_2 are substituted into the above Eq. (18), then the corresponding buckling loads for different vibration mode *n* will be obtained

$$(F)_0^I = \frac{0{,}382H}{\eta} + \frac{C_0^2 k_n^4}{R\eta}, \quad (F)_0^{II} = \frac{2{,}618H}{\eta} + \frac{C_0^2 k_n^4}{R\eta}. \qquad (25)$$

Consequently, $(F)_0^I$ is the critical buckling load corresponding to vibration mode $n = 1$, for this system

$$(F)_0^{cr} = \frac{0{,}382\, KL^2}{\pi^2} + \frac{EI\pi^2}{L^2\left(1 + \frac{EI}{GAkL^2}\pi^2\right)}. \qquad (26)$$

3. 2. Critical buckling load to system with Timoshenko beam resting on Winkler elastic foundation

Consider a simply supported Timoshenko beam under compressive axial loading resting on a Winkler elastic foundation, Fig. 4.

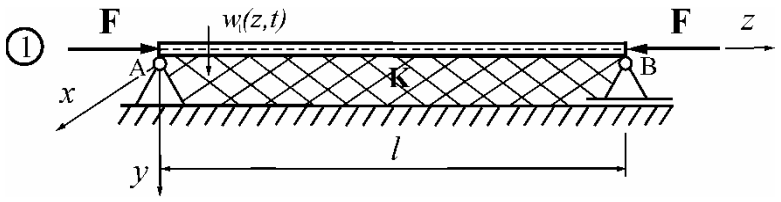

Figure 4. Timoshenko beam supported on a Winkler elastic foundation.

In this case, matrix equation (23) is reduced and it becomes the following algebraic equation

$$(x + RH)A_n = 0. \qquad (27)$$

The solution of this equation is $x = -RH$. If we replace this solution in the above Eq. (18), then the critical buckling load for the corresponding vibration mode $n = 1$ for this system is

$$(F)_b^{cr} = \frac{Kl^2}{\pi^2} + \frac{EI\pi^2}{l^2\left(1 + \frac{EI}{GAk}\frac{\pi^2}{l^2}\right)}. \qquad (28)$$

The change in the critical buckling load in the function of stiffness of elastic layer K for systems with triple, double, and single Timoshenko beam are determined by analytical expressions (22), (26) and (28), and their graphs are given in Fig. 5. These functions also determine the boundaries of static stability of the corresponding system with a triple, double, or single Timoshenko beam under compressive axial loading resting on a Winkler elastic foundation.

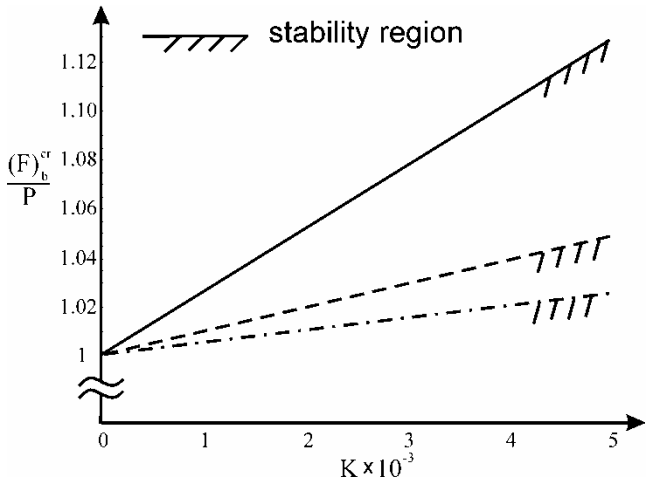

Figure 5. Variations of the critical buckling loads of simple supported beams resting on a Winkler elastic foundation.

4. Summary and conclusions

In the present paper, the equations of dynamic equilibrium and the equations of natural vibration of the triple Timoshenko beam elastically connected to a Winkler elastic foundation are formulated. In order to derive these equations, the influence of constant axial forces at the ends of the same beams (second order theory), as well as the influence of the elastic foundation and elastic layer on the beams, are taken into account. Using the classical Bernoulli-Fourier method, the solutions of the differential equations of motion for the system are formulated. The explicit expressions for the critical buckling load of the systems with a triple, double, and single Timoshenko beam are obtained. It is observed from the numerical results that the critical buckling load is influenced by the Winkler foundation of the stiffness per length *K* and the number of Timoshenko beams. Also, it can be seen that the critical buckling load of the triple and double Timoshenko beam systems is always smaller than the one in the single beam system.

Acknowledgement. This research was supported by the research grant of the Serbian Ministry of Science and Environment Protection under the number ON 174011.

References

[1] Matsunaga H.: Buckling instabilities of thick elastic beams subjected to axial stresses. *Computers & Structures*, **59** (1996), 859-868.
[2] Zhang Q. Y., Lu Y., Wang L. S., Liu X.: Vibration and buckling of a double-beam system under compressive axial loading. *J. Sound Vib*. **318** (2010), 341–352.
[3] Kelly G. S., Srinivas S.: Free vibrations of elastically connected stretched beams. *J. Sound Vib*. **326** (2009), 883-893.
[4] Stojanović V., Kozić P., Pavlović R., Janevski G.: Effect of rotary inertia and shear on vibration and buckling of a double beam system under compressive axial loading. *Arch. Appl. Mech.* DOI 10.1007/s00419-0110532-1.
[5] Li J., Chen Y., Hua H.: Exact dynamic stiffness matrix of a Timoshenko three-beam system. *Int. J. of Mech. Science*. **50** (2008), 1023-1034.
[6] De Rosa M. A.: Free vibrations of Timoshenko beams on two-parameter elastic foundation. *Computers & Structures*, **57** (1995), 151-156.
[7] Ariaei A., Ziaei-Rad S. and Ghaypur M.: Transverse vibration of a multiple-Timoshenko beam system with intermediate elastic connections due to a moving load. *Arch. Appl. Mech*., **81** (2011), 263-281.
[8] Timoshenko S. P., Gere J. M.: Theory of elastic stability. *2nd ed. International student edition McGraw-Hill*; 1964.

LIMIT ANALYSIS OF PLATES

D. Šumarac[1], J. Dragaš[2]

Faculty of Civil Engineering
University of Belgrade, Bulevar kralja Aleksandra 73, 11000 Belgrade, Serbia
[1]e-mail: sumi@eunet.rs
[2]e-mail: jelena.dragas@gmail.com

Abstract. In the present paper static and kinematic limit analysis of plates under bending is examined. An overview of literature is given. It is well know that static theorem gives lower bound, while kinematic theorem upper bound solution. Recently some attempt using numerical approach mostly finite elements have been published. In the paper all solutions will be analyzed, and an attempt of authors to improve them will be given.

1. Introduction

In a society where the main goal is a greater economic benefit, there is a need to build more economical structures. Development of computer technology enabled the rapid progress in many fields of engineering and technology. Many methods that were useless without the use of fast computers now have a wide practical application. This has produced a revolution in building practices using the finite element method and the theory of plasticity. To a period when computers reached the level that allowed them to have practical use in solving complex problems in mathematics and technology, principle of elastic analysis has been prevalent in civil engineering. With limited use of computers and a modest knowledge in the field of theory of plasticity this principle gives us a safe solution. On the other hand elastic analysis provides a structure that is not economical. Designing by means of plastic analysis gives a more efficient and rational construction. Development of commercial software enabled the design of such structures, and the main cost of investors becomes construction material. Therefore, it is necessary to reduce its consumption in structures. Many countries have already exceeded the *allowable stress theory* to the *theory of limit states* to embrace this new principle. Application of the principle of theory of plasticity began in beams, but it quickly expanded its application to two- and three-dimensional elements. For the civil engineer the analysis of plates subjected to bending is of prime importance, so no wonder a lot of interest is shown in finding the exact solutions of capacity of these elements using theory of plasticity.

Preparations for the yield line theory began in the early 90s and became famous thanks to Johanson [7]. The biggest advantage of this method is that it brought a new way of looking at the problems of capacity of plate. In that way it introduced a new view of slabs in our minds, and enabled solving slab systems that are not solvable by equivalent method. The yield line theory is quite well developed, especially the application on reinforced concrete slabs is popular. The fact that the yield line theory only provides an upper bound solution is no restriction for practical applications, because the solutions have been validated thoroughly by both experimental and theoretical research. The yield criterion is solely

based on bending moments. Plastic rotation can occur only if the corresponding bending moment is equal to the plastic moment m_p, also indicated by yield moment or ultimate moment. By formation and increase of hinges, an indeterminate structure initially becomes determinate and then will transform to a mechanism.

In the year of 1986 Manolakos and Mamalis [1] introduced a new technique, the *end-fixity coefficients method*. This method was developed for the prediction of upper- and lower-bound loads to cause the plastic collapse of thin, uniformly loaded rectangular plates of rigid-perfectly plastic material, which is assumed to flow according to the Johansen yield criterion. They introduced an analysis for predicting the limit load of uniformly loaded rectangular plates applicable to various boundary conditions of the plates, based on the *end-fixity coefficients* technique. They concluded that with an increasing number of clamped sides the difference between the lower- and upper-bound loads increases, with the maximum difference obtained in the case of the fully clamped plates.

In 1978, Munro and Da Fonseca invented a computational method for yield line analysis that used triangular finite elements and the LP (linear programming). This method requires from users to define a triangular mesh that represents the actual position of the yield lines in whole slab. The slab was divided into triangular elements and the yield lines were assumed to develop only along the element boundaries. Deficiency of this method is that elements of a mesh introduced by the user may not include a critical yield line pattern. The method of Munro and Da Fonseca uses a fixed, arbitrary mesh of potential yield lines to predict the collapse load of a slab or plate. Although this method represents a considerable advance, the main drawback is that element boundaries of the triangular mesh may lie away from the true critical yield line pattern. Many papers on this subject were published later. It was clear that finding the best FEM was very important for defining yield lines in slabs. Thavalingam wrote a paper [5], which describes an optimization procedure for adjusting the mesh to provide a safer estimate of the collapse load. The authors have recently developed a semiautomatic geometrical optimization technique to examine the effect of adjusting the geometry of Munro and Da Fonseca's stationary triangular mesh. A kinematic formulation is used to generate an LP model for a specific yield line. Results obtained using this mesh adjustment of the Munro and Da Fonseca yield line analysis of slabs using an optimization procedure improved previous solutions. The use of geometrical optimization techniques gives useful insight into characteristics of critical collapse.

A lot of research was done on finding a method which give us a right yield line pattern. Much experimental and theoretical work was done in different software's. Solmaz Pourrezay Khaligh [2] concluded that despite the fact that it is impossible to determine the exact crack path by ANSYS software, however, by observing the strain distribution in the slabs one can achieve the approximate yield line pattern.

2. Limit analysis of plates

Plastic analysis of plates is done using upper bound theory (yield lines) and lower bound theory. Equations which are used in these calculations are firstly equations of work method:

$$W = E_d \tag{1}$$

W is the work done by the external load, E_d is the amount of dissipated energy for a prescribed displacement during failure.

$$W = \sum_A q * S * w \tag{2}$$

S is the area of a plate part, w is the displacement of the centre of gravity.

$$E_d = \sum m_p * |\Delta\varphi_d| * l \tag{3}$$

m_p is the plastic moment, $\Delta\varphi_d$ is the angle between the plate parts, l is the length of the yield line.

For the determination of a lower bound of the load factor at failure the equilibrium equation for the plate field has to be used:

$$\frac{\partial^2 m_{xx}}{\partial x^2} + 2\frac{\partial^2 m_{xy}}{\partial x \partial y} + \frac{\partial^2 m_{yy}}{\delta y^2} + \lambda q(x,y) = 0 \tag{4}$$

3. Upper bound

3.1. Upper bound of simply supported plate

In this chapter rectangular plate (see Fig. 3.1) is being analyzed. The plate is considered with uniformly distributed load λq and sides *a* and *b*. The ratio β=*b*/*a* is a variable with β≥1. The distance between point *E* and side *AC* is set to α*a* (see Fig. 2.1). Energy is dissipated in the yield lines only.

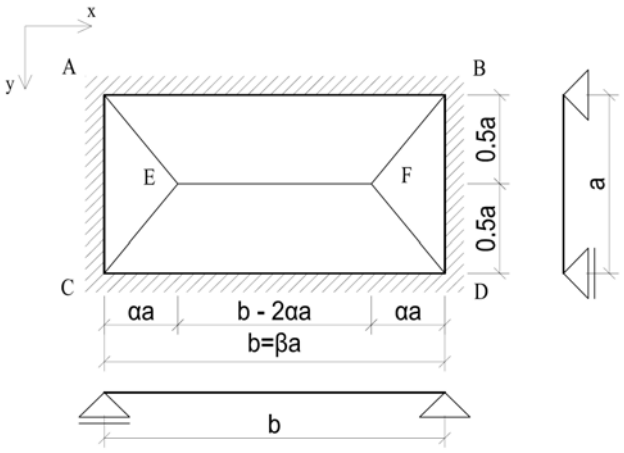

Figure 3.1. Rectangular simply supported plate.

The data required for the work equation are gathered in the table 3.1 below. For the determination of the work, plate part ABEF is subdivided into two triangles after which (1, 2, 3) has been applied. Also in this case the displacement of point E is set to w.

Table 3.1 Data required for the work equation

Plate part	Areas	Displacement	Yield line	l_x	l_y	$\|\Delta\varphi_x\|$	$\|\Delta\varphi_y\|$
ABE	1/2b*1/2a	1/3w	FE	b-2αa	0	4w/a	0
EFB	½(b-2αa)*1/2a	2/3w	AE, CE	αa	1/2a	2w/a	w/(αa)
BDF	1/2a*αa	1/3w	BF, DF	αa	1/2a	2w/a	w/(αa)

The work done by the external load λq yields:

$W=2\lambda q(1/4ba*1/3w+1/4a(b-2\alpha a)*2/3w+1/2\alpha a^2*1/3w)$

$W=1/2\lambda qa(b-2/3\alpha a)w$

The dissipated energy is calculated by making use of (3):

$E_d=m_p((b-2\alpha a)*4w/a)+4*m_p(\alpha a*2w/a+1/2a*w/\alpha a)$

$E_d=4m_p(b/a+1/(2\alpha))w$

Equating these two formulae according to (1, 2, 3) and introducing $b=\alpha a$ provides the following relation for the load factor:

$1/2\lambda qa(b-2/3\alpha a)w = 4m_p(b/a+1/(2\alpha))w$

$$\lambda^{U} = 8\frac{\left(\beta + \frac{1}{2\alpha}\right)}{\left(\beta - \frac{2}{3}\alpha\right)}\frac{m_p}{qa^2} \tag{5}$$

For a given value of β, parameter α has to be determined such that λ is minimized. Naturally, those values of α should correspond to physically possible positions of point *E*. This leads to the following condition:

$$0 \leq \alpha \leq \frac{1}{2}\beta$$

The result of this condition is that boundary minima have to be considered too. The desired stationary values can be obtained through:

$$\frac{d\lambda_r}{d\alpha} = \frac{\left(\beta - \frac{2}{3}\alpha\right)\left(-\frac{1}{2\alpha^2}\right) - \left(-\frac{2}{3}\right)\left(\beta + \frac{1}{2\alpha}\right)}{\left(\beta - \frac{2}{3}\alpha\right)^2} * \frac{m_p}{qa^2} = 0$$

$$\left(\beta - \frac{2}{3}\alpha\right)\left(-\frac{1}{2\alpha^2}\right) - \left(-\frac{2}{3}\right)\left(\beta + \frac{1}{2\alpha}\right) = 0$$

$$-3\beta + 2\alpha + 4\beta\alpha^2 + 2\alpha = 0$$

$$4\beta\alpha^2 + 4\alpha - 3\beta = 0$$

This quadratic equation has two roots, the positive solution of which satisfies the listed condition is given by:

$$\alpha = \frac{-1 + \sqrt{3\beta^2 + 1}}{2\beta} \tag{6}$$

3.2. Upper bound of clamped rectangular plate

In case of the rectangular clamped plate (see Fig. 3.2) this method provides the following relation for the load factor:

$$\lambda^U = 16\frac{\left(\beta + \frac{1}{2\alpha}\right)}{\left(\beta - \frac{2}{3}\alpha\right)}\frac{m_p}{qa^2} \tag{7}$$

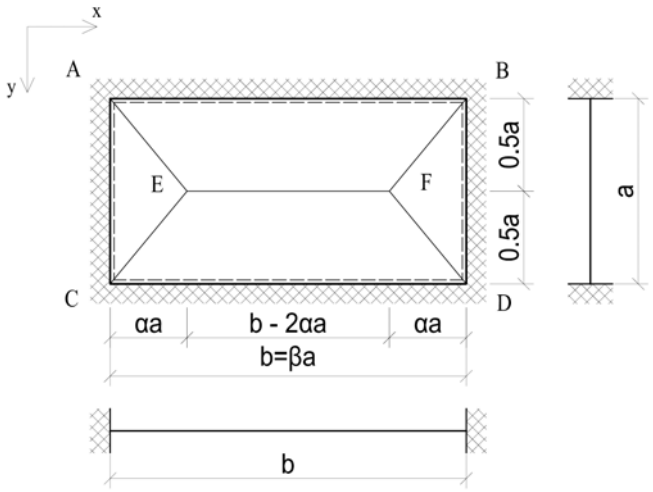

Figure 3.2. Rectangular clamped plate.

The failure mechanism of Fig. 3.2 cannot be the real one. The three yield lines *AB*, *AE* and *AC* cannot come together as indicated without violating the yield criterion in other directions. In reality, yield zones are created in the corners of the plate (Fig. 3.3).

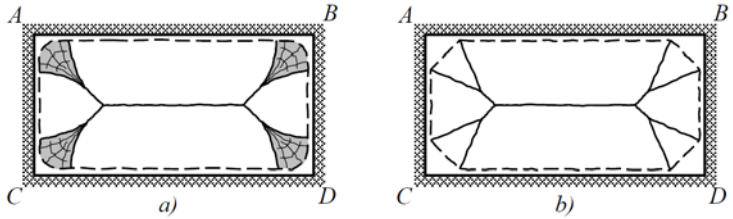

Figure 3.3. Yield zone and approximation by yield lines.

The influence of such zones must be taken into account. In practical examples that is usually done by using an approximating pattern of yield lines (see Fig. 3.3b). The geometry of the yield zone is fixed by two parameters α_1 and α_2 (see Fig. 3.4). These parameters can be determined through a procedure of optimization. The work equation is used to solve the problem.

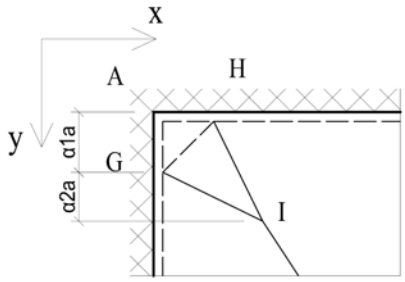

Figure 3.4. Parameters α_1 and α_2.

For the rectangular plate with work method it can be derived:

$$\lambda^{U} = \frac{16 m_p}{q a^2}\left(\frac{\beta + 1 - \frac{4\alpha_1\alpha_2}{\alpha_1 + 2\alpha_2}}{\beta - \frac{1}{3} - \frac{8}{3}\alpha_1^2(\alpha_1 + \alpha_2)}\right) \tag{8}$$

3.3. Solution analysis

A number of examples of simply supported plates are displayed in the table below.

Table 3.2 Simply supported plate.

Type of plate	β	α	$\lambda q a^2/m_p$
b=a	1	0,5	24,00
b=2a	2	0,5	14,00

b=2a; optimized solution	2	0,651	14,14
b=∞	∞	0,866	8,00

For an infinitely long plate of width a ($\beta \to \infty$), the factor α approaches $0.5\sqrt{3} \approx 0.866$ and the load factor is reduced to the minimum value of $8m_p/(qa^2)$. The results are displayed graphically in Fig. 3.5.

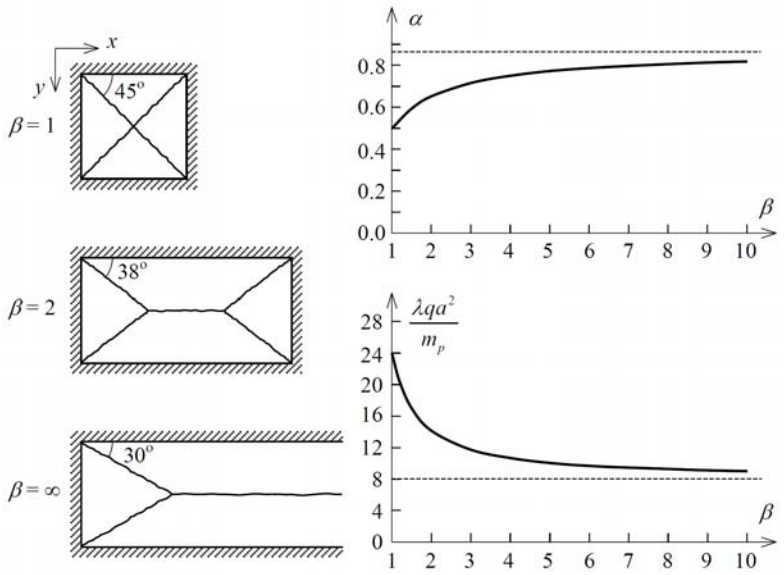

Figure 3.5. Results for rectangular simply supported plate.

Naturally, the found values for λ are upper limits, which mean that the actual load factor is lower. In most cases one has to accept these solutions, because they are the only ones available. However, for this plate by a lower-bound calculation it can be shown that the calculated excess in load carrying capacity over the whole range is not more than 1%. For $\beta=1$ and $\beta=\infty$ even the exact solution is found.

4. Lower bound

4.1. Lower bound for simply supported rectangular plate

As input for the lower-bound calculation of simply supported plate the following moment distribution is assumed:

$$m_{xx} = m_p \left[1 - 4\left(\frac{x}{b}\right)^2\right] \tag{9}$$

$$m_{xy} = m_p \left[4\left(\frac{x}{b}\right)\left(\frac{y}{a}\right)\right] \tag{10}$$

$$m_{yy} = m_p \left[1 - 4\left(\frac{y}{b}\right)^2\right] \tag{11}$$

The moments m_{xx} and m_{yy} have a parabolic distribution with a maximum of m_p in the middle of the plate and zero at both plate edges. This means that the boundary conditions are satisfied. The torque is a bi-linear distribution with a maximum of $\pm m_p$ in the corners and zero in the middle of each span. The largest principal moment has to be smaller than $+m_p$, and the smallest principal moment larger than $-m_p$. The formulas for the determination of the principal moments are:

$$m_1 = \frac{1}{2}(m_{xx} + m_{yy}) + \sqrt{\frac{1}{4}(m_{xx} - m_{yy})^2 m_{xy}^2} \tag{12}$$

$$m_2 = \frac{1}{2}(m_{xx} + m_{yy}) - \sqrt{\frac{1}{4}(m_{xx} - m_{yy})^2 m_{xy}^2} \tag{13}$$

The principal moments in each point can be determined from (12, 13). For both principal moments it then follows (9, 10, 11 and 12, 13) :

$$m_1 = \frac{1}{2} m_p \left[2 - 4\left(\frac{x}{b}\right)^2 - 4\left(\frac{y}{a}\right)^2\right] + 2m_p \left[\left(\frac{x}{b}\right)^2 + \left(\frac{y}{a}\right)^2\right] = m_p$$

$$m_2 = \frac{1}{2} m_p \left[2 - 4\left(\frac{x}{b}\right)^2 - 4\left(\frac{y}{a}\right)^2\right] - 2m_p \left[\left(\frac{x}{b}\right)^2 + \left(\frac{y}{a}\right)^2\right] = m_p \left[1 - 4\left(\frac{x}{b}\right)^2 - 4\left(\frac{y}{a}\right)^2\right]$$

In order to check the equilibrium condition, (9, 10, 11) has to be substituted into (4). It then follows that the moments are in equilibrium when λ is given by:

$$\lambda^L = 8\frac{m_p}{qa^2}\left(\frac{1}{\beta^2} + \frac{1}{\beta} + 1\right) \tag{14}$$

Fig. 4.1 shows λ as a function of β. The different contributions are indicated separately. Remarkable is the quite large contribution of the torque m_{xy}, where it has to be noted that an eventual zeroing of m_{xy} cannot be compensated by an increase of m_{xx} and m_{yy}.

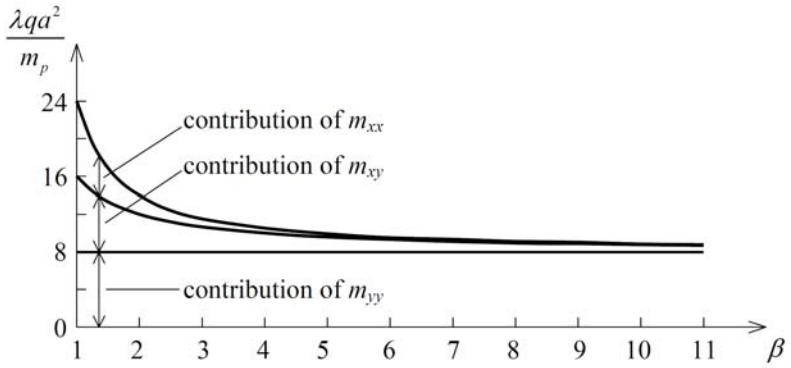

Figure 4.1. Results of lower bound calculation of rectangular simply supported plate.

4.2. Lower bound for clamped rectangular plate

As an input for the lower-bound calculation of clamped plate the following moment distribution is assumed:

$$m_{xx} = -m_p \left[1 + 8\frac{x}{b}\left(\frac{x}{b} - 1\right)\right] \tag{15}$$

$$m_{yy} = -m_p \left[1 + 8\frac{y}{a}\left(\frac{y}{a} - 1\right)\right] \tag{16}$$

For this choice of the bending moment distribution the case becomes thistles, because no freedom is left to chose torsion moments along the edges and in the middle of the plate. The load factor for this thistles lower bound solution can be determined to be:

$$\lambda^U = 16\frac{m_p}{qa^2}\left(\frac{1}{\beta^2} + 1\right) \tag{17}$$

5. Analysis of upper and lower bound for different cases of rectangular plate

5.1. Simply supported plate

Comparison of the upper- and lower-bound calculations leads to the results shown in Table 5.1. For $\beta=1$ and $\beta=\infty$ the upper and lower bounds are equal, in which case the exact failure load is known. For the intermediate values of λ the differences are very small. It can be concluded that failure behavior of the simply supported rectangular plate has been fully analyzed. However such a situation is the exception rather than the rule. In the table the load factors λ_e, for which initial yielding occurs, are indicated too. Striking is that the difference between λ_e and λ_p is smaller for $\beta=1$ compared to $\beta=2$ to 3, while for $\beta=\infty$ the value of λ_e equals λ_p.

Table 5.1 Elastic and lower-upper bound for simply supported plate.

β	Lower bound λ_p	Upper bound λ_p	Elastic λ_e
1,0	24,0	24,0	20,8
1,5	17,1	17,3	12,3
2,0	14,0	14,2	9,8
3,0	11,5	11,7	8,4
4,0	10,5	10,7	8,1
∞	8,0	8,0	8,0
$m_p/qa^2=1$			

5.2. Clamped plate

A number of results obtained by formula (17) are listed in the last column of the Table 5.2. For the square plate a value of λ is found to be 44.0. Compared with the exact solution of λ=42.85 (found by Fox [9]) it can be concluded that the upper bound calculation leads to a very good result for a square plate.

Table 5.2. Elastic and lower-upper bound for clamped plate.

β	Lower bound λ_p	Upper bound λ_p	Elastic λ_e
1,0	32,0	44,0	19,8
1,5	23,1	31,7	13,2
2,0	20,0	27,0	12,0
3,0	17,8	22,8	12,0
4,0	17,0	21,0	12,0
∞	16,0	16,0	12,0
$m_p/qa^2=1$			

The results of the previously discussed thistles lower bound calculation are displayed in the second column. It has to be concluded that the lower bound solution still falls far behind the corrected upper bound solution. Finally, in the first column ,the load factors can be found leading to initial yielding of the plate. The first point of yielding is situated in the middle of the fixed long plate edge. Striking is the big difference between the load factors of initial yielding and total failure, which means that dimensioning with respect to the largest elastic moment is very uneconomical.

6. Conclusion

To utilize the strength of structures beyond the elastic limit, many structures are designed to their ultimate strength. In complicated cases, however, for which an exact solution for the limit load causing collapse cannot be found, it is often necessary to turn to the upper- and lower bound plasticity theory, which enable the necessary collapse load to be bounded. Having this in mind it is obvious why so much attention is focused in finding better techniques for solving this problem. In the paper upper and lower bound of collapse load are presented for clamped or simply supported rectangular plates under bending. Thos solutions, being very important, are useless in case of complicated shapes of plates and complicated boundary conditions. It is shown that numerical approaches in those cases are the best choice for every day engineering applications.

7. References

[1] Manolakos D E and Mamalis A G (1986) Upper and lower bound for rectangular plates transversely loaded, *Int. J. Mech. Sci*. Vol. **28**, No. 12. pp. 815-824, Pergamon Journals Ltd.

[2] Solmaz Pourrezay Khaligh (2009) Application of Optimization Techniques for yield line pattern Determination in Slabs, *International Journal of Recent Trends in Engineering,* Vol 1, No. **6**.

[3] Jacob Lubliner (2006) Plasticity Theory, University of California at Berkeley, Pearson Education, Inc.

[4] Burgoyne C J and Smith A L (2007) Automated lower bound analysis of concrete Slabs, *Magazine of Concrete Research* doi: 10.1680/macr.2007.00005.

[5] Thavalingam A (1998) A computerized method for rigid plastic yield line analysis of slabs, *Computers and Structures* **68,** A Jennings, J McKeown and D Sloan 601±612.

[6] Kristian Krabbenhoft, Lars Damkilde (2002) Lower bound limit analysis of slabs with nonlinear yield criteria, *Computers and Structures*, **80** 2043–2057.

[7] Johansen K W (1972) Yield line formulae for slabs, Taylor & Francis.

[8] Thavalingam A (1999) Computer-assisted generation of yield-line patterns for uniformly loaded isotropic slabs using an optimization strategy, *Engineering Structures* **21**, A Jennings, D Sloan, J McKeown.

[9] Fox E. N. (1974) Limit analysis for plates: the exact solution for a clamped square plate of isotropic homogeneous material obeying the square yield criterion and loaded by uniform pressure, *Philos. Trans. R. Soc.*, Vol. **277A**, pp. 121–55.

STATIC AND KINEMATIC HEIGHT LIMIT OF VERTICAL SLOPE

D. Šumarac[1], S. Jocković[2], M. Marjanović[3]
Faculty of Civil Engineering, University of Belgrade
Bulevar Kralja Aleksandra 73, 11000 Belgrade, Serbia

[1] e-mail: sumi@eunet.rs
[2] e-mail: borovina@grf.rs
[3] e-mail: mimarjanovic@grf.rs

Abstract. In the present paper static and kinematic limit of vertical slope has been analyzed. An overview of literature is given. It is well know from Drucker-Prager paper (1952) that lower bound (static) is $H=2c/\gamma$ where c and γ are cohesion and specific weight of soil respectively, while upper bound (kinematic) is $H=4c/\gamma$. Recently some attempt using numerical approach, mostly finite elements, have been published. In the paper all solutions will be analyzed, and an attempt of authors to improve them will be given.

1. Introduction

Problems of soil mechanics, including stability of slopes, bearing capacity of footings and pressures on retaining walls are often treated as problems of plasticity. Limit analysis is a powerful method for determining upper and lower bounds on the collapse loads of any structure. The upper bound (kinematic) and the lower bound (static) theorem of classical plasticity theory, which assumes a perfectly plastic soil model with an associated flow rule, are useful tools for predicting the stability problems in soil mechanics.

The lower bound theorem states that the limit load calculated from a statically admissible stress field is a lower bound of the true collapse load. A stress field is statically admissible if it obeys the following requirements:

a) Stresses everywhere satisfy differential equations of equilibrium (Eq. 3-5)
b) Stresses comply with loads applied to the boundaries
c) Stress distribution nowhere violates the yield criterion (Eq. 1)
d) Stress discontinuities are permissible, provided that equilibrium is not violated (tangential stress discontinuity is permitted, but continuity of the corresponding normal and shear stress is required)

We assume that slope has a sufficient length for the plane strain hypothesis to be admissible. Its strength properties are defined by a Mohr-Coulomb criterion of failure, with cohesion c and internal friction angle φ, or a Tresca criterion of cohesion c (with internal friction ignored). Tresca yield condition assumes that yield occurs when maximum shear stress τ_{max} exceeds the shear strength of material. In this case (frictionless soil), the shear strength is equal to cohesion c. In a terms of component stresses, the Tresca yield criterion can be expressed as:

$$\tau_{\max} = \sqrt{\left(\frac{\sigma_x - \sigma_y}{2}\right)^2 + \tau_{xy}{}^2} = c \tag{1}$$

According to Eq. (1), statically admissible stress field must satisfy the following condition:

$$F^2 = \left(\frac{\sigma_x - \sigma_y}{2}\right)^2 + \tau_{xy}{}^2 \le c^2 \tag{1}$$

Differential equations of equilibrium (in Cartesian coordinates) are:

$$\frac{\partial \sigma_x}{\partial_x} + \frac{\partial \tau_{xy}}{\partial_y} = 0 \qquad \frac{\partial \tau_{xy}}{\partial_x} + \frac{\partial \sigma_y}{\partial_y} = \gamma \tag{3}$$

Sometimes it is more practical to express equilibrium equations in polar coordinates:

$$\frac{\partial}{\partial r}\left(r \cdot \sigma_r\right) + \frac{\partial \tau_{r\theta}}{\partial \theta} - \sigma_\theta = \gamma \cdot r \sin\theta \tag{4}$$

$$\frac{\partial \sigma_\theta}{\partial \theta} + \frac{\partial}{\partial r}\left(r \cdot \tau_{r\theta}\right) + \tau_{r\theta} = \gamma \cdot r \cos\theta \tag{5}$$

The upper bound theorem states that the power dissipated by any kinematically admissible velocity field can be equated to the power dissipated by external loads to give an upper bound off the true limit load. A kinematically admissible velocity field is one which satisfies compatibility, the flow rule and the velocity boundary conditions. Because an upper bound calculation considers only velocity modes and energy dissipation, the corresponding stress distribution (if one is computed) need not to be in equilibrium. Such a distribution, however, must satisfy the yield criterion. In that case, discontinuous flow states are permissible.

The problem under consideration is the classical problem of the stability of a vertical slope. (Fig. 1). This slope is subjected only to its own weight. The constituent soil is assumed to be perfectly plastic body, homogeneous and isotropic, with a specific weight γ.

Whatever the mechanism of collapse, the collapse equation is usually given in terms of a critical slope height H or stability number Q:

$$\frac{\gamma H}{c} = Q \tag{6}$$

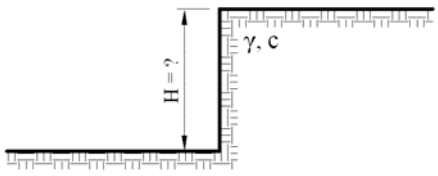

Figure 1. The vertical slope

The critical height is defined as the height at which the unsupported vertical slope will collapse due to its own weight. Solutions of stability number, derived from assumed mechanism of collapse will be upper bounds of the true limit load, while values derived by analyzing of equilibrium stress fields which satisfy the yield condition will give the lower bounds. The range in which the true solution lies can be narrowed down by finding the highest possible lower bound solution and the lowest possible upper bound solution.

Despite the numerous attempts which have been made, the exact solution of the stability number remains unknown. Up to now, only upper and lower bound estimates are available. In the past, for slope stability applications, most research concentrated on the upper bound method. This is due to the fact that the construction of proper statically admissible stress fields for finding lower bound solutions is a difficult task. It is necessary to point out that the validity of assuming the soil to be a perfectly plastic body is not an issue. No account is taken of such important practical matters as the effect of water in the soil or of the essentially different behavior of various constituents such as clay and sand.

2. Static approach

2.1. Drucker-Prager closed form solution (1952)

The simplest possible equilibrium distribution of stress was derived by Drucker and Prager [1]. They divided observed soil into three zones (Fig. 2), assuming the state of stress in zones 1, 2 and 3 to be uniaxial compression, biaxial compression and hydrostatic compression , respectively.

This discontinuous stress field satisfies equilibrium everywhere in the soil mass. Boundary conditions (both normal and shear stress to be zero on all surfaces) are also satisfied, as well as the continuity of the shear stresses between zones. Lower bound for the critical slope height is calculated from Tresca yield criterion (Eq. 1). Maximum shear stresses appear in zones 1 and 2, at the bottom of the slope (y=H), and its value is given by:

$$\tau_{\max} = \frac{1}{2}\gamma H \le c \tag{7}$$

According to Eq. (6), lower bound for the stability number is given by:

$$Q \ge 2 \tag{8}$$

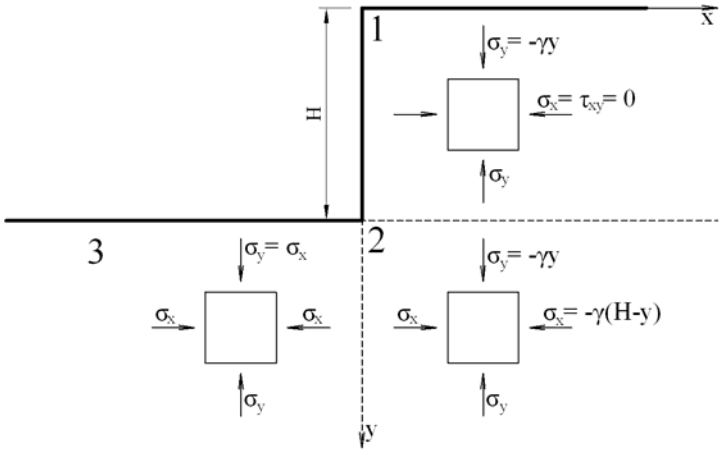

Figure 2. Drucker-Prager lower bound solution

2.2. Heyman's closed form solution (1973)

The better closed form solution of this problem was derived by Heyman [2]. He divided observed soil into seven zones sketched in Figure 3. The boundary PQRS must be free of shear stress and of direct stress normal to the boundary, while direct stresses parallel to the boundary are permitted. Assumed stress functions for each zone (Table 1) satisfy the equilibrium and the boundary conditions along PQRS. Function F (Eq. 2) for each zone is calculated from stress functions.. Continuity of stresses along boundaries between adjacent zones (for example, RB between 1 and 2, or AB between 1 and 4) is satisfied.

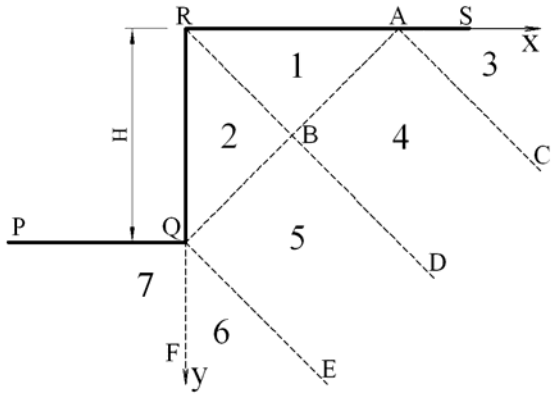

Figure 3. Heyman's lower bound solution

Stress functions for zones 3 and 6 are presented in polar coordinates (with poles in A and Q, respectively), satisfying differential equation of equilibrium in polar coordinates. Stress functions in other zones are presented in Cartesian coordinates.

Maximum values of the F function (Eq. 2) and corresponding stability number for each zone are shown in Table 2. The largest (the most stringent) value of F function leads to lower bound for critical height of vertical slope. This occurs in zones 1, 2, 5 and 6, and lower bound for stability number is:

$$Q \geq 2.8284 \tag{9}$$

which is a better solution in comparison with Drucker-Prager solution.

Table 1a. Stress functions for Heyman's stress zones

Zone	Stress functions	F function
1	$\sigma_x = \frac{1}{2}\gamma(y-x)$ $\sigma_y = \gamma y$ $\tau_{xy} = \frac{1}{2}\gamma y$	$F^2 = \frac{1}{16}\gamma^2\left[(x+y)^2 + 4y^2\right]$
2	$\sigma_x = 0$ $\sigma_y = \frac{1}{2}\gamma(x+y)$ $\tau_{xy} = \frac{1}{2}\gamma x$	$F^2 = \frac{1}{16}\gamma^2\left[(x+y)^2 + 4x^2\right]$
3	$\sigma_r = \gamma r\sin\theta - \frac{1}{4}\gamma H\cos 2\theta - \frac{1}{4}\gamma H$ $\sigma_\theta = \gamma r\sin\theta + \frac{1}{4}\gamma H\cos 2\theta - \frac{1}{4}\gamma H$ $\tau_{r\theta} = \frac{1}{4}\gamma H\sin\theta$	$F = \frac{1}{4}\gamma H$
4	$\sigma_x = \frac{1}{4}\gamma\left(2\sqrt{2}x + 3\sqrt{2}y - H\right)$ $\sigma_y = \frac{1}{4}\gamma\left(2\sqrt{2}x + 2\sqrt{2}y - H\right)$ $\tau_{xy} = \frac{1}{4}\gamma H$	$F^2 = \frac{1}{32}(\gamma y)^2 + \frac{1}{16}(\gamma H)^2$
5	$\sigma_x = \frac{1}{4}\gamma\left(2\sqrt{2}x - \sqrt{2}y + 3H\right)$ $\sigma_y = \frac{1}{4}\gamma\left(2\sqrt{2}x + 2\sqrt{2}y - H\right)$ $\tau_{xy} = \frac{1}{4}\gamma H$	$F^2 = \left[\frac{1}{8}\gamma\left(3\sqrt{2}y - 4H\right)\right]^2 + \left(\frac{1}{4}\gamma H\right)^2$

Table 1b. Stress functions for Heyman's stress zones

Zone	Stress functions	F function
6	$\sigma_r = \sigma\theta + \frac{1}{2}\gamma H \sin 2\theta$ $\sigma_\theta = \gamma r \sin\theta + \frac{1}{4}\gamma H\left(4 + \frac{\pi}{2} - 2\theta - \sin 2\theta\right)$ $\tau_{r\theta} = \frac{1}{4}\gamma H\left(1 + \cos 2\theta\right)$	$F = \frac{1}{2}\gamma H \cos\theta$
7	$\sigma_x = \gamma\left(y + H - \frac{\pi H}{8}\right)$ $\sigma_y = \gamma y$ $\tau_{xy} = 0$	$F = \frac{1}{2}\gamma H\left(1 - \frac{\pi}{8}\right)$

Table 2. Maximum values of yield functions and corresponding stability numbers

Zone	Maximum of F function	Stability number
1	$F^2 = \frac{1}{8}\gamma^2 H^2$ (for x=y=H/2)	$Q \geq 2\sqrt{2} = 2.8284$
2	$F^2 = \frac{1}{8}\gamma^2 H^2$ (for x=y=H/2)	$Q \geq 2\sqrt{2} = 2.8284$
3	$F = \frac{1}{4}\gamma H$	$Q \geq 4$
4	$F^2 = \frac{5}{64}\gamma^2 H^2$ (for $y = \frac{H}{\sqrt{2}}$)	$Q \geq \frac{8}{\sqrt{5}} = 3.5777$
5	$F^2 = \frac{1}{8}\gamma^2 H^2$ (for $y = H\sqrt{2}$)	$Q \geq 2\sqrt{2} = 2.8284$
6	$F = \frac{\sqrt{2}}{4}\gamma H$ (for θ = π/4)	$Q \geq 2\sqrt{2} = 2.8284$
7	$F = \frac{8-\pi}{16}\gamma H$	$Q \geq \frac{16}{8-\pi} = 3.2933$

3. Kinematic approach

3.1. Translational mechanism (Drucker and Prager, 1952)

The notion of a critical height in the context of limit analysis appears in an early paper of Drucker and Prager [1]. They assume that the failure occurs by sliding along a plane making an angle β with the vertical (Fig. 3).

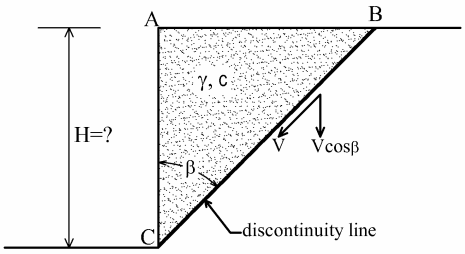

Figure 3. Translation mechanism of failure

Equating the rate of external work to the rate of internal energy dissipation gives:

$$\frac{1}{2}H^2 tg\beta \cdot \gamma \cdot V\cos\beta = c \cdot V \cdot \frac{H}{\cos\beta} \tag{11}$$

and:

$$H = \frac{4c}{\gamma} \cdot \frac{1}{\sin 2\beta} \tag{12}$$

For $\beta = 45°$:

$$H = \frac{4c}{\gamma} \tag{13}$$

and stability number is $Q = 4$.

3.2. Rotational mechanism (Chen, 1975).

The failure surface (velocity discontinuity) is assumed to pass through the toe of the slope. The normality rule in plasticity theory requires that the velocity discontinuity vector be inclined to the rupture surface at the internal friction angle of the soil ϕ, and the shape of the rupture surface in the rigid rotation mechanism must be a log-spiral (Fig. 4):

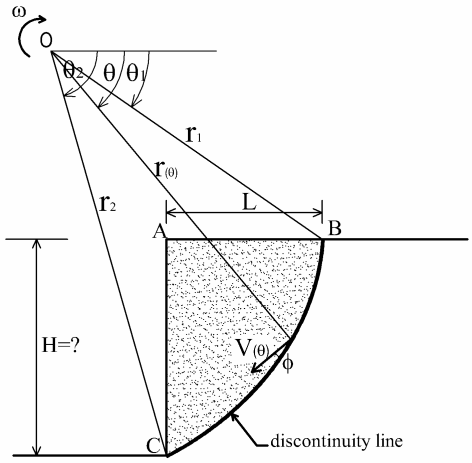

Figure 4. Proposed rotational failure mechanism with velocity field

The region *A-B-C* rotates as a rigid body about the center of rotation *O*, with the materials below the logarithmic surface *BC* remaining at rest, The surface *BC* is a thin layer surface of velocity discontinuity. The assumed mechanism can be specified completely by three variables: θ_1, θ_2 and H. Equation for the logarithmic spiral is given by:

$$r(\theta) = r_1 \cdot e^{(\theta-\theta_1)tg\phi} \tag{14}$$

The rate of energy dissipation in the soil W_i, and the rate of work due to the soil selfweight, W_e were derived by Chen 1975 [8]. The rate of external work for the required region *A-B-C* is found by simple algebraic summation the rates of work W_{e1}, W_{e2}, W_{e3} due to the soil weight in the regions *O-B-C*, *O-A-B* and *O-A-C*, respectively.

Region *O-B-C*: $W_{e1} = \gamma\omega r_1^3 f_1(\theta_1,\theta_2)$ (15)

Region *O-A-B*: $W_{e2} = \gamma\omega r_1^3 f_2(\theta_1,\theta_2)$ (16)

Region *O-A-C*: $W_{e3} = \gamma\omega r_1^3 f_3(\theta_1,\theta_2)$ (17)

where the functions $f_1(\theta_1,\theta_2)$, $f_2(\theta_1,\theta_2)$, $f_3(\theta_1,\theta_2)$ are defined as:

$$f_1(\theta_1,\theta_2) = \frac{(3tg\phi\cos\theta_2 + \sin\theta_2)\cdot e^{3(\theta_2-\theta_1)tg\phi} - 3tg\phi\cos\theta_1 - \sin\theta_1}{3(1+9tg^2\phi)} \tag{18}$$

$$f_2(\theta_1,\theta_2) = \frac{1}{3}\frac{L}{r_1}\sin\theta_1\cos\theta_1 - \frac{1}{6}\frac{L^2}{r_1^2}\sin\theta_1 \tag{19}$$

$$f_3(\theta_1,\theta_2) = \frac{1}{3}\frac{H}{r_1}\cos^2\theta_2\cdot e^{(\theta_2-\theta_1)tg\phi} \tag{20}$$

The rate of work due to the soil selfweight W_e is now obtained by the simple algebraic summation:

$$W_e = W_{e1} - W_{e2} - W_{e3} = \gamma\omega r_1^3 (f_1(\theta_1,\theta_2) - f_2(\theta_1,\theta_2) - f_3(\theta_1,\theta_2)) \tag{21}$$

The internal disipation of energy occurs along the discontinuity surface *BC* (Fig. 4) and it may be found by multiplying the differential area $rd\theta/\cos\phi$ of this surface by cohesion *c* times the tangential discontinuity in velocity, $V\cos\phi$:

$$W_i = \int_{\theta 1}^{\theta 2} c\cdot V\cos\phi\frac{rd\theta}{\cos\phi} = cr_1^2\omega\int_{\theta 1}^{\theta 2} e^{2(\theta-\theta_1)tg\phi}d\theta = \frac{cr_1^2\omega}{2tg\phi}(e^{2(\theta_2-\theta_1)tg\phi}-1) \tag{22}$$

Equating the rate of external work to the rate of internal energy dissipation gives:

$$H = \frac{c}{\gamma}\frac{(e^{2(\theta_2-\theta_1)tg\phi}-1)(\sin\theta_2\cdot e^{(\theta_2-\theta_1)tg\phi} - \sin\theta_1)}{2tg\phi(f_1(\theta_1,\theta_2) - f_2(\theta_1,\theta_2) - f_3(\theta_1,\theta_2))} \tag{23}$$

or:

$$H = \frac{c}{\gamma} f(\theta_1,\theta_2) \tag{24}$$

The function $f(\theta_1,\theta_2)$ is found to have a minimum value near the point θ_1=40°, θ_2=65° for case ϕ=20°, where it has the value $3.831\cdot tg(\frac{\pi}{4}+\frac{\phi}{2})$ for all values of ϕ, so that:

$$H_{cr} = 3.831\frac{c}{\gamma} tg(\frac{\pi}{4} + \frac{\phi}{2}) \tag{25}$$

For Tresca material ϕ=0, the function is found to have a minimum value near the point θ_1 =27.44°, θ_2 =57.52°, so that :

$$H_{cr} = 3.831\frac{c}{\gamma} \tag{26}$$

and stability number is $Q = 3.831$.

The value 3.831 is an improvement of the previous solution 4.0 as given in (12).

3.3 Multiple – rotation mechanism (Bekaert, 1995).

Bekaert [4] considered a subdivision of the soil mass into n blocks B_i=$M_iM_{i+1}S_{i+1}S_i$ and n points Ω_i, located outside the of the soil mass ($0 \le i \le n-1$), where M_iM_{i+1} is an arc of log-spiral of focus Ω_i and S_iS_{i+1} is segment located on the vertical facing of the slope (Fig. 5).

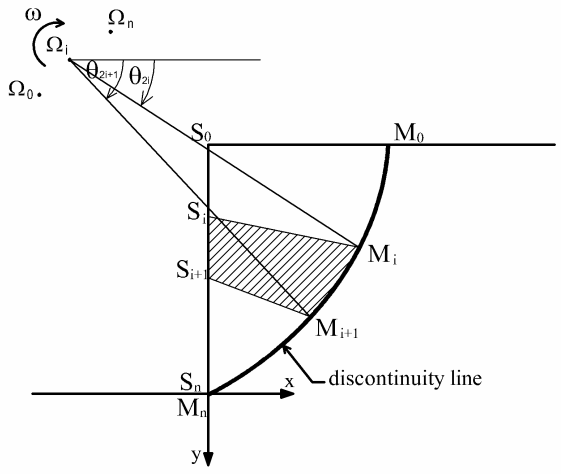

Figure 5. Subdivision of the soil mass into blocks

All the blocks B_i are given a virtual rigid body rotation ω about Ω_i. The mechanism is fully determined by the set of $3n-1$ parameters (θ_i, y_{M_j}) when $0 \le i \le 2n-1$ and $0 \le j \le n-1$.

The mechanism is relevant as far as:

- $(\overline{M_iS_i}, \overline{\Omega_i\Omega_{i+1}}) = \frac{\pi}{2} - \phi$ (27)
- $\forall 0 \le i \le n-1$ Ω_i is not located in the soil (28)
- $\forall 0 \le i \le n-1$ $-1 = y_{S_0} \le y_{S_i} \le y_{S_{i+1}} \le y_{Sn} = 0$ (29)

- $\forall 0 \le i \le n-1 \qquad -1 = y_{M_0} \le y_{M_i} \le y_{M_{i+1}} \le y_{Mn} = 0$ (30)

- $\forall 0 \le i \le 2n-2 \qquad 0 \le \theta_0 \le \theta_i \le \theta_{i+1} \le \frac{\pi}{2}$ (31)

The internal disipation of energy is:

$$W_i = \frac{c\omega}{2tg\phi}\sum_{i=0}^{n-1}\left|\underline{\Omega_i M_i}\right|^2 \cdot (e^{2(\theta_{2i+1}-\theta_{2i})tg\phi} - 1) + c\omega\cos\phi\sum_{i=0}^{n-1}\left|\underline{\Omega_{i-1}\Omega_i}\right| \cdot \left|\underline{M_i S_i}\right| \tag{31}$$

The rate of external work is:

$$\begin{aligned} W_e = {} & \frac{\gamma\omega}{3(1+9tg^2\phi)}\sum_{i=0}^{n-1}\left|\Omega_i M_i\right|^3 \cdot [(3tg\phi\cos\theta_{2i+1} + \sin\theta_{2i+1})e^{3(\theta_{2i+1}-\theta_{2i})tg\phi} - (3tg\phi\cos\theta_{2i} + \sin\theta_{2i})] \\ & + \frac{\gamma\omega}{2}\sum_{i=0}^{n-1}\left|\underline{M_i S_{i+1}} \wedge \underline{M_i S_{i+1}}\right|\left(\frac{x_{M_i}}{3} - x_{\Omega_i}\right) \\ & + \frac{\gamma\omega}{2}\sum_{i=0}^{n-1}\left|\underline{M_i S_{i+1}} \wedge \underline{M_i M_{i+1}}\right|\left(\frac{x_{M_i} + x_{M_{i+1}}}{3} - x_{\Omega_i}\right) \\ & + \frac{\gamma\omega}{2}\sum_{i=0}^{n-1}\left|\underline{\Omega_i M_i} \wedge \underline{\Omega_i M_{i+1}}\right|\left(\frac{x_{M_i} + x_{M_{i+1}}}{3} - \frac{2x_{\Omega_i}}{3}\right) \end{aligned} \tag{33}$$

Equating the rate of external work to the rate of internal energy dissipation gives:

$$Q = \frac{\gamma H}{c} = \min_{relevant\{\theta_i, y_{Mj}\}} f(\theta_i, y_{M_j}) \tag{34}$$

A numerical minimization gives the value of Q (ϕ=0) as a function of the number of blocks (Fig. 6).

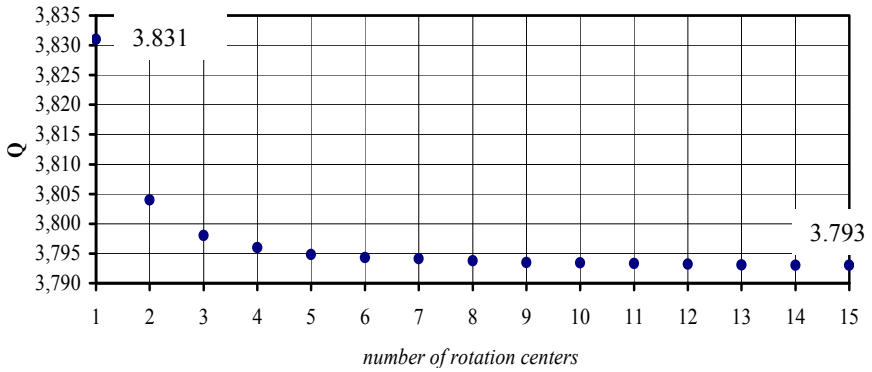

Figure 6. Upper bound estimates for multiple rotation mechanism (case ϕ=0)

The calculus has been performed up to 15 rotation centers and gives the following best upper bound estimate for stability number is $Q(\phi=0) = 3.793$.

4. Numerical solution

Although the lower and upper bound theorems are particularly useful tools for the analysis of stability, they are often difficult to apply to practical problems, involving complicated loadings, inhomogeneous material properties and complex geometry. Constructing the statically admissible stress fields and kinematically admissible velocity fields manually, even for simple problems, is a very difficult task. Alternative method of computing lower and upper bounds is using of numerical methods. The most common numerical formulation of the static and kinematic theorems is based on a finite element discretization of the continuum.

4.1. Static approach

Finite element. The continuum is discretized into a mesh of three-noded triangular elements (Fig. 7), with the nodal variables being the unknown stresses σ_x, σ_y and τ_{xy}.

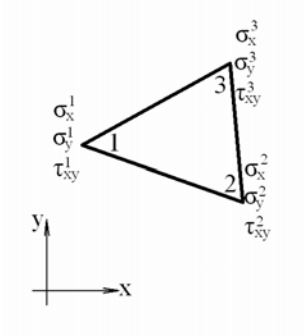

Figure 7. Three-noded triangular element

For each element the vector of nodal stresses is:

$$\{\sigma\} = \begin{Bmatrix} \sigma_x^{(i)} \\ \sigma_y^{(i)} \\ \tau_{xy}^{(i)} \end{Bmatrix} \quad i = 1\text{-}3 \tag{35}$$

Each stress varies throughout an element according to:

$$\sigma_x = \sum_{i=1}^{3} N_i \sigma_{xi} \; ; \qquad \sigma_y = \sum_{i=1}^{3} N_i \sigma_{yi} \; ; \qquad \tau_{xy} = \sum_{i=1}^{3} N_i \tau_{xyi} \tag{36}$$

where σ_{xi}, σ_{yi} and τ_{xyi} are the nodal stresses and N_i are linear shape functions.

Unlike the usual form of the finite element method, each node is unique to a particular element and more than one node may share the same coordinates. This kind of mesh is reffered as "fully discontinuous" mesh.

Discontinuity equilibrium. Statically admissible stress discontinuities are permitted to occur at the boundaries between adjacent triangles. In order to permit statically admissible discontinuities at the edges of adjacent elements, it is necessary to enforce additional constraints on the nodal stresses. Figure 8 illustrates two triangles, a and b, sharing side d defined by nodal pairs (1, 2) and (3, 4). Equilibrium of the discontinuity requires that at every point along d:

$$\sigma_n{}^a = \sigma_n{}^b; \qquad \tau^a = \tau^b \tag{37}$$

Since the stresses vary linearly along each element edge, this condition is equivalent to enforcing the constraints:

$$\sigma_{n1}{}^a = \sigma_{n2}{}^b; \qquad \sigma_{n3}{}^a = \sigma_{n4}{}^b; \qquad \tau_1{}^a = \tau_2{}^b; \qquad \tau_3{}^a = \tau_4{}^b \tag{38}$$

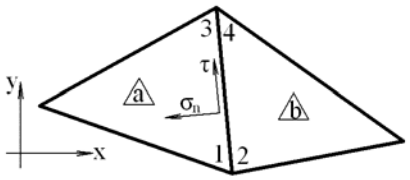

Figure 8. Stress discontinuity between adjacent triangles

Linearization of the yield condition (Pastor, 2000). Since we wish to formulate the lower bound theorem as a linear programming problem, it is necessary to approximate the yield surface by a yield criterion which is a linear function of the unknown stresses. For the Tresca yield criteria, this is achieved by employing a polygonal approximation to the yield surface. Polygon is inscribed inside parent Tresca yield surface, ensuring that the solution obeys the conditions of the lower bound theorem (Eq. 12).

Tresca yield criterion, linearized *from inside*, is expressed by:

$$f_r(\boldsymbol{\sigma}) = (\sigma_x - \sigma_y)\cos\frac{2\pi k}{m} + 2\tau_{xy}\sin\frac{2\pi k}{m} \le 2c\cdot\cos\frac{\pi}{m}, \quad \text{k} = 1 - m \tag{39}$$

where m is a linearization parameter, greater or equal to 3.

Application of the stress boundary conditions, equilibrium equations (Eq. 3-5) and yield criterion (Eq. 37) leads to an expression for the collapse load or stability number which is maximized subject to a set of linear constraints on the stresses.

The best numerical solution for the lower bound, using linear programming, was derived by Pastor [5]. Mesh of triangles included 3232 elements, and its implementation leads to the following stability number:

$$Q \geq 3.76037 \tag{40}$$

Non-linear programming solution (Lyamin and Sloan, 2002). Up to date, the best known lower bound solution of the presented problem was derived by Lyamin and Sloan [7], who used linear finite elements method and non-linear programming. Non-linear programming formulations are more complex to solve, but avoid the need to linearize the yield surface. This new approach is vastly superior to a commonly used linear programming formulation, especially for large scale applications.

In this case, solution algorithm needs to compute first and second derivatives of the yield function with respect to the unknown stresses, which require the yield function to be convex and smooth. For Tresca yield function, which has singularities in their derivatives, it was necessary to adopt a smooth approximation of the original yield surface. In this solution a two-parameter hyperbolic approximation for smoothing the tip and corners of the Mohr-Coulomb model has been used.

The numerical solution for the lower bound using non-linear programming with 6400 elements mesh leads to the best known lower bound for stability number:

$$Q \geq 3.772 \tag{41}$$

4.2. Kinematic approach

Finite element. The three-noded triangle is also used for the upper bound limit analysis (Fig. 9) Each element is associated with six unknown nodal displacements. For each triangle displacement vector is:

$$\{\delta\} = \begin{Bmatrix} u_x^{(i)} \\ u_y^{(i)} \end{Bmatrix} \quad i = 1\text{-}3 \tag{42}$$

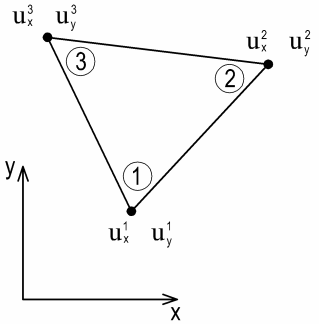

Figure 9. Three-noded triangle

The displacement are assumed to vary linearly throughout each triangle according to:

$$u_x = \sum_{i=1}^{3} N_i u_x^i; \qquad u_y = \sum_{i=1}^{3} N_i u_y^i \tag{43}$$

where u_x and u_y are the nodal displacements in the *x* and *y* directions, respectively, and N_i are linear shape functions.

Linearization of the yield surface (Pastor, 2000). In the kinematic solution, the polygon is defined to circumscribe the parent yield surface so that the solution obtained is a strict upper bound.

The Tresca (or Mises) criterion, here linearized *from the outside*, is expressed by:

$$f_r(\boldsymbol{\sigma}) = (\sigma_x - \sigma_y)\cos\frac{2\pi r}{m} + 2\tau_{xy}\sin\frac{2\pi r}{m} - 2c \le 0\,, \;\; r = 1 - m \tag{44}$$

where *m*, a linearization parameter, is greater than or equal to 3.

The kinematic theorem requires that the strain field υ be kinematically admissible (KA), i.e. υ is derived from a displacement velocity field **u** which satisfies the boundary conditions, and plastically admissible (PA), i.e. υ satisfies the normality law:

$$\upsilon = \lambda\frac{\partial f(\boldsymbol{\sigma})}{\partial \boldsymbol{\sigma}} \quad , \quad \partial f(\boldsymbol{\sigma}) = 0\,, \;\; \lambda \ge 0 \tag{45}$$

Pastor [5] considered the discretized structure in a mesh of NT triangles, denoting by e_k, for which each side is a line of potential discontinuity in displacement velocity (Fig. 10). The displacement velocity tensor at any point of e_k are expressed by (positive compression):

$$\upsilon_{ij} = -\frac{1}{2}(u_{i,j} + u_{j,i}) \tag{46}$$

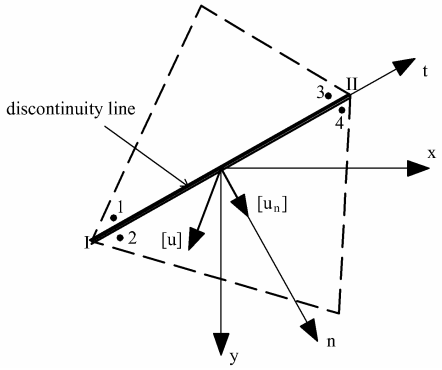

Figure 10. Discontinuity segment S_k

The displacement velocity field is constant on each finite element and is expressed linearly in relation to the nodal variables by appropriate derivation of the interpolation functions. The boundary conditions in displacement velocity will be satisfied by cancelling the components of a fictional node associated with the boundary of the mesh, a potential discontinuity line. Relations (44) and (45) must be written on each element e_k and thus the unknowns of the problem are nodal displacements u_x^k and u_y^k and the plastic coefficients λ_r^k

Discontinuity lines in displacement velocity. A typical velocity discontinuity (segment S_k) is shown in Figure 10. The discontinuity occurs at the common edge between two adjacent triangles, defined by the nodal pairs (1, 2) and (3, 4), and is of zero thickness. The boundaries of the plasticity domain in the Mohr plane are:

$$G(\boldsymbol{\sigma}) = |\tau| - c \le 0 \tag{47}$$

The velocity discontinuity components across the discontinuity mast satisfy the flow rule:

$$[\boldsymbol{u}] = \xi \frac{\partial G(\boldsymbol{\sigma})}{\partial \boldsymbol{\sigma}}, \ \xi \ge 0 \tag{48}$$

$$\exists \boldsymbol{\sigma} = \sigma(\sigma_n, \tau), \quad G(\boldsymbol{\sigma}) = 0 \tag{49}$$

and plastically admissible conditions are obtained as:

$$[u_n]^i = 0, \quad [u_t]^i = \xi_1^i - \xi_2^i, \quad \xi_j^i \ge 0 \quad i= I, II \quad j=1,2 \tag{50}$$

Plastic flow may occur in both the continuum and the velocity discontinuities. The total power dissipated in these modes constitutes the objective function and is expressed in terms of the unknowns. The power dissipated along a velocity discontinuity may be written as:

$$\pi([\boldsymbol{u}]) = \min_{\xi} c(\xi_1 + \xi_2) \tag{51}$$

The power dissipated by plastic flow throughout a triangle is:

$$\pi(\upsilon) = \min_{\lambda} \left\{ 2cs_k \sum_{r=1}^{n} \lambda_r \right\} \tag{52}$$

The functional to optimize is the total dissipated power $P(\upsilon)$ in the structure discretized in triangular finite elements:

$$P(\upsilon) \le \min_{\lambda,\xi} c \left\{ \sum_{k=1}^{NT} \left(\sum_{r=1}^{n} 2\lambda_r^k \right) s_k + \sum_{k=1}^{Ndisc} \left(\sum_{i=1}^{4} \frac{1}{2} \xi_i^k \right) l_k \right\} \tag{53}$$

where NT is number of finite elements, NDISC is number of segments along discontinuity, s_k is the surface of the element S_k and l_k is length of the element S_k.

The optimal form of the discontinuity line separating the mobile block from the rest of the body is Bekaert's kinematic mechanism of rotating blocks [4]. The zone set out by this mechanism is divided into horizontal and vertical bands whose respective widths x_n and y_n are in arithmetic progression so as to make the discretization at the foot of the slope denser. The final problem is the one of linear optimization. The optimal displacement velocity fields $\mathbf{u}$ are then obtained and these fields are analysed using totally independent post-treatment procedures. The results are given in relation to the number of planes n linearizing the criterion (Table 3) and in relation of h, which is the number of elements on the vertical facing of the slope (Table 4):

Table 3. Stabilitu number as a function of the number of planes n linearizing the criterion

N	1	24	36	48	6600	72	84	96
Q	3.800081	3.79620	3.79421	3.9339	3.79279	3.79240	3.79210	3.79185

Table 4. Stabilitu number as a function of h

h	6	12	18	24	30	36	42
Q	3.834987	3.804778	3.796194	3.7992139	3.788489	3.786743	3.785864

The best kinematic value for stability number, obtained for $h=42$ is Q= 3.7859.

5. Conclusion

In the present paper thorough study was made to analyze the problem of height limit of vertical slope. Starting from Drucker-Prager [1] paper via Chen [8], nice closed form solutions were done using both static and kinematic theorem. Despite the numerous attempts which have been made and shown in the paper, the exact solution of the stability problem of vertical slope remains unknown. It turns out that numerical approach is the best way to find solution closed to exact one, which is very important for everyday engineering application.

References

[1] Drucker D C, Prager W (1952) Soil mechanics and plastic analysis or limit design, *Quarterly of Applied Mathematics,* **10**, pp. 157-165.
[2] Heyman J (1973) The stability of a vertical cut, *International Journal of Mechanical Sciences*, **15**, pp. 845-854.
[3] Sloan S W (1989) Upper bound limit analysis using finite elements and linear programming, *International Journal for Numerical and Analytical Methods in Geomechanics*, **13**, pp. 263-282.
[4] Bekaert A (1995) Improvement of the kinematic bound for the stability of vertical cut-off, *Mechanics Research Communications*, **22**, pp. 533-540.
[5] Pastor J, Thai T-H, Francescato P (2000) New bounds for the height limit of a vertical slope, *International Journal for Numerical and Analytical Methods in Geomechanics,* **24**, pp. 165-182.
[6] Lyamin A V, Sloan S W (2002) Lower bound limit analysis using non-linear programming, *International Journal for Numerical Methods in Engineering,* **55**, pp. 573-611.
[7] Lyamin A V, Sloan S W (2002) Upper bound limit analysis using linear finite elements and non-linear programming, *International Journal for Numerical and Analytical Methods in Geomechanics,* **26**, pp. 181-216.
[8] Chen W F (1975) *Limit Analysis and Soil Plasticity*, Elsevier Scientific Publishing Company, Amsterdam
[9] Lubliner J (2006) *Plasticity Theory*, Pearson Education Inc.

SLAB TRACK WITH "MASS-SPRING" SYSTEM

Mirjana Tomičić-Torlaković[1], Vidan Rađen[2]

1 Civil Engineering Faculty University of Belgrade, Bul. kralja Aleksandra 73, 11000 Belgrade, Serbia

e-mail: mtomicic@grf.rs

2 „ Interkop“

e-mail: vidra@yahoo.com

Abstract: Development of ballastless slab track structure with "mass-spring" system was starting about 20 years ago and different kinds of those track systems have been successfully in use for urban transportation systems. By these systems under the slab the elastic elements are inserted to provide protection from bothersome vibration and noise. The present article explains the principal aspects of calculation verifications by means of simulation model for the selected type of "mass-spring" track system.

1. Introduction

Rail traffic are an integral part of the public transportation systems in the central arias of many cities. The proximity to the neighboring buildings, the sensitivity of the population and the necessity to share the route with motor trafic are factors for track design and construction.

Rail traffic causes vibrations that are mainly caused by rolling between the running wheel and the rails (direct structure borne noise) and propagate via superstructure and the tunnel through the ground into nearby buildings and can cause audible secondary air-borne noise.

Railway tracks within urban environment have usually to fulfil certain reqirements concerning emission of noise and vibration. The decisive range of vibration is: 5 Hz to 20 Hz and of structure borne air noise is: 40 Hz to 80 Hz.

Comparisons between different possibilities concerning reduction of noise and vibration showed that measures at the railway superstructure itself are usually preferable from a technical and economic point of view. A wide variety of measures are available and effective tools for reducing structure borne noise at the source. These measures include the use of highly alastic pads for rail fasteners, ballast and sleeper mats, elastic supports for slab tracks of so-called "mass-spring" systems. Decisive parameter for vibration absorption is the natural frequency (eigen- frequency) of the selected superstructure system.

2. Types of "mass-spring" systems

"Mass-spring" systems are used in applications where the isolation demands, in terms of structure-borne noise, are very high (Figure 1.). Over recent decades, a wide range of mass-spring systems have been developed. There are systems that use in-situ concrete or pre-fabricated concrete components, their combination, with or without a ballast bed. The type

of chosen construction is a basic factor in the design of elastic supports for mass-spring systems.

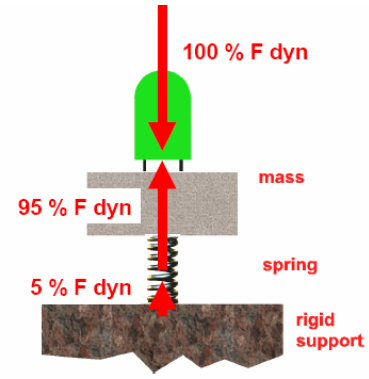

Figure 1. – Damping efect of mass-spring system

There are three different types of such systems (Figure 2.) /1/ :

- full surface layer,
- linear support,
- discrete bearings.

Figure 2. Types of mass-spring systems

In all types of such systems elastic elements make possible the following /1/:

- reduce the loads on the superstructure, the substructure and the subgrade
- reduce wear of rails and wheels
- increase track elasticity
- protect the environment against vibrations and structure-born noise
- fast construction
- keep track maintenance costs very low.

3. "Mass-spring" systems with discrete bearings

Discrete bearings are predetermined by the form of the track slab or track trough sections. These slabs can be prefabricated or cast in site.
When cast in site, an insulation sheet is placed on the foundation to prevent from bonding, so that the slab can be later raised. The slab is lifted after hardening and than the bearings are inserted through the installation holes in the slab sections. If the longitudinal sides of the slab are free, it is possible to lift the slab with jacks that can be applied from the sides.
The joints between the slabs are connected with plastic-coated pins, which will be cemented with morter, or with resin in a dovetail pattern. The bearings close to the joints will be 1,5 times stiffer than the standard ones.
In the transition zones between the mass-spring system and the conventional slab track bearings with a higher degree of stiffness are installed to reduce track depresion, in order to prevent excessive track fatigue and the risk of crack /2/.
Due to the relatively low surface area of the supports, special attention must be paid to the horisontal forces arising from train operations. In order to limit the deflections as reqired, the perfect balance between the shear modulus, elasticity, support thickness and the surface area of the support must be found.
By using individual bearings the lowest tuning freqencies can be achieved. Depending of the mass of superstructure toward the well-known formula:

$$f\,[\mathrm{Hz}] = 1/2\pi\,(k/m)^{1/2}$$

the natural (eigen) freqency is between 5 and 10 Hz. Low eigen frequncy of less than about 20 Hz is required. It allows the maximum isolation level against structure-borne noise of up to 30 dB /2/.
There is a descrepancy between reqired natural structure freqency and the rail deflection: the softer the bearing material is, the lower the natural freqency and the higher the deflection is.
New generation of high performance elastomers (for example Sylomer® by Getzner) are materials for elastic supports in all mass-spring systems. They offer many advantages when used as elastic bearings for slab track and ballast mats, such as /2/:

- reliable, homogeneous and durable alastic properties
- resistance to short-term, extreme overloading
- ease to use in compensating construction tolerances
- adaptable to all application by varying the density of the material, the thickness and the surface area of the support.

For justification the statements exposed previously a number of Sylomer® bearings installed in mass-spring systems are listed /2/.

Type of bearing	Bearing thickness /mm/	Natural frequency /Hz/	Track deflection /mm/	Mass of superstructure /t/m/
Sylodyn® N 70	70	5,2	9,2	11,0
Sylodyn® N 70	59	6,0	7,0	7,5
Sylomer® S 50	50	8,0	3,9	7,0

Sylomer® S 50	50	10,0	2,5	4,5

Natural rubber is widely used material for discrete bearings (for example Tiflex), meanly because of its unbeatable dynamic characteristics and long proven service record on bridges.

4. **Modelling the "heavy mass-spring" systems**

The example of track superstructure system is designed as "heavy mass-spring" system (Figure 3.) for the open track section at light rail system as a part of rail public transportation system in the city /6/.

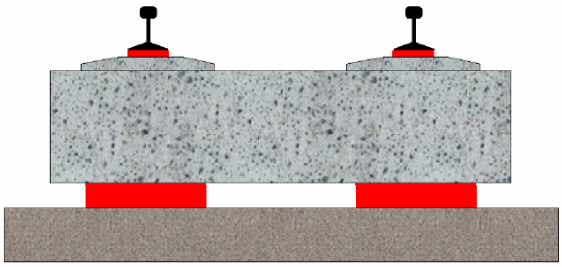

Figure 3. - Heavy mass-spring system

The structure consistes of prefabricated concrete track slab dimensions of 240×390×50 cm, surrounds by in-situ concrete trough and supported by discrete elastic bearings 400×400 mm with thickness of 40 mm. The static elasticity coefficient is of 30,7 N/m^3 and the density is of 400kg/m^3 (Figure 4.).

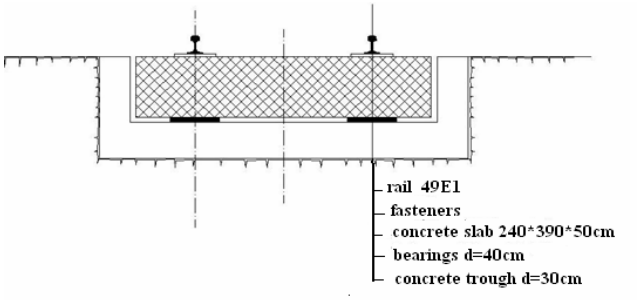

Figure 4. – Charateristics of the example of heavy mass-spring system

The input for track parameters are:
- type of rail 49E1
- fasteners spacing 65cm

- rail pad elasticity 200 kN7cm

The competent load is the electric locomotive of passenger ICE train with an axleload of 196 kN and the axle distance of 3,0 m.

The elastic line of the rail and rail supporting forces (Figure 5.) acting on the slab are calculated toward the Zimmerman's theory of the elasticaly supported beam, using the Vincler's hypothesys, as folows /12/.

Rail deflection:

$$y = \frac{k}{2U}\sum Q_i \eta_i \quad (1)$$

where:

$\eta_i = \frac{\sin(k \cdot x_i) + \cos(k \cdot x_i)}{e^{(k \cdot x_i)}}$ - influence coefficient of wheel distance x_i

$k = \sqrt[4]{\frac{U}{4EI_x}}$ - coefficient of relative stiffness of the track supports toward the rail

$U=D/L$ - elasticity modulus of the track

EI_x - bending stiffness of the rail.

Supporting forces:

$$S = \frac{kL}{2}\sum Q_i \eta_i \quad (2)$$

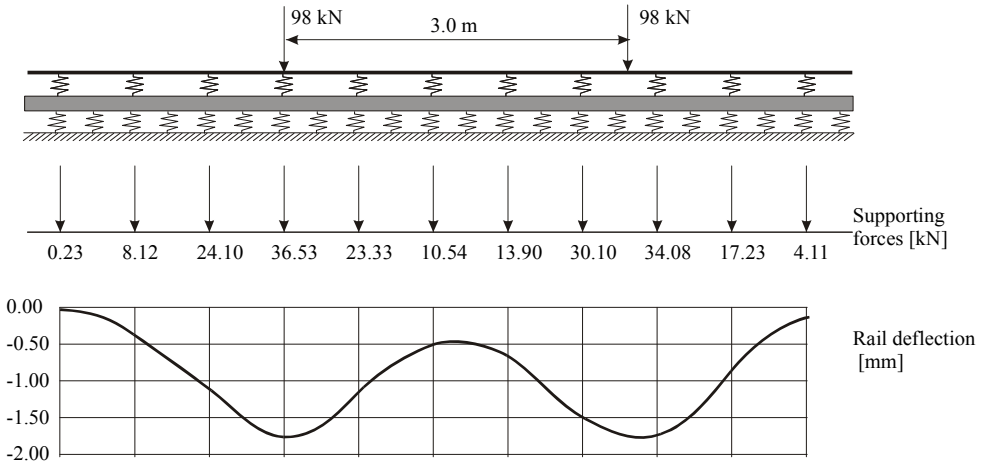

Figure 5. - Rail supporting forces and deflections for ICE electric loco

The forces and the deformations of the slab track structure are calculated by means of program TOWER in the finite elements method.

The settlements of soil substructure are obtained from the Schlicher's formula /6/:

$$s = \frac{\left(1-\nu_o^2\right)P}{E_o F} B\alpha \qquad (3)$$

where:

ν_0 - soil Poisson's coefficient
E_0 - soil elasticity modulus
P - slab load
F - track structure supporting surface
B - width of the track structure
α - coefficient depending on the shape of the structure surface and the position of the point where
the settlement is determined

The soil stiffness is:

$$k = \frac{P}{s} = \frac{98 \cdot 8}{0{,}0054} = 145185\,\mathrm{kN/m} \qquad (4)$$

The stiffness of the members that simulate the slab bearings:

$$k_{zi} = c\, F_{ppi} \qquad (5)$$

where: $c = 30{,}7\mathrm{N/cm}^3$ - elasticity coefficient of Sylomer ®

F_{ppi} - slab area that corresponds to one member.

The model consists of five track slabs of the shape in the Figure 4 elasticaly supported on the soil with the stiffness velue defined with formula (4). The discretisation of the three-dimensional computational model is presented in the Figure 6.
The load are the rail supporting forces calculated for the ICE train, represented in the figure 5.

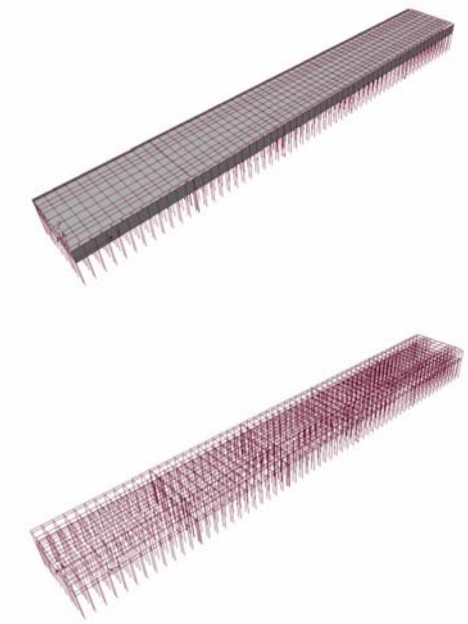

Figure 6. - Computational model

The position of the load on the slabs is shown in the Figure 7 /6/.

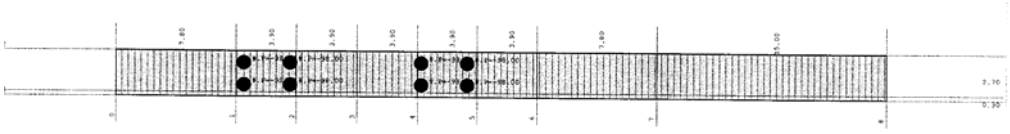

Figure 7. - Load on the slabs

In the Figure 8. the diagram of track slabs deflections and the deformed shape of the model are given /6/.

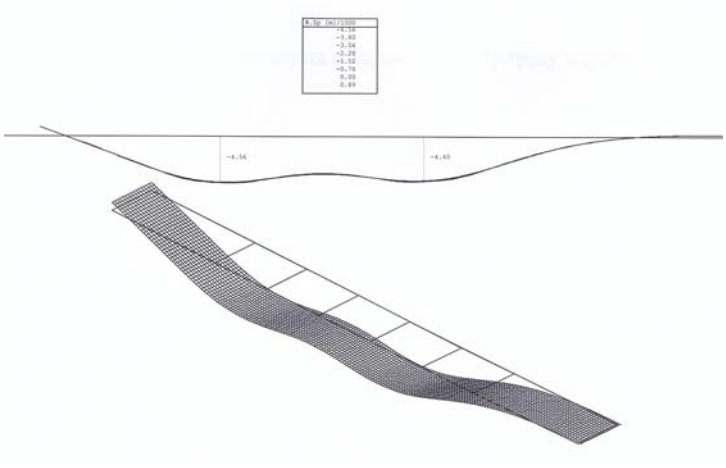

Figure 8. - Track slabs deflections and the deformed shape of the model

5. Conclusion

The track slab "mass-spring" system is used in urban area although it is fairly expensive, becouse it completely fulfilled the special requirements, especially for the slab deflection limits and isolation from vibration and noise at the source. Depending on the used elastic elements materials, it is possible to influence on the slab stress and strain state within wide limits. in the presented example the maximum deflection of 4,56 mm is acceptable, because it agrees with the measured one /3/.

6. References

/1/ Getzner: Elastic supports for slab tracks and ballast troughs - "mass-spring" system.
/2/ Getzner: Inform aktuell - edition 2(2000), 3(2000), 2(2001).
/3/ Lenz U., Stank H., Stummeyer H. J.(2007): Dimensionitung von Masse-Feder-Systemen für Eisenbahn, Eisenbahningenieur, Marz, pp 12-18
/4/ Mosheuvel J.(1999): Ballastless track, Proceedings of symposium "Ballastless Track for the Netherland High Speed Line", Utrecht
/5/ Puzavac L. (2003): Track superstructure of ''mass-spring'' system (in Serbian), diploma work, Civil Engineering faculty University of Belgrade (Serbia)
/6/ Rađen V. (2010): Track superstructure of ''heavy mass-spring'' system (in Serbian), diploma work, Civil Engineering faculty University of Belgrade (Serbia)
/7/ Stevanovic S.: Foundation I (in Serbian), Naucna knjiga, Belgrade, 1989.
/8/ Tiflex Trackelast-Bearings (prospects)
/9/ Tomicic-Torlakovic M. (2001): Contribution to slab track structure calculation, PAMM-meeting, Balaton (Hungary)
/10/ Tomicic-Torlakovic M., Korica, N. (2002): "Tram-train" system - one solution for the track superstructure, (in Serbian), "Zeleznice", 7-8 , pp 247-254.
/11/ Tomicic-Torlakovic M., Puzavac L. (2003): Contribution to Calculation the Slab Track ''Mass-Spring'' System, ZEL 2003, Ziline (Slovakia)

/12/ Tomicic-Torlakovic M., Lelovic S. (2003): Static Calculation of the Track ''Mass-Spring'' System, PAM-meeting, Balaton (Hungary), Bulletins for Applied&Computer Mathematics, No 2148, pp 549-555
/13/ Verbic B., Schmid G., Köpper H. D., Best H.(1997): Investigating the dynamic behaviour of rigid track, Railway Gazette International, september, pp 583-586

REANALYSIS FOR STRUCTURAL DYNAMIC MODIFICATIONS

Nataša Trišović[1], Tatjana Lazović[2], Ljubica Milović[3]

[1] Nataša Trišović, Faculty of Mechanical Engineering, Belgrade, SERBIA,
E-mail: ntrisovic@mas.bg.ac.rs,

[1] Tatjana Lazović, Faculty of Mechanical Engineering, Belgrade, SERBIA,
E-mail: tlazovic@mas.bg.ac.rs,

[1] Ljubica Milovic, Faculty of Technology and Metalurgy, Belgrade, SERBIA,
E-mail: acibulj@tmf.bg.ac.rs,

Several methods for a calculation of derivatives of eigenvectors with respect to design parameters are described here. These are the finite-difference method, the modal method, a modified modal method, Nelson's method, an improved first-order approximation of eigenvalues and eigenvectors and an iterative method. By combining the other structural reanalysis techniques and one of these sensitivity methods, it is possible to enhance the efficiency and the accuracy of structural optimization techniques for determining the optimum condition of mechanical structure specified by an analyst.

INTRODUCTION

A number of techniques exist that can be applied to the dynamic reanalysis of mechanical structures. One of the most popular of these is sensitivity analysis which has been developed and applied by several workers to the general eigenvalue problem [1] and, more specifically, to applications of structural dynamic modification analysis in references [2-3]. Some of the areas where sensitivity analysis has been applied include (i) system identification, (ii) development of insensitive control systems, (iii) use in gradient-based mathematical programming methods, (iv) approximation of system response to a change in a system parameter, and (v) assessment of design changes on system performance [4]. In this area, both first- and higher-order eigenvalue and eigenvector sensitivities have been investigated with a view to predicting the response of a modified structure from knowledge of its spatial and modal properties in the original, or unmodified, state. The sensitivity analysis of a mechanical structure is based on a Taylor expansion of eigenvalues and eigenvectors of the unmodified structure. Traditionally, a truncated Taylor or matrix power series evaluated at a nominal design point is used to approximate the eigen parameters of modified structures [5,6].

MODAL SENSITIVITY ANALYSIS

Modal design sensitivities are the derivatives of the eigensystem of a dynamic system with respect to those variables which are available for modification by the designer. A typical modification would be the change in diameter of a circular section. This would affect both the mass of the section, proportional to the square of the diameter, and its stiffness, which depends on the second moment of area of the section. A change in length

would have a mass effect directly proportional to length, but a stiffness change depending on the cube of length. Changing material would similarly affect mass, stiffness and damping. The design variables depend on the type of optimization problem. In the design of structural components, such as stiffened panels and cylinders, the design parameters represent the spacing of the stiffeners, the size and shape of the stiffeners, and the thickness of the skin. If the skin and/or stiffeners are made of layered composities, the orientation of the fibers and their proportion can become additional variables. The sizes of the elements are design variables of a structural system of fixed configuration (frames, trusses, wings, fuselages, etc). The thickness of plates, cross-sectional areas of bars, areas, moments of inertia, and torsional constants of beams represent sizes of the elements. The parameters may be spatial if the optimization includes configuration. Shape sensitivity analysis of physical systems under dynamic loads may be important from different points of view (i) to understand and model the system's behavior better with respect to shape, (ii) to optimize the physical shapes of the desired systems responses in a prescribed time interval, or (iii) to identify shapes by utilizing the system's measured response in time.

PROBLEM STATEMENT. DERIVATION

The matrix form of the equation of undamped motion of an FE model is:

$$[M]\cdot\{\ddot{x}(t)\}+[K]\cdot\{x(t)\}=\{0\} \tag{1}$$

The free-vibration natural frequencies and mode shapes of a linear structural system can be computed by solving the above eigenvalue problem

$$[K]\{Q_i\}=\lambda_i[M]\{Q_i\} \tag{2}$$

where $[K],[M]$ are the structural stiffness and mass matrix, respectively. The system matrices are considered to be a general function of the design variables denoted by $\{V\}=\{v_1,v_2,...,v_j,...,v_p\}$, and λ_i and $\{Q_i\}$ are the eigenvalue and the eigenvector of mode *i*, respectively. The eigenvalue and eigenvector derivatives can be calculated by performing partial differentiation of the equation (2) to an updating structural parameter v_j:

$$([K]-\lambda_i[M])\frac{\partial\{Q_i\}}{\partial v_j}=\left(\lambda_i\frac{\partial[M]}{\partial v_j}+\frac{\partial\lambda_i}{\partial v_j}[M]-\frac{\partial[K]}{\partial v_j}\right)\{Q_i\}. \tag{3}$$

This is an equation for the eigenvector sensitivity and

$$\frac{\partial\lambda_i}{\partial v_i}=\{Q_i\}^T\left(\frac{\partial[K]}{\partial v_j}-\lambda_i\frac{\partial[M]}{\partial v_j}\right)\{Q_i\} \tag{4}$$

the formula for the eigenvalue sensitivity of the i^{th} mode to the j^{th} design parameter.
Equations (3-4) have been derived under the assumption that the baseline eigenvectors have been mass normalized: $\{Q_i\}^T\cdot[M]\cdot\{Q_i\}=1$.

From this formula, it can be seen that the sensitivity of an eigenvalue to an design parameter can be calculated from the eigenvalue, the corresponding eigenvector, and the sensitivities of the stiffness and mass matrices to the design parameter (variable).

DESCRIPTION OF THE SENSITIVITY METHODS

There mainly exist three categories in the literature: the modal method, the direct method, and the iterative method. Several methods for calculating eigenvector derivatives, $\partial\{Q_i\}/\partial v_j$, are described. Every method, exept the finite-difference method, requires the mass matrix and stiffness matrix derivatives, $\partial[M]/\partial v_j$ and $\partial[K]/\partial v_j$, respectively.

Finite-Difference Method

The most straightforward approach for calculating the derivatives is the finite-difference method. In the finite-difference method, Eq. (2) is solved for $\{Q_i\} = \{Q_i\}_{old}$, the j^{th} design variable is perturbed by Δv_j, and a new eigenvector $\{Q_i'\} = \{Q_i\}_{new}$ is obtained by solving Eq. (2) again, where $v_{j,new} = v_{j,old} + \Delta v_j$. The derivative is approximated by the expression

$$\frac{\partial\{Q_i\}}{\partial v_j} = \frac{\{Q_i\}_{new} - \{Q_i\}_{old}}{\Delta v_j} \tag{5}$$

To reduce numerical errors associated with Eq. (5), attention should be paid to the step size Δv_j. An algotithm for determining the optimum step size has been developed to further reduce numerical errors and is described in Ref. [8].

Modal Method

The modal method expresses the derivative of an eigenvector as a series expansion of the system eigenvectors. Because this method is based on the series expansion of the eigenvalues and eigenvectors of the modified (perturbed) system, the efficiency of this method is limited. The approximate derivative is expressed as [11]:

$$\frac{\partial\{Q_i\}}{\partial v_j} = \sum_{k=1}^{N} A_{ijk}\{Q_k\}, \tag{6}$$

where the coefficients A_{ijk} are calculated using

$$A_{ijk} = \frac{\{Q_k\}^T\left(\frac{\partial[K]}{\partial v_j} - \lambda_i\frac{\partial[M]}{\partial v_j}\right)\{Q_i\}}{\lambda_i - \lambda_k}, \quad k \neq i. \tag{7}$$

Considering the orthogonality property of the eigenvector, $\{Q_i\}$, $\{Q_i\}^T[M]\{Q_i\} = 1$, and partial-differentiating this equation with respect to the updating parameter, v_j, for $k \neq i$, it can be obtained that:

$$2\{Q_i\}^T[M]\frac{\partial\{Q_i\}}{\partial v_j} + \{Q_i\}^T\frac{\partial[M]}{\partial v_j}\{Q_i\} = 0\ . \tag{8}$$

The expression for $\partial\{Q_i\}/\partial v_j$ from Eq. (6) is substituted into Eq. (8), and using the orthogonality condition $\{Q_i\}^T[M]\{Q_i\}=1$, the coefficients A_{ijk} are obtained:

$$A_{ijk}=-\frac{1}{2}\{Q_i\}^T\frac{\partial[M]}{\partial v_j}\{Q_i\},\quad k=i. \tag{9}$$

Modified Modal Method

The modified modal method uses a pseudostatic solution of Eq (3) as an initial approximation to the mode shape derivative. This is similar in principle to the mode-acceleration method used in transient structural analysis [9]. Equation (3) is solved by neglecting the quantity $\lambda_i[M]\left(\partial\{Q_i\}/\partial v_j\right)$ and obtaining the pseudostatic solution for $\left(\partial\{Q_i\}/\partial v_j\right)_s$, which is

$$\left(\frac{\partial\{Q_i\}}{\partial v_j}\right)_s=[K]^{-1}\cdot\left(\lambda_i\frac{\partial[M]}{\partial v_j}+\frac{\partial\lambda_i}{\partial v_j}[M]-\frac{\partial[K]}{\partial v_j}\right)\cdot\{Q_i\}. \tag{10}$$

This pseudostatic solution is added to Eq. (6) to obtain

$$\frac{\partial\{Q_i\}}{\partial v_j}=\left(\frac{\partial\{Q_i\}}{\partial v_j}\right)_s+\sum_{k=1}^{N}\overline{A}_{ijk}\{Q_k\}, \tag{11}$$

where $\overline{A}_{ijk}$ are coefficients for the modified modal method. To obtain the coefficients $\overline{A}_{ijk}$, Eq. (11) is substituted into Eq. (3), and the result is premultiplied by $\{Q_k\}^T$. When simplified, this result becomes

$$\overline{A}_{ijk}=\frac{\lambda_i\{Q_k\}^T\left(\frac{\partial[K]}{\partial v_j}-\lambda_i\frac{\partial[M]}{\partial v_j}\right)\{Q_i\}}{\lambda_k\cdot(\lambda_i-\lambda_k)},\quad k\neq i, \tag{12}$$

$$\overline{A}_{ijk}=-\frac{1}{2}\{Q_i\}^T\frac{\partial[M]}{\partial v_j}\{Q_i\},\quad k=i. \tag{13}$$

The relative convergence of the modified modal method vs the modal method for a given number of eigenvectors can be anticipated by dividing Eq. (12) by Eq. (7):

$$\frac{\overline{A}_{ijk}}{A_{ijk}}=\frac{\lambda_i}{\lambda_k} \tag{14}$$

Assuming that to calculate $\partial\{Q_i\}/\partial v_j$ accurately i modes or more are needed; then for $k>i$, $\overline{A}_{ijk}$ is smaller than A_{ijk}, and Eq. (11) will converge faster than Eq. (6).

Nelson's Method

Nelson's method (the direct method) obtains an exact solution to Eq. (3). This method expresses the eigenvector derivative in terms of a particular solution $\{\xi_{ij}\}$ and a complementary solution $\{Q_i\}\cdot c_{ij}$ where c_{ij} is an undetermined coefficient. In this case, any solution for equation (3) can be written in the form of [7]:

$$\frac{\partial\{Q_i\}}{\partial v_j} = \{\xi_{ij}\} + \{Q_i\}\cdot c_{ij}, \tag{15}$$

The particular solution is found by identifying the component of the eigenvector $\{Q_i\}$ with the largest absolute value and constraining the derivative of that component to zero. Combining equations (15) and (8), it is shown that

$$2\{Q_i\}^T[M]\left(\{\xi_{ij}\} + \{Q_i\}\cdot c_{ij}\right) + \{Q_i\}^T \frac{\partial[M]}{\partial v_j}\{Q_i\} = 0 . \tag{16}$$

The coefficient c_{ij} can be obtained by the following formula:

$$c_{ij} = -\left(\{Q_i\}^T[M]\{\xi_{ij}\} + \frac{1}{2}\{Q_i\}^T \frac{\partial[M]}{\partial v_j}\{Q_i\}\right) \tag{17}$$

Improved First-Order Approximation of Eigenvalues and Eigenvectors

A method based on reduced basis approximation concepts is presented for improved first-order approximation of eigenvalues and eigenvectors of modified structural dynamic systems [10]. The approximation procedure involves the use of the baseline eigenvector and the first-order approximation term as basic vector for Ritz analysis of the perturbed eigenvalue problem. An assumption is made that the eigenvector of the perturbed system can be approximated in the subspace spanned by $\{Q_i\}$ and $\{\Delta Q_i\}$, an approximation for the perturbed eigenvector can be written as

$$\{\hat{Q}_i\} = \zeta_1\{Q_i\} + \zeta_1\{\Delta Q_i\} \tag{18}$$

where ζ_1 and ζ_2 are undetermined scalar quantities in the approximate representation of the perturbed eigenvector. The assumption implicit in this proposition is that, even for moderate to large perturbations in the structural parameters, the first-order approximation yields a $\{\Delta Q_i\}$ vector, which usually gives a reasonable indication of the likely change of a baseline eigenvector, although the magnitude or even direction of change may be erroneous. Eq. (18) can be expressed in matrix form as

$$\{\hat{Q}_i\} = [T]\{Z\} \tag{19}$$

where $[T]=[Q_i, \Delta Q_i] \in \Re^{n\times 2}$ and $\{Z\}^T = \{\zeta_1, \zeta_1\} \in \Re^{1\times 2}$.

Substituting equation (19) in to equation (2) and premultiplying by $[T]^T$, the resulting set of equations can be expressed as

$$[K_T]\{Z\} = \lambda[M_T]\{Z\} \tag{20}$$

where

$$[K_T] = [T]^T[K'][T] \in \Re^{2\times 2} \tag{21}$$

and

$$[M_T] = [T]^T [M'][T] \in \Re^{2\times 2}. \tag{22}$$

After matematical transformation, the mass normalized perturbed eigenvector can be written as [10]:

$$\{\hat{Q}_i\} = \frac{1}{\{Z\}^T [M_T]\{Z\}} \cdot \left[\{Q_i\} - \frac{(k_{11} - \hat{\lambda}_i m_{11})}{(k_{12} - \hat{\lambda}_i m_{12})} \cdot \{\Delta Q_i\} \right]. \tag{23}$$

The following inequality relationship can be estabilished as criteria for selection of the best approximation

$$\hat{\lambda}_i^{\min} \le \lambda_i^{rqa0} \le \hat{\lambda}_i^{\max} \tag{24}$$

where λ_i^{rqa0} is the zero order Rayleigh quotient approximation which is defined below as

$$\lambda_i^{rqa0} = \frac{\{Q_i\}^T [K]\{Q_i\}}{\{Q_i\}^T [M]\{Q_i\}}. \tag{25}$$

Hence, criteria for selection of the best approximation are (i) maximum value of $|\zeta_1 / \zeta_2|$, (ii) minimum distance from the zero-order Rayleigh quotient λ_i^{rqa0}, (iii) minimum distance from λ_i, (iv) minimum magnitude, (v) minimum distance from the root selected for the previous mode. This approximation procedure could also be interpreted as an improved Rayleigh quotient approximation procedure with one free parameter, i.e., $|\zeta_2 / \zeta_1|$.

Iterative Method for Calculating Eigenvectors Derivatives

The calculation of the eigenvector derivatives involves extensive computational effort. The direct method is one of the most efficient methods that produces exact solutions and does not need eigenvectors more than those whose derivatives are to be computed. But because its amount of computational effort is proportional to the number of eigenvector derivatives required, the application of the method becomes expensive when many eigenvector derivatives are demanded. On the other hand, the truncated modal method has an insuperable efficiency but suffers a serious accuracy problem. To improve the accuracy of the modal method, Wang [12] proposed a modified modal method, which was extended by Liu et al. [13] and Zhang and Zerva [14] to an *iterative algorithm* that can be used as an exact method as well as an approximate method and, just like the direct method, does not require additional eigenvalues and eigenvectors. The method assumes that the inverse stiffness matrix exists. Recently, Lin and Lim [15] and Zeng [16] presented an approach to deal with singular stiffness matrices. The convergence rate of the iterative method depends mainly on the ratio of the specified eigenvalue to the lowest unavailable one, and when the ratio approaches 1, the convergence rate of the corresponding eigenvector derivative will reduce quickly and the method becomes more expensive than the direct method. The iterative method used here was derived originally in Ref. [14]. The basic iterative equation after $p(p \ge 1)$ iterations is

$$\{V_{ku}\}_p = \sum_{i=q+1}^{n}\left[1-\left(\frac{\lambda_k}{\lambda_i}\right)^p\right]\frac{\{Q_k\}^T\left(\dfrac{\partial[K]}{\partial v_j}-\lambda_i\dfrac{\partial[M]}{\partial v_j}\right)\{Q_i\}}{\lambda_i-\lambda_k}\{Q_k\}+\sum_{i=q+1}^{n}\left(\frac{\lambda_k}{\lambda_i}\right)^p\{Q_k\}^T[M]\{V_{ku}\}_0\{Q_i\},$$

$$k<q; \quad p=1,2,... \tag{26}$$

where

$\{V_{ku}\}$ = component of $\partial\{Q_k\}/\partial v_j$ in the range of *unavailable* eigenvectors $\{Q_{q+1}\},...,\{Q_n\}$,

$\{V_{ku}\}_p$ = pth iterative solution for $\{V_{ku}\}$,

$\{V_{ku}\}_0$ = stands for the initial value.

The term $(\lambda_k/\lambda_i)^p$ represents the error because of the ith unknown eigenvector. When p tends to infinity, $(\lambda_k/\lambda_i)^p$ vanishes because $\lambda_k/\lambda_i<1$, and $\{V_{ku}\}_p$ converges to the exact solution with any initial value. Equation (26) also suggests that $\{V_{ku}\}_0$ can be set equal to zero. Note that in each iteration, the roundoff error in the subspace spanned by the lower *available* eigenvectors $\{Q_1\},...,\{Q_q\}$ will be automatically wiped out, which results in a very stable iterative process.

CONCLUDING REMARKS

This paper reviewed several methods for eigensensitivity analysis with respect to design variables. These were *the finite-difference method, the modal method, a modified modal method, Nelson's method, an improved first-order approximation of eigenvalues and eigenvectors and an iterative method*. *Nelson's method* was the least computationally intensive, and since it is an exact method, it is the method recommended. When the original mode shapes were used as initial approximations to the subspace eigensolution of the perturbed problem, *the finite-difference method* was competitive with Nelson's method. The *modified modal method* always converged faster than the modal method when at least as many modes were used in the approximation as the number of the mode shape being differentiated. *The modified modal method* can compete with *Nelson's method* for the first mode shape derivative when the number of modes needed in the summation was known before the eigensolution was performed. Detailed comparasion *an improved first-order approximation* [10] with other approximation techniques indicate that significant improvements are achieved with a relatively small extra computational effort. An *iterative* method is simple, systematic, efficient and numerically stable.

Acknowledgment

This work has been performed within the projects TR 35011 and ON 74001. These projects are supported by the Republic of Serbia, Ministry of Science and Technological Development, which financial help is gratefully acknowledged.

REFERENCES

[1] Jung, H., *Structural Dynamic Model Updating Using Eigensensitivity Analysis*, IC, Univ. of London, PhD, 1992.
[2] Wang, J., Heylen., W. and Sas, P., *Accuracy of Structural Modification Techniques*, Proc. of the 5th Int. Modal Analysis Conf., 1987., pp. 65-71
[3] Noor, A.K. and Whitworth, S., *Reanalysis Procedure for Large Structural Systems*, Int. J. Numer. Methods Eng. Vol. 26, 1988. pp. 1729-1748
[4] Prasad, B. and Emerson, J.F., *A General Capability of Design Sensitivity for Finite Element Systems,* A Collection of Technical Papers, Part 2: Structural Dynamics and Design Engineering, AAIA/ASME/ASCE/AHS 23rd Structures, Structural Dynamics and Material Conf., May 1982, pp. 175-186.
[5] Schmit, L.A. and Farshi, B., *Some Approximation Concepts For Structural Synthesis,* AIAA Journal, Vol. 2, No.5, 1974, pp. 692-699.
[6] Minas, C. and Inman, D.J., *Matching Finite Element Models to Model Data*, ASME Journal of Vibration and Acoustics, Vol. 112, 1990.
[7] Nelson, R.B., *Simplified Calculation of Eigenvectors Derivatives*, AAIA Journal, Vol. 14, 1976, pp.1201-1225.
[8] Iott, J., Haftka, R.T., and Adelman, H.M., *On a Procedure for Selecting Step Sizes in Sensitivity Analysis by Finite Differences*, NASA TM-86382, Aug.1985.
[9] Craig, R.R., Jr., *Structural Dynamics – An Introduction to Computer Methods*, Wiley, New York, 1981.
[10] Nair, B.P., Keane, A.J., and Langley, R.S., *Improved First-Order Approximation of Eigenvalues and Eigenvectors,* AIAA Journal, Vol. 36, No. 9, September 1998, pp. 1722-1727.
[11] Sutter, T.R., Camarda.,C.J., Walsh.,J.L., Adelman.,H.M., *Comparison of Several Methods for Calculating Vibration Mode Shape Derivatives*, AIAA Journal, Vol. 26, No. 12, Feb. 1987, pp. 1506-1511.
[12] Wang, B.P., *Improved Approximate Methods for Computing Eigenvector Derivatives in Structural Dinamycs,,* AIAA Journal, Vol. 29, No. 6, 1991, pp. 1018-1020.
[13] Liu, Z.S., Chen, S.H., Yu, M., and Zhao, Y.Q., Contribution of Truncated Modes to Eigenvector Derivatives, AIAA Journal, Vol. 32, No. 7, 1994, pp. 1551-1553.
[14] Zhang, O., and Zerva, A., *Iterative Method for Calculating Derivatives of Eigenvalues*, AIAA Journal, Vol. 34, No. 5, 1996, pp. 1088-1090.
[15] Lin, R.M., and Lim, M.K., *Eigenvector Derivatives of Structures with Rigid Body Modes*, AIAA Journal, Vol. 34, No. 5, 1996, pp. 1083-1085.
[16] Zeng, Q.H., *Highly Accurate Modal M ethod for Calculating Eigenvectors in Viscous Damping Systems,* AIAA Journal, Vol. 33, No. 4, 1995, pp. 746-751.

HIGH TEMPERATURE INFLUENCE ON SANDWICH BEAM STABILITY

N. Vasić[1], I. Čamagić[1], Z. Vasić[1]

[1] Faculty of Technical Sciences,
The University of Priština, Kneza Miloša 7, 38220 Kosovska Mitrovica
e-mail: nemanja.vasic@pr.ac.rs

Abstract. Sandwich beam has two, thin, outer layers made of elastic material and middle layer-core with relatively low stiffness, compared to outer layers stiffness. Calculation of these structures is based on assumptions that all three layers deform simultaneously and that there is a joint neutral line between outer layers. With this approach to the calculation it is possible to describe, with high grade of accuracy, the stress and the strain state of structure as well as local influence within each of the layers. In this paper is presented the influence of high temperature on critical buckling pressure force for a sandwich beam composed of two, thin elastic, outer layers of same thickness and middle layer with bending stiffness that can be neglected compared to the outer layers stiffness, based on the broken cross section line hypothesis. The critical temperature during buckling is determined on the example of a beam with restrained ends, and non uniform temperature distribution.

1. Introduction

Sandwich beam stability in elastic deformation area, at high temperatures, was reviewed in this paper. Sandwich beam consists of two outer layers (supporting layers) of small thickness δ and middle layer with height of $2h$ made of material with trivial strength compared to the strength of outer layers material. Outer layers deform according to Bernoulli's hypothesis on perpendicular cross section, while cross section of middle layer rotates as stiff set and does not need to be perpendicular to the bended central axis of a beam. This hypothesis is kinematic. It sets the law of point displacement variation in terms of beam thickness and does not depend on material properties. Normal stress is linearly distributed along cross section height, with zero value on central axis. That means that edge fibbers are completely used, and as fibbers approaches to the central axis their participation in bending action becomes insignificant. That leaded to the appearance of sandwich structures with two outer layers made of solid material, set on a certain distance and connected by middle layer in form of ribs made of the same material or this interspace is filled with less solid material, which provides corporate action of a structure. Calculation of structures with solid middle layer does not differ from the calculation of thin homogenous rods, and calculation of structures with middle layer made of less solid material is based on the broken line hypothesis [1], [2], Fig. 1.

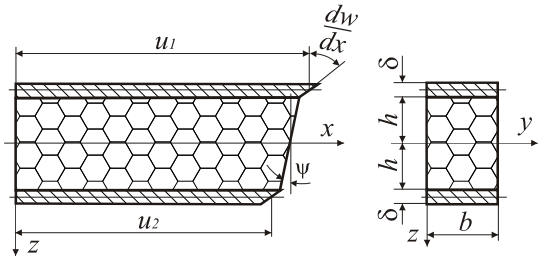

Figure 1. Sandwich beam

Supporting layers of fully restrained beam are submitted to heating in such way that temperature in direction of its longitudinal axis changes according to parabolic law, while temperature change along the thickness of supporting layers is linear:

$$t_1(x,z) = T_0 - \frac{T_1}{\delta}\left(1-\left(\frac{2x-l}{l}\right)^2\right)(z+h), \tag{1}$$

$$t_2(x,z) = T_0 + \frac{T_2}{\delta}\left(1-\left(\frac{2x-l}{l}\right)^2\right)(z-h), \tag{2}$$

and middle layer temperature equals T_0, as shown in Fig. 2. Critical temperature T_{cr} was determined for a beam heated in such way. In first case, maximal temperature values of outer layers are equal (T_1=T_2), and in they are different (T_1≠T_2).

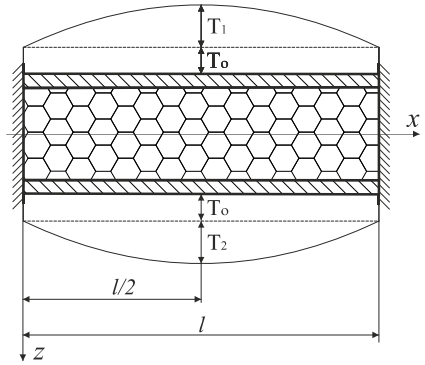

Figure 2. Temperature distribution on fully restrained beam

2. Displacement and Deformation Component

If beam cross section deforms into the broken line shown in Fig. 1, displacement component of a random point on the cross section will be:

- for upper layer, $-(h+\delta) \le z \le -h$,

$$u_{\mathrm{u}}(x,z)=u_1(x)-\left(z+h+\frac{\delta}{2}\right)\frac{\mathrm{d}w}{\mathrm{d}x}\,, \qquad w_{\mathrm{u}}(x)=w(x), \tag{3}$$

- for lower layer, $h\le z\le(h+\delta)$,

$$u_{\mathrm{b}}(x,z)=u_2(x)-\left(z-h-\frac{\delta}{2}\right)\frac{\mathrm{d}w}{\mathrm{d}x}\,, \qquad w_{\mathrm{b}}(x)=w(x), \tag{4}$$

- for middle layer, $-h\le z\le h$,

$$u_{\mathrm{m}}(x,z)=u_\alpha(x)-\frac{z}{h}\left[u_\beta(x)-\frac{\delta}{2}\frac{\mathrm{d}w}{\mathrm{d}x}\right], \quad w_{\mathrm{m}}(x)=w(x), \tag{5}$$

where

$$u_\alpha=(u_1+u_2)/2\,,\ u_\beta=(u_1-u_2)/2\,. \tag{6}$$

Deformation components, different than zero, are determined according to the known expressions of elastic theory:

$$\varepsilon_x=\frac{\partial u}{\partial x}, \quad \gamma_{xz}=\frac{\partial u}{\partial z}+\frac{\partial w}{\partial x}\,. \tag{7}$$

3. Forces and Bending Moments

Normal stress $\sigma_{x\mathrm{u}}$ and shear stress $\tau_{z\mathrm{u}}$ will appear in outer layers of a beam, and only shear stress $\tau_{z\mathrm{m}}$ in the middle layer. Deformation $\varepsilon_{x\mathrm{u}}$, at any point in direction of longitudinal axis of a beam upper layer, is defined as:

$$\varepsilon_{x\mathrm{u}}=\frac{\sigma_{x\mathrm{u}}}{E}+\alpha\cdot t_1(x,z)\,, \tag{8}$$

where E – is elasticity modulus, $t_1(x, z)$ – is temperature [$^{\mathrm{o}}$C] at any point of a beam upper layer determined in Eq. (1) and α - is coefficient of material linear expansion. On the other hand that deformation, according to Eqs. (7) and (3), is calculated as:

$$\varepsilon_{x\mathrm{u}}=\frac{\mathrm{d}u_1}{\mathrm{d}x}-\left(z+x+\frac{\delta}{2}\right)\frac{\mathrm{d}^2w}{\mathrm{d}x^2}\,. \tag{9}$$

Expression for bending moment $M_{x\mathrm{u}}$ will be obtained if right-hand sides of Eqs. (8) and (9) are multiplied by $\left(z+x+\frac{\delta}{2}\right)$ and integrated over layer thickness. Bending moment in lower layer of a beam $M_{x\mathrm{b}}$ is determined the same way, so it follows:

$$M_{x\mathrm{u}} = -\frac{E\delta^3}{12}\frac{\mathrm{d}^2 w}{\mathrm{d}x^2} + \alpha \cdot \frac{E\delta^2}{12}\Theta_1 , \tag{10}$$

$$M_{x\mathrm{b}} = -\frac{E\delta^3}{12}\frac{\mathrm{d}^2 w}{\mathrm{d}x^2} + \alpha \cdot \frac{E\delta^2}{12}\Theta_2 , \tag{11}$$

where temperature influence is determined by parameters:

$$\Theta_1 = -\frac{12}{\delta^2}\int_{-h-\delta}^{-h} t_1(x,z)\left(z + h + \frac{\delta}{2}\right)\mathrm{d}z , \tag{12}$$

$$\Theta_2 = -\frac{12}{\delta^2}\int_{h}^{h+\delta} t_2(x,z)\left(z - h - \frac{\delta}{2}\right)\mathrm{d}z . \tag{13}$$

Forces, in each layer of a beam, are obtained by stress integration for the central line of a beam cross section, over the appropriate layer height as shown in Fig. 3. Total forces and moments of sandwich package are determined by summing of appropriate forces and moments for each layer. Those forces and moments, according to Eqs. (3) to (6), can be expressed by displacement components as:

$$N_x = 2B\frac{\mathrm{d}u_\alpha}{\mathrm{d}x} + B\alpha\left(\Omega_1 + \Omega_2\right), \tag{14}$$

$$\begin{aligned} M_x = &-2D\frac{\mathrm{d}^2 w}{\mathrm{d}x^2} - 2B\left(h + \frac{\delta}{2}\right)\frac{\mathrm{d}u_\beta}{\mathrm{d}x} + \\ &+ \alpha\frac{E\delta^2}{12}\left(\Theta_1 + \Theta_2\right) - B\alpha\left(h + \frac{\delta}{2}\right)\left(\Omega_1 - \Omega_2\right) \end{aligned} , \tag{15}$$

$$\begin{aligned} Q_x = &-2D\frac{\mathrm{d}^3 w}{\mathrm{d}x^3} - 2G_3\left[u_\beta - \left(h + \frac{\delta}{2}\right)\frac{\mathrm{d}w}{\mathrm{d}x}\right] - \\ &- B\delta\frac{\mathrm{d}^2 u_\beta}{\mathrm{d}x^2} + \alpha\frac{E\delta^2}{12}\frac{\mathrm{d}}{\mathrm{d}x}\left(\Theta_1 + \Theta_2\right) - \alpha B\frac{\delta}{2}\frac{\mathrm{d}}{\mathrm{d}x}\left(\Omega_1 - \Omega_2\right) \end{aligned} , \tag{16}$$

where G_3 – is shearing modulus for middle layer material, $B = Ed$ – is axial stiffness, $D = Ed^3 / 12$ – is bending stiffness per unit width of beam outer layers and temperature parameters are:

$$\Omega_1 = -\frac{1}{\delta}\int_{-h-\delta}^{-h} t_1(x,z)\mathrm{d}z , \tag{17}$$

$$\Omega_2 = -\frac{1}{\delta}\int_{h}^{h+\delta} t_2(x,z)\mathrm{d}z . \tag{18}$$

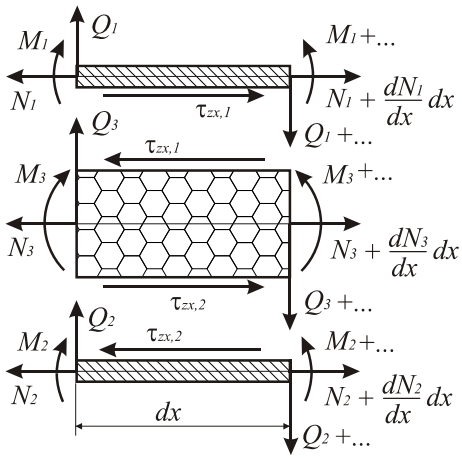

Figure 3. Positive forces and moments in sandwich beam cross section

4. Differential Stability Equations and Contour Conditions

Differential stability equations are obtained from static equilibrium condition for forces appearing in cross sections of a beam element, as shown in Fig. 3. Those equations, expressed by displacement components u_α, u_β and w, are reduced to:

$$\frac{\mathrm{d}^2 u_\alpha}{\mathrm{d}x^2} = 0\,, \tag{19}$$

$$\frac{Bh}{bG_3}\frac{\mathrm{d}^2 u_\beta}{\mathrm{d}x^2} - u_\beta + \left(h + \frac{\delta}{2}\right)\frac{\mathrm{d}w}{\mathrm{d}x} = \frac{\alpha Bh}{2G_3}\frac{\mathrm{d}}{\mathrm{d}x}\left(\Omega_1 - \Omega_2\right), \tag{20}$$

$$\begin{aligned} &-2D\frac{\mathrm{d}^4 w}{\mathrm{d}x^4} - 2B\left(h + \frac{\delta}{2}\right)\frac{\mathrm{d}^3 u_\beta}{\mathrm{d}x^3} + N_x\frac{\mathrm{d}^2 w}{\mathrm{d}x^2} = \\ &-\alpha\frac{E\delta^2}{12}\frac{\mathrm{d}^2}{\mathrm{d}x^2}\left(\Theta_1 + \Theta_2\right) + \alpha\left(h + \frac{\delta}{2}\right)B\frac{\mathrm{d}^2}{\mathrm{d}x^2}\left(\Omega_1 - \Omega_2\right) \end{aligned} \tag{21}$$

Eq. (19) is independent to Eqs. (20) and (21) and it has trivial solution in terms of function u_α, so the beam stability problem is reduced to solving the system of two differential equations (20) and (21) with unknown functions $u_\beta(x)$ and $w(x)$, which must satisfy contour conditions as well. Contour conditions can be expressed by displacement components or by appropriate transversal forces and moments. Valid geometric leaning conditions for fully restrained beam are:

$$w = 0, \qquad \frac{\mathrm{d}w}{\mathrm{d}x} = 0\,, \qquad u_\beta = 0, \qquad \text{for } x = 0 \text{ and } x = l. \tag{22}$$

Temperature influence to the beam stability is determined by parameters Θ and Ω, and it can be seen from Eqs. (20) and (21). The basic differential equations are not different from the stability equations of a beam submitted to pressure forces, if parameters are equal ($\Omega_1 = \Omega_2$) or if they are constant in longitudinal axis direction, or if they change by linear law.

5. Numerical Results and Conclusions

Solving of a beam differential stability equations is shown on the example of fully restrained beam with length l, shown in Fig. 1, submitted to the heating of outer layers in longitudinal axis direction according to Eqs. (1) and (2). Pressure force will appear at the beam restrain point as:

$$N_x = -N_{x0} = -(N_{x\mathrm{u}} + N_{x\mathrm{b}}), \tag{23}$$

where $N_{x\mathrm{u}}$ and $N_{x\mathrm{b}}$ are pressure forces in the beam outer layers, determined as:

$$\begin{aligned} N_{x\mathrm{u}} &= \frac{E\delta}{l}\Delta l = \frac{E\delta}{l}\alpha \int_{-h-\delta}^{-h}\left(\int_0^l (t_1(x,z) - T_0)\,\mathrm{d}x\right)\mathrm{d}z \\ N_{x\mathrm{b}} &= \frac{E\delta}{l}\Delta l = \frac{E\delta}{l}\alpha \int_{h}^{h+\delta}\left(\int_0^l (t_2(x,z) - T_0)\,\mathrm{d}x\right)\mathrm{d}z \end{aligned}, \tag{24}$$

Total pressure force is obtained by integration of Eqs. (24), based on Eqs. (1), (2) and (23), as:

$$N_x = -N_{x0} = -\alpha\frac{E\delta^2}{3}(T_1 + T_2), \tag{25}$$

where T_1 and T_2 are maximal temperature values on upper and lower supporting layer of the beam, respectively. Required temperature parameters in basic stability equations, according to Eqs. (12), (13), (17) and (18), are:

$$\Theta_1 + \Theta_2 = \frac{4\left(xl - x^2\right)}{l^2}(T_1 - T_2), \tag{26}$$

$$\Omega_1 - \Omega_2 = \frac{2\left(x^2 - xl\right)}{l^2}(T_1 - T_2). \tag{27}$$

If dimensionless coordinate is introduced as:

$$\xi = \frac{\pi}{l}x, \tag{28}$$

differential stability equations (20) and (21) are reduced to the following form:

$$k\frac{\mathrm{d}^2 u_\beta}{\mathrm{d}\xi^2} - u_\beta + \left(h + \frac{\delta}{2}\right)\frac{\mathrm{d}w}{\mathrm{d}\xi} = p_1(2\xi - \pi)\Delta t, \tag{29}$$

$$r\frac{\mathrm{d}^4 w}{\mathrm{d}\xi^4}+\frac{1}{h_1}\frac{\mathrm{d}^3 u_\beta}{\mathrm{d}\xi^3}+\varphi\frac{\mathrm{d}^2 w}{\mathrm{d}\xi^2}=-p_2\,\Delta t\,, \tag{30}$$

where pressure force coefficient φ and shearing coefficient k are defined in terms of pressure force N_{x0}, and shearing modulus G_3, respectively as:

$$\varphi=\frac{N_{x0}\,l^2}{2B\left(h+\frac{\delta}{2}\right)^2\pi^2}\,,\qquad k=\frac{Bh}{G_3 b}\frac{\pi^2}{l^2}\,, \tag{31}$$

and dimensionless geometric coefficients r and h_1 are:

$$r=\frac{\delta^2}{12\left(h+\frac{\delta}{2}\right)^2}\,,\qquad h_1=\frac{\pi\left(h+\frac{\delta}{2}\right)}{l}\,, \tag{32}$$

and temperature parameters are:

$$p_1=\alpha\,k\frac{l}{\pi^3}\,,\qquad p_2=\alpha\frac{l^2}{\left(h+\frac{\delta}{2}\right)^2}\frac{\delta+6}{3\pi^4}\,,\qquad \Delta t=T_1-T_2\,. \tag{33}$$

Right-hand sides of Eqs. (29) and (30) are equal to zero if heating temperatures of the outer beam layers are equal ($t_1(x,z)=t_2(x,z)$), so the stability problem is reduced to the solving of homogenous differential equations with unknown displacement components $w(\xi)$, $u_\beta(\xi)$. Displacement components that satisfy these homogenous differential equations, for the stress state before critical ($D = 0$, $r = 0$), can be assumed as:

$$w(\xi)=C_1\sin(s\xi)+C_2\cos(s\xi)+C_3\xi+C_4\,, \tag{34}$$

$$u_\beta(\xi)=-\frac{\pi}{l}\left(h+\frac{\delta}{2}\right)\left[\frac{s}{1+ks^2}\left(C_2\sin(s\xi)-C_1\cos(s\xi)\right)-C_3\right], \tag{35}$$

where axial pressure force coefficient is:

$$\varphi=\frac{s^2}{1+ks^2}\,. \tag{36}$$

Unknown integration constants C_1 to C_4 are calculated from contour conditions (22) as:

$$w=u_\beta=0\,,\qquad \text{for } \xi=0 \text{ and } \xi=\pi. \tag{37}$$

Condition for the system of algebraic equations with unknown constants C_1 to C_4 to have nontrivial solutions, when displacement components (34) and (35) are included in contour conditions (37), is reduced to the following equation:

$$\sin\left(\frac{s\pi}{2}\right)\left[2\sin\left(\frac{s\pi}{2}\right)-\frac{s\pi}{1+ks^2}\cos\left(\frac{s\pi}{2}\right)\right]=0\,, \tag{38}$$

which is satisfied for the lowest value of parameter $s = 2$. Minimal value of pressure force coefficient is:

$$\varphi=\frac{4}{1+4k}\,, \tag{39}$$

and minimal value of the critical temperature is:

$$T_{\mathrm{cr}}=\frac{3\pi^2(2h+\delta)^2}{\alpha\cdot l^2\delta(1+4k)}\,. \tag{40}$$

In case that the beam outer layers are submitted to the temperatures t_1 and t_2, determined by Eqs. (1) and (2), the stability problem is reduced to the solving of non homogenous system of differential equations (29) and (30). For the strain before critical ($D = 0$, $r = 0$), considering parameters (17) and (18), this system of differential equations is:

$$k\frac{\mathrm{d}^2u_\beta}{\mathrm{d}\xi^2}-u_\beta+\left(h+\frac{\delta}{2}\right)\frac{\mathrm{d}w}{\mathrm{d}\xi}=p_1(2\xi-\pi)\Delta t\,, \tag{41}$$

$$\frac{1}{\left(h+\frac{\delta}{2}\right)}\frac{\mathrm{d}^3u_\beta}{\mathrm{d}\xi^3}+\varphi\frac{\mathrm{d}^2w}{\mathrm{d}\xi^2}=-p_2\ \Delta t\,. \tag{42}$$

System of differential equations (41) and (42) will be satisfied if displacement components are assumed as:

$$\begin{aligned}w(\xi)&=C_1\sin(s\xi)+C_2\cos(s\xi)+\frac{C_3}{h_1}\xi+C_4-\\&-\frac{p_1\pi\Delta t}{h_1}\xi-\frac{p_2\Delta t}{2\varphi}\xi^2\end{aligned}\,, \tag{43}$$

$$\begin{aligned}u_\beta(\xi)&=B_1\sin(s\xi)+B_2\cos(s\xi)+B_3-2p_1\pi\Delta t\,\xi-\\&-\frac{p_2\Delta t\,h_1}{\varphi}\xi\end{aligned}\,. \tag{44}$$

When Eqs. (43) and (44) are included into contour conditions (37), following system of algebraic equations in terms of unknown constants C_i ($i = 1,...,4$), is obtained:

$$
\begin{aligned}
&C_2 + C_4 = 0,\\
&C_1 \sin(s\pi) + C_2 \cos(s\pi) + C_3 \frac{\pi}{h_1} + C_4 = \frac{p_1 \pi^2 \Delta t}{h_1} +\\
&+ \frac{p_2 \pi^2 \Delta t\left(1 + ks^2\right)}{2s^2},\\
&C_1 \frac{h_1 s}{1 + ks^2} + C_3 = 0,\\
&C_1 \frac{s\, h_1 \cos(s\pi)}{1 + ks^2} - C_2 \frac{s\, h_1 \sin(s\pi)}{1 + ks^2} + C_3 = 2 p_1 \pi \Delta t +\\
&+ \frac{p_2 \pi \Delta t\, h_1\left(1 + ks^2\right)}{s^2}.
\end{aligned}
\tag{45}
$$

Solving of system (45), in terms of unknown constants C_i (i = 1,...4), gives:

$$
\begin{aligned}
C_1 &= -\frac{\pi \Delta t\left(1 + ks^2\right)\left[2 p_1 s^2 + p_2 h_1\left(1 + ks^2\right)\right]}{2 h_1 s^3},\\
C_2 &= -C_4 = -\frac{\pi \Delta t\left(1 + ks^2\right)\left[2 p_1 s^2 + p_2 h_1\left(1 + ks^2\right)\right]\cos\left(\frac{s\pi}{2}\right)}{2 h_1 s^3 \sin\left(\frac{s\pi}{2}\right)},\\
C_3 &= \frac{\pi \Delta t\left[2 p_1 s^2 + p_2 h_1\left(1 + ks^2\right)\right]}{2 s^2},
\end{aligned}
\tag{46}
$$

where φ is pressure force coefficient, determined by Eq. (31).

The lowest value of parameter s, of critical pressure force coefficient φ, is determined from contour condition dw/dx = 0 for $\xi = \pi$, from the following equation:

$$
\left(1 + ks^2\right) \cdot \sin\left(\frac{s\pi}{2}\right) \cdot \left[s\pi \cos\left(\frac{s\pi}{2}\right) - 2\left(1 + ks^2\right) \cdot \sin\left(\frac{s\pi}{2}\right)\right] = 0\,. \tag{47}
$$

Eq. (47) has one solution equal to zero, real solutions $s = 2n$ (n=1, 2, ...) and real solutions of following equation:

$$
s\pi \cos\left(\frac{s\pi}{2}\right) - 2\left(1 + ks^2\right) \cdot \sin\left(\frac{s\pi}{2}\right) = 0\,. \tag{48}
$$

Solutions of Eq. (48), in terms of parameter s, different than zero are determined as:

$$
s = \frac{S}{\pi}\,, \tag{49}
$$

where S is a solution of following function:

$$f(z) = 8\sin(z)k^2z^2\pi^2 + 4\sin(z)k^2\pi^2 + \sin(z)z^2\pi^4 + \\ + 4\sin(z)\pi^4 - 4z\pi^4 - 4kz^3\pi^2 \quad . \tag{50}$$

Values of parameter S depend on material parameters and geometry of the beam, as it can be seen from Eqs. (31) and (50). Function $f(z)$ is illustrated in Fig. 4, for the following values of these parameters: E = 21 000 kN/cm^2, δ = 0,2 cm, h = 4 cm, G_3 = 35 kN/cm^2, α = 0,0000125 1/^{0}C. Solutions of the illustrated function are S = 1,723153076; 6,8826688; 8,939108457; …, and minimal solution is S = 1.723153076, and minimal value of parameter s is s = 0,548496594.

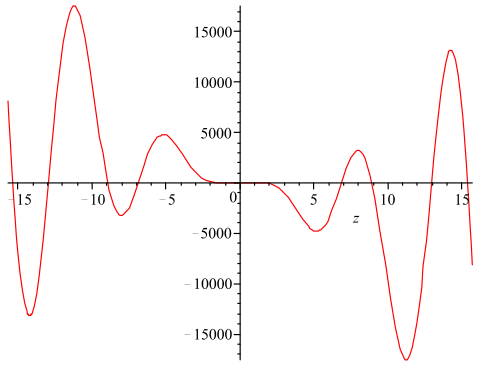

Figure 4. Function $f(z)$

Thence, equation for determination of the critical temperature minimal value, according to Eqs. (25), (31) and (36), is reduced to:

$$T_{cr} = \frac{3\varphi\pi^2(2h+\delta)^2}{2\alpha \cdot l^2\delta(1+c)} , \tag{51}$$

where coefficient c is related to the ratio of maximal temperature values on outer layers of the beam:

$$c = \frac{T_2}{T_1} . \tag{52}$$

Variation of the critical temperature T_{cr}, is illustrated in Fig. 5 for the coefficient values c = 0,1; c = 0,5; c = 0,9 and k = 0,1; k = 0,25; k = 0,5 determined according to Eq. (31). Lines a correspond to variation of the critical temperature minimal value for sandwich beam submitted to non uniform heating of outer layers and equal maximal temperature values (T_1 = T_2), and lines b correspond to the case of different maximal temperature values ($T_1 \neq T_2$). Lines c, in the same diagram, show the critical temperature variation for homogenous beam with bending stiffness $D = EH^3 / 12$ and cross section height $H = h + \delta$.

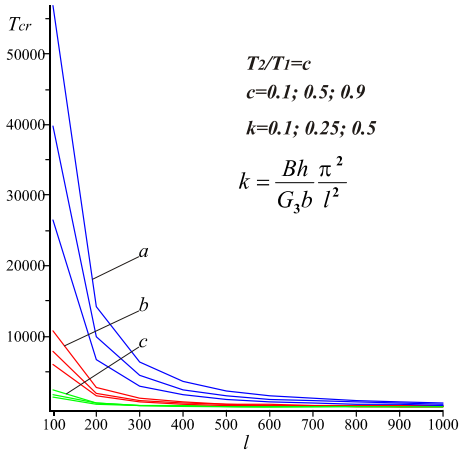

Figure 5. Critical temperature
a – sandwich beam, $T_1 = T_2$
b – sandwich beam, $T_1 \neq T_2$
c – homogenous beam

It can be seen that, in all three cases, critical temperature values are less different with increment of a beam length. For shorter beams these differences are higher. Critical temperature values for sandwich beam, with middle layer of high shearing stiffness ($G_3=\infty$, $k=0$), are not much different than critical temperature values for homogenous beam, as shown in Fig. 6.

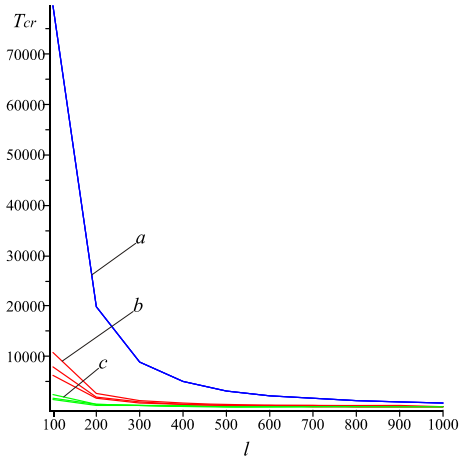

Figure 6. Critical temperature, $G_3 = \infty$
a – sandwich beam, $T_1 = T_2$
b – sandwich beam, $T_1 \neq T_2$
c – homogenous beam

Displacement components $u_\beta(\xi)$ i $w(\xi)$ of sandwich beam submitted to non uniform heating with critical temperature $T_1 = T_{cr}$ determined according to Eq. (51) are shown in Fig. 7 and Fig. 8.

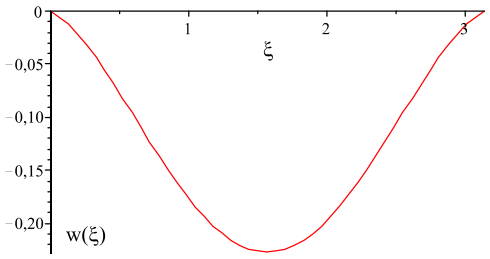

Figure 7. Sandwich beam deflection $w(\xi)$

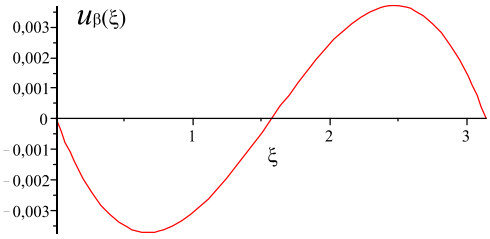

Figure 8. Displacement component $u_\beta(\xi)$

References

[1] Volimir S A (1963) *Ustoicivost uprugih system*, FM, Moskva.
[2] Grigolyuk E I and Culkov P P (1973) *Ustojcivost i kolebanija trehslojnih obolocek*, Masinostroenie, Moskva.
[3] Bezuhov N I and Lužin N V and Kolkunov N V, *Stabilnost i dinamika konstrukcija u primerima i zadacima* Prevod, Gradjevinska knjiga, Beograd.
[4] Vasic Z (1999) Application on a more accurate bending theory of a sandwich plate with light core, *Facta Universitatis*, **9**, .
[5] Vasic Z and Raičević V and Jović S (2005) Sandwich beam stability analysis application of sandwich constructions bending theory, *Facta Universitatis*, **19**, .

THE ANALYSIS OF CONTACT EFFECTS IN WIRE ROPE STRAND USING THE FINITE ELEMENT METHOD

N. Vidanović[1], G. Kastratović[2], A. Grbović[3]

[1] Faculty of Transport and Traffic Engineering,
The University of Belgrade, ul. Vojvode Stepe 305 11000 Belgrade
e-mail: n.vidanovic@sf.bg.ac.rs
[2] Faculty of Transport and Traffic Engineering,
The University of Belgrade, ul. Vojvode Stepe 305 11000 Belgrade
e-mail: g.kastratovic@sf.bg.ac.rs
[3]Faculty of Mechanical Engineering,
The University of Belgrade, Kraljice Marije 16, 11120 Belgrade
e-mail: agrbovic@mas.bg.ac.rs

Abstract. This paper discusses the problem of contact effects in wire rope strand subjected to axial loading, to be more specific, it explores how different types of contact affect the wire rope static behavior. The analysis was carried out by finite element method based computer program. The software used allowed three different types of contacts, including friction, and all of them were applied in this analysis. The wire rope was subjected to two different types of axial loading. The comparison of the obtained results was carried out on the parametric 3D model of 6x7 IWRC.

1. Introduction

High strength wire ropes are very important tensile structural members. Due to their flexibility and high strength, ropes are in widespread use throughout the mechanical, electrical, mining and naval engineer industries. Applications include lifts, suspension bridges, electrical power transmission, aircraft arresting cables, and mining equipment. It is well known that a major advantage of such elements is their capacity to support large axial load.

In order to predict the wire rope behavior, several theoretical models and analytical studies have been presented in the literature, [1, 2]. Most of them neglect frictional and contact effects, but there are some, that takes those effects into consideration.

As technology and computer sciences were developing and became more available, numerical analyses started to be frequently used in predicting the wire rope behavior.

One of the first finite element analysis of simple straight strand has been presented by Jiang et. al in [3].

Elata et. al [4] developed a new model for simulating the mechanical response of an IWRC.

Elasto-plastic contact problem of laying wire rope using finite element analysis has been presented in [5].

A realistic 3D structural model and finite element analysis of a simple wire strand has been briefly explained in [6], by Imrak and Erdonmez. The same authors presented 3D solid model and wire-by-wire analysis of IWRC in [7].

The frictionless contact effects in wire rope strand subjected to axial loading was analyzed in [8].

Some of the mentioned analyses ignored frictional effects, but there were some [3, 4, 6, 7, 8], that took those effects into consideration. However, analysis of other contact effects in IWRC was neglected in available literature. Also, all of them introduced axial loading as applied axial strain, except in [9] were authors used axial force which was evenly distributed between wires.
Because of these reasons and its complex geometry, it is still very difficult to model and analyze wire ropes, using numerical methods, such as finite element method. Also, this kind of analysis requires substantial computer resources.
Nevertheless, numerical analysis must be employed to provide a better understanding, and hence prediction, of the mechanical behavior of the wire rope strands, thus reducing the need for expensive tests (because of which the experimental results reported in the literature are very limited). In order to accomplish all of that, the aim of this paper was to explore some aspects of behavior of wire rope strand subjected to axial loading, using the finite element method based computer program. The special emphasis was the effect of different types of contact and different types of axial loading, regarding force distribution, on the wire rope static behavior.

2. Finite element model and analysis

Model of the wire rope considered here is shown in Figure 1. As it can be seen, the cross section of a wire rope consists of one simple, straight, seven-wire strand surrounded by six seven wire strands. Such cross section is often used as a rope core in a more complex rope and as such is sometimes called an independent wire rope core or IWRC. It is a member of complex wire ropes that carries the greatest amount of axial loading.

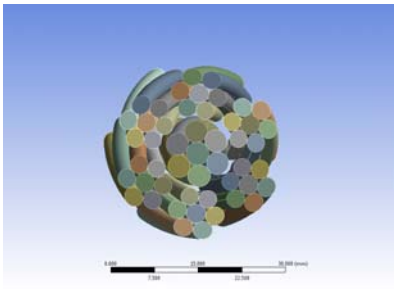

Figure 1. Cross section of IWRC.

A 3D finite element model of IWRC was created by using both CATIA and Ansys13 Workbench. First, the parametric geometrical model was created in Generative Shape Design mode of Catia. The obtained geometrical model was then imported to Ansys13 Workbench. This program allowed specification of material properties, application of loads, generation of finite element mesh, and contact definition as well as solving and obtaining necessary output data.

It is well known that very important issue in any finite element analysis is the element selection and mesh size. If the created mesh is too coarse then the problem may not converge due to increased time steps and there will be no solution. On the other hand, too fine mesh may cause similar difficulty because of large number of elements and nodes, i.e. large numbers of equations. This can also significantly increase computational time. So, several different 3D models were made, with different numbers of elements in order to obtain the optimal FEM model, regarding accuracy and computational time.
Finite element used for meshing all analyzed models was SOLID186, a brick solid element that is used in 3D modeling of solid structures, as default element.
The software used in this study allows two types of linear contacts, and both of them were applied in this analysis. Bonded contact is the default configuration of contact and applies to all contact regions (surfaces, solids, lines, faces, edges). If contact regions are bonded, then no sliding or separation between faces or edges is allowed, as if the bodies were *glued*.
No Separation contact setting is similar to the bonded case. It only applies to regions of faces (for 3-D solids) or edges (for 2-D plates). Separation of faces in contact is not allowed, but small amounts of frictionless sliding can occur along contact faces.
Also, frictional contact was available, and this nonlinear analysis was carried out, as well. In this setting, two contacting faces can carry shear stresses up to a certain magnitude across their interface before they start sliding relative to each other. It only applies to regions of faces. This state is known as "sticking." The model defines an equivalent shear stress at which sliding on the face begins as a fraction of the contact pressure. Once the shear stress is exceeded, the two faces will slide relative to each other. The coefficient of friction can be any non-negative value.
The axial loading behavior was analyzed, with two different load settings.

2.1. Axial loading by applying evenly distributed axial force

First, axial loading behavior was investigated by applying an axial force to the free end of the IWRC 6x7 wire rope, while the other end of the IWRC was fixed. The total force of 900 kN was applied in increments of 100 kN. The total force was evenly distributed between wires.
The IWRC 6x7 wire rope has been taken as an example. The core strand radius of center wire was r_1=1.97mm, and outer wire r_2=1.865mm, and pitch length 70mm; the outer strand center wire radius was r_3=1.6mm, and outer wire radius r_4=1.5 mm and pitch length 193mm. The overall length of the wire rope model was 18mm.
The model was meshed, and the prescribed boundary conditions (Figure 2) were used for solving. As mentioned, on one end of the model the degrees of freedom in all three directions were constrained, and on the other end the displacement in x and y directions were restrained to zero.

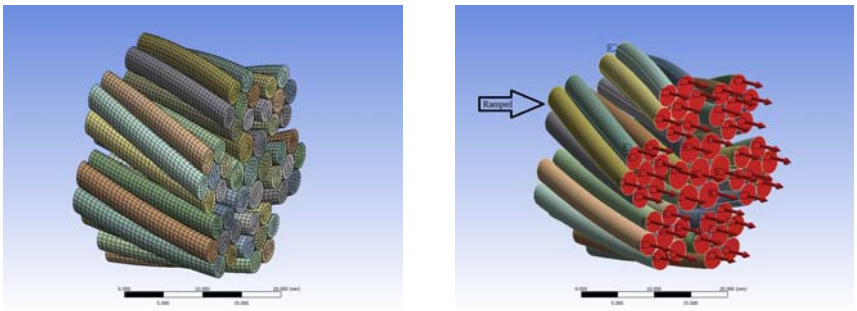

Figure 2. 3D Finite element model – mesh and boundary conditions

For two types of linear contacts elastic behavior was analyzed, were the modulus of elasticity was E=1.88e11 Pa, and was Poisson's ratio ν=0.3.

For model with frictional contact, nonlinear analysis was carried out. The additional IWRC material properties used in elastic-plastic analysis are defined as: the yield strength $R_{p0.2}$=1.54e9 Pa, tangent modulus E_t=2.46e10 Pa, ultimate tensile strength R_m=1.8e9 Pa, while the friction coefficient was μ=0.115.

The solutions were obtained for three different meshed models, also for 298683, 616646 and 1531845 numbers of nodes or 61166, 134925 and 341925 numbers of elements respectively, for two types of linear contact settings. For nonlinear model the solution was obtained only for 298683 number of nodes, because this type of analysis is time consuming and requires significant computer resources.

The solution calculated in this analysis was total deformation. The maximum deformation, i.e., strain occurs on the outer wire of outer strand (Figure 3) for all mashed models.

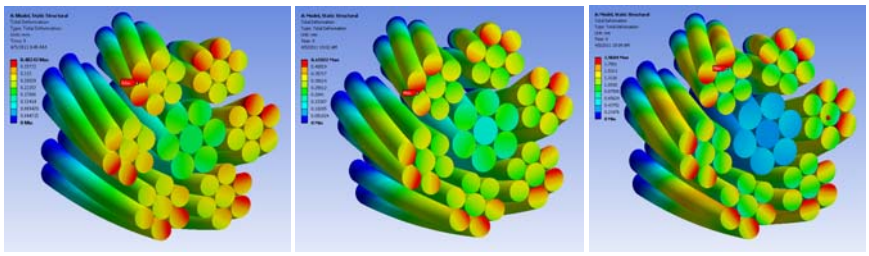

Figure 3. FEM solution-Total deformation

As mentioned, the numerical models were solved, and results are presented in the following diagrams.

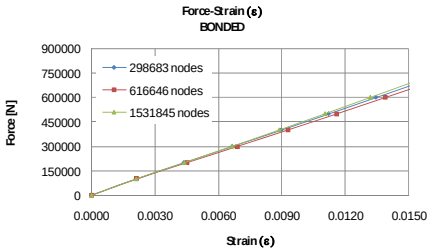

Figure 4. Diagram of axial force - BONDED

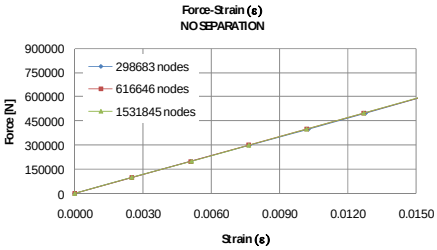

Figure 5. Diagram of axial force - NO SEPARATION

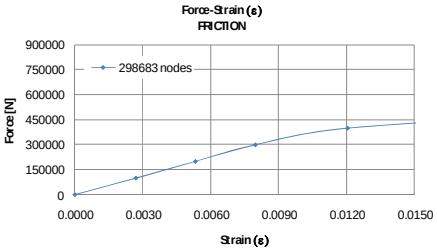

Figure 6. Diagram of axial force - FRICTION

The output data in this load case were axial strain, which was calculated for each individual wire. The applied forces are given as a function of maximal calculated strain. The maximum value of strain on the axis is 0.015 on all diagrams. This enabled comparison of the obtained results.

As it can be seen on first two diagrams (Figures 4, 5), there is no major difference between results obtained for different number of nodes, and that is the reason why the nonlinear model for this load case was calculated only for minimum number of nodes (Figure 6).

The following diagram (Figure 7) shows the solutions obtained for all three different types of contact for the meshed model with minimal numbers of nodes.

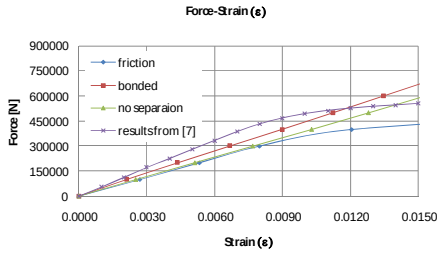

Figure 7. Diagram of axial force for three different types of contact

As it can be seen, there are rather good agreement between results in the elastic area, i.e. until value of resulting axial strain reaches 0.008. As the value of the applied axial force rises, the difference between obtained solutions becomes more significant.

2.2. Axial loading by applying unevenly distributed axial force

Also, axial loading behavior was investigated by applying unevenly distributed axial force to the free end of the IWRC 6x7 wire rope, while the other end of the IWRC was fixed. The total force of 900 kN was applied in increments of 100 kN.
The axial force distribution used in this analysis is simplified load distribution obtained from wire by wire analysis in [7], and it is shown in Table 1. When the loads are sorted according to those percentages, center wire of the core strand, labeled CCW (Figure 8), carries the major portion of axial force. The next layer of outer core wires (OCW) carries slightly lesser portion of axial force. Similar relation of axial force distribution exists in the outer strand. The outer strand wires (OSW) carry the smallest amount of applied axial force.

IWRC	**Axial force distribution**
Central Core Wire (CCW)	3.86%
Outer Core Wire (1 of 6) (OCW)	2.72%
Core Strand	**20.18%**
Strand Central Wire (SCW)	2.21%
Outer Strand Wire (1 of 6) (OSW)	1.85%
Outer Strand (1 of 6)	**13.30%**
Total	**20,18% + 6 x 13,3%=100%**

Table 1. Axial force distribution

If the axial load of the core strand is compared with the outer strand of the IWRC, core strand carries an average 20.18% while one of the outer strands carries an average 13.30% of the total axial load.

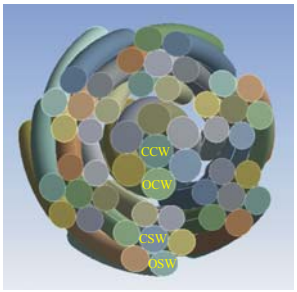

Figure 8. Wire labeling

The other applied settings for two linear contacts, and nonlinear frictional contact were the same as in previous analysis.
As before, the solutions were obtained for three different meshed models, for two types of linear contact settings. For nonlinear type of contact the solution was obtained only for model with 298683 number of nodes.
The solution calculated in this analysis, also, was total deformation. The maximum deformation, i.e., strain occurs, again, on the outer wire of outer strand (Figure 9) for all mashed models.

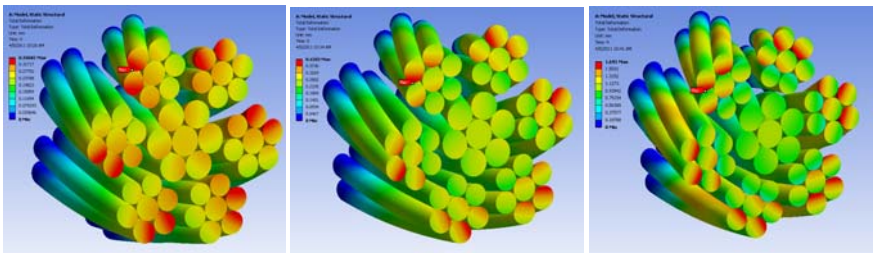

Figure 9. FEM solution-Total deformation

Again, results for solved numerical models are presented in the following diagrams.

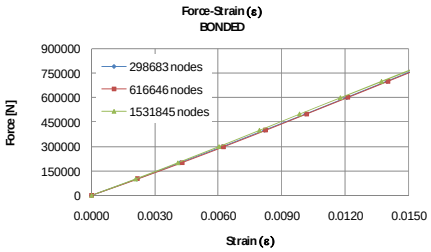

Figure 10. Diagram of axial force - BONDED

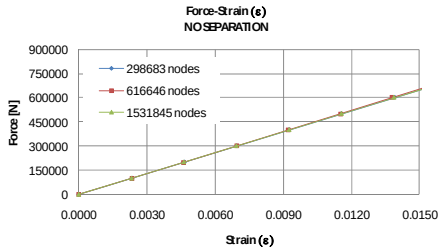

Figure 11. Diagram of axial force - NO SEPARATION

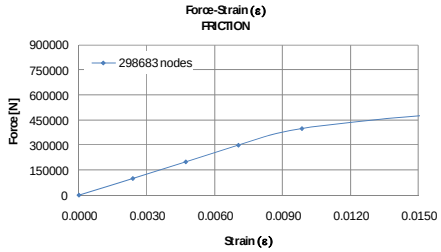

Figure 12. Diagram of axial force - FRICTION

As before, the output data in this load case were axial strain, which was calculated for each individual wire. The applied forces are given as a function of maximal calculated strain. As it can be seen on diagrams shown on Figures 10 and 11, there is excellent agreement between results obtained for different number of nodes, and that is the main reason why the nonlinear model for this load case was calculated only for minimum number of nodes (Figure 12).

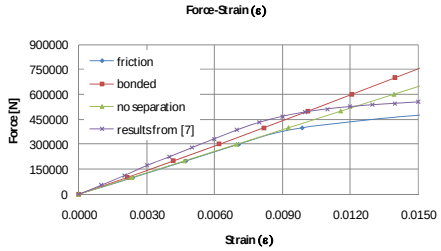

Figure 13. Diagram of axial force for three different types of contact

The diagram presented on Figure 13 shows the solutions obtained for all three different types of contact for the meshed model with minimal numbers of nodes.
As it can be seen, there is rather good agreement between results in the elastic area, i.e. until value of resulting axial strain reaches 0.008. Also, the agreement between results is better than in previous load settings.

3. Comparison of the results

The next diagram (Figure 14) shows the comparison between results obtained in two different load cases, to be more accurate, it represents the variation of axial force with axial strain for two load cases calculated in this analysis, and results from [7].

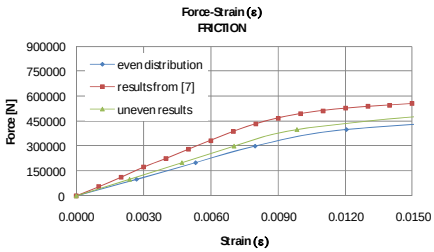

Figure 14. Variation of axial force with axial strain for two load cases

As it can be seen, there is good agreement of the results. The relative error between results from [7] and solution obtained for second load settings is about 10%, which could be quite acceptable from an engineering point of view. It can be concluded that improving of accuracy can be achieved by employing better axial force distribution. However, it is obvious that refining the mesh and increasing the number of finite elements will lead to enhanced accuracy.

4. Conclusion

Using commercial software, which is currently widely available, some aspects of behavior of wire rope strand subjected to axial loading were investigated, using the finite element method based computer program. The wire rope was subjected to two different types of axial loading, regarding force distribution. The two different types of linear contacts between wires were applied, as well as frictional contact. It is established that there is no major difference between solutions obtained for different node numbers, when linear contacts are consered. The obtained results in the case when the load was applied as evenly distibuted axial force, showed rather good agreements with the results from the literature that was available, especially in the elastic area. In the other load case, when the load was applied as unevenly distributed axial force, the agreement of the results was improuved. In both load cases it has been shown that linear type of contact is more than adequate in the elastic domain. However, in plastic area, frictional contact must be used, in order to achive acceptable accuracy. This analysis showed that suitable load distribution can be used to improuve results. This emphasis, once more, the significance of creating suitable finite element model of IWRC, in order to provide a better understanding, and hence prediction, of the mechanical behavior of the wire rope strands.

5. References

[1] Love A. E. H., A treatise on the mathematical theory of elasticity, *Dover Publications, 4th ed, Chapter XVIII-XIX*, (1944) New York, pp. 381-426.
[2] Costello G. A., Theory of wire rope, *Springer,* (1990), Berlin.
[3] Jiang W. G., et. al., A concise finite element model for three layered straight wire rope strand, *International Journal of Mechanical Sciences* Vol. **42**, (2000), pp. 63-86.

[4] Elata D., et. Al., The mechanical behavior of wire rope with an independent wire rope core, *International Journal of Solids and Structures*, Vol. **41**, (2004), pp. 1157-1172.
[5] Sun J. E. et. al., Elasto-plastic contact problem of laying wire rope using FE analysis*, Int J Adv Manuf. Technol.*, Vol. **26**, (2005), pp.17-22.
[6] Erdonmez C., Imrak C.E., Modeling and numerical analysis of the wire strand, *Journal of Naval Science and Engineering*, Vol. **5**, No.**1**, (2009), pp. 30-38.
[7] Erdonmez C., Imrak C.E., On the problem of wire rope model generation with axial loading, *Mathematical and Computational Application*, Vol. **15**, No. **2**, (2010), pp. 259-268.
[8] Kastratović G. and Vidanović N., The analysis of frictionless contact effects in wire rope strand using the finite element method, *Transport&Logistics*, Beograd, Vol. **19**, (2010) pp. 33-40.
[9] Kastratović G. and Vidanović N., Some aspects of 3D finite element modeling of independent wire rope core, *FME-Transaction*, Beograd, Vol. **39**, No **1**, (2011) pp. 37-40.

REQUIRED MECHANICAL PROPERTIES OF THE MATERIAL DURING CALCULATION OF MASONRY BUILDINGS IN SEISMIC AREAS

Slavko Zdravković[1], Tomislav Igić[2], Dragana Turnić[3]

[1] Ph D, full professor, Expert of the Federal Ministry of Sciece, Technology and Development, the Faculty of Civil Engineering and Architecture of Nis, Aleksandra Medvedeva 14. Niš, Serbia
e-mail: slavkozdravkovic@gaf.ni.ac.rs
[2] Ph D, full professor redovni profesor, The Faculty of Civil Engineering and Architecture of Nis, Aleksandra Medvedeva 14. Niš, Serbia
e-mail: tigic@gaf.ni.ac.rs
[3] Student at doctoral studies at GAF and research assistant at the University of Niš, Univerzitetski trg 2., 18000 Niš, Serbia
e-mail: draganaturnic@yahoo.com

ABSTRACT. Starting from the theoretical foundations of the structural dynamics we come to the equation for calculating the effects of seismic forces, while introducing at the same time certain simplifications that do not have a significant impact on its accuracy. Special attention is paid to the studying of the behavior of masonry buildings and their significance, since majority of such facilities are located in most rural and suburban areas, and they suffer mostly during earthquakes, which was also the case during Kraljevo earthquake. For the so-called "simple masonry buildings" direct evidence of safety is not required (EC8), which, in this case, has not proven justified. The regulations for the construction of high buildings in earthquake areas [31/81] say: Checking the resistance of masonry buildings is performed by: 1) the method of allowable stresses, when the tightening control of the main stresses in individual elements (walls) should not exceed the values given in Table 4. of the regulations manual, which also provides a form for their calculation, 2) in cases when the assessment is carried out in accordance to the Final element method, the resistance of buildings is compared to the total horizontal seismic force, in accordance to the Article 21, comprising the use of values for main tightening tension from the Table 5. of the regulations manual. As for the Eurocode 8, structural analysis and proof of safety depends on the computational model of the building. Elastic response spectra of ground acceleration represent the spectral envelope of different types of ground vibrations. Seismic hazard is described by only one parameter. Seismo-genetic characteristics define, in different countries, a large number of parameters, so that national organizations can adapt them according to their specific conditions.

Keywords: mechanical properties, masonry buildings, allowable stresses, final element method, calculation.

1. **Dynamic calculation of seismic forces**

1.1. Introduction

The theoretical approach to consideration of earthquake effects is the analysis of forced vibrations generated due to the displacement of subsoil, such as in the event of displacement of the soil on which rest foundations of a structure. Displacement of subsoil affects the structure as an external disturbance force, that is, the task is reduced to the analysis of forced vibrations of the dynamic system which modeled the observed structure. The dynamic calculation of structures in respect to the effects of seismic forces is carried out, as a rule, on the simplified mechanical models, using discretization of the created distribution of masses, whether by the set of the finite number of concentrated masses, or by the application of the finite elements method. Due to the complexity of the issue, no entirely adequate calculation method has been developed up to date, and the principal difficulty is predicting the character and intensity of an earthquake. Very strong earthquakes are rare, and precise seismological measurements were successful in a relatively small number of strong earthquakes. The other difficulty is that a realistic analysis of earthquake effects can be provided only if the behaviour of the structure outside the elastic area is taken into consideration. In earthquakes, plastic deformations are regular, thus it would not be cost-efficient to design the structures supposing they are completely elastic. However, analysis of a system with a large number of degrees of freedom in the plastic area, adjoined by an irregular and insufficiently certain nature of soil movement makes any accurate solution almost impossible. For this reason, in practice, this problem is reduced to a static problem, even though there are also tendencies to consider the structures in dynamical terms. The analysis of seismic effects is very successfully conducted by implementing the so called spectral theory where the dependency of maximum amplitudes of displacement, velocity, acceleration, stress etc. on the own frequency of the system is observed. In this manner the "response spectra" are obtained, showing the maximum amplitudes (of displacement, velocity, acceleration and other) of all the possible linear systems with one degree of freedom (fig. 1) in respect to some given cause, such as soil movement. The abscissae of such "spectrum" are characteristic of system frequency, and the ordinates are characteristic of maximum value of amplitudes. Therefore, the response spectrum indicates how a dynamic system reacts at various values characteristic for frequencies.

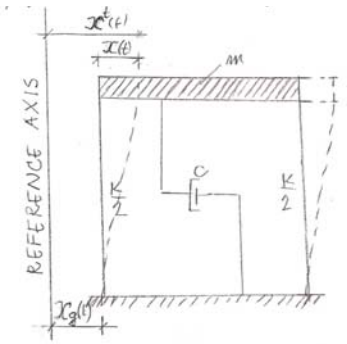

fig. 1. Dynamic model of the system with one degree of freedom

As already mentioned, the correct seismic calculation must include behaviour of the structure in the plastic area, so recently, the non-linear analysis methods are being progressively developed. Existence of contemporary automatic computers, enables development of such methods requiring very extensive calculation, but which much better describe the behaviour of a structure in earthquakes. Simultaneously with the theoretical approach, the experimental methods are developed, either on the models or the structures themselves, where the data required for evaluation of dynamic behaviour of a structure in earthquake are measured and recorded.

2. Determination of seismic forces

2.1. Forced vibrations of a system with one degree of freedom

In the case of the system with one degree of freedom (Fig.1.) the differential equation in the most general case is:

$$m\ddot{x} + c\dot{x} + kx = F(t). \tag{1}$$

It is the equation of forced damped vibrations, where (1), m is mass, c- damping coefficient, k- stiffness constant and F(t)- disturbing force. If F(t)=0, the vibration is free and with damping, and if c=0, there are free vibrations without dumping. For the solution of the equation (1) it is necessary to know the initial kinematic state, that is the initial velocity $v_0 = \dot{x}_0$ and initial displacement x_0. The force F(t), as it has been said, is an arbitrary disturbance force. The solution of the inhomogeneous equation (1) is equal to the sum of the general solution of the homogeneous par of equation (the so called left side) and the particular solution of the entire equation. In the first part of this solution, the influence of the initial conditions is reflected, and it can be laid down as:

$$x(t) = e^{-\xi\omega t}\left[x_0\left(\cos\omega_d t + \frac{\xi\omega}{\omega_d}\sin\omega_d t \right)\right] + \frac{\dot{x}_o}{\omega_d}\sin\omega_d t\,. \tag{2}$$

Where $\xi = \dfrac{c}{c_{kr}}$, is the ratio between the actual and critical damping, also called the relative damping, and ω_d is the frequency of damped vibrations, i.e. :

$$\omega_d = \omega\sqrt{1-\xi^2}\,. \tag{3}$$

If the damping is strong, i.e. $\xi \geq 1$, the system motion is aperiodic, there no vibrations.
The second part of the solution, the so called particular integral, can give as steady forced vibration which can be written as:

$$x_p(t) = \frac{1}{m\omega_d}\int_0^t F(\tau)e^{-\xi\omega(t-\tau)}\sin\left[\omega_d(t-\tau)\right]d\tau\,. \tag{4}$$

If there is no damping, the solution of a homogeneous part is given by the expression :

$$x(t) = x_0 \cos \omega t + \frac{\dot{x}_0}{\omega} \sin \omega t \tag{5}$$

And the solution of the steady forced vibration is:

$$x_p(t) = \frac{1}{m\omega} \int_0^t F(\tau) \sin[\omega(t-\tau)] d\tau \,. \tag{6}$$

This integral is very important in the dynamic analysis of structures and is called the Duhamel integral, or superposition integral, or convolution integral. Its value depends, of course, of time variable function F(t). The more accurate measure of the intensity of ground displacement can be obtained by observing the simple oscillator with one degree of freedom (fig.1.) which is exposed to moving ground xg(t).
In earthquakes, principally important are the vibrations generated due to the soil displacement. If the displacement is given by the function x(t), and if the new variable $x^t = x_g + x$, is introduced, then the differential equation is reduced to the form:

$$m(\ddot{x}_g + \ddot{x}) + c\dot{x} + kx = 0 \tag{7a}$$

$$m\ddot{x} + c\dot{x} + kx = -m\ddot{x}_g \tag{7b}$$

That is, the displacement of the subsoil here plays the role of the disturbing force having the value $-m\ddot{x}_g$, so the solution is:

$$x(t) = -\frac{1}{\omega_d} \int_0^t \ddot{x}_g(\tau) e^{-\xi\omega(t-\tau)} \sin[\omega_d(t-\tau)] d\tau \,. \tag{8}$$

For the system without damping it is:

$$x(t) = -\frac{1}{\omega} \int_0^t \ddot{x}_g(\tau) \sin[\omega(t-\tau)] d\tau \,. \tag{9}$$

Earthquakes can be treated as a system of vibration waves propagating through the ground from the place where the sudden displacement of earth mass occurred due to a certain tectonic disturbance. The impulse displacement disturbance propagates in all directions so the instruments can record displacement, velocity and acceleration. An accelerographic recording of three components of soil displacement would be the complete description of an earthquake, but from the standpoint of effects of earthquake on behaviour of the structure, the most important data are the amplitude, the frequent spectrum and duration.

2.2. Spectral analysis method

In Fig. 1. the system is exposed to soil displacement $x_g(t)$ and the displacement is expressed by the Duhamel integral which due to the disturbing force $F_{ef} = -m\ddot{x}_g$ has the form:

$$x(t) = \frac{1}{m\omega_d}\int_0^t (-)m\ddot{x}_g(\tau)e^{-\xi\omega(t-\tau)}\sin\left[\omega_d(t-\tau)\right]d\tau\,. \tag{10}$$

If here the approximation $\omega_d \approx \omega$, is adopted, that is, the frequency of vibrations with damping is substituted by vibrations without damping, and if the mark "-" is omitted, because it has no importance for the analysis of earthquake effects, for the Duhamel integral, the following expression is obtained:

$$x(t) = \frac{1}{\omega}\int_0^t \ddot{x}_g(\tau)e^{-\xi\omega(t-\tau)}\sin\left[\omega(t-\tau)\right]d\tau\,. \tag{11}$$

If for the measure of the earthquake intensity the maximum value of the system response (oscillator) is adopted, it can be written as:

$$x_{\max} = \frac{1}{\omega}S_v \tag{12}$$

Where:

$$S_v(\xi,\omega) = \left\{\int_0^t \ddot{x}_g(\tau)e^{-\xi\omega(t-\tau)}\sin\left[\omega(t-\tau)\right]d\tau\right\}_{\max}\,. \tag{13}$$

This parameter (13) is called the spectral pseudo velocity of soil displacement ω_g. It depends not only of the history of soil displacement, but also on the frequency of vibrations and relative damping of oscillator. Such spectra, for the various values of damping ξ are drawn in the form of adequate nomograms. In the similar manner, the spectral displacement:

$$x_{\max} = S_d = \frac{1}{\omega}S_v(\xi,T) = S_d(\xi,T) \tag{14}$$

and spectral acceleration are introduced:

$$S_a = \omega S_v = \omega^2 S_d\,. \tag{15a}$$

It can also be defined pseudo range rate S_{pv} and pseudo acceleration $S_{pa.}$

$$S_{pv} = mS_d \qquad S_{pa} = \omega^2 S_d = \omega S_{pv} \tag{15b}$$

These spectra are characteristic functions of frequencz and damping

$$S = S(\omega,\xi)$$

The spectral acceleration is the measure for maximum elastic force of the oscillator

$$\left(f_s\right)_{\max} = kS_d\left(\xi,T\right) = m\omega^2 S_d\left(\xi,T\right) = mS_{pa}\left(\xi,T\right). \tag{16}$$

$$\ddot{x}^t \approx S_a\left(\xi,T\right). \tag{17}$$

The mentioned spectra are basic characteristics of an oscillator when soil is displacing, that is, also the characteristics of a structure in earthquakes. These spectra are valid only in linearly-elastic area, because the Duhamel integral is valid only for such areas. The response spectrum can be applied only with modal analysis.

According to previous statements, the theoretical basis of the structural design, complying to our regulations, utilize the application of spectral analysis, at which the static influences required for further calculation of the structures (moments, transversal forces) are obtained. These influences are added to the existing load of the structures as an additional load for the definitive static design. In our country, the calculation according to the standing rules for determination of seismic forces is obligatory, and there it is precisely specified what forces in the calculation are combined with the action of seismic forces. It is assumed that the seismic forces act on the structure in horizontal planes in an arbitrary direction. For high-rise buildings, it is assumed that the forces act at the level of ceilings. The calculation is, as a rule, carried out for two orthogonal directions, separately for each one. The effects of vertical components of seismic forces should be taken into consideration, especially in those structures where such action could generate a significant increase of load, or endanger their stability.

A particularly important point in analyzing the earthquake effects is interaction of the foundation soil and the structure. When there is no structure, in earthquake the soil can move freely. But a structure by virtue of its movement, causes additional movement of soil. In order to process the problem mathematically, the finite elements method is successfully employed, where the soil and the structure are modeled according to the existing geometry and mechanical characteristics of such heterogeneous media.

In practice, often the character of an earthquake is obtained from the recorded accelerogram, i.e. it is known that the time dependency of acceleration in earthquake is known. In this case, a dynamic analysis of the structure is conducted, in a way that the disturbing force for all masses is this function of acceleration a(t) multiplied with a corresponding mass m_k, applying the method of vibration propagation according to characteristic forms when the systems with multiple degrees of freedom are in question. The latest research and observations of earthquakes indicated that here were very severe damage and demolition even of those structures that had been properly designed to withstand the action of seismic forces. The reasons lie in the fact that the nature of earthquakes is still not sufficiently researched, and also in the fact that the behaviour of the structures in post-elastic area has not been sufficiently explained. Nowadays it is known that he actual seismic forces in the structure calculated on the basis of the theory of elasticity are at times 5-6 times bigger than the predicted ones, calculated according to the regulations. However, the structures withstand such stresses, as they absorb a certain amount of received kinetic energy through its ductility and adapt in the plastic area to the action of such generated great force. Therefore, the correct calculation of structures should equally observe the necessary stiffness and ductility. The ductility factor comprises the relation between the maximum elasto-plastic displacement and displacement on the limit of yield.

By its nature, the earthquake is the phenomenon which, by many parameters has a probabilistic character. These are the disturbing forces which are stochastically (randomly) variable in time, so the analysis must be based on the theory of mathematical statistics and probability theory.

3. Design and calculation of seismically resistant masonry buildings according to Eurocode 8 (EC8)

3.1. Basic mechanical characteristics of non-reinforced walls

Mechanical characteristics of non-reinforced walls which are important for design of compressive strength (*f*), shear strength (f_v) and bending strength (f_x)- are in principle determined by corresponding standard (experimental) research, serving for definition of the so called characteristic values of strengths. EC6, through the appropriate European norms, prescribes the testing procedures for the mentioned strengths, and when defining the characteristic values, it presents the conditions for fractal of 5 %. However, it also permits it to be determined on the basis of the expression (it primarily refers to the characteristic compressive strength, in the case of walls built using general purpose mortar):

$$f_k = K f_b^{0,65} f_m^{0,25} \left(N \big/ mm^2 \right).$$

Here the compressive strength f_b of the used element for building is normalized, and f_m is the compressive strength of mortar. The value of the constant *K*, on the other hand, in the observed case depends on the group to which the used building elements belong, then on the type of the wall and some other conditions (which is all precisely defined in EC6) and its range varies between 0,4 to 0,6.
For the walls built using the light mortars, EC6 provides the relations

$$f_k = K f_b^{0,65}$$

Providing that f_b cannot be higher than $15N/mm^2$, and $K=0,55\text{-}0,80$.
Characteristic wall shear strength is defined by EC6 through the expression:

$$f_{vk} = f_{vk0} + 0,4\sigma_d$$

Where f_{vk0} is the so called basic shear strength (for the case $\sigma_d=0$) and σ_d is the compressive stress in the wall. For the walls built using general purpose mortar, having streZa zidove izvedene primenom maltera opšte namene čvrstoće fvk0 definisani su tabelarno pri čemu mora da bude ispunjen uslov fvk≤0,065fb pri čemu fkv nikada ne može da bude veće od graničnih vrednosti u tabeli.

3.2. Design of seismically resistant masonry buildings according to EC8

The paper makes prominent the requirements formulated by Eurocode 8 with a view of the presentation of local soil conditions, and they are defined by relevant seismic parameters.
The elastic and design spectra were designed. For the structures built in seismic areas, in EC8 there are requirements that the structure must not collapse and the damage must be limited. The difference in the level of reliability was applied in classification of the

structures into various importance categories, marked as K_0 coefficient. Each importance category is assigned a corresponding importance factor g_t *(K0)*. In order to satisfy the mentioned requirements, one must allow for the limit state, bearing capacity, and ensure that the structure possess the prescribed resistance and ductility, check the structural stability to toppling and sliding, as well as of the foundation and foundation soil the limit state of serviceability refers to checking and limitation of characteristic deformations, such as the relative displacements of floors etc. The construction site location and the nature of the foundation soil should be such so as there is no risk of soil failure, slope instability and permanent settlement caused by liquefaction or densification in the event of earthquakes. In the framework of EC8, the classification to A, B and C categories, from good to weak soil, was done.

EC8 provides for the division of national territories into seismic areas depending on the local hazard, and it is constant within this zones and described via one parameter, that is via the value of effective maximum acceleration of soil at the level of bedrock or solid soil, which is called the design acceleration of soil a_g. The design acceleration of soil for each seismic zone is adopted by appropriate national institutions, and it corresponds to the relevant return period of $\|475\|$ years. If the design acceleration a_g is not higher than $\|0{,}10\|$ g those are low seismic activity zones. Earthquake action in EC8 is presented in principle by the elastic spectrum of soil acceleration response. As a reference return period, EC8 defines elastic spectra of response $S_e(T)$ for the masonry buildings by a relation

$$0 \le T \le T_B \Rightarrow S_e(T) = a_g S\left[1 + \frac{T}{T_B}\left(\eta\beta_0 - 1\right)\right] \tag{18}$$

Where $S_l(T)$ is the ordinate of elastic spectrum of response, T is the period of vibrations of the linear system with one degree of freedom, a_g is the design acceleration of soil for the reference return period, β_0 is the factor of amplification of spectral acceleration for 5% of viscous damping, T_B is the limit of the interval of constant spectral acceleration and S is the soil parameter. The corrective factor of damping is $\eta = \sqrt{7/(2+\xi)} \ge 0{,}7$, where ξ is the value of viscous damping of structure in percents. Elastic response spectra in EC8, s it is presented represent the envelope of spectra of various types of soil oscillations which have not been mentioned here. due to a great discrepancy in seismic hazard and seismo-tectonic characteristics in the variety of member states, earthquake action was defined via a sufficiently number of parameters whose numerical values are given only as indicative, so the national organizations in each member state can adapt the earthquake effects according to their specific conditions.

The design spectrum is obtained by modification and reduction of the elastic spectrum of response, and it is a non-dimensional parameter which represents the total seismic parameter for horizontal direction (in analogy with the Code [3]).

According to our regulations, for the specific category of soil the form of the curve of this coefficient is relatively simple to define in the function of the system period, because it depends only on the dynamic coefficient K_d (the remaining parameters defining it are adopted). The design spectra are introduced with the goal to avoid the non-linearity of analyses, and in order to include the energy dissipation and ductile behaviour, the reduction is accomplished by introduction of the behaviour factor q. This factor q approximates the relation of seismic forces if its response would be elastic with 5% of viscous damping. For

the reference return period, the design spectrum $S_d(T)$ is defined by the following expression which would correspond to the masonry buildings:

$$0 \le T \le T_B \Rightarrow S_d(T) = \alpha S\left[1 + \frac{T}{T_B}\left(\frac{\beta_0}{q} - 1\right)\right] \tag{19}$$

Where $S_d(T)$ is the ordinate of the designed spectrum which is normalized with g, and with d is normalized the ratio of the design soil acceleration ag and the gravitational acceleration $(\alpha = a_g / g)$. The design spectrum is non-dimensional parameter, and represents, in fact, the total seismic coefficient for the horizontal direction K (in compliance with the definition [3]). The method of determination of seismic effects is simplified or multi-modal to the analysis (to which corresponds the method of equivalent load in the Code [3]). In this method, for each considered tone of vibrations, it is necessary to determine the appropriate shear force in F_{bi}, which is the result of multiplication of effective mass $m_{ef,i}$ and ordinate $S_{da}(T_i)$. The design spectrum of acceleration $S_{da}(T_i)$ is obtained when the design spectrum $S_d(T_i)$ is multiplied with the gravitational acceleration g :

$$S_{da}(T_i) = S_d(T_i)g \tag{20}$$

In our Code [3] the diagrams M, depending on the soil category are given.
The other approach to presentation of seismic action is via the intensity spectrum and time history, though in this case which entails the method of analysis of mechanical behaviour of the structure they are not necessary because it is needed to design a separate design spectrum for each specific structure, and they mostly relate to very significant structures, and the masonry buildings in the country and suburban districts are very similar and bear no importance for the application of direct dynamic analysis.

3. National regulations and numerical examples

The standing Code of technical standards for construction of high-rise structures in seismic areas, devotes twenty seven articles to masonry buildings. The code was put into effect in 1981, after the Temporary regulations of 1964. Formulation of new regulations was aimed at introducing new findings, to use the existing experiences and to simplify the calculation as much as possible. In the regulations, firstly was performed a detailed categorization of high-rise buildings, according to the importance degree K_0 (≥1,5-0,75). The Code was conceived in such manner so that he earthquakes of strongest intensity can cause damage, but not collapse of bearing structures, which in turn defines the degree of seismic risk. In the code further describes seismic activity and seismic parameters (coefficient of seismic activity K_s and dynamic coefficient K_d). In relation to this, a detailed categorization of soil is given as a basis for determination of seismic parameters. According to the code, the bearing structure analysis is carried out either according to the limit state theory, or the elasticity theory, thus to this aim the corresponding safety coefficients, maximum deflections, etc. have been prescribed. Seismic design of structures according to the Code is carried out either by the application of equivalent static load or dynamic analysis method.

3.1. Equivalent static load method

According to the standing Code (31/81) [3] the total seismic forces S is determined according to the expression (article 21)

$$S = KG \tag{21}$$

Where K is the total seismic coefficient for horizontal direction, and G is total weight of the structure and equipment. The total seismic coefficient for horizontal K is calculated according to he expression

$$K = K_0 K_s K_d K_p \tag{22}$$

Where in our case the designations are:
K_0 = 1,0, coefficient of the structure category ,
K_s = 0,100, coefficient of seismic intensity for 9°MSK-64,
K_d = 0,70/T, dynamic coefficient (II soil category)
K_p = 1,6, ductility and damping coefficient.
Limit values of coefficient K_d are: $1,0 > K_d > 0,47$.
According to the Code, verification of resistance of masonry buildings is carried out by the method of permissible stresses or limit state methods. the calculation of resistance of walls to shearing is obligatory. If the building's height and width are higher than 1,5 the walls are also checked to bending, on which occasion the permissible stresses for vertical load of walls according to technical norms for building walls are increased for 50%.
If the verification of resistance is performed according to the permissible stresses method, the main tensile stresses in certain elements (walls) are checked, whose values for certain types of walls must not exceed the values given in the table 4 of the Code.

3.2. Numerical example

In the considered case, for the solid brick wall (6×12×24cm)
M_0 100, MM 25, $\sigma_{n,doz}$=9N/cm^2
The principal tensile stresses in certain elements (walls) are calculated according to the formula:

$$\sigma_n = \sqrt{\frac{\sigma_0^2}{4} + (1{,}5\tau_0)^2} - \frac{\sigma_0}{2} \le \sigma_{n,doz} \tag{23}$$

Where:
τ_0- is the average shear stress in the wall element from the seismic action received by the elements .
σ_0- is the average stress in the wall element from vertical load,
$\sigma_{n,doz}$- is the permitted main tensile stress.

$$\sigma_n = \sqrt{\frac{39{,}242^2}{4} + (1{,}5 \times 13{,}775)^2} - \frac{39{,}242}{2} = 8{,}873 N/cm^2$$

$$\sigma_n = 8{,}873 N/cm^2 < \sigma_{n,doz} = 9{,}0 N/cm^2$$

which satisfies the required condition.
Should the verification of the resistance is performed according to the limit state method, what is compared is the resistance of the structure with the total horizontal seismic force according to he article 21 of this code, when the safety factor is no less than Y=1,5. The resistance of the wall element is calculated according to the formula:

$$\tau_0 = \frac{\sigma_{n,rus}}{1{,}5} \sqrt{1 + \frac{\sigma_0}{\sigma_{n,rus}}} \tag{24}$$

Where:
$\sigma_{n,ruš}$ – is the main tensile stress in the wall at demolition, whose values for the individual types of walls are given in the table 5 of the code, and concretely $\sigma_{n,ruš}$ is: for solid brick (6×12×24cm) M_0 100, MM 25, $\sigma_{n,ruš}$=18,0N/cm^2

$$\tau_0 = \frac{18}{1{,}5}\sqrt{1+\frac{39{,}242}{18{,}0}} = 21{,}40 N/cm^2$$

$$\tau_0 = 21{,}40 N/cm^2 > \sigma_{n,ruš} = 18{,}0 N/cm^2$$

which satisfies the required condition.
If the building walls are made of material (blocks, mortar), for which the values of permissible and failure main tensile stresses are not given in the tables 4 and 5 (there are 5 types of walls) these stresses are determined on the basis of the results obtained through experimental research.

4. Conclusion

Due to the action of earthquake, the structure foundation may move, caused by the movement of the foundation soil. Dynamic calculation of the structure in respect to the effects of seismic forces is, as rule, reduced to a simplified mechanical model, using the discretization of actual distribution of masses. Aseismic engineering represents a number of contradictions and opposites for which an appropriate compromise must be found, that will not be at the expense of safety of people and property. Due to the complexity of the issue, no entirely adequate calculation method has been developed up to date, and the principal difficulty is predicting the character and intensity of an earthquake. The other difficulty is that a realistic analysis of earthquake effects can be provided only if the behaviour of the structure outside the elastic area is taken into consideration, which is very complicated even when contemporary computing machines are used. All this also applies to the design of masonry buildings with their mechanical characteristics, which are unfavorable for this type of effects. Due to their great stiffness, that is, small deformations and considerable dead weight, the masonry buildings attract large seismic forces which due to their low ductility, resilience and damping, they are not able to receive and transfer, so they prevalently sustain damage from the shear stress. Unfortunately, brick is among the most widespread material in our parts, particularly in the country and suburban areas and it must by taken into account. Connecting of vertical and horizontal ring beams a s well as connecting of bearing and partition walls via floor slabs is very important for the aseismic behavior of the structure as whole, and its individual elements.
Determination of design seismic forces is based on the analysis of forced vibrations of the system with one or more degrees of freedom. The most employed theory, both worldwide and nationwide is the spectral theory, which represents the basis both international and national regulations for design of structures to withstand earthquake effects. The essence of the procedure applied in the systems with one degree of freedom, that is, the spectra of responses by definition represent the maximum response of the system depending on the nature of the system and of the damping, for a specific dynamic load. Apart from the elastic, there are also non-elastic spectra of response, design spectra, standardized design spectra for various categories of soil, in the function of damping and the period, spectra of strength (EC8), furrdevo spectra, as well as other types of spectra. Also, the design accelerograms are used, and determination of design earthquake loads, etc.

In our Code as well as in EC8 it is specified that the structure must not collapse and that the damage must be limited. In order to satisfy the mentioned requirements, the limit states of bearing capacity must be verified (resistance, ductility, stability, toppling, sliding, foundation and foundation soil), and the limit state of serviceability (deformation, floor displacement, etc.).
According to our Code [3] the check of masonry buildings is performed by: the methods of permissible stresses when the main tensile stresses in walls are controlled, and which are given in the table 4 of the code, and according to the limit states method, when the resistance of the structure with the total seismic force is compared, and the corresponding stresses of collapsibility are given in table 5 of the code.
Nevertheless, the preventive protection is the best form of protection of human lives and property, given it is harmonized with the level of development and future needs of a society. Aseismic engineering, as an important component of civil engineering and designing, undergoes an intensive development. If the status of technical regulations in the field of seismic is considered, it can be perceived that it is being intensively improved, both world and nationwide, as a number of Codes and Technical Standard Regulations have been enacted in this area in the recent years.

References

[1] Brčić V (1977) Osnovi dinamičkog proračuna seizmičkih uticaja, *Savetovanje „Izgradnja objekata na seizmičkim područjima“*, Partizantske Vode, str. 143-180.
[2] Clough R W, Penzien J (1975) Dynamics of Stuctures, *Mc. Graw-Hill*, New York.
[3] Pravilnik o tehničkim normativima za izgradnju objekata visokogradnje u seizmičkim područjima, *Sl.list SFRJ br. 31 od 5.VI 1981.*, Beograd.
[4] Liu Hui-Xian, Yang Yu Cheng (1980) Behavior of brick masonary buildings during destructive earthquakes, *Institute of Engineeging Mechanics Chinese Academy of Sciences, Chine, International research conference on Earthquake engineering,* Skoplje, Yugoslavia, pp. 393-404.
[5] Lađimović Đ, Folić R (1997) Zidane zgrade, okviri sa zidanim ispunama i montažne betonske konstrukcije, *Fakultet tehničkih nauka Novi Sad, Evrocodovi, posebna izdanja EC5-EC8,* Beograd, str. 135-150.
[6] Turnešk V, Sheppad P (1980) The shear and flexural resistance of masonary walls, *Institute for Structures Ljubljana, International research conference on Earthquake engineering,* Skoplje, Yugoslavia, pp. 517-579.
[7] Brčić S, Lađimović Đ (1997) Seizmička dejstva pema EC8, *Građevinski fakultet Beograd, Tehnički fakultet Novi Sad, Evrocodovi, posebna izdanja EC5-EC8,* Beograd, str. 101-114.
[8] Milićević M, Zdravković S (1985) Oštećenja na objektima posle Skopskog i zemljotresa na Crnogorskom zemljotresu, *Zbornik radova, Građevinski fakultet u Nišu, br. 6,* Niš, str. 375-388.
[9] Zdravković S (1986) Obezbeđenje zgrada od seizmičkih razaranja, *V Naučni skup, FZNR,* Niš, str. 17-26.
[10] Muravljov M (1995) Evrokod 6: Proračun zidanih konstrukcija, *Građevinski fakultet Beograd, Evrokodovi, generalna izdanja,* Beograd, str. 249-274.

DESIGN OF SYSTEMS WITH SEMI-RIGID CONNECTIONS BY DEFORMATION METHOD ACCORDING TO THE SECOND-ORDER THEORY

D. Zlatkov[1], S. Zdravković[2], T. Igić[3], B. Mladenović[4]

[1] Faculty of Civil Engineering and Architecture,
The University of Nis, Aleksandra Medvedeva 14, 18000 Nis
e-mail: dragan.zlatkov@gmail.com
[2] Faculty of Civil Engineering and Architecture,
The University of Nis, Aleksandra Medvedeva 14, 18000 Nis
e-mail: slavko.zdravkovic@gaf.ni.ac.rs
[3] Faculty of Civil Engineering and Architecture,
The University of Nis, Aleksandra Medvedeva 14, 18000 Nis
e-mail: tigic@gaf.ni.ac.rs
[4] Faculty of Civil Engineering and Architecture,
The University of Nis, Aleksandra Medvedeva 14, 18000 Nis
e-mail: mbiba@gaf.ni.ac.rs

Abstract. Structures in which the connections are not absolutely rigid, but allow some relative rotation of the cross sections at the ends of a member, are the systems with elastic, i.e. semi-rigid connections. Having in mind that such connections are quite common in constructions, especially in the precast ones, it is of interest to consider their design taking into account the elasticity of joint connections. Review of the design using Deformation method, with detailed derivation and explanations, is given by M. Djuric, M. Milicevic and S. Zdravkovic in their papers [1], [2]. Here, the method will be briefly presented with the necessary terms for its practical application. The numerical example of calculation of the influences in a simple structure with semi-rigid connections according to the second order theory, the critical load and buckling length of the members, is given in the paper with corresponding analysis. On the base of author's detailed study it is concluded that the degree of rigidity of connections is of special importance for precast structures, as well as for earthquake-damaged structures where connections become semi-rigid due to earthquake action. Knowing that a small change of the connection rigidity significantly affects the redistribution of static and deformation values, this must be given adequate attention, as in Euro codes, because it affects the safety and security, as well as the cost of the structure.

Keywords: semi-rigid connection, The deformation method, The second-order theory, critical load, buckling length.

1. Introduction

In the case of the optimal dimensioning of real structures there is a need to take into account the elasticity of joint connections in the design, i.e. real rigidity of the connection. The structures with elastic (semi-rigid) connections are the systems where connections between members are not absolutely rigid, but generally allow some relative flexibility in the direction of generalized displacements, which for the linear in plane element means: horizontal and vertical displacement and rotation of the end cross sections in joints. It was

observed that the level of rigidity of connection is of special importance for precast and earthquake-damaged structures, where it affects the redistribution of static and deformation values, critical load, buckling length and the basic dynamic characteristics of structure. European regulations, i.e. Eurocodes for structures (in particular Eurocode 3, 4 and Eurocode Eurocode 8), take due account to the design and construction of systems with semi-rigid connections.

The basic ideas of deformation method originating from the end of the twentieth century when, at the suggestion of Professor Asimont's Munich Technical High School announced a competition to find methods of analyzing trusses with rigid joints. The award went to H. Manderla and this method is basically known as an accurate method of deformation. Otto More, solving this problem approximately (1892), neglecting the effect of normal forces on the deformation of beam, gave a method known as the approximate method of deformation. Further development in the direction of simplification was made by K.A. Čališev, and continued by Hardy Cross (1930) who applied the infinite series for finding of finite values of the actual end moments. Kani's procedure followed, so that he has obtained bending moments as limits of infinite sequences. Significant contribution to the further development of deformation method for the calculation of frames according to the theory of the second order and to the solution of the problem of stability of structures was given by M. Djuric [1]. Deformation method is a contemporary method of the theory of structures and is now its main method.

Wilson, Moore and Batho have also contributed to the development of design of structures with semi-rigid connections since 1917 by experimental tests on steel structures. Similar tests were performed during the 1930th by Rowan and Rathbun, and Monforton and Wu (1963). Russian scientist Denkevič (1967) has occupied himself with the calculation of reinforced concrete frames with semi-rigid connections, while Lionberger and Weaver (1969), Lightfoot and Le Messuvier (1974), Batizan (1978) and the Russian Shapiro (1974) have continued.

COST C1 project contributes to creating the necessary new knowledge about the behavior of joints in order to improve design, safety and economy of structures, and to develop and integrate approaches in design of semi-rigid connections by organizing symposia.

The economic studies have shown that regardless of the material the savings are between 5% and 20% of the total construction cost, which is not negligible.

2. Design according to the second order theory

2.1. The basic design assumptions

Linear statics of structures, which is applied in everyday engineering practice, is based on the following assumptions:

a) Strains ε in the member axis, rotation of the cross-sections φ and their derivatives are small sizes, whose squares and higher powers can be neglected (the assumption of small deformations).

b) Displacements of the points of application of external and internal forces are small compared to the basic dimensions of beams, and that the conditions of equilibrium can be established on undeformed system configuration (assumption of small displacements of the points of application of external and internal forces);

c) The stress-strain relationship or temperature changes is linear (Hooke's law applies).

The first assumption provides the geometric, the second static, and the third physical or material linearity in solving the problems of statics of structures.
The equilibrium between internal and external forces, however, really is established on the deformed configuration of the system and consequently equilibrium conditions are nonlinear. Relationships between strains and displacements in the rigorous formulation are also nonlinear.
The special forms of general nonlinear theories may be obtained by introducing additional assumptions in general theories of material and geometrical nonlinearity, such as The theory of plasticity in the field of material nonlinearity, and The second-order theory in the frame of geometrically nonlinear analysis. These theories are of particular practical importance in analyzing the behavior of civil engineering structures. In this paper briefly will be presented the design according to The second-order theory, which is particularly important in solving the problem of stability of structures.

2.2. Design of the system with rigidly fixed members according to The second order theory

Strain state of the straight beam before and after deformation (Fig. 1.), can be described by the angle of rotation of the beam and deformation angles at the ends of the beam in all analog as well as in The first order theory,

$$\tau_{ik} = \varphi_i - \psi_{ik}; \qquad \tau_{ki} = \varphi_k - \psi_{ik} \tag{1.a, b}$$

based on the principle of superposition, according to Fig.2. Expressions (1) can be written as:

$$\tau_{ik} = \alpha_{ik,o} + \alpha_{ik,\Delta t} + M_{ik}\alpha_{ik} - M_{ki}\beta_{ik}, \qquad \tau_{ki} = \alpha_{ki,o} + \alpha_{ki,\Delta t} + M_{ik}\beta_{ik} - M_{ki}\beta_{ik} \tag{2 a, b}$$

Where:

- α_{ik} and β_{ik} or β_{ik} and α_{ki} are deformation angles due to unit values of moments M_{ik} i M_{ki},

while

- $\alpha_{ik,o}$ and $\alpha_{ki,o}$ or $\alpha_{ik,\Delta t}$ and $\alpha_{ki,\Delta t}$ are deformation angles due to the loading or temperature differences Fig.2. All these values are determined by the second-order theory for the same value of normal force S_{ik} or the value ω by use of well-known method of initial parameters [2], [4].

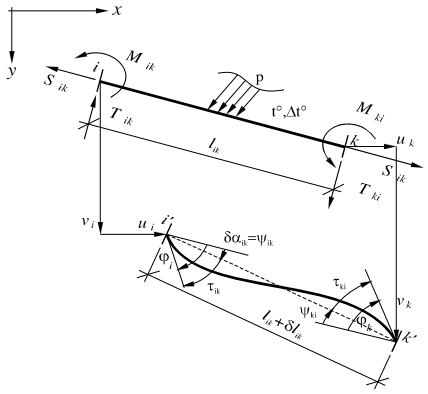

Figure 1. Straight beam before and after deformation

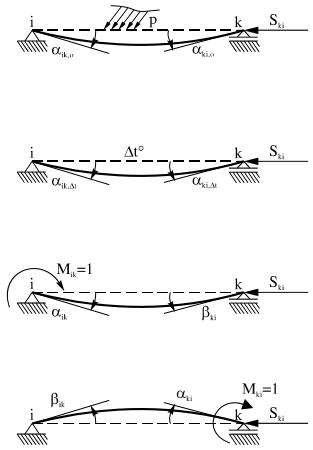

Figure 2. Deformation angles of the straight beam

If the following notation is introduced:

$$\omega = L_{ik}\sqrt{\frac{S_{ik}}{EI_{ik}}} \quad , \tag{3}$$

it is:

$$\alpha_{ik} = \alpha_{ki} = \frac{L_{ik}}{EI_{ik}}\overline{\alpha} = \frac{L_{ik}}{EI_{ik}}\frac{\sin\omega - \omega\cos\omega}{\omega^2\sin\omega} \quad , \quad \beta_{ik} = \beta_{ki} = \frac{L_{ik}}{EI_{ik}}\overline{\beta} = \frac{L_{ik}}{EI_{ik}}\frac{\omega - \sin\omega}{\omega^2\sin\omega} \tag{4}$$

The bending moments at the ends of a rigidly fixed beam, called beam of type ***k***, can be determined from (1) and (2) as:

$$M_{ik} = a_{ik}\varphi_i + b_{ik}\varphi_k - c_{ik}\psi_{ik} + m_{ik}\,, \qquad M_{ki} = b_{ik}\varphi_i + a_{ki}\varphi_k - c_{ki}\psi_{ik} + m_{ki} \tag{5}$$

For the beam of type ***g***, which is fixed at one end and hinged at the opposite, the moment at the end ***i*** is determined according to:

$$M_{ig} = d_{ig}(\varphi_i - \psi_{ig}) + \overline{m}_{ig} \tag{6}$$

In the second-order theory it is necessary to determine the expression for the moment at the end of the member of type ***s*** (cantilever) which in the first-order theory does not depend on the deformation of this member and is introduced in the calculation as a known value [4]. In the second-order theory, if the cantilever is loaded by normal force, the bending moment at fixed end depends on the deformation of the structure, that is on the rotation of the fixed end and it is determined according to:

$$M_{is} = e_{is}\varphi_i + \overline{\overline{m}}_{is} \tag{7}$$

In expressions (7) and (10) there are:

$$a_{ik} = \frac{EI}{\ell}\overline{a}; \quad \overline{a} = \frac{\omega\sin\omega - \omega^2\cos\omega}{2(1-\cos\omega) - \omega\sin\omega}; \quad b_{ik} = \frac{EI}{\ell}\overline{b}; \overline{b} = \frac{\omega^2 - \omega\sin\omega}{2(1-\cos\omega) - \omega\sin\omega}$$

$$c_{ik} = \frac{EI}{\ell}\bar{c}; \quad \bar{c} = \bar{a} + \bar{b} = \frac{\omega^2 - \omega^2\cos\omega}{2(1-\cos\omega) - \omega\sin\omega}$$

$$d_{ig} = \frac{EI}{\ell}\bar{d}; \quad \bar{d} = \frac{\omega^2\sin\omega}{2(1-\cos\omega) - \omega\sin\omega} \qquad e_{is} = \frac{EI}{\ell}\bar{e}; \bar{e} = -\omega tg\omega \tag{8}$$

so called beam constants according to the second-order theory.

Rotation angles (4), beam constants (8) and initial bending moments $m_{ik}, m_{ki}, \overline{m}_{ig} i \overline{\overline{m}}_{is}$, in expressions (5) to (7) depending of the $\boldsymbol{\omega}$ value given in (3) are, for example, presented in tables in [3], [4].

Since these considerations are based on the approximate method of deformation, where the influence of axial forces on the deformation is taken approximately, there are the same kind and number of deformation unknown values in the second-order theory as in the first-order theory. Number of deformation unknown values is (m+n), where m is the number of unknown angles of rotation of joints, and n number of independent parameters of displacement of the system truss. These values are determined from the m equations of rotation of joints and n equations of displacement, but according to M. Djuric [2], the work of distributed fictitious moments is added to the work of external load in the equations of displacement.

The equations of rotation are:

$$A_{ii}\varphi_i + \sum_k A_{ik}\varphi_k + \sum_{j=1}^{n} B_{ij}\Delta_j + A_{io} = 0, (i = 1,2,...,m)\ , \tag{9}$$

where notation is introduced:

$$\begin{aligned} A_{ii} &= \sum_k a_{ik} + \sum_g d_{ig} + \sum_s e_{is}\ A_{ik} = b_{ik}; i \neq k \\ B_{ij} &= -(\sum_k c_{ik}\psi_{ik,j} + \sum_g d_{ig}\psi_{ig,j})\ A_{io} = \sum_k m_{ik} + \sum_g \overline{m}_{ig} + \sum_s \overline{\overline{m}}_{is} \end{aligned}\ . \tag{10}$$

The equations of displacement are:

$$\sum_{i=1}^{m} B'_{ji}\varphi_i + \sum_{l=1}^{n} C_{jl}\Delta_l + C_{jo} = 0, (j,l = 1,2,...,n) \tag{11}$$

where:

$$\begin{aligned} B'_{ji} &= -(\sum_k c_{ik}\psi_{ik,j} + \sum_g d_{ig}\psi_{ig,j}) \\ C_{jl} &= \sum_{ik}(c_{ik} + c_{ki})\psi_{ik,j}\psi_{ik,l} + \sum_{ig} d_{ig}\psi_{ig,j}\psi_{ig,l} \mp \sum_{ab} \frac{EI_{ab}}{\ell_{ab}}\omega_{ab}^2\psi_{ab,j}\psi_{ab,l} \\ C_{jo} &= -\left[\sum_{ik}(m_{ik} + m_{ki})\psi_{ik,j} + \sum_{ig}\overline{m}_{ig}\psi_{ig,j} + R_j\right] \mp \sum_{ab}\frac{EI_{ab}}{\ell_{ab}}\omega_{ab}^2\psi_{ab,j}(\psi_{ab,t} + \psi_{ab,c}) \end{aligned} \tag{12}$$

In the equations (12) the upper sign refers to compressed members and the lower to tensioned members, while $\sum_{ab}$ means the sum of the members of type $\boldsymbol{k}$, type $\boldsymbol{g}$ and at the both ends hinged members.

2.3. Design of the structures with semi-rigid connections according to the second-order theory

This method is presented with detailed derivation of expressions and corresponding explanations by M. Milicevic and S. Zdravkovic in the works [5], [7]. Here the method will be briefly presented with the necessary terms for its practical application.

If one assumes that the level of rigidity of connection of the member *ik* in joint *i* is μ_{ik} and μ_{ki} in joint *k,* and rotations of the joints due to deformation are φ_i and φ_k, while member end cross-section rotations are φ_i' and φ_k'.

Bending moments M'_{ik} and M'_{ki} at the ends of the member with semi-rigid connections can be determined from the expression:

$$M'_{ik} = a_{ik}\varphi_i' + b_{ik}\varphi_k' - c_{ik}\psi_{ik} + m_{ik}^{(o)} + m_{ik}^{(\Delta t)} \tag{13a}$$

$$M'_{ki} = b_{ik}\varphi_i' + a_{ki}\varphi_k' - c_{ki}\psi_{ik} + m_{ki}^{(o)} + m_{ki}^{(\Delta t)} \tag{13b}$$

or in terms of φ_i, φ_k :

$$M'_{ik} = a'_{ik}\varphi_i + b'_{ik}\varphi_k - c_{IK}\psi_{ik} + m'^{(o)}_{ik} + m'^{(\Delta t)}_{ik} \tag{14a}$$

$$M'_{ki} = b'_{ik}\varphi_i + a'_{ki}\varphi_k - c'_{ki}\psi_{ik} + m'^{(o)}_{ki} + m'^{(\Delta t)}_{ki} \tag{14b}$$

Relations between well known beam constants, as well as initial moments, for members with semi-rigid connections of the first-order theory and new ones of the second-order theory are derived on the basis of their physical meaning shown in (Fig.3).

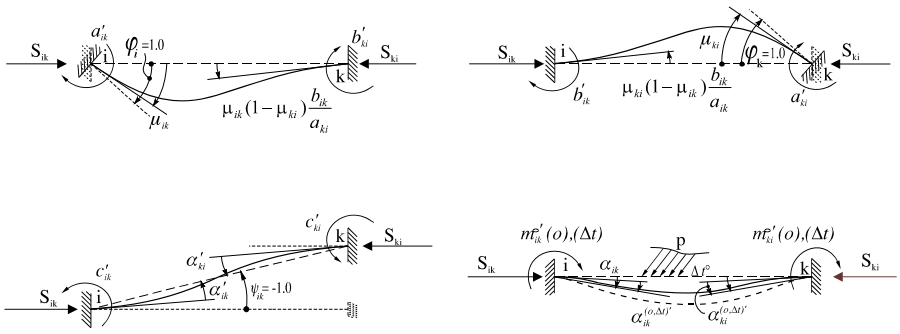

Figure 3. The physical meaning of beam constants and initial moments for members with semi-rigid connections

Deformation angles of the members with semi-rigid connections at the same value of normal force in this case can be also determined by the principle of superposition:

$$\alpha'_{ik} = \mu_{ik} - (1-\mu_{ik})\mu_{ki}\frac{b_{ik}}{a_{ik}}; \qquad \alpha'_{ki} = \mu_{ki} - (1-\mu_{ki})\cdot\mu_{ik}\cdot\frac{b_{ik}}{a_{ki}} \tag{15}$$

$$\alpha'^{(o,\Delta t)}_{ik} = \mu_{ik}\alpha^{(o,\Delta t)}_{ik} - (1-\mu_{ik})\cdot\mu_{ki}\cdot\frac{b_{ik}}{a_{ik}}\alpha^{(o,\Delta t)}_{ik}$$

$$\alpha'^{(o,\Delta t)}_{ki} = \mu_{ki}\alpha^{(o,\Delta t)}_{ki} - (1-\mu_{ki})\cdot\mu_{ik}\cdot\frac{b_{ik}}{a_{ki}}\alpha^{(o,\Delta t)}_{ki}\ , \tag{16}$$

beam constants and initial moments for members with semi-rigid connections are:

$$a'_{ik} = \mu_{ik}\left[a_{ik} - (1-\mu_{ki})\frac{b_{ik}}{a_{ki}}b_{ik}\right], \qquad b'_{ik} = b_{ki}\cdot\mu_{ik}\cdot\mu_{ki} \tag{17a,b}$$

$$c'_{ik} = \mu_{ik}\left[c_{ik} - (1-\mu_{ki})\frac{b_{ik}}{a_{ki}}c_{ki}\right] \quad , \quad c'_{ki} = \mu_{ki}\left[c_{ki} - (1-\mu_{ik})\frac{b_{ik}}{a_{ik}}c_{ik}\right] \tag{17c,d}$$

$$a'_{ki} = \mu_{ki}\left[a_{ki} - (1-\mu_{ik})\frac{b_{ik}}{a_{ik}}b_{ik}\right]\ , \tag{17e}$$

$$m'_{ik} = \mu_{ik}\left[m_{ik} - (1-\mu_{ki})\frac{b_{ik}}{a_{ki}}m_{ki}\right], \qquad m'_{ki} = \mu_{ki}\left[m_{ki} - (1-\mu_{ik})\frac{b_{ik}}{a_{ik}}m_{ik}\right] \tag{17f,g}$$

$$M'_{ik} = \mu_{ik}\left[M_{ik} - (1-\mu_{ki})\frac{b_{ik}}{a_{ki}}M_{ki}\right], M'_{ki} = \mu_{ki}\left[M_{ki} - (1-\mu_{ik})\frac{b_{ik}}{a_{ik}}M_{ik}\right] \tag{17h,i}$$

As it could be seen, here the beams of type *k* and type *g* are treated as a unique type *k* that is member with semi-rigid connections. From expression (17) it follows that for $\mu_{ik} = \mu_{ki} = 1$ the member is rigidly fixed at both ends, that is type k, and for $\mu_{ik} = 1; \mu_{ki} = 0$ the member is rigidly fixed in *i* and elasticaly in *k*, that is type g in the first order-theory. For $\mu_{ik} = \mu_{ki} = 0$ the member is hinged at its both ends. Cantilevers are also elastically fixed in joints. All constants of members are to be determined depending on the value of normal force in the member by use of expressions (8).

The bending moments at the ends of the member M'_{ik} and M'_{ki} can be determined from the expressions:

$$M'_{ik} = a'_{ik}\varphi_i + b'_{ik}\varphi_k - c'_{ik}\sum_{j=1}^{n}\psi^{(j)}_{ik}\Delta_j + m'_{ik} \tag{18a}$$

$$M'_{ki} = b'_{ik}\varphi_i + a'_{ki}\varphi_k - c'_{ki}\sum_{j=1}^{n}\psi^{(j)}_{ik}\Delta_j + m'_{ki} \tag{18b}$$

The equations of rotation and displacement look like:

$$\sum_k M'_{ik} + M_i = 0\,, \qquad \text{(i=1,2,...,m)} \tag{19a}$$

$$\sum_{ik}(M'_{ik} + M'_{ki})\psi^{(j)}_{ik} + R_j(p) + R_j(m^f) = 0\,, \qquad \text{(j=1,2,...,n)} \tag{19b}$$

where $R_j(m^f)$ is, similar as in [2], the work of fictitious distributed moments.

After some matematical transformations, the conditional equations (19) in the deformation method for the system with semi-rigid connections according to the second-order theory are obtained in the form:

$$A'_{ii}\varphi_i + \sum_k A'_{ik}\varphi_k + \sum_{j=1}^{n} B'_{ij}\Delta_j + A'_{i0} = 0 \qquad \text{(i=1,2,...,m)} \tag{20a}$$

$$\sum_{i=1}^{m} B''_{ji}\varphi_i + \sum_{l=1}^{n} C'_{jl}\Delta_l + C'_{j0} = 0 \qquad \text{(j=1,2,...,n)} \tag{20b}$$

where the folloing notation is introduced:

$$A'_{ii} = \sum_k a'_{ik} + \sum_s e'_{is}\,; \qquad A'_{ik} = b'_{ik}\,; \qquad A'_{i0} = \sum_k m'_{ik} + M'_i \tag{21a}$$

$$B'_{ij} = -\sum_k c'_{ik}\psi^j_{ik} = B''_{ji} \tag{21b}$$

$$C'_{jl} = C'_{lj} = \sum_{ik}(c'_{ik} + c'_{ki})\psi^{(j)}_{ik}\psi^{(l)}_{ik} \mp EI_c \sum_{ab}\frac{\omega^2_{ab}}{L'_{ab}}\psi^{(j)}_{ab}\psi^{(l)}_{ab} \tag{21c}$$

$$C'_{j0} = -\sum_{ik}(m'_{ik} + m'_{ki})\psi^{(j)}_{ik} - R_j(p) \mp EI_c \sum_{ab}\frac{\omega^2_{ab}}{L'_{ab}}\psi^{(j)}_{ab}(\psi^{(t)}_{ab} + \psi^{(c)}_{ab}) \tag{21d}$$

Unknown deformation values $\varphi_i (i = 1,2,...,m)$ and $\Delta_j (j = 1,2,...,n)$ are determined by solving the system of equations (20), and after that the bending moments at the ends of members with semi-rigid connections can be calculated according to (18).

Equations (20) can be presented in matrix form using the block matrices:

$$\begin{bmatrix} A' & B' \\ B'' & C' \end{bmatrix}\begin{Bmatrix} \vec{\varphi} \\ \vec{\Delta} \end{Bmatrix} = \begin{Bmatrix} \vec{A}'_{0_0} \\ \vec{C}'_{0_0} \end{Bmatrix} \tag{22}$$

The block matrix A' is square matrix of order *m* x *m*, block matrix C' is square matrix of order *n* x *n*, B' is rectangular matrix of order *n* x *m*, while B'' is transposed matrix B'. The vector of unknowns $\vec{\varphi}$ is of order 1 x *m*, and vector of unknowns $\vec{\Delta}$ of order 1 x *n*, as well as the vectors of free terms $\vec{A}_0$ and $\vec{C}_0$, respectively. The coefficients of these matrices are determined by expressions (21).

3. Determination of critical load

According to one definition given in [2], critical load is the smallest value of load for which a homogeneous system of equations of The second-order theory has at least one solution other than trivial. Homogeneous problem of The linearized second-order theory is given by the system of equations (20) or (22) when the free terms A_{i0} and C_{j0} are omitted, and shown in matrix form it is as follows:

$$\begin{bmatrix} A' & B' \\ B'' & C' \end{bmatrix} \begin{Bmatrix} \vec{\varphi} \\ \vec{\Delta} \end{Bmatrix} = 0 \tag{23}$$

The coefficients of these matrices are determined by expressions (21).

Necessary and sufficient condition of existence of nontrivial solution of the system of equations (23) is that its determinant is zero:

$$\det \begin{bmatrix} A' & B' \\ B'' & C' \end{bmatrix} = 0 \tag{24}$$

Equation (24) is the stability equation of the system with semi-rigid connections based on that, considering that here is the problem of eigenvalues, may be determined many values ω and thus the corresponding values of critical load parameter. Of course, the smallest value ω which determines the smallest value of load parameter is of the most practical importance.
In the works [5], [6], [7], [8] through numerical examples of frames with a simple structure values of bending moments, critical load and buckling length of members for different levels of rigidity of connections are calculated.

4. Numerical example

In order to illustrate the design of structures according to the above presented theory for the systems with semi-rigid connections, using technical method of deformation, the frame shown in Fig.4. is analyzed.

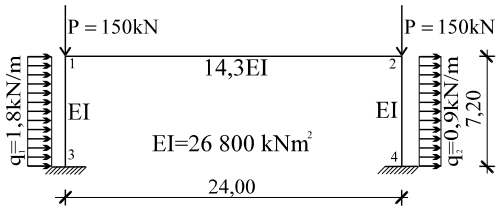

Figure 4. Frame with semi-rigid connections in joints

Given system is three times deformationaly indeterminate. Unknown are angles of rotation φ_1 and φ_2, as well as a displacement parameter of the system truss. State $\Delta_1 = 1$ of displacements of system truss is shown in Fig.5. A conditional equations for determining the unknowns can be shown in a matrix form:

$$\begin{bmatrix} A_{11}^* & A_{12}^* & B_{11}^* \\ A_{21}^* & A_{22}^* & B_{21}^* \\ B_{11}'^{*'} & B_{12}^{*'} & C_{11}^* \end{bmatrix} \begin{Bmatrix} \varphi_1 \\ \varphi_2 \\ \Delta_1 \end{Bmatrix} + \begin{Bmatrix} A_{10}^* \\ A_{20}^* \\ C_{19}^* \end{Bmatrix} = 0$$

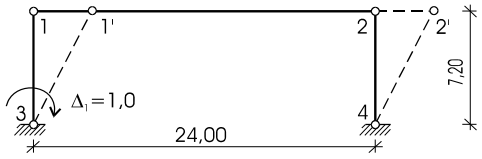

Figure 5. State of displacement of system truss

Design procedure for this frame is shown in details for the case when degree of fixing in joints 1 and 2 is $\mu_{13} = \mu_{24} = \xi = 0$, and in joints 3 and 4 $\mu_{31} = \mu_{42} = \eta = 0{,}95$.

4.1. The design of the frame according to the second-order theory

In the second-order theory coefficients $a_{ik}, a_{ki}, b_{ik}, c_{ik}, c_{ki}$, and moments m_{ik}, m_{ki} are defined according to (17). Based on the calculated normal forces according to the first-order theory and expression (3) it is:

$$\omega_{13} = \omega_{24} = 7{,}2\sqrt{\frac{150}{26800}} = 0{,}539$$

For the calculated values ω, based on Table 1 in [3], the following coeficients are determined:

$$\bar{a}_{12} = 4;\ \bar{b}_{12} = 2;\ \bar{c}_{12} = 6$$
$$\bar{a}_{13} = \bar{a}_{24} = 3{,}9610; \bar{b}_{13} = \bar{b}_{24} = 2{,}0098; \bar{c}_{13} = \bar{c}_{24} = 5{,}9708$$

Constants rigidly restrained members according to the theory of second order are:

$$a_{12} = \frac{4 \cdot 14{,}3EI}{24} = 2{,}383EI; a_{13} = a_{24} = \frac{3{,}9996EI}{7{,}2} = 0{,}555EI;$$
$$b_{12} = \frac{2 \cdot 14{,}3EI}{24} = 1{,}192EI; b_{13} = b_{24} = \frac{2{,}0001EI}{7{,}2} = 0{,}278EI;$$
$$c_{12} = \frac{6 \cdot 14{,}3EI}{24} = 3{,}575EI; c_{13} = c_{24} = \frac{5{,}9997EI}{7{,}2} = 0{,}833EI$$

Based on Table 8 in [3], the bending moments for rigid fixing are calculated according to the second-order theory:

$$m_{13} = -m_{31} = 0{,}08374 \cdot 1{,}8 \cdot 7{,}2^2 = 7{,}81kNm;$$
$$m_{24} = -m_{42} = 0{,}08374 \cdot 0{,}9 \cdot 7{,}2^2 = 3{,}90kNm$$

The bar constants for semi-rigidly fixed members according to the second-order theory are determined by expressions (17):

$$a'_{31} = a'_{42} = 0.95\left[0{,}555 - (1-0) \cdot 0{,}278\frac{0{,}278}{0{,}555}\right]EI = 0{,}395EI$$
$$c'_{31} = c'_{42} = 0.95\left[0{,}829 - (1-0) \cdot 0{,}278\frac{0{,}829}{0{,}555}\right]EI = 0{,}393EI$$

,

and the initial moments for semi-rigidly fixed members according to the second-order theory by (17f) and (17g):

$$m'_{31} = 0.95\left[-7{,}81-(1-0)\cdot 0{,}278\frac{7{,}810}{0{,}555}\right] = -11{,}17kNm$$

$$m'_{42} = 0.95\left[-3{,}90-(1-0)\cdot 0{,}278\frac{3{,}900}{0{,}555}\right] = -5{,}56kNm$$

Similar to the first-order theory, this system can be seen as once deformationaly indeterminate with an unknown displacement parameter Δ_1, which is determined from the equation:

$$C'_{11}\Delta_1 + C'_{10} = 0$$

According to (21c) it is:

$$C'_{11} = (0+0{,}393EI)1{,}0^2\cdot 2 - 2\frac{0{,}539^2 EI}{7{,}2} = 0{,}705EI$$

and (21d):

$$C'_{10} = -(0-11{,}17)\cdot 1{,}0-(0-5{,}56)\cdot 1{,}0-(1{,}8+0.9)\cdot 7{,}2\cdot 1.0\cdot 3.6 = -53{,}25$$

The nknown displacement parameter Δ_1 now is:

$$\Delta_1 = -C'_{10}/C'_{11} = 75{,}53/EI$$

(according to the first-order theory is $\Delta_1 = 67{,}53/EI$),

based on which, according to equations (18) the bending moments diagram is determined in accordance with the second-order theory, which is shown in Fig.6.

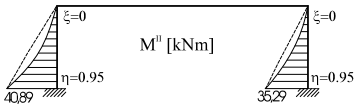

Figure 6. Diagram of bending moments in accordance with the second order theory

4.2. Determination of critical load and buckling length

For the purpose of determination of the critical load, the system shown in Fig.4. is replaced by an equivalent system (Fig.7.), where the intensity of uniformly distributed load is expressed by the load parameter P.

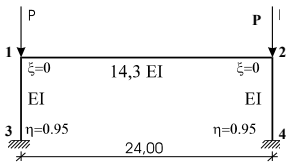

Figure 7. System equivalent to the system in Fig.4.

Based on the values of axial forces and expressions (3) defines the following:

$$\omega_u = \sqrt{\frac{P}{EI}}\,,\quad \omega_{12} = 0\,,\quad \omega_{13} = \omega_{24} = 7{,}2\omega \tag{a}$$

The system of Fig.7. is three times the deformation due to the vague but can be seen as once a strain vague, and according to (23) and (24) equation of stability in this case reduces to:

$$\det\left[C'_{11}\right] = 0$$

Based on (21c) equations of stability in this case is:

$$C'_{11} = (c'_{13} + c'_{31})\cdot 1{,}0^2 + (c'_{42} + c'_{24})\cdot 1{,}0^2 - (\omega_{13}^2 + \omega_{24}^2)\frac{EI}{7.2} = 0 \tag{b}$$

$$c'_{13} = c'_{42} = 0; c'_{31} = 0{,}95\left[c_{13} - (1-0)\frac{b_{13}}{a_{13}}c_{13}\right]; c'_{24} = 0{,}95\left[c_{24} - (1-0)\frac{b_{24}}{a_{24}}c_{24}\right]$$

$$a_{13} = \frac{EI}{7{,}2}\bar{a}_{13(0{,}539\omega)}; b_{13} = \frac{EI}{7{,}2}\bar{b}_{13(0{,}539\omega)}; c_{13} = \frac{EI}{7{,}2}\bar{c}_{13(0{,}539\omega)}$$

$$a_{24} = \frac{EI}{7{,}2}\bar{a}_{24(0{,}539\omega)}; b_{24} = \frac{EI}{7{,}2}\bar{b}_{24(0{,}539\omega)}; c_{24} = \frac{EI}{7{,}2}\bar{c}_{24(0{,}539\omega)}$$

Value of ω, for which the condition (b) is fulfilled, based on (a), determines the value of critical load:

$$P_{cr} + \omega_{cr}^2 EI$$

In the case of considered frame structure is:

$\omega_{cr} = 0{,}214$, and therefore

$P_{cr} = 0{,}0458EI = 0{,}0458 \cdot 26800 = 1227{,}44kN$.

and buckling length,

$$l_k = \sqrt{\frac{\pi^2}{P_{kr}}EI} = \sqrt{\frac{\pi^2}{0{,}0458EI}EI} = 14{,}68m.$$

5. Conclusion

The structures with elastic (semi-rigid) connections are the systems where connections between members are not absolutely rigid, but generally allow some relative flexibility in the direction of generalized displacements. The paper deals with plane frames that consist of straight members.

On the basis of performed analysis it can be concluded that the level of rigidity of connections should be taken into account in structural design. The relatively low level of rigidity of connections in precast structures and structures damaged due to earthquake can favorably affect the redistribution of bending moments, and this fact should be used when calculating, as accompanying measures are easy to achieve. Also, not enough secured but assumed rigid connections may have adverse consequences in the structural design. Depending on the physical and mechanical properties of materials used and the behavior of joint connections, i.e. on the flexibility of the system during the action of forces, the most often influences have to be calculated according to The second-order theory. This paper presents such calculation of influences by use of Deformation method and determination of the critical load and buckling length. In this way, more real behavior of the system is calculated, i.e. the behavior of structure in its deformed position. The detailed calculation of the structure in accordance with the second-order theory and the determination of critical load and buckling length is shown by presented numerical example, which is of special importance for practical use.

Acknowledgement. This research was conducted in the framework of the research in the field of technological development in the period 2011-2014, in the domain of Transport, town planning and civil engineering, project no. 36016, entitled Experimental and theoretical investigation of frames and plates with semi-rigid connections from the view of the second-order theory and stability, University of Nis, The Faculty of Civil Engineering and Architecture.

References

[1] Đurić M. (1965) Metoda deformacije, *Građevinarstvo 1*, Beograd, str. 1-30.
[2] Đurić M. (1977) Stabilnost i dinamika konstrukcija, Građevinski fakultet, Beograd, str. 1-131.
[3] Zdravković S. (1984) Stabilnost konstrukcija, *Zbirka rešenih zadataka sa izvodima iz teorije.*, Univerzitet u Nišu, Građevinski fakultet, str. 1-166.
[4] Čaušević M., Zdravković S. (1992) Statika i stabilnost konstrukcija po teoriji drugog reda, IP Svetlost, Sarajevo, str. 1-310.
[5] Zdravković S., Zlatkov D., Mladenović B., Mijalković M. (2009) Seizmic Analysis of Plane Linear Systems with Semi-rigid Connections, Earthquake Resistant Engineering Structures, *VII World Conference, ERES VII-Limasol,* Cypros, pp. 105-115.
[6] Milićević M., Zdravković S., Zlatkov D., Kostadinov-Mladenović B. (1998) Matrix Formulation of Design and Testing of Structures with Semi-Rigid Connection, *SEWC-Structural Engineering World Congress,,* San Francisko, California pp. 266, T 233-3.
[7] Zdravković S., Milićević M., Zlatkov D. (1996) Static and dynamic design of structures with semi-rigid connections, *ABSE Colloquium,* Istanbul, pp. 137-144.
[8] Zdravković S., Milićević M., Folić R., Zlatkov D. (1996) Significance and part of elastic connections of members with joints in earthquake engineering, *11 WCEE,* Acapulco, Mexico, pp. 626.

DYNAMICAL BEHAVIOR OF A POLYMER GEL DURING IMPACT. FRACTIONAL DERIVATIVE VISCOELASTIC MODEL

M. Žigić[1], N. Grahovac[2]

Faculty of Technical Sciences,
The University of Novi Sad, Trg Dositeja Obradovića 6, 21000 Novi Sad
[1]e-mail: mzigic@uns.ac.rs
[2]e-mail: ngraho@uns.ac.rs

Abstract. In this paper a modified Zener model of viscoelastic body was used for modeling a polymer gel. The proposed model includes fractional derivatives of contact impact force and elongation as well as restrictions on the coefficients that follow from the second law of thermodynamics. Reimann-Liouville fractional derivatives were approximated numerically using the Grünwald-Letnikov definition. Four coefficients of the model have been calculated by numerical procedure on the basis of the experiment given in [1], where polymer gel in a cylindrical column was collided by a weight in the vertical direction. The acceleration and the displacement of the contact surface were measured during the experiment. Dynamical behavior of the polymer gel modeled by modified Zener model as well as other fractional derivative models given in [1] were compared.

1. Introduction

In recent years polymers have become an engineering structural material of choice due to low cost, ease of processing, weight savings, corrosion resistance and other major advantages. In fact modern polymeric adhesives and polymer matrix composites (PMC) or fiber-reinforced plastics (FRP) are today being used in many severe structural environments of the aerospace, automotive and other industries. The use of polymeric materials pervades our experience both in our daily lives and in our engineering profession.

Fundamental deformation of materials is classified into three types: elastic, plastic, and viscous deformations. Polymeric material shows time-dependent properties even at room temperature. Deformation of metallic materials is also time-dependent at high temperature. One manifestation of the time dependent character of polymers is that they exhibit characteristics of both an elastic solid and that of a viscous fluid. For this reason, materials such as polymers that exhibit such properties are often said to be viscoelastic. Viscoelasticity considers in addition a dissipative phenomenon due to "internal friction," such as between molecules in polymers.

According to [2], not all models which arise in applications are suitable for describing viscoelastic behaviour. The selection of the proper constitutive model from all the available ones plays important role in studying dynamical behaviour of polymers. Because of the fact that stress is proportional to the zeroth derivative of strain for solids and to the first derivative of strain for fluids, it is natural to suppose that for materials that have properties

of both solids and fluids (viscoelastic materials), stress may be proportional to the strain derivative of noninteger order α, where $0 < \alpha < 1$, [3]. Namely, fractional calculus based constitutive models are a powerful extension of the standard integer calculus based models, that offer a new alternative for describing the properties of viscoelastic materials. A number of fractional derivative models have been proposed, see [4], [5], [6] and [7].

Silicone belongs to a large class of polymeric synthetic materials in solid, liquid, or gel form, that usually have resistance to temperature, water, and chemicals, and good insulating and lubricating properties, making them suitable for wide use as oils, water-repellents, resins, etc. It has numerous industrial applications such as vibration isolation, shock absorption, thermal conductivity and many others.

Fukunaga and Shimizu proposed several nonlinear fractional derivative models for describing the properties of a silicone gel and compared them to experimental data of impulsive motion, see [1]. Impact problems in the framework of Hertz type theory and application of fractional derivatives can be seen in [8] and [9]. Our intention was to apply a modified Zener model (which predicts behaviour of viscoelastic materials with significant accuracy, including only four constants) to the experimental data of [1] and to compare it with the ones proposed by Fukunaga and Shimizu. Four constants of the viscoelastic model will be calculated by numerical procedure, and by fitting through experimental data reported in [1]. Good agreement between experimental results and theoretical predictions are expected.

2. The model

Consider a rigid body of mass M moving without rotation in a vertical direction and impacting with a velocity v_0 at $t=0$ against a viscoelastic material, which is fixed on a horizontal surface, Fig. 1. Viscoelastic body is modeled as a straight cylindrical rod of height H and diameter d. The mass of the rod is negligibly small compared to the mass of the rigid body.

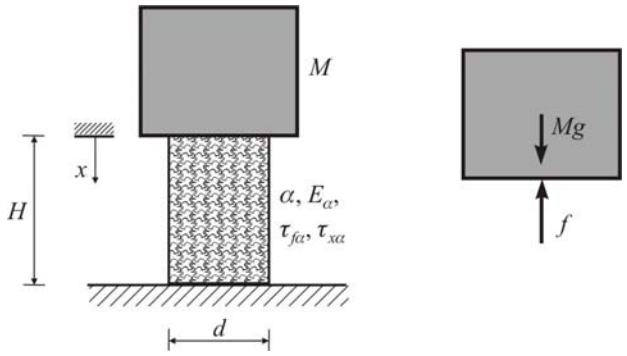

Figure 1. Collision between a rigid body and a viscoelastic rod, free body diagram.

We assume that the viscoelastic rod undergoes uniaxial isothermal affine compression where the deformation is measured by coordinate x and every part of the rod deforms in the same ratio as its bulk.

The differential equation of motion of the body together with initial conditions read

$$Mx^{(2)} = Mg - f, \quad x(0) = 0, \quad x^{(1)}(0) = v_0, \quad f(0) = 0. \tag{1}$$

where we used $(\cdot)^{(k)}=d^k(\cdot)/dt^k$ to denote the k-th derivative with respect to time t, g to denote gravitational acceleration and f to denote the contact force between the rigid body and the viscoelastic rod.

For describing dynamical behaviour of the viscoelastic rod a modified Zener model was used. It comprises fractional derivatives of stress and strain and it has more advantages than model which include integer order derivatives (Zener or Kelvin-Voight model) [2]. The relation between contact force f and displacement x during the compression of the viscoelastic rod reads

$$f + \tau_{f\alpha} f^{(\alpha)} = \frac{E_\alpha A}{H}\left(x + \tau_{x\alpha} x^{(\alpha)}\right), \tag{2}$$

where α is a real number ($0<\alpha<1$), E_α is the modulus of elasticity of the rod, $\tau_{f\alpha}$ and $\tau_{x\alpha}$ are the constants of dimension $[time]^\alpha$. $(\cdot)^{(\alpha)}$ stands for the α-th derivative taken in the standard Riemann-Liouville form:

$$\left[g(t)\right]^{(\alpha)} = \frac{d^\alpha}{dt^\alpha} g(t) = \frac{d}{dt}\left[\frac{1}{\Gamma(1-\alpha)} \int_0^t \frac{g(u)}{(t-u)^\alpha} du\right], \tag{3}$$

Γ denotes the Euler Gamma function. The contact force f is given as $f=A\sigma$ where A is the cross sectional area of the rod and σ is the stress. It is assumed that the cross sectional area remains the same during the deformation. In order to be well behaved it is assumed that coefficients of the model satisfy restrictions, which follow from the second law of thermodynamics [10],

$$E_\alpha > 0, \quad \tau_{f\alpha} > 0, \quad \tau_{x\alpha} > \tau_{f\alpha}. \tag{4}$$

There exists a number of methods for identification of the parameters of fractional models based on stress relaxation and creep experiments and various dynamical tests, see [11], [12], [13], [14] and [15].

We shall use the impulse response of the viscoelastic material in order to determine the four unknown parameters of a modified Zener model (α, E_α, $\tau_{f\alpha}$, $\tau_{x\alpha}$). Experimental data are taken from the paper of Fukunaga and Shimizu [1]. They conducted experiments where mass M impinges against a viscoelastic rod made of a polymer gel (silicone gel, type $\theta - 5$ of Taica Corporation), see Fig.1. In these experiments the acceleration $x^{(2)}$ and the displacement x of the mass m during the collision were measured.

We applied the differential equation of motion Eq. (1) together with the constitutive equation Eq. (2) to the experimental results. Several values of the displacement were

chosen from the experimental impulse response curve presented in Fig. 6 of the paper [1], which were used in the fitting procedure. The least squares method was used for calculation of four unknown parameters (α, E_α, $\tau_{f\alpha}$, $\tau_{x\alpha}$).

3. Identification of the parameters of the modified Zener model

In order to determine the values of four model parameters for describing dynamical behaviour of silicone gel it is necessary to find the solution of Eqs. (1) and (2) together with Eq. (4). To do so the Laplace transform method was used. If $X(s)$ and $F(s)$ are the Laplace transform of $x(t)$ and $f(t)$ respectively, from Eq. (2) one can get

$$F = \frac{E_\alpha A}{H}\frac{1+\tau_{x\alpha}s^\alpha}{1+\tau_{f\alpha}s^\alpha}X, \tag{5}$$

where we have used the standard expression for the Laplace transform of fractional derivative

$$\mathsf{L}\{x^{(\alpha)}(t)\} = s^\alpha X(s) - \left[\frac{1}{\Gamma(1-\alpha)}\int_0^t \frac{x(u)}{(t-u)^\alpha}du\right]_{t=0},$$

where $\mathsf{L}\{x(t)\} = X = X(s)$ and where the term in brackets vanishes if $\lim_{x\to 0^+} z(t)$ is bounded, see [16]. The inversion of Eq. (5) yields the following relation between the contact force $f(t)$ and the displacement $x(t)$

$$f(t) = \frac{E_\alpha A}{H}\left[x(t) + \left(\frac{\tau_{x\alpha}}{\tau_{f\alpha}} - 1\right)\int_0^\infty x'(t-u)e_\alpha(u;\frac{1}{\tau_{f\alpha}})du\right]. \tag{6}$$

In this term $e_\alpha(t;\lambda) = E_\alpha(-\lambda t^\alpha)$ stands for the Mittag-Leffler-type function, see [17] and [18]. Substituting $f(t)$ into Eq. (1) one can obtain that the impact problem is governed by a single integro-differential equation

$$x^{(2)} + \frac{E_\alpha A}{MH}\left[x(t) + \left(\frac{\tau_{x\alpha}}{\tau_{f\alpha}} - 1\right)\int_0^\infty x'(t-u)e_\alpha(u;\frac{1}{\tau_{f\alpha}})du\right] = g,$$

$$x(0) = 0, \quad x^{(1)}(0) = v_0. \tag{7}$$

For computing the solution of the impact problem the numerical method presented in [3] was applied. First of all, by introducing the variable $z(t) = x(t) - v_0 t$ the non-homogeneous initial condition Eq. $(1)_3$ was removed and Eqs. (1) and (2) become

$$mz^{(2)} = mg - f, \quad z(0) = 0, \quad z^{(1)}(0) = 0, \quad f(0) = 0, \tag{8}$$

$$f + \tau_{f\alpha}f^{(\alpha)} = \frac{E_\alpha A}{H}\left(z + v_0 t + \tau_{x\alpha}z^{(\alpha)} + \tau_{x\alpha}v_0\frac{\Gamma(2)t^{1-\alpha}}{\Gamma(2-\alpha)}\right). \tag{9}$$

Secondly, for a time step h, $(t_m = m \cdot h,\ m = 0,1,2,...)$, we take the first and second derivatives as standard difference approximations: $z_m^{(1)} = \left(z_{m+1} - z_m\right)/h$, $z_m^{(2)} = \left(z_{m+1} - 2z_m + z_{m-1}\right)/h^2$, and the fractional derivative in the form

$$u^{(\psi)} = h^{-\psi} \sum_{j=0}^{m} \omega_j u_{m-j}, \tag{10}$$

where ψ is a real number $0 < \psi < 1$, and coefficients $\omega_j\ (j = 0,...,m)$ are calculated by the recurrence relationships:

$$\omega_0 = 1, \quad \omega_j = \left(1 - \frac{\psi + 1}{j}\right)\ \omega_{j-1}, \quad \left(j = 1,\ 2,\ 3,...\right). \tag{11}$$

From Eqs. (8) and (9) using Eqs. (10) and (11) we get the algorithm for obtaining the numerical solution for $m = 1,2,...$

$$f_m = \frac{E_\alpha A}{\left(1 + \tau_{f\alpha} h^{-\alpha}\right) H} \left\{ z_m \left(1 + \tau_{x\alpha} h^{-\alpha}\right) + v_0 mh + \tau_{x\alpha} v_0 \frac{\Gamma(2) t^{1-\alpha}}{\Gamma(2-\alpha)} + \right.$$

$$\left. + h^{-\alpha} \sum_{j=1}^{m} \left[\omega_j \left(\tau_{x\alpha} z_{m-j} - \frac{H}{E_\alpha A} \tau_{f\alpha} f_{m-j} \right) \right] \right\},$$

$$z_{m+1} = h^2 \left(g - \frac{f_m}{M} \right) + 2z_m - z_{m-1}, \tag{12}$$

where $z_0 = z_1 = 0, f_0 = 0.$ Finally the displacement x reads

$$x_m = z_m + v_0 mh, \quad m = 0,1,2,... \tag{13}$$

For the purpose of determination of unknown parameters of the viscoelastic material the displacement x should be defined as a function of time and these four parameters $x = x\left(t,\ \alpha,\ E_\alpha,\ \tau_{x\alpha},\ \tau_{f\alpha}\right)$. Forcing this function to pass through the several points of experimental curve by the least squares method, which means finding the minimum of the following function

$$\vartheta\left(t, \alpha, E_\alpha, \tau_{x\alpha}, \tau_{f\alpha}\right) = \sum_{i=0}^{N} \left[x\left(t_i, \alpha, E_\alpha, \tau_{x\alpha}, \tau_{f\alpha}\right) - x_{EXPi} \right]^2, \tag{14}$$

where x_{EXPi} are experimental values of the displacement in time instants $t_i\ \ (i = 1,2,...,N)$ leads to the values of the model parameters. In the following section E_α is given in MPa, x in mm, $\tau_{x\alpha}$ and $\tau_{f\alpha}$ in s^α, while time t is measured in miliseconds.

4. Results

In this section we interpret the behaviour of a viscoelastic material (silicone gel) during impact by the single integro-differential equation, Eq. (7). In the experiment reported in [1], the viscoelastic specimen was of diameter d=20 mm and height H=5 mm. Mass of the rigid body was M=0.276 kg and initial velocity was v_0=0.77 m/s. By choosing fifteen points from the experimental curve given in Fig. 6. of the mentioned paper, and by applying the suggested numerical procedure the following values of the four parameters of the modified Zener model were obtained:

$$\alpha = 0.74,\ E_\alpha = 0.1195,\ \tau_{x\alpha} = 0.112,\ \tau_{f\alpha} = 0.023. \tag{15}$$

The agreement between predicted and experimental results can be seen in Fig. 2.

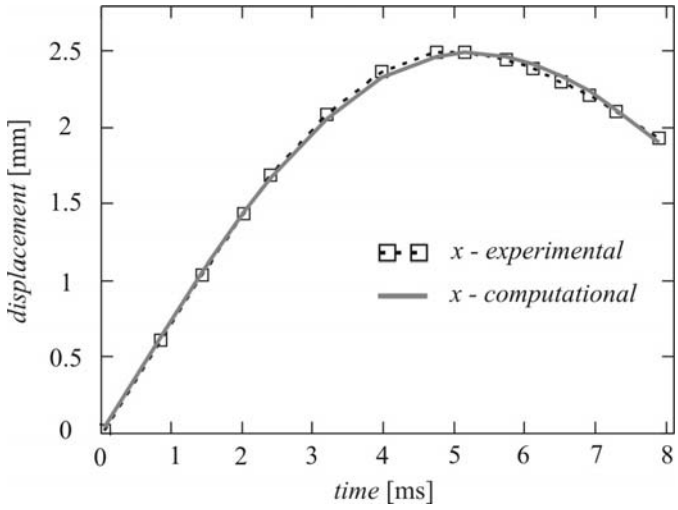

Figure 2. .Predicted and experimental values of the displacement during the impact.

Experimental values of the displacement x during the collision are presented with a dashed line with marks while the values obtained by the fractional model are presented with a solid line. The normalized root mean square error is less than 1.5%. By use of a modified Zener model a good approximation of experimental results was obtain. In addition, important properties of this fractional model are: its simplicity and small number of parameters (α, E_α, $\tau_{f\alpha}$, $\tau_{x\alpha}$).

Several nonlinear fractional-derivative models have been proposed by Fukunaga and Shimizu, see [7] and [19]. Some of these models are suitable for description of the mechanical properties of viscoelastic materials but they require more parameters and model refinement.

5. Conclusion

In this paper we have analyzed impulse response of a polymer gel. A modified Zener model was used to describe mechanical properties of a viscoelastic material during impact. The problem was formulated by a single integro-differential equation, Eq. (7) which was solved numerically. On the basis of experimental data from [1], four parameters of the fractional model were obtained by the fitting procedure described in the section three of this paper. Good agreement between experimental results and theoretical predictions can be seen in Fig. 2.

Stress relaxation and creep tests are usually performed for determination of the coefficients of rheological models. In this paper four parameters of the fractional model were calculated from experimental data of an impact experiment whose duration was much shorter than duration of a stress relaxation or creep experiment. It would be interesting to use the last two mentioned experiments to predict the response of the system and compare these results with ones given in this paper.

Presented results are obtained with the assumption that mass of a viscoelastic rod can be neglected. In cases where the mass must be taken into account, the assumption of affine deformation of the specimen would not be correct because displacement would depend on a position of a point, see [20], [21]. What is more, the bulk of a viscoelastic rod would perform an oscillatory motion which should be measured during experiment in order to get more precise results.

References

[1] Fukunaga M and N Shimizu (2010) Nonlinear fractional-derivative models for viscoelastic materials. II. Comparison of models with experimental data, In: *Proceedings of FDA'10. The 4th IFAC Workshop Fractional Differentiation and its Applications,* Badajoz.

[2] Catania G and Sorrentino S (2007) Analytical modelling and experimental identification of viscoelastic mechanical systems, In: *Advances in fractional calculus: Theoretical developments and applications in physics and engineering* J. Sabatier et al. (Eds.), pp. 403-416.

[3] Podlubny I (1999) *Fractional differential equations*, Academic Press, London.

[4] Rabotnov Y N (1980) *Elements of hereditary solid mechanics*, Mir Publishers, Moscow.

[5] Bagley R L and Torvik P J (1983) A theoretical basis for the application of fractional calculus to viscoelasticity, *J. of Rheology*, **27**, pp. 201-210.

[6] Atanackovic T M (2003) On a Distributed derivative model of a Viscoelastic Body, *Comptes Rendus de L'Academie des Sciences, Paris, Mechanics*, **331(10)**, pp. 687-692.

[7] Fukunaga M and N Shimizu (2010) Nonlinear fractional-derivative models for viscoelastic materials. I. Physics and constitutive equations, In: *Proceedings of FDA'10. The 4th IFAC Workshop Fractional Differentiation and its Applications,* Badajoz.

[8] Atanackovic T M and D T Spasic (2004) On viscoelastic compliant contact-impact models, Transactions of ASME Journal of Applied Mechanics, **71**, pp. 134-138.

[9] Grahovac N M, Zigic M M and Spasic D T (2010) On impact scripts with both fractional and dry friction type of dissipation, In: *Proceedings of FDA'10. The 4th IFAC Workshop Fractional Differentiation and its Applications,* Badajoz.

[10] Atanackovic T M (2002) A modified Zener model of a viscoelastic body, *Continuum Mech. Thermodyn.*, **14**, pp. 137-148.

[11] Petrovic LJ M, Spasic D T and Atanackovic T M (2005) On a mathematical model of a human root dentin, *Dental materials*, **21**, pp. 125-128.
[12] Magnusson S P, Simonsen E B, Dyhre-Poulsen P, Aagaard P, Mohr T and Kjaer M (1996) Viscoelastic stress relaxation during static stretch in human skeletal muscle in the absence of EMG activity, *Scand J Med Sci Sports*, **6**, pp. 323-328.
[13] Nasuno H, Shimizu N and Fukunaga M (2007) Fractional derivative consideration on nonlinear viscoelastic statical and dynamical behavior under large pre-displacement, In: *Advances in fractional calculus: Theoretical developments and applications in physics and engineering* J. Sabatier et al. (Eds.), pp. 363-376.
[14] Lewandowski R and Chorazyczewski B (2010) Identification of the parameters of the Kelvin-Voight and the Maxwell fractional models, used to modeling of viscoelastic dampers, *Computers and Structures*, **88**, pp. 1-17.
[15] Dankuc D V, Kovincic N I and Spasic D T (2010) A new model for middle ear structures with fractional type dissipation pattern, In: *Proceedings of FDA'10. The 4th IFAC Workshop Fractional Differentiation and its Applications,* Badajoz.
[16] Oldham K B and Spanier J (1974) *The fractional calculus*, Academic Press, New York.
[17] Gorenflo R, Luchko Y and Loutchko J (2002) Computation of the Mittag-Leffler function Eαβ(z) and its derivative, *Fractional Calculus & Appl. Anal.*, **5**, pp. 491-518.
[18] Gorenflo R. and Mainardi F (2000) Fractional Calculus: Integral and Differential Equations of Fractional Order. In: *Fractals and Fractional Calculus in Continuum Mechanics*, A. Carpinteri and F. Mainardi (Eds.), pp. 223-276.
[19] Fukunaga M, Shimizu N and Nasuno H (2009) A nonlinear fractional derivative model of impulse motion for viscoelastic materials, *Physica Scripta*, T136, 014010.
[20] Atanackovic T M, Pilipovic S and Zorica D (2011) Distributed-order fractional wave equation on a finite domain. Stress relaxation in a rod, *International Journal of Engineering Science*, **49**, pp. 175-190.
[21] Atanackovic T M, Pilipovic S and Zorica D (2010) Distributed-order fractional wave equation on a finite domain: creep and forced oscillations of a rod, *Continuum Mech. Thermodyn*, s00161-010-0177-2.

HOPKINSON BAR AS MOST USEFULLY TECHNIQUE IN MATERIAL TESTING AT HIGH STRAIN RATE

M. Živković[1], A. Dišić[2]

[1] Faculty of Mechanical Engineering,
The University of Kragujevac, Sestre Janjic 6, 34000 Kragujevac
e-mail: zile@kg.ac.rs
[2] Faculty of Mechanical Engineering,
The University of Kragujevac, Sestre Janjic 6, 34000 Kragujevac
e-mail: aleksandardisic@gmail.com

Abstract. One of the most valid techniques of material testing at high strain rate is Split Pressure Hopkinson bar. Obtained information have one of the main role in many industries like automotive, aerospace, military, structural, etc. Analytical equation of stress, strain and strain rate and numerical modeling of bars and specimen was presented in this paper. The equations that stand behind Hopkinson bar use measurements of the strain in incident and transmitter bar to calculate the stress - strain rate relationship for specimen. Stress waves that propagate trough bars and specimen, need to be acquire at two reference points on both bars. One point is for incident and reflected waves from specimen and other point is for transmitted wave. Numerical modeling of bars and specimen was used to collect strain data in this reference points. Obtained results from simulation for different impact velocity were discussed. Conclusion will be use as relevant data in design of Hopkinson bar set-up.

1. Introduction

Increasing demand in design of structures under extreme dynamic conditions requires determining accurate and reliable material properties at high strain rate. Front structures of passenger vehicle, ballistic and mine protections on military vehicles are one of the main areas that require additional information's that describe mechanical deformation behavior of the material under high strain rate in detail. Collecting that kind of information's, require appropriate experimental set-up. But, because of his complexity, numerical simulations of material tests can be very useful. The LS-DYNA code was applied for finite-element simulations of Split Hopkinson Pressure Bar (SHPB). The use of LS-DYNA helped reduce the number of experimental set-ups and provide answers to initial related design questions such as characteristics of the striker and bars.

2. Propagation of Elastic Wave in Solids

In solids, elastic waves can propagate in four principle modes that are based on the way the particles oscillate. Sound can propagate as longitudinal waves, shear waves, surface waves, and in thin materials as plate waves. Longitudinal and shear waves are the two modes of propagation most widely used in material testing. The most important and basic wave forms, according to [1] in solids are:

• On first place, we have *longitudinal waves*, Fig 1., of compressive or tensile type which cause particle motions along the propagation direction and they are the fastest wave forms in solids. In literature, they are also called *primary waves* and, sometimes, *density waves* because their particle density changes as they move. The longitudinal wave propagation speed is usually denoted by c_L

• The next fastest waves propagating, denoted as c_s, are the *shear* or *secondary waves*, Fig 1. They are causing particle motion perpendicular to the wave propagation. Shear waves require an acoustically solid material for effective propagation and they are relatively weak when compared to longitudinal waves. Also, shear waves are usually generated in materials using some of the energy from longitudinal waves.

• Along the surfaces of solids propagate so called *Rayleigh waves* setting surface particles into elliptic motion.

• In structures of finite bending stiffness *flexural waves* propagate upon dynamic loading.

For mathematical representation of wave propagation in solids, two methods can be established: the momentum equation and equilibrium considerations. The last one will be used to find relations which describe the motion of waves involving the sound speed of the medium as well as displacements and their spatial and time derivatives.

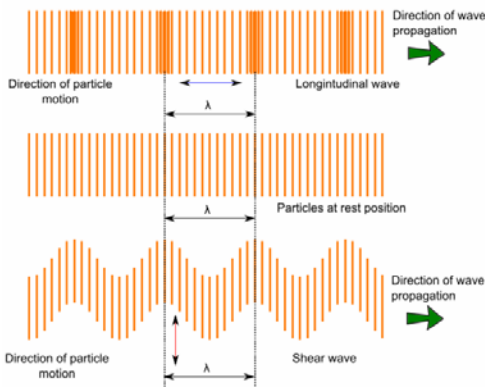

Figure 1. Graphical representation of waves, λ – wave length

3. Hopkinson Bar set-up

Dynamic loading of structures can act with different strain rate level, Fig 2. Proper selection of set-up and instrumentations for various level of strain rate is very important and is not easy. One of the approaches in selecting is defining strain rate level as low, moderate and high strain rate in terms of instrumentations [1]. According to this approach, the low dynamics are considered to be around $\dot{\varepsilon} = 10^2$ [s^{-1}], the moderate regime covers $\dot{\varepsilon} < 10^4$ [s^{-1}] and the high dynamic strain rates are related to shock wave propagation processes with strain rates up to $\dot{\varepsilon} \leq 10^7$ [s^{-1}].

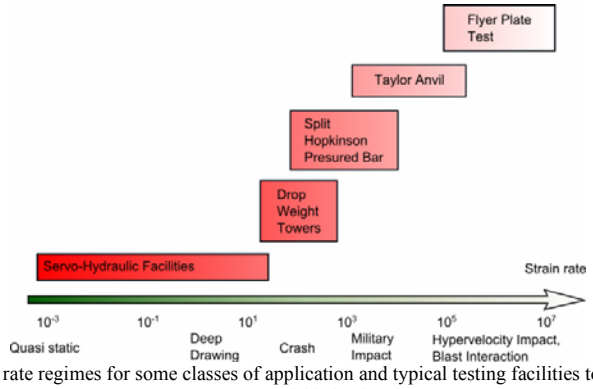

Figure 2. Strain rate regimes for some classes of application and typical testing facilities to characterize the related material behavior, [1]

One of the most adequate set-up to test materials in the strain rate regime between a few hundred and several 10^3 [s^{-1}] is the *Split Hopkinson bar* (SHB). It was first developed by Hopkinson as a single bar facility and the second bar was added by Kolsky, today known as Split Hopkinson Pressure Bar (SHPB), or just Kolsky bar. In meanwhile, there are various variations of the Hopkinson-Kolsky bars which include compressive, tensile and torsion loading form of specimens.

Widely used form of bars is compressive Split Hopkinson Pressure Bar (SHPB) in which a specimen is placed between two bars, an incident and a transmitter bar, Fig. 3. Impacting the incident bar with a striker introduces an acoustic wave propagating towards the specimen. At the interface between incident bar and specimen, the acoustic wave is partly transmitted into the specimen and partly reflected back into the incident bar. The transmitted component travels through the specimen. At the interface to the transmitter bar, again, a partly transmission and reflection takes place. An elastic wave of finally transmitted intensity travels into the transmitter bar. The derivation of stress-strain relations from the set-up uses strain signals measured with stain gages on the incident bar and on the transmitter bar, respectively.

Another, highly interest set-up of Hopkinson bar, was represented in [2]. In this configuration, one bar act as pre-stressed bar for energy storage and in same time as incident bar. After releasing of blocking device, an incident tension pulse propagates through the specimen and transmitter bar on same way as descry ibe above. This set-up will be the part of the future work.

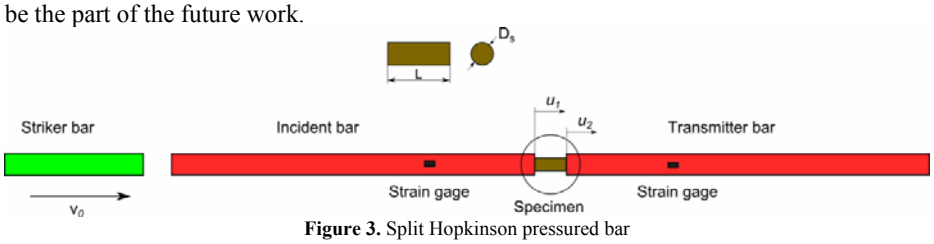

Figure 3. Split Hopkinson pressured bar

3. Equations of wave propagations

Equations that describe one-dimensional propagations of longitudinal wave can be started with the differential element that belongs to one bar [3], Fig. 4. Since the two bars are identical, it is only necessary to consider one of them in developing the equation of motion. The differential element has length dx and cross sectional area A_o. After impact, on all particles that belongs to differential element, act two compression forces F_1 and F_2. For lineal elastic solid, with applications of Hooke's low and linear strain-deformations, according to Newton's second low, equilibrium equation will be

$$A_0 E \frac{\partial u_2}{\partial x} - A_0 E \frac{\partial u_1}{\partial x} = A_0 dx \rho \frac{\partial^2 u_1}{\partial t^2} \tag{1}$$

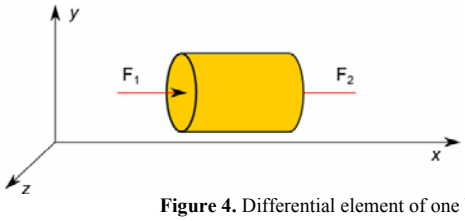

Figure 4. Differential element of one bar

For constant particle acceleration in section of differential element, equation (1) can be simplify

$$C_o^2 \left[\frac{\partial u_2}{\partial x} - \frac{\partial u_1}{\partial x} \right] = \frac{\partial^2 u_1}{\partial t^2} dx \tag{2}$$

Where C_0 is longitudinal wave sound speed

$$C_o = \sqrt{\frac{E}{\rho}} \tag{3}$$

where E and ρ are the bars elastic modulus and mass density, respectively.
Next, displacement imposed on one side of the differential elements in terms of the displacement of the other side, with assumption that rates of displacement of the two sides are equal, is

$$u_2 = u_1 + \frac{\partial u_1}{\partial x} dx \tag{4}$$

After differentiation, this equation becomes

$$\frac{\partial u_2}{\partial x} = \frac{\partial u_1}{\partial x} + \frac{\partial^2 u_1}{\partial x^2} dx \tag{5}$$

By substituting the above term into equation(2), the equation of motion for the bar reduces to

$$C_o^2 \frac{\partial^2 u_1}{\partial x^2} = \frac{\partial^2 u_1}{\partial t^2} \tag{6}$$

3.1 Specimen stress

The average stress in the specimen can be expressed in terms of the forces exerted on each surface of the specimen. When the specimen is sandwiched between the pressure bars forces $F_1(t)$ and $F_2(t)$ exist on the specimen of instantaneous diameter D_S. The average force on the specimen is given by

$$F_{AVG}(t) = \frac{F_1(t) + F_2(t)}{2} \tag{7}$$

and hence the average stress on the cylindrical specimen is given by

$$\sigma_{AVG}(t) = \frac{F_{AVG}(t)}{\pi D_s^2 / 4} \tag{8}$$

The forces at the ends of the pressure bars, for a specimen in dynamic equilibrium, may be expressed in terms of the incident and reflected pressure bar strains as

$$F_1(t) = E\left[\varepsilon_I(t) + \varepsilon_R(t)\right]\frac{\pi D_{BAR}^2}{4} \tag{9}$$

$$F_2(t) = E\varepsilon_T \frac{\pi D_{BAR}^2}{4} \tag{10}$$

where D_{BAR} is the diameter of the pressure bars. Substituting equations(7), (9) and (10) into equation (8) results in an expression for the average stress on the specimen in terms of the pressure bar strains

$$\sigma_{AVG}(t) = \frac{ED_{BAR}^2}{2D_s^2}\left[\varepsilon_I(t) + \varepsilon_R(t) + \varepsilon_T(t)\right] \tag{11}$$

For uniform deformations of specimen, the strains in the incident bar are equal to the strain in the transmitter bar

$$\varepsilon_I(t) + \varepsilon_R(t) = \varepsilon_T(t) \tag{12}$$

The expression for the average specimen stress can be reduced to

$$\sigma_{AVG}(t) = \frac{ED_{BAR}^2}{D_s^2}\varepsilon_T(t) \tag{13}$$

If we are go back to the equation of motion for pressured bar, we can recognize that

$$\frac{\partial^2 u_1}{\partial t^2} = \frac{\partial v}{\partial t} \tag{14}$$

where v is the particle velocity, and

$$E\frac{\partial}{\partial x}\left(\frac{\partial u_1}{\partial x}\right) = \frac{\partial p}{\partial x} \tag{15}$$

where p is the pressure across the cross section, so the equation of motion can be rewritten in terms of the pressure and velocity across the bar cross section as

$$-\frac{\partial p(x,t)}{\partial x} = \rho\frac{\partial v}{\partial t} \tag{16}$$

For a positive traveling, harmonic wave have next form

$$p(x,t) = Pe^{i(\omega t - kx)} \tag{17}$$

where P is the amplitude of the pressure, ω is the frequency, t is the time, k is the wave number and is defined as $k = \frac{\omega}{C_0}$ and x is the spatial location of the wave. Taking the first derivative of equation (17) with respect to x

$$\frac{\partial p(x,t)}{\partial x} = -ikPe^{i(\omega t - kx)} \tag{18}$$

and multiplying right-hand side of equation (6) with heavyside operator, after equaling equations (16) and (18), we can write

$$ikPe^{i(\omega t - kx)} = \rho i\omega v(x,t) \tag{19}$$

Particle velocity is than given by equation

$$v(x,t) = \frac{k}{\rho\omega} Pe^{i(\omega t - kx)} \tag{20}$$

Substituting the expression for k and $p(x,t)$ back into the expression for the particle velocity

$$v(x,t) = \frac{1}{\rho C_o} p(x,t) \tag{21}$$

where P is the pressure across the cross section and for a uniaxial state of stress, the pressure is equal to the stress over the pressure bar cross section, so $p(x,t)$ can be written in terms of the bar strain as

$$p(x,t) = \varepsilon(x,t)E \tag{22}$$

Particle velocity in terms of the bar strain is

$$v(x,t) = C_o\varepsilon(x,t) \tag{23}$$

The average strain rate at any time for specimen with L length is given as

$$\frac{d\varepsilon_s}{dt} = \frac{v_{\text{interface1}} - v_{\text{interface2}}}{L} \tag{24}$$

The velocity at *interface1* is comprised of the incident (+ wave) and the reflected (- wave) as

$$v_{\text{interface1}} = C_o\varepsilon_I - C_o\varepsilon_R = C_o(\varepsilon_I - \varepsilon_R) \tag{25}$$

The velocity at *interface2* is

$$v_{\text{interface2}} = C_o\varepsilon_T \tag{26}$$

By substituting these interface velocities into the expression for the specimen strain rate (24) an expression for the specimen strain rate in terms of the pressure bar strains is

$$\frac{d\varepsilon_s}{dt} = -\frac{C_o(\varepsilon_T - \varepsilon_I + \varepsilon_R)}{L} \tag{27}$$

Negative sign represent compression and if specimen deforms uniformly such that

$$\varepsilon_I(t) + \varepsilon_R(t) = \varepsilon_T(t) \tag{28}$$

the expression for strain rate of specimen can be write as

$$\frac{d\varepsilon_s}{dt} = -\frac{2C_o}{L}\varepsilon_R \tag{29}$$

After integration, specimen strain becomes

$$\varepsilon_s(t) = -\frac{2C_0}{L}\int \varepsilon_R(t)dt \tag{30}$$

4. Numerical model

Numerical simulation was done in LS-DYNA as a general-purpose explicit/implicit finite element code for analyzing the nonlinear dynamic response of three-dimensional inelastic structures [4, 5]. Both, incident and transmitter bar were modeled with a diameter of 10 mm and a length of 3000 mm. The striker had 300 mm in length with the same diameter and the specimen was 6 mm in diameter and 30 mm in length.
An assembly that contains all parts (bars, striker and specimen) was modeled using three-dimensional solid 8-node elements. The incident velocity of the striker was varying from 6 to 20 m/s. In all simulations, a perfect contact between the bars and specimen was assumed and the frictional forces were ignored. Reference points acting as gauges were placed on input and output bars, with the main purpose of collect incident, transmitted and reflected waves. Distance from specimen to reference point on both, transmitter and incident, bars are the same and it is 780mm.
Values of 6, 12 and 18 m/s for impact velocities V_o were chosen. Reflected waves have been recorded in each case and strain rate has been calculated by differentiating in time according to expression (29).

4.1 Material properties
Isotropic elastic material MAT_001 was used to simulate the bars. MAT_003 in LS-DYNA is suited to model isotropic and kinematic hardening plasticity with the option of including rate effects and it was used to simulate specimen material response. This model implies a bilinear stress/strain curve.
Characteristics of the specimen and bar materials are given in Table 1. The materials are Steel and Aluminum, respectively.

Table 2. Material properties used for bars, striker and specimen

Physical properties	**Bars and striker**	**Specimen**
	Steel	**Aluminum**
Density, ρ (kg/m^3)	7.83E+3	2.690 E+3
Yield Strength, σ_y (Pa)	N/R	335 E+06
Elastic Modulus, E (Pa)	2.07 E+11	7.308 E+10
Poisson's Ratio, ν	0.3	0.33
Tangent Modulus, E_t, (Pa)	N/R	645.7 E+06
Failure Strain, f_s	N/R	0.54

N/R: Not Required

4.2 Results and discussion

Progression of the stress wave as a function of time was presented on Fig. 5. in 0.585 ms, 0.593 ms and 0.605 ms of simulation for velocity of 12 m/s. LS-DYNA Post-Processor shows the behavior of the wave propagating in the incident bar, transmitter bar and specimen. When the striker moves with the initial velocity and impacts the incident bar, a one dimensional compressive stress wave which is in a trapezoidal shape is generated in the incident bar as shown in the below Fig. 6. After the impact, the stress wave travels along the bar towards the specimen where same of the wave is reflected back into the incident bar.

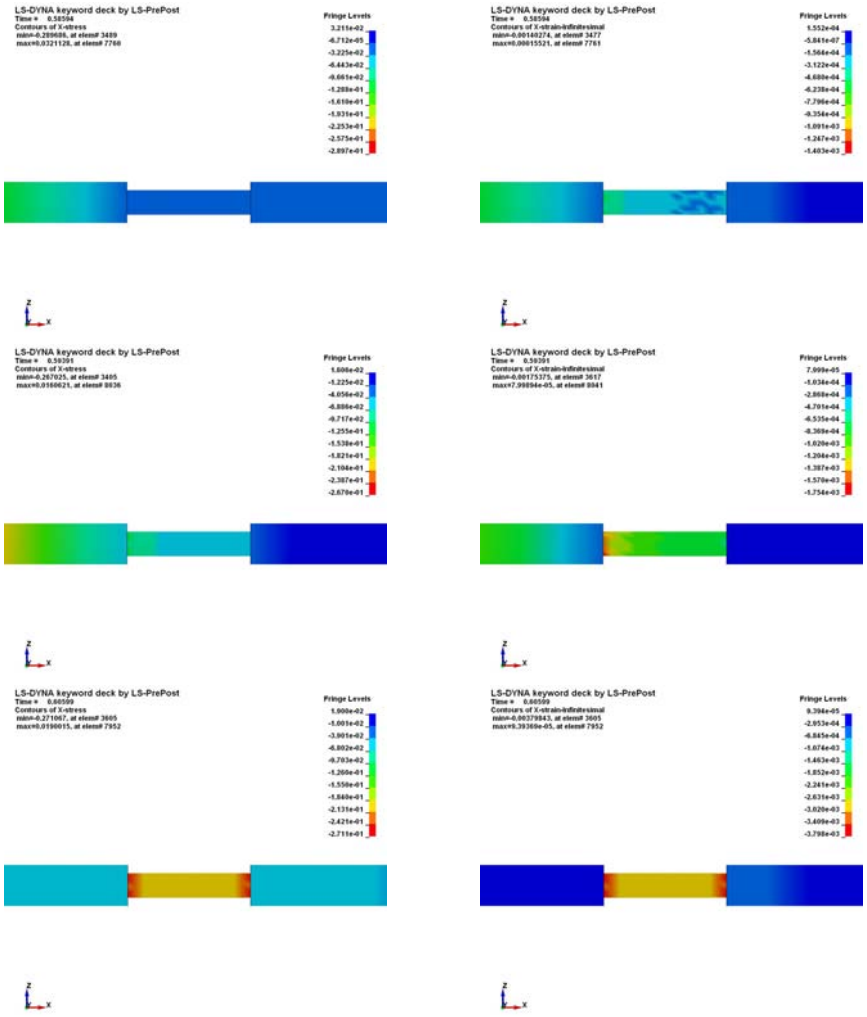

a) Stress propagation b)Strain propagation

Figure 5. Representation of wave propagation in incident bar, specimen and transmitter bar

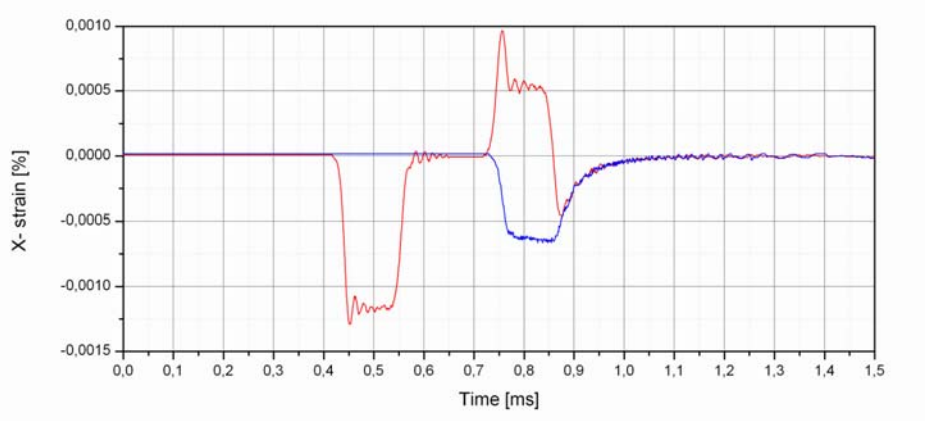

Figure 6. Typical strain propagation through incident and transmitter bar for impact velocity of 12 m/s

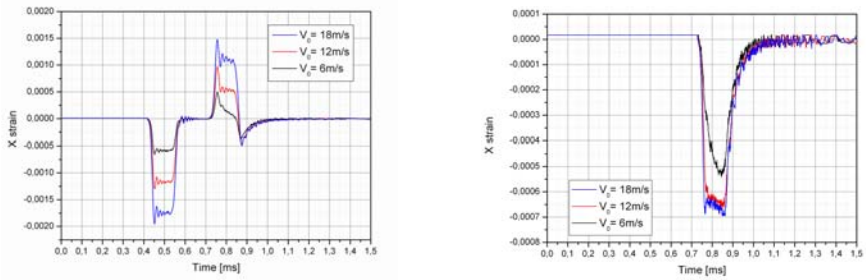

Figure 7. Strain wave in incident and transmitter bars for different impact velocity

Figure 7. presents the strain , ε, values estimated for all three impact velocities (V_0) through the incident and transmitter bars as function of the time. It is evident in this figure the strong dependence that has the strain wave with the impact velocity.

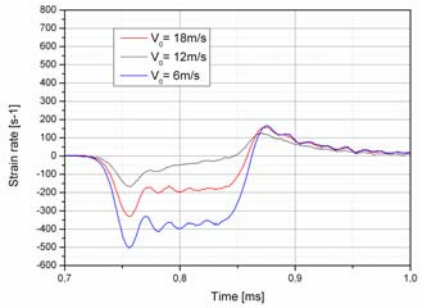

Figure 8. Strain rate wave for different impact velocity

On Figure 8. distinguish strain rates was presented for the range of 100 to 400 s^{-1}. This data is relevant for testing because allow knowing the suitable impact velocities that can be reached and the range within the user could make his selection.

5. Conclusion

Mechanical behavior at high strain rate, e.g. explosive charges, high velocity impact or blast, differs from that observed at quasi-static strain rate. At high strain rates, the material deforms at rates between 10 [s^{-1}] to10^6 [s^{-1}]. The split Hopkinson bar is one of the most common experimental methods used to obtain material properties at high strain rates.
The propagation of elastic waves through the incident and transmitted bars was described by one-dimensional wave theory. Using LSDYNA code, a three-dimensional split Hopkinson pressure bar was modeled.
Three different striker velocities were used in the numerical simulations and the results show that when the velocity of the striker increases, than in same time, the amplitude of the compressive wave generated also increases. The results from this work will be significant to the next step in design on Hopkinson bar with pre-stressed incident bar.

Acknowledgment

The part of this research is supported by Ministry of Education and Science, Republic of Serbia, Grant TR32036.

References

[1] Hiermaier J. S., Structures Under Crash and Impact, *Fraunhofer Institut fur Kuzzeitdynamik*, Freiburg, Germany, 2008.
[2] Albertini C., Cadoni E. and Labibes K, Precision Measurements of Vehicle Crashworthiness by Means of a Large Hopkinson Bar, *European Commission, Joint Research Centre, Institute for Systems, Informatics and Safety, TP 480,* 21 020 Ispra (Va), Italy, 1997.
[3] Kaiser A. M., Advancements in the Split Hopkinson Bar Test, *Faculty of the Virginia Polytechnic Institute and State University*, Blacksburg, Virginia, 1998.
[4] Kojić M., *et al.*, Finite element method I - linear analysis, *Faculty of Mechanical Engineering*, Kragujevac, Serbia, 1998.
[5] LS-DYNA, Keyword user's manuals, Version 971, *Livermore software technology corporation*, Livermore, California, 2007.

ABAQUS SUBROUTINE DEVELOPMENT AND IMPLEMENTATION FOR NEO-HOOK HYPERELASTIC MATERIAL MODEL

M. Živković[1], M. Topalović[2], R. Slavković [3], V. Dunić[4]

[1] Faculty of Mechanical Engineering
Sestre Janjić 6, 34000 Kragujevac, Serbia
e-mail: zile@kg.ac.rs
[2] Faculty of Mechanical Engineering,
Sestre Janjić 6, 34000 Kragujevac, Serbia
e-mail: dtopalovic1@sbb.rs
[3] Faculty of Mechanical Engineering,
Sestre Janjić 6, 34000 Kragujevac, Serbia
e-mail: radovan@kg.ac.rs
[4] Faculty of Mechanical Engineering,
Sestre Janjić 6, 34000 Kragujevac, Serbia
e-mail: dunic@kg.ac.rs

Abstract. ABAQUS solver offers possibility of implementing custom material models which are not implemented in it. These material models are programmed in user subroutine UMAT. In this paper process of creating UMAT subroutine is explained on Neo-Hook hyperelastic material which is implemented in ABAQUS solver. Since existing and well known material is used, validity of UMAT subroutine can be verified. Theory of hyperelastic materials with emphasis on Neo-Hook material model is given. Constitutive equations and stress for Neo-Hook material model are implemented (using FORTRAN programming language) into ABAQUS subroutine UMAT. Entire subroutine code is given with references to the equations discussed in the theory part of the paper. Subroutine and material model is verified on example. At the end of the paper advantages and disadvantages of using UMAT subroutine in ABAQUS analysis are discussed.

1. Introduction

1.1. Definition of hyperelastic materials

Hyperelastic or Green elastic material is a type of constitutive model for ideally elastic material for which the stress-strain relationship derives from a strain energy density function. The hyperelastic material is a special case of a Cauchy elastic material.
For many materials, linear elastic models do not accurately describe the observed material behaviour. The most common example of this kind of material is rubber, whose stress-strain relationship can be defined as non-linearly elastic, isotropic, incompressible and generally independent of strain rate. Hyperelasticity provides a means of modeling the stress-strain behavior of such materials. The behavior of unfilled, vulcanized elastomers often conforms closely to the hyperelastic ideal. Filled elastomers and biological tissues are also often modeled via the hyperelastic idealization.

Ronald Rivlin and Melvin Mooney developed the first hyperelastic models, the Neo-Hook and Mooney–Rivlin solids. Many other hyperelastic models have since been developed. Other widely used hyperelastic material models include the Ogden model and the Arruda–Boyce model.

1.2. Neo-Hook material model

Neo-Hook solid is a hyperelastic material model that is used for describing the stress-strain behavior of materials undergoing large deformations. The model was proposed by Ronald Rivlin in 1948. In contrast to linear elastic materials, the stress-strain curve of a Neo-Hook material is not linear. Instead, the relationship between applied stress and strain is initially linear, but at a certain point the stress-strain curve will lose its steepness due to the release of energy as heat while straining the material. The Neo-Hook model does not account for the dissipative release of energy as heat while straining the material and perfect elasticity is assumed at all stages of deformation. In Neo-Hook hyperelastic material model strain energy density function $\boldsymbol{W}$ is a function of first invariant of the left Cauchy-Green deformation tensor **B**. This strain energy density function is used for expression of Cauchy stress and for derivation of constitutive matrix for Neo-Hook material model.

1.3. Cauchy stress expression and constitutive matrix

For Neo-Hook compressible material strain energy density function is

$$W = C_1\left(\bar{I}_1 - 3\right) + \frac{1}{D_1}\left(J - 1\right)^2 \tag{1}$$

where C_1 and D_1 are empirically derived constants while $\bar{I}_1$ represent strain invariant expressed in terms of the modified left Cauchy-Green tensor $\overline{B}_{ij}$.

$$I_1 = \lambda_1^2 + \lambda_2^2 + \lambda_3^2 \quad ; \quad I_1 = \mathrm{tr}\left(\mathbf{B}\right) = B_{mm} \tag{2}$$

$$\bar{I}_1 = \frac{I_1}{J^{2/3}} \quad ; \quad \bar{I}_1 = \mathrm{tr}\left(\overline{\mathbf{B}}\right) = \overline{B}_{mm} \tag{3}$$

In term $(2)_1$ $\lambda_k\left(k = 1,2,3\right)$ represents principal stretches of **B** while Jacobian J in (1) and $(3)_1$ is determinant of deformation gradient $\mathbf{F}$.

$$J = \det\left(\mathbf{F}\right) \tag{4}$$

Left Cauchy-Green tensor is given with

$$\mathbf{B} = \mathbf{F}\mathbf{F}^{\mathrm{T}} \quad ; \quad B_{ij} = F_{ik}F_{jk} \tag{5}$$

While modified Left Cauchy-Green tensor is

$$\overline{B}_{ij} = \frac{B_{ij}}{J^{2/3}} \tag{6}$$

or in terms of modified deformation gradient

$$\overline{\mathbf{B}} = \overline{\mathbf{F}}\,\overline{\mathbf{F}}^{\mathrm{T}} \quad ; \quad \overline{B}_{ij} = \overline{F}_{ik}\overline{F}_{jk} \tag{7}$$

Modified deformation gradient tensor in equation (7) can be calculated as

$$\overline{\mathbf{F}} = \frac{\mathbf{F}}{J^{1/3}} \qquad ; \qquad \overline{F}_{ik} = \frac{F_{ik}}{J^{1/3}} \tag{8}$$

Cauchy true stress $\boldsymbol{\sigma}$ relation with first Piola-Kirchhoff stress $\mathbf{P}$ is given with equation

$$\boldsymbol{\sigma} = \frac{1}{J}\mathbf{P}\mathbf{F}^{T} \tag{9}$$

First Piola-Kirchhoff stress in terms of strain energy density function is given by

$$P_{kj} = \frac{\partial W}{\partial F_{kj}} \tag{10}$$

Substituting (10) in (9) and calculating partial differentiation $\frac{\partial W}{\partial F_{kj}}$, final expression for Cauchy true stress is

$$\boldsymbol{\sigma} = \frac{2}{J}C_1\left(\overline{\mathbf{B}} - \frac{1}{3}\mathrm{tr}\left(\overline{\mathbf{B}}\right)\mathbf{1}\right) + \frac{2}{D_1}\left(J-1\right)\mathbf{1} \tag{9}$$

or in more convenient index notation

$$\sigma_{ij} = \frac{2}{J}C_1\left(\overline{B}_{ij} - \frac{1}{3}\delta_{ij}\overline{B}_{mm}\right) + \frac{2}{D_1}\left(J-1\right)\delta_{ij} \tag{10}$$

Kirchhoff stress is

$$\boldsymbol{\tau} = J\boldsymbol{\sigma} \qquad ; \qquad \tau_{ij} = J\sigma_{ij} \tag{11}$$

Constitutive matrix C_{ijkl} is calculated by partial differentiation of Kirchhoff stress [4]

$$\mathsf{C}_{ijkl} = \frac{\partial \tau_{ij}}{\partial F_{km}}F_{lm} \tag{12}$$

Substituting Kirchhoff stress with Cauchy stress in (12) while using $(11)_2$ and equality $\frac{\partial J}{\partial F_{km}} = JF^{-1}_{mk}$ we get

$$\mathsf{C}_{ijkl} = J\sigma_{ij}\delta_{kl} + J\frac{\partial \sigma_{ij}}{\partial F_{km}}F_{lm} \tag{13}$$

Calculating partial differentiation $\frac{\partial \sigma_{ij}}{\partial F_{km}}$ using (10) we get constitutive matrix for compressible Neo-Hook material model

$$\mathsf{C}_{ijkl} = \frac{2}{J}C_1\left(\begin{array}{l}\frac{1}{2}\left(\delta_{ik}\overline{B}_{jl} + \overline{B}_{ik}\delta_{jl} + \delta_{il}\overline{B}_{jk} + \overline{B}_{il}\delta_{jk}\right) \\ -\frac{2}{3}\delta_{ij}\overline{B}_{kl} - \frac{2}{3}\overline{B}_{ij}\delta_{kl} + \frac{2}{9}\delta_{ij}\delta_{kl}\overline{B}_{mm}\end{array}\right) + \frac{2}{D_1}\left(2J-1\right)\delta_{ij}\delta_{kl} \tag{14}$$

2. Programming

2.1. UMAT subroutine

Programming of UMAT subroutine is done in Microsoft Visual Studio 2005 with Intel Visual Fortran compiler installed. Entire subroutine code is given in appendix.

3. Verification of UMAT Neo-Hook subroutine

3.1. Example: rubber strip stretching

In this example a $20 \times 20\ mm^2$ rubber strip is clamped and stretched as shown in Figure 1. Strip is $1\ mm$ thick. Because of the symmetry only a quarter of the problem is actually modeled using 100 hybrid formulation hex elements C3D8H. Material is defined as user material with constants $C_1 = 0.4225$; $D_1 = 0.4$ Displacement of nodes for one quarter of a model simulates strip stretching to three times its original length.

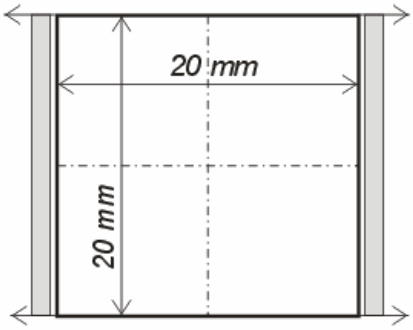

Figure 1. Geometry of rubber strip model

Results of analysis are shown in Figures 2 and 3.
Deformed rubber strip with displacement in x direction is shown in Figure 2.

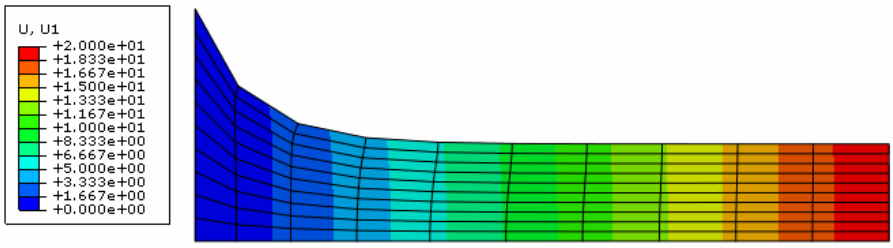

Figure 2. Deformed rubber strip with displacement

Von Misses Stress is shown on figure 3

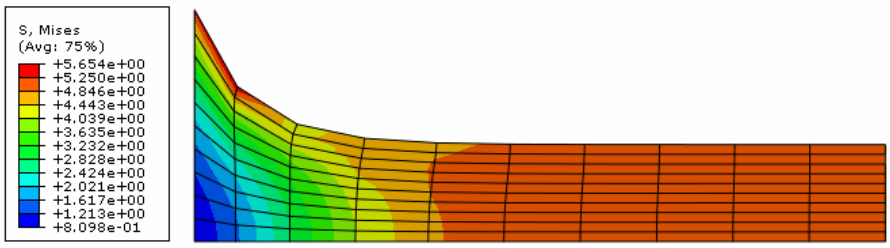

Figure 3. Deformed rubber strip with Von Mises Stress

4. Conclusion

4.1. Advantages and disadvantages of using UMAT subroutine in ABAQUS analysis

Using UMAT subroutine enables testing of new material models on existing FEA software so researchers can focus only on material model. Creation of UMAT requires derivation of Cauchy stress equation and constitutive matrix which is used to formulate relation between stress and deformation. Results of analysis using this UMAT subroutine are identical to results of analysis using built in material model in ABAQUS solver but analysis with subroutine lasted significantly longer. Another disadvantage of using UMAT is that when using beam and shell elements, transverse shear stiffness must be specified, which is automatically calculated by ABAQUS if built-in material model is used. UMAT is a powerful tool for testing and verification of new material models but if material model already exist as an option in ABAQUS, using built-in solution has all advantages. The aim of this paper was to establish methodology of development and testing new material models using well known Neo-Hook material model. Comparison of results from UMAT and built-in material model verify validity of subroutine programming.

Acknowledgment

The part of this research is supported by Ministry of Education and Science, Republic of Serbia, Grant TR32036.

References

[1] ABAQUS Version 6.9 Documentation
[2] Holzapfel G (2001) *Nonlinear Solid Mechanics a Continuum Approach for Engineering*, John Wiley &Sons,Ltd
[3] Bonet J, Wood R(1997) *Nonlinear continuum mechanics for finite element analysis*, Cambridge University Press, Cambridge.
[4] http://solidmechanics.org/text/Chapter8_4/Chapter8_4.htm

APPENDIX subroutine code

```
      SUBROUTINE UMAT(STRESS,STATEV,DDSDDE,SSE,SPD,SCD,
     1 RPL,DDSDDT,DRPLDE,DRPLDT,STRAN,DSTRAN,
     2 TIME,DTIME,TEMP,DTEMP,PREDEF,DPRED,MATERL,NDI,NSHR,NTENS,
     3 NSTATV,PROPS,NPROPS,COORDS,DROT,PNEWDT,CELENT,
     4 DFGRD0,DFGRD1,NOEL,NPT,KSLAY,KSPT,KSTEP,KINC)
C
      INCLUDE 'ABA_PARAM.INC'
C
      CHARACTER*8 MATERL
      DIMENSION STRESS(NTENS),STATEV(NSTATV),
     1 DDSDDE(NTENS,NTENS),DDSDDT(NTENS),DRPLDE(NTENS),
     2 STRAN(NTENS),DSTRAN(NTENS),DFGRD0(3,3),DFGRD1(3,3),
     3 TIME(2),PREDEF(1),DPRED(1),PROPS(NPROPS),COORDS(3),DROT(3,3)
C
C     LOCAL ARRAYS
C ----------------------------------------------------------------
C     BBAR   - MODIFIED LEFT CAUCHY-GREEN TENSOR : EQUATION (7)
C     DISTGR - MODIFIED DEFORMATION GRADIENT : EQUATION (8)
C ----------------------------------------------------------------
C
      DIMENSION BBAR(6),DISTGR(3,3)
C
      PARAMETER(ZERO=0.D0, ONE=1.D0, TWO=2.D0, THREE=3.D0, FOUR=4.D0)
C
C ----------------------------------------------------------------
C     UMAT FOR COMPRESSIBLE NEO-HOOK HYPERELASTICITY
C     CANNOT BE USED FOR PLANE STRESS
C ----------------------------------------------------------------
C     PROPS(1) - C1
C     PROPS(2) - D1
C ----------------------------------------------------------------
C
C     ELASTIC PROPERTIES
C
      C1=PROPS(1)
      D1 =PROPS(2)
C
C     JACOBIAN DETERMINANT OF DEFORMATION GRADIENT
C     TENSOR : EQUATION (4)
C
      DET=DFGRD1(1, 1)*DFGRD1(2, 2)*DFGRD1(3, 3)
     1   -DFGRD1(1, 2)*DFGRD1(2, 1)*DFGRD1(3, 3)
      IF(NSHR.EQ.3) THEN
        DET=DET+DFGRD1(1, 2)*DFGRD1(2, 3)*DFGRD1(3, 1)
     1         +DFGRD1(1, 3)*DFGRD1(3, 2)*DFGRD1(2, 1)
     2         -DFGRD1(1, 3)*DFGRD1(3,1)*DFGRD1(2, 2)
```

```
     3       -DFGRD1(2, 3)*DFGRD1(3, 2)*DFGRD1(1, 1)
      END IF
C
C    MODIFIED DEFORMATION GRADIENT : EQUATION (8)
C
      SCALE=DET**(-ONE/THREE)
      DO K1=1, 3
       DO K2=1, 3
        DISTGR(K2, K1)=SCALE*DFGRD1(K2, K1)
       END DO
      END DO
C
C    CALCULATE MODIFIED LEFT CAUCHY-GREEN TENSOR : EQUATION (7)
C
      BBAR(1)=DISTGR(1, 1)**2+DISTGR(1, 2)**2+DISTGR(1, 3)**2
      BBAR(2)=DISTGR(2, 1)**2+DISTGR(2, 2)**2+DISTGR(2, 3)**2
      BBAR(3)=DISTGR(3, 3)**2+DISTGR(3, 1)**2+DISTGR(3, 2)**2
      BBAR(4)=DISTGR(1, 1)*DISTGR(2, 1)+DISTGR(1, 2)*DISTGR(2, 2)
     1       +DISTGR(1, 3)*DISTGR(2, 3)
      IF(NSHR.EQ.3) THEN
       BBAR(5)=DISTGR(1, 1)*DISTGR(3, 1)+DISTGR(1, 2)*DISTGR(3, 2)
     1        +DISTGR(1, 3)*DISTGR(3, 3)
       BBAR(6)=DISTGR(2, 1)*DISTGR(3, 1)+DISTGR(2, 2)*DISTGR(3, 2)
     1        +DISTGR(2, 3)*DISTGR(3, 3)
      END IF
C
C    CALCULATE THE STRESS : EQUATION (10)
C
      TRBBAR=(BBAR(1)+BBAR(2)+BBAR(3))/THREE
      EG=TWO*C1/DET
      PR=TWO/D1*(DET-ONE)
      DO K1=1,NDI
       STRESS(K1)=EG*(BBAR(K1)-TRBBAR)+PR
      END DO
      DO K1=NDI+1,NDI+NSHR
       STRESS(K1)=EG*BBAR(K1)
      END DO
C
C    CALCULATE THE STIFFNESS MATRIX : EQUATION (14)
C
      EG23=EG*TWO/THREE
      EK=TWO/D1*(TWO*DET-ONE)
      DDSDDE(1, 1)= EG23*(BBAR(1)+TRBBAR)+EK
      DDSDDE(2, 2)= EG23*(BBAR(2)+TRBBAR)+EK
      DDSDDE(3, 3)= EG23*(BBAR(3)+TRBBAR)+EK
      DDSDDE(1, 2)=-EG23*(BBAR(1)+BBAR(2)-TRBBAR)+EK
      DDSDDE(1, 3)=-EG23*(BBAR(1)+BBAR(3)-TRBBAR)+EK
      DDSDDE(2, 3)=-EG23*(BBAR(2)+BBAR(3)-TRBBAR)+EK
```

```
      DDSDDE(1, 4)= EG23*BBAR(4)/TWO
      DDSDDE(2, 4)= EG23*BBAR(4)/TWO
      DDSDDE(3, 4)=-EG23*BBAR(4)
      DDSDDE(4, 4)= EG*(BBAR(1)+BBAR(2))/TWO
      IF(NSHR.EQ.3) THEN
        DDSDDE(1, 5)= EG23*BBAR(5)/TWO
        DDSDDE(2, 5)=-EG23*BBAR(5)
        DDSDDE(3, 5)= EG23*BBAR(5)/TWO
        DDSDDE(1, 6)=-EG23*BBAR(6)
        DDSDDE(2, 6)= EG23*BBAR(6)/TWO
        DDSDDE(3, 6)= EG23*BBAR(6)/TWO
        DDSDDE(5, 5)= EG*(BBAR(1)+BBAR(3))/TWO
        DDSDDE(6, 6)= EG*(BBAR(2)+BBAR(3))/TWO
        DDSDDE(4,5)= EG*BBAR(6)/TWO
        DDSDDE(4,6)= EG*BBAR(5)/TWO
        DDSDDE(5,6)= EG*BBAR(4)/TWO
      END IF
      DO K1=1, NTENS
        DO K2=1, K1-1
          DDSDDE(K1, K2)=DDSDDE(K2, K1)
        END DO
      END DO
C
C     END OF USER SUBROUTINE
C
      RETURN
      END
```

NUMERICAL SIMULATION OF MECHANICALLY FASTENED JOINTS BY FINITE ELEMENTS

Ivana Ilić[1], Mirjana Djuric[1]

[1] Military Technical Institute
Ratka Resanovića 1, 11000 Belgrade, Serbia
e-mail: ivilic76@yahoo.com

Abstract: The weakest parts of a composite laminate structure are often the joints. Hence the need to design reliable and efficient load-carrying joints has become increasingly important. This study deals with the bearing strength, failure mode and failure load in laminated composite plate with circular hole subjected to a traction force by a rigid pin. The investigation is focused on developing reliable computation procedure to analyze initial failure load for pin-loaded holes at the layered composite structures. Finite element method (FEM) is used to determine stress distribution around the fastener hole. Combining Chang-Scott-Springer characteristic curve model and Tsai-Wu initial failure criterion is used to determine initial failure load of mechanically fastened joint. Special attention in this work is focused on pin-load distributions and it's the effects on load level of failure and its location. The local contact between the mechanical fastener and the composite laminate may induce large strains, high stress concentration and delamination failure near the contact edge of a hole and eventually failure of the laminate. Initial failure analysis were carried out using cosine distribution and contact finite element pin/lug models between pin/lug mechanically fastened joint. The computation results are compared with own and available experimental results. Good correlations were obtained.

1. Introduction

It is well known that mechanically fastened joints play important role in structures that have to be detached or easily replaced. Since structural failure can be coursed by failure of joint it is obvious that strength of a joint is an important characteristic of every structure.
Because joints represent potential weak points in the structure, the design of the joint can have a large influence over the structural integrity and load-carrying capacity of the overall structure. Methods for analysis of composite joints include analytical methods and finite element methods [6-23].
Some of the earlier studies [15-17, 24]. In later studies, explicit modeling of contact between the bolt and hole has been used. [19-21, 23]. In these cases, nonlinear finite element codes were needed to solve for the continuously changing boundary conditions brought about by changes in contact between the bolt and laminate. Some authors modeled the bolt as a rigid cylindrical contact surface [20, 21], while others considered it as elastic and modeled it with three-dimensional finite elements [19, 23].
To evaluate the strength of the mechanically fastened joints, several prediction methods have been proposed [1–17]. One of the main prediction methods is Chang`s model. In this model the joint is taken to have failed when certain combined stresses have exceeded a prescribed value in any of the plies along the characteristic curve. The combined stress limit is evaluated using Yamada–Sun failure criterion [1–6]. Other main prediction method is progressive damage model. In this model, the logical methodology for modeling the joint

problem is composed of three important steps: stress analysis, failure criteria and property degradation rules. Stress distributions in the plate are calculated and then a failure criterion is tested. If there is no failure, the load is increased. In the case of failure, material properties of failure nodes are reduced to an appropriate property degradation rules. Stresses are then redistributed at the same load and re-examined for any additional failures. The procedure continues until a point where excessive damage is reached [7–17]. In earlier works, Icten et al. [14] established the behavior of mechanically fastened joints in woven glass-epoxy composites with $[(0/90)3]_s$ and $[(\pm 45)3]_s$ material configurations. The failure analysis based on Hashin and Hoffman criteria was performed and compared with experimental results. Okutan and Karakuzu [15] studied on the response of pin loaded laminated E/glass-epoxy composites for two different ply orientations such as $[0/\pm 45]_s$ and $[90/\pm 45]_s$. The objective of this work is to study the behavior of graphite-epoxy pin loaded joints both numerically and experimentally, with particular attention given to the sensitivity of the model to different geometric dimensions. The two-dimensional finite element method was used to obtain stress distribution of the material. To determine the failure load and failure mode progressive damage prediction model was selected with Tsai-Wu Criteria. The mechanical properties of the composite material are obtained from standard tests [9, 10, 20, 21].

2. Problem description

In this analysis, based on the Chang et al. strength prediction model [1], the point stress failure criterion will be used to evaluate the characteristic lengths in tension and compression and a two-dimensional finite element analysis used to evaluate the stress distribution in the vicinity of the joint.

A practical method considered to predict the failure load of composite joints with the least amount of testing is the characteristic length method. This method was proposed by Whitney and Nuismer [24, 25], and has been developed by Chang et al. [3–8]. It is still used for the failure analysis of composite joints [26]. In the characteristic length method, two parameters, i.e. compressive and tensile characteristic length should be determined by the stress analysis associated with the results of bearing and tensile tests on the laminates with and without hole. Once the characteristic lengths are determined, an artificial curve connecting the compressive and tensile characteristic lengths named characteristic curve is assumed [1]. Failure of a joint is evaluated on the characteristic curve, not on the edge of the fastener hole. In this method the joint is taken to have failed when certain combined stresses have exceeded a prescribed in any of the plies along the characteristic curve.

In order to evaluate the strength of composite pinned joints, Fig. 1, the stress distribution along a characteristic dimension around the hole must first be evaluated. The conditions for failure can then be predicted with the aid of an appropriate failure criterion. The Tsai-Wu and Yamada-Sun failure criterions were used for analysis.

Failure envelope in the general case can be written as:

$$F_i\sigma_i + F_{ij}\sigma_i\sigma_j = 1, \qquad i,j = 1,2,...,6$$

where F_i, F_{ij} are longitudinal and transverse tensile/compressive strengths, $\sigma_i\,(i=1,2,3)$ are normal stress komponents with respect to material principal axes and $\sigma_i\,(i=4,5,6)$ are shear stress components.

In case of orthotropic ply subjected in-plane loads Tsai-Wu initial failure criteria can be written as:

$$(F.I) = F_1\sigma_1 + F_2\sigma_2 + F_6\sigma_6 + F_{11}\sigma_1^2 + F_{22}\sigma_2^2 + F_{66}\sigma_6^2 + 2F_{12}\sigma_1\sigma_2 \quad (1)$$

$$F_1 = \frac{1}{X_t} + \frac{1}{X_c} \qquad F_2 = \frac{1}{Y_t} + \frac{1}{Y_c} \qquad F_2 = \frac{1}{Y_t} + \frac{1}{Y_c} \qquad F_{12} = 0$$

$$F_{11} = -\frac{1}{X_t X_c} \qquad F_{22} = -\frac{1}{Y_t Y_c} \qquad F_{22} = -\frac{1}{Y_t Y_c}$$

where *F.I* is failure index, $X_{t,c}, Y_{t,c}$ are longitudinal and transverse tensile/compressive strengths of unidirectional lamina and S is the ply shear strength.
Yamada-Sun failure criterion can be written as:

$$(F.I.) = \left(\frac{\sigma_1}{X_t}\right)^2 + \left(\frac{\sigma_6}{S}\right)^2 \quad (2)$$

In this model, failure is expected to occur when the value of F.I is greater than or equal to unity.
Two geometry types of mechanical joints (metal/composite)

- composite plate (shown in Figure 1)
- composite tube (shown in Figure 2).

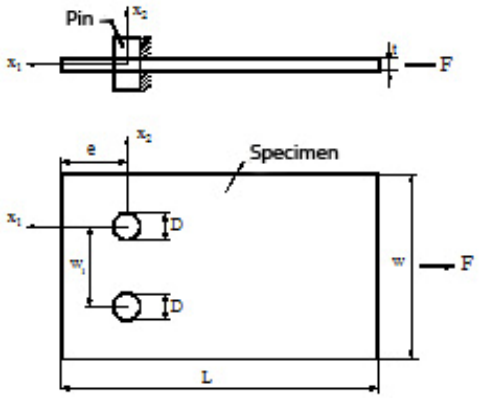

Fig. 1. Composite plate geometry

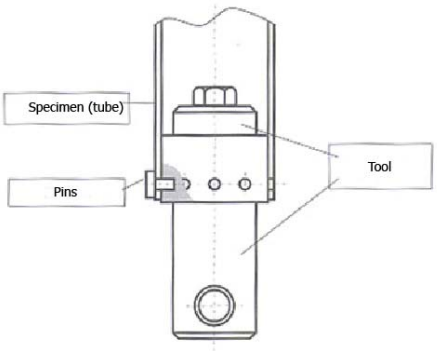

Fig. 2. Composite tube geometry

Basic difference in behavior of composite joints in regard to joints made of isotropic materials is failure location. While failure of joints made of isotropic materials occurs at the point of contact, for composite joints failure is located at certain distance from the contact point and is defined by characteristic curve.

The characteristic curve is an artificial curve made of compressive and tensile characteristic lengths. Since the characteristic lengths are determined just for pure compression and tension, other combined failure modes are evaluated on the characteristic curve.

A popular method to construct the characteristic curve is proposed by Chang and Scott [1]. The characteristic curve is expressed as follows:

$$r_c(\theta)=R+R_t+(R_c-R_t)\cos\theta \tag{3}$$

where R_{oc} and R_{ot} are compressive and tensile characteristic lengths, respectively. The angle θ is measured counterclockwise or clockwise from the loaded direction toward the sides of the fastener hole as shown in Fig. 3.

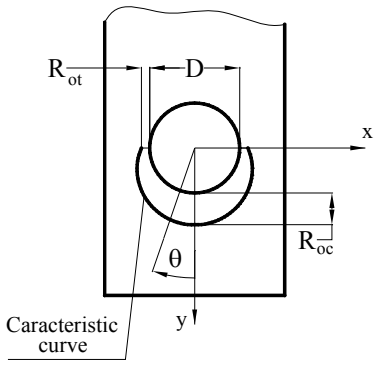

Fig. 3. Characteristic curve schematic diagram

3. Numerical verification

3.1 Numerical validation of mechanically fastened joints at composite plates

To determine failure load of mechanical fastened joint the procedure is composed of stress analysis and failure analysis using adequate initial failure criteria along characteristic curve. The strategy for the finite element modeling of the joints is the same as in the finite element model of the laminate for bearing tests shown in Fig. 4. Nonlinear finite element analysis for the joints is conducted by MSC/NASTRAN [27]. Interface between fasteners and laminates is modeled by the slide line contact element provided by the software. The slide line element in MSC/NASTRAN was adopted to simulate the contact between the pins and the laminates. For this case, one-half of plate was modeled. The pin and the laminate were modeled using CQUAD4 shell elements.
Force was applied to the pin as uniformly distributed load. A typical finite element model of the mechanically fastened joint is shown in Fig. 4.

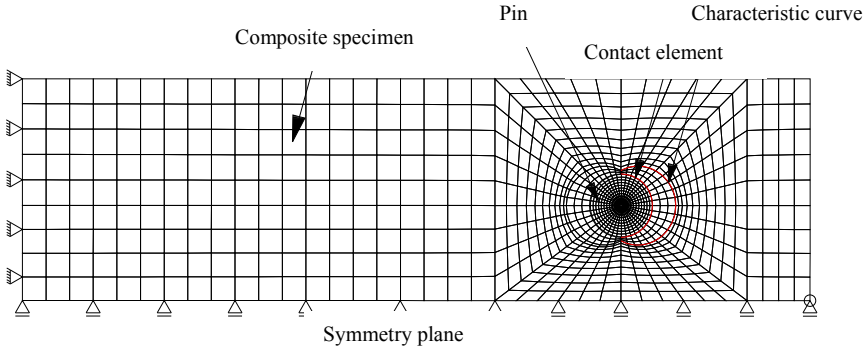

Fig. 4. Finite element model of mechanically fastened joint (plate)

In this paper the problem of mechanically fastened joints of a laminated composite plate with frictional contact conditions are analyzed. Coulomb friction law is used and the contact constraints are handled by extended interior penalty methods. The perturbed variation principle is adopted to treat the non-differential term due to the coulomb friction. The computed results by our formulations are compared with experiment results.
To validate computation procedure of mechanical fastened joints numerical examples are included. Geometry properties of mechanical fastened joint at composite structure are shown in Fig. 1 and in Table 3. Finite element model of contact problem of pin-loaded joint is shown in Fig. 4. Lug and pin are made from CFC composite and steel materials, respectively. Mechanical properties of these materials are given in Tables 1 and 2.

Table 1: Mechanical properties of CFC material

Longitudinal Young's Modulus	$E_{11}=14686\frac{daN}{mm^2}$
Transverse Young's Modulus	$E_{22}=1172\frac{daN}{mm^2}$
Shear Modulus	$G_{12}=618\frac{daN}{mm^2}$
Pooission's Ratio	$\nu=0.3$
Longitudinal Tensile Strength	$F_{11}^{T}=136.2\frac{daN}{mm^2}$
Longitudinal Compressive Strength	$F_{11}^{C}=133\frac{daN}{mm^2}$
Transverse Tensile Strength	$F_{22}^{T}=4.2\frac{daN}{mm^2}$
Transverse Compressive Strength	$F_{22}^{C}=17.2\frac{daN}{mm^2}$
Rail Shear Strength	$F_{12}=4.9\frac{daN}{mm^2}$
One Layer Thickness	$t=0.13\,mm$

Table 2: Mechanical properties of pin

Young's Modulus	$E_{12}=21000\frac{daN}{mm^2}$
Shear Moduluss	$G_{12}=8140\frac{daN}{mm^2}$
Pooission's Ratio	$\nu=0.29$
Ultimate Tensile Strength	$\sigma_{doz}=125\frac{daN}{mm^2}$
Ultimate Shear Strength	$\tau_{doz}=80\frac{daN}{mm^2}$
Static Friction Coefficient	$\mu=0.25$

Table 3. Geometrical characteristics of mechanically fastened joint

Width of specimen	$w=56\,mm$
Distance between holes	$w_1=24\,mm$
Diameter of holes	$d=8\,mm$
Height of specimen	$L=100\,mm$
Distance from edge of specimen to center of hole	$e=24\,mm$
Specimen thickness	$t=3.9\,mm$

Comparison of numerical and experimental results is shown in Table 4. Distribution of Failure Index for experimentally and numerically calculated failure load are shown on Fig. 5-8.

Table 4. Comparisons computation with experimental results

Stacking sequence	$\begin{bmatrix} \pm 45°/0°_3/\pm 45°/0°/ \\ 90°/0°_2/\pm 45°/0°_2 \end{bmatrix}_S$
Tensile characteristic length	$R_{ot}=0.437\,mm$
Compressive characteristic length	$R_{oc}=2.949\,mm$
Experimental failure load	$F^{exp}=2300\,daN$
Failure Index for experimental load	$F.I.^{exp}=0.98$
Numerical failure load	$F^{num}=2320\,daN$
Failure Index for numerical load	$F.I.^{num}=1$
Difference between F^{exp} and F^{num}	0.9 %
Failure mode	tension

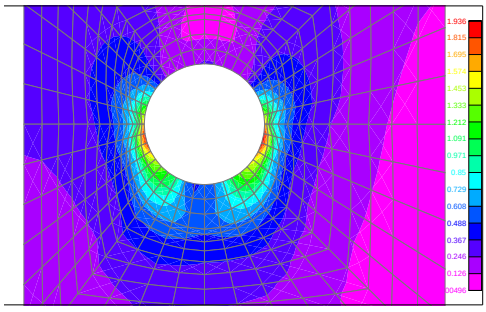

Fig 5. Distribution of F.I. at composite lug for experimental failure load (F=2300 daN)

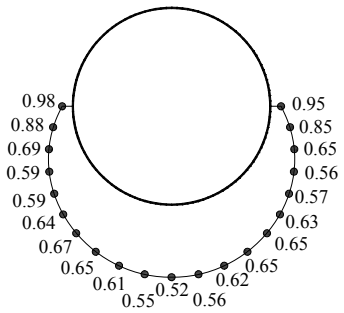

Fig 6. Distribution of F.I. along characteristic curve for experimental failure load (F=2300 daN)

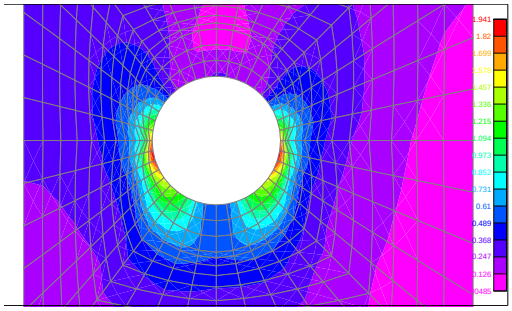

Fig 7. Distribution of F.I. at composite lug for numerical failure load (F=2320 daN)

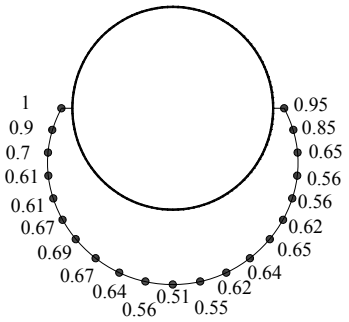

Fig 8. Distribution of F.I. along characteristic curve for numerical failure load (F=2320 daN)

3.2 Numerical validation of mechanically fastened joints at composite tubes

Composite tube/steel pin configuration of the mechanical joints was considered. Strength analysis was performed in MSC/NASTRAN software. Material of the tube is aramid/epoxy. Composite tubes were modeled using CQUAD4 plate elements. The cosine load distribution was used to simulate the contact between the pins and composite tubes. Finite element mesh for composite tube with 4 and 12 holes is shown in Figure 9.

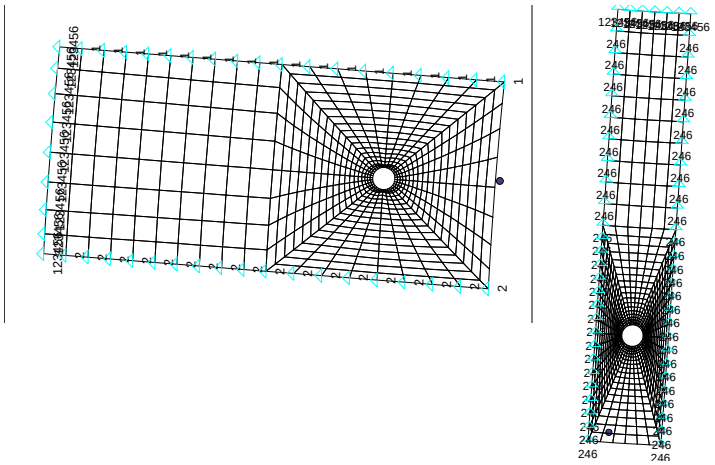

Fig. 9. Finite element model of mechanically fastened joint (tubes)

Mechanical properties of aramid composite material is given in Table 5. Geometrical properties of composite tubes with 4 and 12 pins are given in Table 6.

Table 5. Mechanical properties of aramid/epoxy material

Longitudinal Young's Modulus	$E_{11} = 2390\,daN/mm^2$
Transverse Young's Modulus	$E_{22} = 0.231\,daN/mm^2$
Shear Modulus	$G_{12} = 7.95\,daN/mm^2$
Poisson's Ratio	$\nu = 0.3$
Longitudinal Tensile Strength	$F_{11}^t = 75.91\,daN/mm^2$
Longitudinal Compressive Strength	$F_{11}^c = 13.82\,daN/mm^2$
Transverse Tensile Strength	$F_{22}^t = 1.105\,daN/mm^2$
Transverse Compressive Strength	$F_{22}^c = 4.63\,daN/mm^2$
Rail Shear Strength	$F_{12} = 1.26\,daN/mm^2$
One Layer Thickness (angle 90°)	$t_{90^0} = 0.4\,mm$
One Layer Thickness (angle 61°)	$t_{\pm 61^0} = 1.1\,mm$
Tensile Characteristic Length	$R_t = 0.459\,mm$
Compressive Characteristic Length	$R_c = 2.469\,mm$

Table 6. Geometric characteristic of composite tubes

Number of pins	Stacking sequence	Inner diameter (mm)	Outer diameter (mm)	Length (mm)	Pin diameter (mm)
4 (4P)	$[90/\pm 61/90]$	64.2	70.2	250	5
12 (12P)	$[90/\pm 61/90]$	64.2	70.2	250	5

Distribution of Failure Index for numerically calculated failure load are shown on Fig. 10-11.

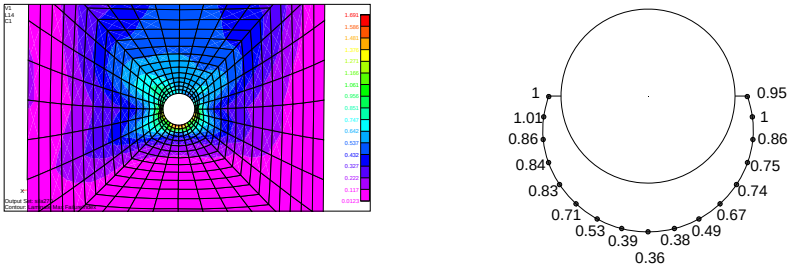

Fig. 10. Distribution of F.I. at composite tube 4P and along characteristic curve for numerical failure load (F=270daN)

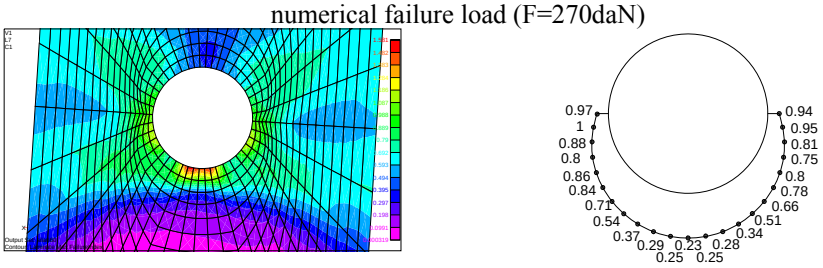

Fig. 11. Distribution of F.I. at composite tube 12P and along characteristic curve for numerical failure load (F=660daN)

Experimental results for 4P and 12P type tubes are shown in Fig. 12-13.

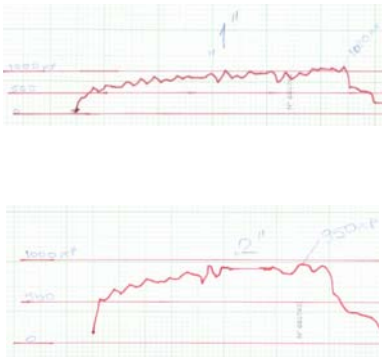

Fig. 12. Experimental load for 4P tubes

Fig. 13. Experimental load for 12P tubes

Fig. 14. Picture of specimens with 12 and 4 pins

In Table 7. is given comparison between numerical and experimental failure load for composite tubes.

Table 7. Comparisons computation initial failure load at the composite tube with experiments

Specimen	Experimental failure load (daN)	Computation failure load (daN)	Difference between experimental and computation failure load
4 pins	346	270	22 %
12 pins	796	660	17 %

4. Conclusions

In this paper, a numerical and experimental study on the failure load and failure mode of pin loaded composite joints at the composite plates and the composite tubes is presented. In numerical study, a Tsai-Wu failure criterion is used to predict the initial failure load and failure mode. Computation analysis was performed to evaluate failure of pin loaded composite joints based on the Chang Scott–Springer characteristic curve model using the Tsai-Wu failure criterion and finite element stress analysis. In this investigation initial

failure analysis were carried out using cosine distribution and contact finite element pin/lug models between pin/lug mechanically fastened joint. The computation results are compared with own and available experimental results. Good correlations were obtained.

REFERENCES

[1] Chang F.K., Scott R.A., Springer G.S., Strength of mechanically fastened composite joints, J Compos Mater 1982; 16:470–94.
[2] Maksimović S., Ilić I., Failure Analysis of Composite Pin Loaded Joints, Technical Diagnostics, Vol. 4, No. 3-4, 2005.
[3] Chang F.K., The effect of pin load distribution on the strength of pin loaded holes in laminated composites, J Compos Mater 1986; 20: 401–8.
[4] Chang F.K., Scott R.A., Springer G.S., Failure of composite laminates containing pin loaded holes—method of solution, J Compos Mater 1984; 18: 255–78.
[5] Maksimović S., Some computational and experimental aspects of the optimal design process of composite structures, Int. J. of Composite Structures, Vol. 16. pp. 237-258, 1990.
[6] Wu T.J., Hahn T., The bearing strength of E-glass/vinylester composites fabricated by Vartm, Compos Sci Technol 1998; 58: 1519–29.
[7] Ilic I., Numerical Simulation of Composite Structure Failure in the Areas of Geometric Discontinuities, Scientific Technical Rewiew, Vol. LVIII, No. 2, Belgrade, 2008. ISSN 1820-0206, page 32-37
[8] Lessard L.B., Shokrieh M.M., Two-dimensional modelling of composite pinned-joint failure. J Compos Mater 1995; 29: 671–97.
[9] Aktas A., Karakuzu R., Failure analysis of two-dimensional carbon-epoxy composite plate pinned joint, Mech Compos Mater Struct 1999; 6: 347–61.
[10] Icten B.M., Karakuzu R., Progressive failure analysis of pin-loaded carbon-epoxy woven composite plates. Compos Sci Technol 2002; 62: 1259–71.
[11] Camanho P.P., Matthews F.L., A progressive damage model for mechanically fastened joints in composite laminates, J Compos Mater 1999; 33: 2248–80.
[12] Okutan B., Karakuzu R., The failure strength of pin-loaded multidirectional fiber-glass reinforced epoxy laminate, J Compos Mater 2002;36:2695–712.
[13] Lin H.J., Tsai C.C., Failure analysis of bolted connections of composites with drilled and moulded-in hole, Compos Struct 1995; 30: 159–68.
[14] Icten B.M., Okutan B., Karakuzu R., Failure strength of woven glass fiber-epoxy composite pinned joint, J Compos Mater 2003; 36: 1337–51.
[15] Okutan B., Karakuzu R., The strength of pinned joints in laminated composite plates, Compos Sci Technol 2003; 63: 893–905.
[16] Okutan B., The e.ects of geometric parameters on the failure strength for pin-loaded multi-directional fiber-glass reinforced epoxy laminate, Compos Part B 2002; 33: 567–78.
[17] Pierron F., Cerisier F., A numerical and experimental study of woven composite pin-joints, J Compos Mater 2000;34:1028–54.
[18] Maikuma H., Kobomura K., Bearing strength and damage progress for PAN-based and pitch based carbon fiber composites, J Compos Mater 1993; 27: 1739–61.
[19] Okutan B., Aslan Z., Karakuzu R., A study of the e.ects of various geometric parameters on the failure strength of pin-loaded wovenglass- fiber reinforced epoxy laminate, Compos Sci Technol 2001; 61: 1491–7.

[20] Jones R.M., Mechanics of composite material. Philadelphia: Taylor & Francis; 1999.
[21] Gibson R.F., Principals of composite material mechanics, McGraw-Hill; 1994.
[22] Chandrupatla T.R., Belengundu A.D., Introduction to finite elements in engineering, Prentice-Hall; 2002.
[22] Chandrupatla T.R., Belengundu A.D., Introduction to finite elements in engineering, Prentice-Hall; 2002.
[23] Bathe K.J., Finite element procedures in engineering analysis, Englewood Cliffs, NJ: Prentice-Hall; 1996.
[24] Whitney J.M., Nuismer R.J., Stress fracture criteria for laminated composites containing stress concentration. J Compos Mater 1974;10:253–65.
[25] Nuismer R.J., Labor J.D., Application of the average stress failure criterion: Part II: Compression. J Compos Mater 1978;12:49–60.
[26] Whitworth H.A., Othieno M., Barton O., Failure analysis of composite pin loaded joints. Compos Struct 2003;59:261–6.
[27] MSC/NASTRAN, Theoretical Mannuals